# Modified 2D $MoS_2$ and $SnS_2$ Flakes for Sensing Applications

*A Thesis submitted by*

**Ashok Kumar**

*in partial fulfillment of the requirements for the award of the degree of*

**Doctor of Philosophy**




**Indian Institute of Technology Jodhpur**
**Electrical Engineering**

*December 2024*

# Declaration

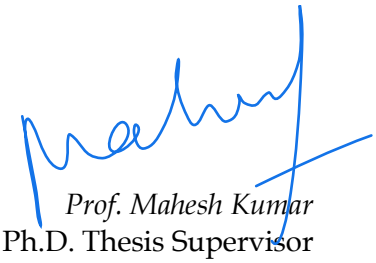
I hereby declare that the work presented in this Thesis titled ***Modified 2D $MoS_2$ and $SnS_2$ Flakes for Sensing Applications*** submitted to the Indian Institute of Technology Jodhpur in partial fulfilment of the requirements for the award of the degree of Doctor of Philosophy, is a bonafide record of the research work carried out under the supervision of Professor Mahesh Kumar. The contents of this thesis in full or in parts, have not been submitted to, and will not be submitted by me to, any other Institute or University in India or abroad for the award of any degree or diploma.



*Ashok Kumar*
P19EE203

# Certificate

This is to certify that the thesis titled ***Modified 2D $MoS_2$ and $SnS_2$ Flakes for Sensing Applications***, submitted by *Ashok Kumar* (P19EE203) to the Indian Institute of Technology Jodhpur for the award of the degree of *Doctor of Philosophy*, is a bonafide record of the research work done by him under my supervision. To the best of my knowledge, the contents of this report, in full or in parts, have not been submitted to any other Institute or University for the award of any degree or diploma.



*Prof. Mahesh Kumar*
Ph.D. Thesis Supervisor
Department of Electrical Engineering
IIT Jodhpur, India

# Acknowledgements

First, I would like to express my sincere gratitude to my supervisor, *Professor Mahesh Kumar*, for his consistent guidance and motivation. He has been a constant support of encouragement, and his exceptional research aptitude plays a crucial role in the success of this thesis work. Without his support, this work would not have been possible. He is always open to discussion and tried his best to provide a good research environment and facilities to work in the lab. I acquired valuable insights from him about investigating and interpreting experimental data, and his confidence in my work inspired me to strive for better outcomes. He always pushes to think high and achieve goals in life. It was an incredibly fortunate and unforgettable experience to have the opportunity to work under his reflective and revered guidance. His optimistic nature and boundless kindness cannot be fully expressed in words, but I am immensely grateful for his unwavering support throughout this journey.

Also, I am thankful to the members of the Doctoral Committee, *Professor Shree Prakash Tiwari, Professor Manikandan Paranjothy* and *Professor Satyajit Sahu*, for their guidance and support during this research work. I am also thankful to all faculty and staff members of the Department of Electrical Engineering for their constant support during my tenure.

I sincerely acknowledge our collaborators, *Professor Pradeep Kumar* (IIT Mandi, India), *Professor Mukesh Kumar* (IIT Ropar, India), and *Professor Michael S. Strano* from Department of Chemical Engineering, Massachusetts Institute of Technology, Cambridge, Massachusetts, United States for sharing their labs facilities and their contribution in carrying out present thesis work.

My funding agencies, the Prime Minister Research Fellowship, MHRD fellowship, and SERB-International Travel Grant for financially supporting my research work. I am highly grateful to the Centre for Research & Development of Scientific Instruments (CRDSI at IIT Jodhpur for providing characterization facilities. Additionally, I appreciate the support provided by the technical staff/ operators, Mr. Pawan Sharma (FE-SEM and XRD), Mr. Mukesh Rajpurohit (SEM, UV-Vis Spectrometer), and Mr. Sanjay Nimbark (Raman). I gratefully acknowledge Mr. Ummed Singh Rathore, Sr. Assistant, Department of Electrical Engineering, for smoothly carrying up all the documentation work. Also, I would like to thank the Library, IIT Jodhpur, for granting me access to research papers and books essential to my work.

Additionally, my heartfelt gratitude goes out to my colleagues and alumni of the Nanosensors Research Group lab. I am highly grateful to the Doctoral group (Dr. Rahul Kumar, Dr. Neeraj Goel, Dr. Vijendra Bhati, Dr. Sapna Ranwa, Dr. Adarsh Nigam, Dr. Amit Shringi, Dr. Nipun Sharma and Dr. Surajit Das) for their discussions and suggestions. I want to thank my laboratory mates and juniors: Amit, Sumit, Ruksana, Vikas, Jai Mishra, Suraj Barala, Mubashir, Suresh, Arpita, Chayan, Pooja, Kishan, Rovins for their assistance in the lab activities. It was wonderful to work with you all and I really appreciate the time, when we worked together in the lab. Everyone owes a special place in my heart that I cannot express in a few words. I have learned a lot from you all. Apart from that, I really cherished those parties that we were having outside the lab. I want to thank Dr. Chandra Prakash, Dr. Ramavtar, Dr. Kiran, Dr. Mohammad Rahil, Anil Lodhi, Shalu Saini, Anurag, Gargi, Saqib, Somnath, Vandana, Ankit, Dibyajyoti, Minakshi, Priyanka for his assistance in many lab activities. I am grateful to Miss. Neelu Sharma and Mr. Akash Popat Gutkal Ghosh for their contribution to my research article.

Also, I am highly thankful to Prof. Sandeep Yadav, Prof. Ankur Gupta, Prof. Chandan Pandey, Ganapat Choudhary, Kamal Kishore and Shubham Pandey for always being supportive

and keeping me motivated. They are more like a friend or brother to me, and I really enjoyed her company during campus life.

First and foremost, I would like to express my deepest gratitude to my parents, whose unwavering support, unconditional love, and sacrifices have been the foundation of all my achievements. Their guidance and encouragement throughout my journey have been my constant source of strength and inspiration. To my beloved wife Ms. Leela, your patience, understanding, and belief in me during the most challenging times have been immeasurable. Your love and unwavering support have provided me with the motivation and focus to persevere through this journey. I am deeply grateful for all the sacrifices you made to help me succeed. To my dear son Master Ishan Patel, you are my pride and joy. Your smiles and laughter have been a source of relief and happiness during stressful times. You remind me of the importance of balance and joy in life. I would also like to extend my heartfelt gratitude to my uncle, Day Ram Patel, for his unconditional support, encouragement, and guidance. Your blessings and belief in me have been a source of strength throughout this journey. I am also profoundly thankful to my brother, Mr. Rajendra Pal, and Dr. Ram Nivas for his constant encouragement and unwavering belief in me. Your words of motivation have always pushed me to give my best.

At last, I am thankful to the almighty God for his blessings and making me capable of completing this task successfully.

*Ashok Kumar*
Ph.D. Student

# Abstract

The emergence of two-dimensional (2D) transition metal dichalcogenides (TMDCs), particularly $SnS_2$ and $MoS_2$, has sparked significant interest in the field of advanced materials due to their unique layered architecture and atomic-scale thickness. These materials exhibit exceptional electrical, optical, and chemical properties, rendering them highly suitable for a wide range of applications, including sensors, photodetectors, and various optoelectronic devices. However, the full potential of $SnS_2$ and $MoS_2$ is often hindered by common challenges such as large-area controlled growth, limited optical absorption in pristine materials, and slow response and recovery times attributed to inefficient charge transfer dynamics.

To address these challenges, we employed a thermal chemical vapor deposition (CVD) technique to optimize the growth conditions for high-quality $SnS_2$ and $MoS_2$ films. By systematically adjusting parameters, we achieved vertically aligned structures and uniform layers, laying the groundwork for enhanced device performance. Comprehensive characterization techniques, including scanning electron microscopy (SEM), X-ray diffraction (XRD), energy dispersive X-ray spectroscopy (EDX), X-ray photoelectron spectroscopy (XPS), Raman spectroscopy, and photoluminescence (PL) were utilized to analyze and confirm the structural, morphological, and optical properties of the synthesized materials. Based on the results from these analyses, we propose a detailed growth mechanism in which in-plane $SnS_2$ and mixed $MoS_2$ flakes acts as a seed layer for the initial development of vertically aligned $SnS_2$ and $MoS_2$, ultimately leading to the formation of an interconnected three-dimensional network of these flakes.

We developed a highly sensitive gas sensor based on vertically aligned $SnS_2$ flakes, which exhibited exceptional selectivity toward $NO_2$ over various other toxic and combustible gases[Kumar et al., 2022]. The sensor demonstrated stable performance and strong selectivity, supported by electronic structure calculations. To further enhance gas sensing capabilities, we implemented defect and interface engineering techniques, specifically inducing optimal sulfur vacancies in the $SnS_2$ lattice through nitrogen plasma treatment[Kumar et al., 2023a]. This vacancy engineering significantly improved electronic conductivity and increased the active surface area for gas adsorption, resulting in a remarkable sensitivity to $NO_2$ and complete recovery at 120°C.

In parallel, we explored the functionalization of mixed $MoS_2$ flakes for $NO_2$ gas sensing. Recognizing the limitations of pristine $MoS_2$, which suffers from low response and slow recovery times, we modified the material through nitrogen doping and decoration with silver nanoparticles. The resulting nitrogen-doped $MoS_2$ (N-$MoS_2$) and silver-decorated nitrogen-doped $MoS_2$ (Ag-N-$MoS_2$) sensors exhibited substantial improvements in $NO_2$ sensing performance. Notably, the Ag-N-$MoS_2$ sensor demonstrated nearly double the response of pristine $MoS_2$ at 100°C, illustrating the synergistic effects of nitrogen doping and silver decoration.

Finally, we investigated the application of $MoS_2$ in optoelectronic systems through the development of a self-powered broadband photodetector utilizing a van der Waals heterostructure composed of $MoS_2$ and $WS_2$. The fabricated heterostructures exhibited enhanced responsivity, detectivity, and response times compared to pristine $MoS_2$, showcasing the potential of these materials in next-generation optoelectronic applications. Furthermore, the anticipated challenges and future perspectives in the rapidly evolving research on $SnS_2$ and $MoS_2$ for sensing applications are similarly explored.

# Contents


| | | page |
|---|---|---|
| *Acknowledgements* | | v |
| *Abstract* | | vii |
| *Contents* | | ix-xi |
| *List of Figures* | | xii-xvii |
| *List of Tables* | | xviii |
| *List of Symbols* | | xix |
| *List of Abbreviations* | | xx-xxi |

**Chapter 1: Introduction**

| | | |
|---|---|---|
| 1.1 | Background | 1 |
| 1.2 | Molybdenum disulfide ($MoS_2$) and Tin disulfide ($SnS_2$) | 3 |
| | 1.2.1 Properties of $MoS_2$ | 3 |
| | 1.2.2 Properties of $SnS_2$ | 10 |
| 1.3 | Synthesis of 2D materials | 13 |
| | *1.3.1 Top-Down Approach* | 14 |
| | *1.3.2 Bottom-up Approach* | 16 |
| 1.4 | Gas Sensor | 18 |
| | *1.4.1 NO2 Gas Sensor* | 19 |
| | *1.4.2 Classification of gas sensors* | 20 |
| | *1.4.3 Characteristics of Gas Sensor* | 21 |
| 1.5 | Gas Sensing Mechanism of 2D Materials | 22 |
| 1.6 | Literature Review on $MoS_2$ and $SnS_2$ Gas Sensor | 24 |
| 1.7 | Photodetector | 28 |
| | 1.7.1 The Figure of Merits of a Photodetector | 28 |
| | 1.7.2 Photodetector Mechanism | 30 |
| 1.8 | Literature survey on photodetectors based on $MoS_2$ | 32 |
| 1.9 | Challenges and Motivation | 34 |
| 1.10 | Objective of the present thesis work | 36 |
| 1.11 | Outline of Thesis | 36 |

**Chapter 2: Fabrication and Characterization of Materials and Devices**

| | | |
|---|---|---|
| 2.1 | Deposition techniques | 39 |
| | 2.1.1 Chemical Vapor Deposition (CVD) | 39 |
| | 2.1.2 Magnetron sputtering | 41 |
| | 2.1.2 Thermal Evaporation | 42 |
| 2.2 | Characterization Techniques | 44 |
| | *2.2.1 Field Emission Scanning Electron Microscopy (FESEM)* | 44 |
| | *2.2.2 Energy Dispersive X-Ray Analysis Spectroscopy (EDX)* | 45 |
| | *2.2.3 Raman Spectroscopy* | 45 |
| | *2.2.4 X-ray Photoelectron Spectroscopy (XPS)* | 46 |
| | *2.2.5 Photoluminescence Spectroscopy (PL)* | 47 |
| | *2.2.6 Ultraviolet-Visible (UV-VIS) Spectroscopy* | 48 |

*2.2.7 X-ray Diffraction (XRD)* 49
*2.2.8 Kelvin probe force microscopy (KPFM)* 50
2.3 Plasma treatment 51
2.4 Device fabrication and characterization 52
*2.4.1 Deposition of Metal Contact Using Thermal Evaporation* 52
*2.4.2 Gas Sensing Measurement* 53
*2.4.3 Photodetector measurement* 53

**Chapter 3: Growth and Characterization of $MoS_2$ and $Sns_2$ Flakes**
3.1 Necessity and Challenges for Controlled growth of $MoS_2$ and $SnS_2$ Flakes 55
3.2 *Growth of $MoS_2$ and $SnS_2$ Flakes by CVD Method* 56
*3.2.1 Synthesis of $MoS_2$ Flakes* 56
*3.2.2 Characterizations of $MoS_2$ Flakes* 57
*3.2.3 Synthesis of vertically Aligned $SnS_2$ flakes* 59
*3.2.4 Characterizations of $SnS_2$ Flakes* 60
3.3 Proposed Growth Mechanism 62
3.4 Synthesis of $WS_2$ 64
3.5 Nitrogen Plasma Treatment 65
3.6 Synthesis of Silver Nanoparticles Using DC Sputtering Technique 66
3.7 Device Fabrication Process 67
3.5 Summary 68

**Chapter 4: Effects on Gas Sensing Characteristics of $MoS_2$ flakes using Surface and Structural Modifications**
4.1 Requirement of Fast highly response $NO_2$ Gas Sensor and Challenges 69
4.2 Synthesis and Fabrication of Ag NPs anchored-nitrogen plasma treated $MoS_2$ flakes 71
4.3 Results and Discussion 71
*4.3.1 Structure and chemical properties* 71
*4.3.2 $NO_2$ Gas Sensing Performance of MoS2 Flakes* 74
*4.3.3 Effect of nitrogen plasma treatment on MoS2 (N-$MoS_2$) Flakes toward $NO_2$ Gas Sensing Performance* 76
4.3.4 Effect of surface functionalization of silver nanoparticles (Ag NPs) on pristine-$MoS_2$ and N-MoS2 Flakes toward $NO_2$ Gas Sensing Performance 77
4.3.5 Response and recovery time of the pristine-$MoS_2$, Ag-$MoS_2$, N-$MoS_2$ and Ag-N-$MoS_2$ sensors 78
4.4 Long-term stability, Effect of Humidity, Short-term repeatability, and Selectivity of $MoS_2$ sensors 79
4.5 Gas sensing mechanism 81
4.5 Summary 82

**Chapter 5: Improved Gas Sensing Performance of $SnS_2$ via Defect Engineering**
5.1 Requirement of highly selective and high response $NO_2$ Gas Sensor and Challenges 83
5.2 Synthesis, and nitrogen plasma treatment of Vertically Aligned $SnS_2$ flakes 85
5.3 Characterization 85
*5.3.1 Structure and chemical properties of $SnS_2$ flakes* 85
*5.3.2 Vacancy and Doping Investigation using FE-SEM Raman Spectroscopy, and XPS* 86
5.4 Gas Sensing Properties of Vertically Aligned $SnS_2$ Flakes 88
5.4.1 Optimization of the operating temperature and Static response behaviour VA-$SnS_2$ 88
5.4.2 Repeatability, Response time, Selectivity, and Limit of Detection of VA-$SnS_2$ sensor 90

5.4.3 Effect of humidity 91
5.4.4 Gas sensing mechanism 93
5.5 Effects of Vacancy on Gas Sensing Characteristics of Vertically Aligned $SnS_2$ Flake 94
5.5.1 I-V characteristics and surface resistances 94
5.5.2 Static response behaviour Vs-$SnS_2$ sensor 95
5.5.3 Repeatability, Selectivity, Response time, and Limit of Detection of Vs-$SnS_2$ sensor 96
5.5.4 Gas sensing mechanism 98
5.6 Summary 100

**Chapter 6: DFT studies and Gas Sensor Modelling**
6.1 Requirement of Theoretical Investigations of $NO_2$ Adsorption 101
6.2 Vienna Ab initio Simulation Package (VASP) 102
6.3 Computational Method 103
*6.3.1 Ag NPs anchored-nitrogen plasma treated $MoS_2$ (Ag-N-$MoS_2$) flakes* 103
*6.3.2 Vertically Aligned $SnS_2$ (VA-$Sn_{S2}$) flakes* 103
*6.3.3 Vacancy-Assisted Vertically Aligned $SnS_2$ (Vs-$SnS_2$) flakes* 103
6.4 Result and Discussion 104
*6.4.1 Adsorption properties of Ag NPs anchored-nitrogen plasma treated $Mo_{S2}$ (Ag-N-$MoS_2$) flakes* 104
*6.4.2 Adsorption properties of Vertically Aligned $SnS_2$ (VA-$SnS_2$) flakes* 106
*6.4.3 Adsorption properties of Vacancy-Assisted Vertically Aligned $SnS_2$ (Vs-$SnS_2$) flakes* 107
6.5 Gas sensor modelling 109
6.5.1 Gas adsorption-desorption kinetics in 2D material 109
6.5.2 Transient response cycles with fitting curve of Pristine $SnS_2$ flakes 111
6.5.3 Transient response curve with fitting curve of nitrogen plasma treated $SnS_2$ flakes 111
6.6 Summary 114

**Chapter 7: High-Performance Broadband Photodetector Based on $MoS_2$-$WS_2$ Heterojunction**
7.1 Requirement of highly sensitive, fast, and broadband photodetectors 115
7.2 Device fabrication from MoS2-WS2 heterojunction and light-sensing experimental details 116
7.3 Characterization of $MoS_2$-$WS_2$ heterojunctions 117
7.4 Effects of visible to near-infrared wavelength on the $MoS_2$-$WS_2$ heterojunctions 119
7.5 Speed and stability of the photodetector 123
7.6 Self-powered functionality of CVD-synthesized $MoS_2$ photodetector 124
7.7 Light sensing mechanism of the photodetector 127
7.8 Summary 128

**Chapter 8: Conclusions and Future Scope**
8.1 Conclusions 129
8.2 Scope for Future Work 131

List of Publication 133
*References* 135

# List of Figures


| *Figures* | *Title* | *page* |
|---|---|---|
| 1.1 | (a) Transition metal dichalcogenides materials in the periodic table that form layered materials and an example of 2D materials, (b) Stacking of hexagonally packed planes bounded by the van der Waals force. Possible coordination unit of layered TMDs, and (c) Trigonal prismatic (AbA) (d) Octahedron (AbC) | *3* |
| 1.2 | Crystal structures of MoS2 polymorphs. (a) 1T phase (octahedral), (b) 2H phase (trigonal prismatic) and (c) 3R phase (trigonal prismatic). | *4* |
| 1.3 | Crystal structure of $MoS_2$ (a) 2H phase (b) 1T phase, with a schematic representation of the gradual filling of d orbitals that are situated in the bandgap between bonding (σ) and anti-bonding states (σ*) | *5* |
| 1.4 | (a) Top view of the 2H-$MoS_2$ structure. (b) Corresponding Brillouin zones for the 2H-$MoS_2$. Theoretically calculated band structures for the (c) Bulk $MoS_2$ and quadrilateral MoS2. (d) Schematics of orbitals combinations of CBM and VBM electronic states and corresponding Mo and S orbitals for bulk $MoS_2$. Band structures for the (e) Bilayer $MoS_2$ and monolayer MoS2. (f) Schematics of orbitals combinations of CBM and VBM electronic states and corresponding Mo and S orbitals for monolayer $MoS_2$. | *6* |
| 1.5 | (a) Two Raman ($A_{1g}$ and $E_{2g}{}^1$) active mode in mono and few-layers $MoS_2$, and (b) All possible vibrational modes ($E_{2g}{}^2$, $E_{1g}$, $E_{2g}{}^1$, $A_{1g}$ and $E_{1u}{}^1$, $A_{2u}{}^1$) in bulk $MoS_2$. | *7* |
| 1.6 | (a) Optical absorption spectra for $MoS_2$ from monolayer to six layers, and (b) The absorption coefficient was calculated for the $MoS_2$. | *8* |
| 1.7 | (a) Band structure of the bulk and monolayer $MoS_2$, where A and B indicate the direct-gap transitions, and I represent the indirect-gap transition. The indirect gap for the bulk is denoted by $E_g{}'$ and direct gap for the monolayer is indicated as $E_g$. (b) Schematic for excitons and trions. (c) PL spectra for mono and bilayer $MoS_2$, inset displaying the relative quantum yield of $MoS_2$ as a function of layer number, (d) The normalized PL spectra with respect to layer number. (e) Schematic illustration of the optical transition occurring at the K-point of the Brillouin zone in different regions of $MoS_2$, including monolayer, bilayer, and bulk. The A exciton peak experiences a red shift due to the reduction of the first exciton level. The B-exciton peak position remains relatively the same because the decrease in the exciton level is balanced by an increase in the valence band splitting energy. | *9* |
| 1.8 | Properties of $SnS_2$. (a) Crystal structure, (b) band position, and (c) Band position of $SnS_2$ for photocatalytic reactions. | *11* |
| 1.9 | Side view and top view of ball and stick model schematic diagram of $SnS_2$ | *12* |
| 1.10 | ((a, b) Optical absorption spectra temperature corresponding to direct and indirect energy band gaps for a crystal structure of $SnS_2$. (c) Raman spectra of $SnS_2$ at varying temperature (150 °C for 1 h, 150 °C for 2 h, and 300 °C for 1 h). | *13* |
| 1.11 | Schematic image of top-down approach for synthesis of 2D material (a) mechanically exfoliated $MoS_2$ (Scotch tape method), (b) Electrochemical lithiation process, (c) Liquid exfoliation method, and (d) Sputtering. | *15* |
| 1.12 | Schematic illustration of different bottom-up methods for the synthesis and growth of 2D material | *17* |
| 1.13 | Schematic representation of a gas sensor | *19* |
| 1.14 | Classification of the gas sensor based on sensing operation principles. | *20* |
| 1.15 | Schematics of gas sensing mechanism of in 2D material-based gas sensors. | *24* |
| 1.16 | Schematic of a photodetector device | *28* |

| | | |
|---|---|---|
| 1.17 | Schematic diagram of photoconductive effect (a) without illumination and under external bias, (b) under illumination with energy of photons (Eph), (c) IDS – Vg curves under light (solid red line) and in the dark (solid blue line), (d) traces of IDS – VDS in the dark (solid blue line) and when illuminated (solid red line), (e) Schematic view of photogating effect. | 30 |
| 1.18 | (a), (b) Schematic view of photovoltaic effect arising from a metal–semiconductor Schottky barrier and p–n junction, and (c) IDS – VDS traces in the dark (solid black line) and under illumination (solid red line). | 31 |
| 2.1 | (a) Schematic illustration of the CVD steps, and (b) Optical images of thermal chemical vapor deposition (CVD) system which is used for this thesis work | 41 |
| 2.2 | (a) Schematic representation of the RF sputtering system, and (b) Optical images of sputtering system at the microfabrication lab, IIT Jodhpur. | 42 |
| 2.3 | (a) Schematic illustration of the thermal evaporation system, and (b) Optical images of Thermal evaporation system at Microfabrication lab, IIT Jodhpur | 43 |
| 2.4 | (a) Schematic representation of working of FESEM, and (b) Optical images of SEM and FESEM in central facility IIT Jodhpur | 44 |
| 2.5 | (a) Schematic of the XPS setup, which provides both elemental and chemical detail, and (b) Optical images of XPS system, IIT Mandi. | 45 |
| 2.6 | (a) Schematic of the XPS setup, which provides both elemental and chemical detail, and (b) Optical images of XPS system, IIT Mandi. | 47 |
| 2.7 | Schematic of a PL spectroscopy. | 47 |
| 2.8 | (a)Schematic representation of a UV-VIS spectrometer, and (b) Optical images of UV-VIS spectrometer, IIT Jodhpur | 48 |
| 2.9 | (a) Schematic for the X-ray diffraction used to study the crystal structure of the film, (b) Diagram of Bragg's law for X-ray diffraction, and (c) Optical images of X-ray diffraction system (D8 Advance, Bruker) at IIT Jodhpur. | 49 |
| 2.10 | (a) Schematic view of band alignment between the sample and the tip in a typical KPFM set-up under different conditions: Non-contact, External electrical contact, Applied DC voltage, and (b) Optical images of KPFM system at IIT Mandi. | 50 |
| 2.11 | (a) Optical images of RF Plasma chamber | 51 |
| 2.12 | Interdigitated electrode physical shadow mask used for electrode deposition | 52 |
| 2.13 | (a) Schematic illustration of gas sensing setup, and (b) Optical Image of the gas sensing system, which is used for this thesis work. | 53 |
| 2.14 | (a) Schematic representation of the experimental setup used to measure spectral response of MoS2 based photodetectors, and (b) Optical Image of the photodetector system, which is used for this thesis work. | 54 |
| 3.1 | (a) Schematic of thermal chemical vapor deposition (CVD) technique used to grow $MoS_2$ flakes. $SiO_2$/Si substrate was placed on top of $MoO_3$ powder in zone 1, (b) temperature profile for $MoO_3$ and S powders in Zone 1, Zone 2, respectively and (c, d) Show the different growth conditions and nomenclatures of synthesized sample | 57 |
| 3.2 | SEM images of $MoS_2$ flakes grow at different deposition temperature (a) 750 °C, (b) 800 °C, (c) 850 °C, and (d) 9000 °C. The flow of argon of 80 sccm keep constant during the growth. | 58 |
| 3.3 | SEM images of $MoS_2$ flakes grow at different gas flow rates (a) 60 sccm, (b) 70 sccm, (c) 80 sccm and (d) 100 sccm. The growth temperature for all these samples was fixed at 850°C | 58 |
| 3.4 | (a) High-resolution FE-SEM images of CVD grown $MoS_2$ on SiO2/Si substrate, (b) XRD spectra of optimized $MoS_2$ flakes, the peaks become sharper, highly intense and with more planes of MoS2, and (c) Raman spectra of the optimized MoS2 flakes. Raman spectra consist of two strong peaks that corresponds to in-plane, $E^1_{2g}$, and out-of-plane, $A_{1g}$, vibrations of S- Mo-S atoms | 59 |

| | | |
|---|---|---|
| 3.5 | (a) Schematic of the thermal chemical vapour deposition (CVD) technique used in growing $SnS_2$ flakes. $SiO_2$/Si substrate place in in zone 3. (b)The temperature profiles of S and $SnO_2$ powders in zones 1 and 2, respectively and (c, d) illustrate the various growth circumstances (Temperature, gas flow) and grown sample names | 60 |
| 3.6 | SEM images of $SnS_2$ flakes grow at different deposition temperature (a) 750 °C, (b) 800 °C, (c) 850 °C, and (d) 9000 °C. The flow of argon gas (80 sccm) keep constant during the growth. | 61 |
| 3.7 | SEM images of $SnS_2$ flakes grow at different gas flow rates (a) 60 sccm, (b) 80 sccm, (c) 100 sccm and (d) 120 sccm. The growth temperature for all these samples was fixed at 1000°C | 61 |
| 3.8 | (a) High-resolution SEM images of CVD grown vertically aligned $SnS_2$ flakes on $SiO_2$/Si substrate, (b) Raman spectra of the optimized $SnS_2$ flakes. Raman spectra consist of two strong peaks that corresponds to in-plane, Eg, and out-of-plane, A1g, vibrations of S- Sn-S atoms, (c) XRD spectra of optimized $SnS_2$ flakes, the peaks become sharper, highly intense and with more planes of $SnS_2$. | 62 |
| 3.9 | The suggested growth mechanism for edge-enriched $MoS_2$ and $SnS_2$ flakes. (a) Represents the diffusion and absorption stage of in-plane $MoS_2$ and $SnS_2$ formation. In this phase, in-plane MoS2 and SnS2 development is more rapid, resulting in the production of monolayer to multilayer flakes on the substrate, (b) Growth of edge-enriched flakes at the nucleation and chemical reaction stage. The incoming S and Mo, Sn atoms adsorb on the substrate and $MoS_2$ and $SnS_2$ flakes, causing edge-enriched flakes to develop, (c) Schematic illustration the growth stage for finally as grown interconnected $MoS_2$ and $SnS_2$ flakes, and (d) SEM image of the $MoS_2$ and $SnS_2$ flakes. | 63 |
| 3.10 | (a) Schematic illustration of $WS_2$ nanoparticle synthesis using the hydrothermal method, (b) FE-SEM image showing the morphology of the synthesized $WS_2$ nanoparticles, and (c) Raman spectra confirming the characteristic vibrational modes of $WS_2$ | 65 |
| 3.11 | Schematic illustration of (a) nitrogen plasma treatment and subsequent functionalization with silver (Ag) nanoparticles on CVD-grown $MoS_2$ flakes, and (b) nitrogen plasma treatment on CVD-grown $SnS_2$ flakes, showcasing the process of sulfur vacancy creation, nitrogen doping, and nanoparticle deposition to enhance material properties. | 66 |
| 3.12 | Device Fabrication Process for Interdigitated Electrode (IDE) Structures on CVD-grown $SnS_2$ and $MoS_2$. | 68 |
| 4.1 | FE-SEM images of (a) Grown MoS2 flakes, (b) High-resolution image of MoS2 flakes, (c) Nitrogen plasma treated MoS2 (N-MoS2) flakes, (d) High magnification view of N-MoS2, (e) Ag NPs anchored N-MoS2 (Ag-N-MoS2) flakes, and (f) High-resolution image of Ag-N-MoS2 flakes. The average size of Ag NPs is 50nm. | 72 |
| 4.2 | Energy dispersive spectroscopy (EDX) elemental mapping of Ag-N-MoS2 sample (a) Area selected, Elemental mapping of (b) Molybdenum (Mo), (c) sulfur (S), (d) Nitrogen (N), and (e) Silver (Ag). | 72 |
| 4.3 | Raman spectra of the pristine MoS2, Ag-MoS2, N-MoS2 and Ag-N-MoS2. (a) High-resolution XPS spectra for the N pristine MoS2, Ag-MoS2, N-MoS2 and Ag-N-MoS2, (b) Mo 3d, (c) S 2p, (d) N1s, and (e) Ag 3d | 74 |
| 4.4 | Optical emission spectra (OES) of atmospheric air SDBD plasma source operated at 5.0 kV/25 kHz, and (b) electron temperature profile at different applied voltage and at a fixed frequency of 25 kHz | 75 |
| 4.5 | (a) Schematic of the Ag NPs-decorated N-MoS2 sensor, (b) Comparison of variation in baseline resistance (absence of gas) and relative response of the pristine-$MoS_2$ sensor with temperature, (c) Resistance versus time plot of the pristine-MoS2 under exposure to NO2 gas ranging from 50 to 1 ppm at RT, (d) Relative response characteristics of the pristine-MoS2 sensor at RT, (e) Resistance versus time plot of the pristine-MoS2 under exposure to NO2 gas ranging from 50 to 1 ppm at 100 °C, (f) Relative response characteristics of the pristine-MoS2 sensor at 100 °C. | 76 |
| 4.6 | (a) Comparison of response of N0, N1, N5, and N8 sensors for 50 ppm of NO2, respectively, (b) Comparison of baseline resistance and response of N0, N1, N5, and N8 sensors for 50 | 76 |

ppm of $NO_2$, respectively, (c) Real time change in resistance, and (d) Transient relative response of N-$MoS_2$ device for different concentration of $NO_2$ at 100 °C

4.7 (a) Comparison of the relative response for pristine $MoS_2$, nitrogen plasma treated $MoS_2$ (N-$MoS_2$), Ag functionalized sensor (Ag-$MoS_2$, and Ag-N-$MoS_2$) for 50 ppm of $NO_2$, (b) Baseline resistance and relative response curve of the pristine $MoS_2$, Ag-$MoS_2$, N-$MoS_2$, and Ag-N-$MoS_2$ sensors for 50 ppm of $NO_2$, and (c) Relative response versus different concentration of $NO_2$ gas curve of the pristine $MoS_2$, Ag-$MoS_2$, N-$MoS_2$, and Ag-N-$MoS_2$ sensors for 50 ppm of $NO_2$ at 100 °C, respectively *77*

4.8 Transient relative resistance and response for different concentration of $NO_2$ at 100 °C (a, b) Ag-$MoS_2$, and (c, d) Ag-N-$MoS_2$ *78*

4.9 Response time and Recovery time of sensor under a 50 ppm $NO_2$ concentration at 100 °C. (a) pristine $MoS_2$, (b) Ag-$MoS_2$, (c) N-$MoS_2$, and (d) Ag-N-$MoS_2$. *79*

4.10 (a) The long-term stability of the pristine $MoS_2$, Ag-$MoS_2$, N-$MoS_2$, and Ag-N-$MoS_2$ devices to 50 ppm $NO_2$ gas at 100 °C, (b) Baseline resistance versus different relative humidity (RH %) of pristine $MoS_2$, Ag-$MoS_2$, N-$MoS_2$, and Ag-N-$MoS_2$ devices to $NO_2$ gas at 100 °C, (c) Repeatability of Ag-N-$MoS_2$ toward 50 ppm of $NO_2$ gas at 100 °C, and (d) Selectivity performance of pristine $MoS_2$, Ag-$MoS_2$, N-$MoS_2$, and Ag-N-$MoS_2$ devices to 50 ppm of various gases at 100 °C *80*

4.11 Schematic diagram proposed sensing mechanism. *82*

5.1 (a) SEM images of the vertically aligned $SnS_2$, (b) a magnified view of the flakes network, (c) Raman spectra of the vertically aligned $SnS_2$ flakes at 532 nm laser, and (d) X-Ray diffraction pattern of vertically aligned $SnS_2$ flakes. *85*

5.2 (a) FE-SEM image of the nitrogen plasma treated $SnS_2$ (Vs-$SnS_2$) flakes, Energy dispersive spectroscopy (EDX) elemental mapping of Vs-$SnS_2$ sample (b) Area selected, Elemental mapping of (c) Tin (Sn), (d) sulfur (S), (e) EDX spectrum of Vs-$SnS_2$ sample. *86*

5.3 (a) Raman spectra of the $SnS_2$ nanoflakes, and (b) Change in Raman shift and Line width, before and after $N_2$ plasma treatment of N0, N4, N8, N12 and N16 samples *87*

5.4 XPS spectra from pristine VA- $SnS_2$ and $N_2$ plasma treated VA- $SnS_2$, (a) Sn 3d5/2, (b) Sn 3d3/2, (c) S 2p, and (d) N1s *87*

5.5 (a) Schematic diagram of the fabricated device, (b, c) Real-time change in resistance of the sensor with the temperature at RT, and 120 °C, respectively (d) Response time plot at RT with various concentration of $NO_2$, (e) Response verses concentration of $NO_2$ plot at 120 °C, and (f) Response of $SnS_2$ as a function of $NO_2$ concentration under room temperature, and 120 °C *89*

5.6 (a) Response at 120 °C with same concentration of 50 ppm of $NO_2$, (b) Response time plot of single cycle to calculate response time at 120 °C and 50 ppm of $NO_2$, (c) Response of 50 ppm of $NO_2$ at various temperature from RT to 120 °C, (d) Selectivity test histogram of $NO_2$, $H_2S$, $H_2$, $NH_3$, CO, $CO_2$, and $CH_4$ gas, (e) Response and recovery time as a function of $NO_2$ concentration (5-5- ppm) at 120 °C, and (f) Limit of detection calculation for $NO_2$ gas *90*

5.7 (a) Variation of baseline resistance with relative humidity from 25% to 75% for vertically aligned $SnS_2$ flakes at 120 °C, and (b) Response variations when $SnS_2$ gas sensor exposed to 50 ppm $NO_2$ under different relative humidity conditions at 120 °C. *93*

5.8 Schematic representation of sensing mechanism of the $SnS_2$ flakes *94*

5.9 (a) Schematic illustration and SEM image of the fabricated Vs-$SnS_2$ device, (b) Linear I-V plots of the pristine $SnS_2$ sensor at RT and 120 °C, respectively, (c) I-V plots of the pristine $SnS_2$ and plasma treated $SnS_2$ (N4, N8, N12 and N16) samples sensor at 120 °C, respectively, and (d) Variation of baseline resistance at different interval of $N_2$ plasma (N0, N4, N8, N12, and N16) at 120 °C. *95*

5.10 (a) Comparison of response of N0, N4, N8, N12, and N16 sensors for 50 ppm of $NO_2$ concentrations, respectively, (b) Comparison of the gas responses of N0, N4, N8, N12 and N16 samples at temperature 120 oC for 50 ppm $NO_2$ gas, (c) Sensing response of N12 device toward $NO_2$ gas at concentrations ranging from 1 to 50 ppm under the operation *96*

temperature of 120 °C, and (d) Response–concentration plot of pristine $SnS_2$ and Vs-$SnS_2$ (N12 )samples

5.11 (a) Vs-$SnS_2$ sensor repeatability for 50 ppm gas at 120 °C, (b) Selectivity of sensor to 50 ppm different gases at 120 °C, (c) Response time and Recovery time of N12 gas sensor under a 50 ppm $NO_2$ concentration at 120 °C, and (d) Response versus $NO_2$ concentration curve. (Inset) Linear fitting curve of N12 sample of $SnS_2$ (12 min plasma treatment) at 120 oC, for calculation of the Limit of detection (LoD). *97*

5.12 Schematic illustration of the sensing mechanism for the boosted gas response to $NO_2$ *99*

6.1 The top and side views of $NO_2$ gas adsorption on the (a) pristine $MoS_2$ (b) N-$MoS_2$ and (c) Ag decorated N-$MoS_2$, and (d) Histogram of adsorption energy pristine $MoS_2$, N-$MoS_2$, Ag decorated N-$MoS_2$, for $NO_2$ gas. *104*

6.2 (a) The top and side view of a unit cell of monolayer $SnS_2$, (b) Optimized N atom of $NO_2$ molecule is adsorbed onto the surfaces of $SnS_2$ top and side view, (c) Other gases $CO_2$, $H_2S$ and $H_2$ kept similar fashion giving optimised structures (1)- (3), and (d) Histogram of adsorption energy for $NO_2$, $CO_2$, $H_2S$ and $H_2$ gas *106*

6.3 Computational model geometries of gas surface system. (a) Initial and optimized structures (from top and side view) of gas-monolayer adsorption system with $NO_2$ above the sulfur vacant sites with supercell containing single vacant site (I), (b) conjugated double vacant sites (II), and (c) Nitrogen doped single vacant site (III) *108*

6.4 (a) Histogram of adsorption energy for pristine ($SnS_2$), structure containing sulfur vacant site (Vs-$SnS_2$) and Nitrogen doped monolayer with sulfur vacant site(N2-Vs-$SnS_2$), (b) Histogram of adsorption energy for $NO_2$, $CO_2$, and $H_2S$ gas, and optimized structures of other gases (c) $CO_2$, and (d) $H_2S$. *109*

6.5 Irreversible Adsorption: Experimental (scattered point) and fitted (solid dashed red line) response of VA-$SnS_2$ based sensor to $NO_2$ gases for different concentration (5-50ppm) at (a-c) RT, and 120 °C. *111*

6.6 Irreversible Adsorption (Nonlinear fit model): Response transients of nitrogen plasma treated $SnS_2$ (Vs-$SnS_2$) samples are plotted as a function of (Cat) vs log response the points collapse to a single model operating at 120 oC (a, b) N4 sample, (c, d) N8 sample, (e, f, g) N12 sample, and (h, i) N16 sample, fitted (red color short dashed line), respectively *112*

7.1 (a) FE-SEM image of $WS_2$ nanoparticles decorated $MoS_2$ flakes network, (b, c, d) EDX element mapping pictures of the $MoS_2$-$WS_2$, confirming the existence of Mo, W and S. *117*

7.2 (a) Raman spectrum of pristine-$MoS_2$ and $MoS_2$-$WS_2$ heterostructures (b) PL spectra of pristine-$MoS_2$ and $MoS_2$-$WS_2$ heterostructures. XPS spectra of pristine-$MoS_2$ and $MoS_2$-$WS_2$ heterostructures (c) Mo 3d, (d) S 2p, and (e) W 4f peaks, respectively *118*

7.3 Self-powered Electrical characterizations and photoresponse characteristics $MoS_2$-$WS_2$ heterostructure devices. (a) Schematic of the device. Current-voltage (I-V) characteristics measured in the dark and under different wavelengths. (b) Dark current, (c) Pristine-$MoS_2$, (d) $MoS_2$-$WS_2$ heterostructure, (e) I–V curves of the pristine-$MoS_2$ and $MoS_2$-$WS_2$ heterojunction under light illumination (580 nm, 120 μW/cm2), and (f) Comparison of semi-logirthm I-V of Pristine $MoS_2$ and $MoS_2$-$WS_2$ in the dark condition and light illumination (580 nm, 120 $\mu W/cm^2$ *120*

7.4 Photoresponse characteristics of self-powered device. (a) Responsivity, (b) Detectivity, (c) EQE of pristine $MoS_2$ and $MoS_2$-$WS_2$ under irradiation of Visible-NIR spectrum, respectively with an input power density (Pin) of 120 μW/cm2, (d, e) Responsivity and Detectivity with function of different incident optical power density, and (f) Comparison of Responsivity of pristine $MoS_2$ and $MoS_2$-$WS_2$ under light illumination of 580nm with various bias voltages. *121*

7.5 Comparative transient of pristine $MoS_2$ and $MoS_2$-$WS_2$ heterostructure with (a, b) Wavelength-dependent photoresponse, (c, d) different incident optical power density, and (e, f) Transient photoresponse measurement at different bias voltage at 580 nm wavelength of light at an incident optical power of 120 $\mu W/cm^2$ *122*

7.6 Rise time and fall time of (a) Pristine MoS2, (B) MoS2-WS2 heterojunction, and (c, d ) Long-term stability of Pristine MoS2 and MoS2-WS2 heterostructure device with 100 cycles under 580 nm light illumination after 30days in ambient air *123*

7.7 Hysteresis behavior of I–V as a function of different sweeping rates (a) 1V/s, (b) 500 mV/s, (c) 100 mV/s, (d) 10 mV/s, with inset graph showing the magnified I-V of device, and (e) Schematic of the defects generate charge redistribution in pristine MoS2 *126*

7.8 Raman mapping of Pristine MoS2 (a, b) position mapping shows clear intensity difference between E2g and A1g mode, (c, d) and KPFM study of Pristine MoS2 (e-f) mapping of variation in thickness, (g, h) Surface potential images for pristine-MoS2 *126*

7.9 (a) Schematic illustration of the measurement configuration for the modulation of light, and (b-d) Representative photoresponse of the heterojunction photodiode under 580 nm light illumination with the modulated chopper frequency of 1 Hz, 100 Hz, and 1kHz respectively, Band alignment and charge transfer at the heterostructures. (e) a sketch of WS2 particle-decorated on MoS2-based photodetector, and (f) Schematic of Band profiles of MoS2 and WS2, which forms a type II heterojunction relative to the vacuum level. *128*

# List of Tables


| *Table* | *Title* | *page* |
|---|---|---|
| 1.1 | Comparison among different structures of $MoS_2$ | *4* |
| 4.1 | Comparison of Various $MoS_2$ materials based $NO_2$ gas sensor | *80* |
| 5.1 | Comparison of the $NO_2$ sensors based on $SnS_2$ materials | *92* |
| 5.2 | A comparison of $NO_2$ sensor sensing performance based on 2D material | *98* |
| 6.1 | Adsorption energies of $NO_2$ gas over different surface systems. The structural changes in configurations are given by bond lengths and bond angles of the constituent elements | *105* |
| 6.2 | Adsorption energy and equilibrium distance along with charge transfer of the developed adsorption systems | *107* |
| 6.3 | Calculated gas adsorption energies of the gas adsorbed over $SnS_2$ surface | *109* |
| 6.4 | A summary of forward rate ($k_{ir(ads)}$) constant and maximum response of pristine $SnS_2$ and nitrogen plasma $SnS_2$ for various concentration of $NO_2$ at various operating temperatures using irreversible adsorption | *113* |
| 6.5 | Values of various parameter derived by fitting of the response curve as a function of concentration. | *113* |
| 7.1 | Comparison of self-powered photodetector figure of merit | *124* |

# List of Symbols

| *Symbol* | *Description* |
|---|---|
| $\theta$ | Angle of incident |
| A | Area |
| $E_g$ | Bandgap energy |
| $\Phi_B$ | Barrier height |
| k | Boltzmann constant |
| $V_{bi}$ | Build-in potential |
| $\Delta I$ | Change in current |
| $\Delta R$ | Change in resistance |
| $\Delta V$ | Change in voltage |
| $\Delta Ec$ | Conduction band offset |
| $I_a$ or $I_o$ | Current in air |
| $I_g$ | Current in the target gas |
| $E_c$ | Conduction band energy |
| $\tau_d$ | Decay time |
| $I_d$ | Dark Current |
| D* | Detectivity of photodetector |
| W | Depletion width |
| q | Electron charge |
| G | Electron conduction |
| $\chi$ | Electron effinity |
| $\mu$ | Electron mobility |
| $q\ \phi_r$ | Energy difference in conduction band and Fermi level |
| $\upsilon$ | Frequency |
| $\eta$ | Ideality factor |
| Pi | Input power |
| c | Lattice constant |
| l | Length |
| $\Phi_m$ | Metal work function |
| T | Operating temperature |
| h | Plank constant |
| $I_p$ | Photocurrent |
| n | Power coefficient |
| S | Relative response |
| $R_a$ | Resistance in air |
| $R_g$ | Resistance in the target gas |
| R | Responsivity of photodetector |
| $A^*$ | Richardson constant |
| $\tau_r$ | Rise time |
| $E_v$ | Valance band energy |
| $\Delta E_v$ | Valance band offset |
| $V_a$ | Voltage in air |
| $V_g$ | Voltage in the target gas |
| $\lambda$ | Wavelength |
| W | Watt |

# List of Abbreviations

| Abbreviation | Full form |
|---|---|
| 2D | Two-dimensional |
| TMDs | T Transition metal dichalcogenides |
| AFM | Atomic force microscopy |
| BE | Binding energy |
| CL | Cathodoluminescence |
| CVD | Chemical vapor deposition |
| I-V | Current-voltage |
| D | Dimentional |
| DFT | Density functional theory |
| FESEM | Field emission scanning electron microscopy |
| FWHM | Full-width half maxima |
| FET | Field-effect transistor |
| HA | Horizontally aligned |
| IoT | Internet of Things |
| LED | Light-emitting diode |
| LDL | Low detection limit |
| MFC | Mass flow controller |
| MOCVD | Metal-organic chemical vapour deposition |
| Mo | Molybdenum |
| $MoS_2$ | Molybdenum disulfide |
| Sn | Tin |
| $SnS_2$ | Tin disulfide |
| 1D | One-dimensional |
| PL | Photoluminescence |
| PVD | Physical vapour deposition |
| ppm | Parts per million |
| ppb | Parts per billion |
| RF | Radiofrequency |
| $WS_2$ | Tungsten disulfide |
| RMS | Root mean square |
| RT | Room temperature |
| RH | Relative humidity |
| NPs | Nanoparticles |
| SEM | Scanning electron microscopy |
| S | Sulfur |
| Sv | Sulfur vacancy |
| SCCM | Standard cubic centimetres per minute |
| TE | Thermionic emission |
| Pt | Platinum |
| Pd | Palladium |
| Au | Gold |
| Ag | Silver |
| Uv-Vis | Ultraviolet- visible |
| VOC | Volatile organic compound |
| VA | Vertically aligned |
| XPS | X-ray photoelectron spectroscopy |
| XRD | X-ray diffraction |

| | |
|---|---|
| 0D | Zero-dimensional |
| N | Nitrogen |
| JCPDS | Joint Committee of Power Diffraction Standards |
| EDX | Energy dispersive X-ray spectroscopy |
| KPFM | Kelvin probe force microscopy |
| Ar | Ar |
| $O_2$ | Oxygen |
| $CO_2$ | Carbon dioxide |
| $NO_2$ | Nitrogen dioxide |
| $NH_3$ | Ammonia |
| $H_2$ | Hydrogen |
| CO | Carbon monoxide |
| $H_2S$ | Hydrogen sulfide |
| $SO_2$ | Sulfur dioxide |
| Vis | Visible |
| NIR | Near-infrared |
| nm | Nanometer |
| $I_{photo}$ | Photocurrent |
| $I_{dark}$ | Dark current |
| PDCR | Photo-to-dark current ratio |
| P | Incident power |
| A | Active area |
| R | Responsivity |
| D* | Specific detectivity |
| EQE | External quantum efficiency |
| SNR | Signal to noise ratio |
| NEP | Noise equivalent power |
| h | Planck constant |
| $T_{rise}$ | Rise time |
| $T_{fall}$ | Fall time |
| α | Absorption coefficient |

# 1
# Introduction

This chapter provides a comprehensive examination of transition metal dichalcogenides (TMDCs), emphasis primarily on $SnS_2$ and $MoS_2$. It investigates the fundamental structural, optical, and electrical properties of $SnS_2$ and $MoS_2$, including an in-depth analysis of their layer-dependent optical characteristics. The chapter discusses the merits and demerits of the different synthesis methods, both top-down and bottom-up, utilized in the fabrication of $SnS_2$ and $MoS_2$ films. In addition, $SnS_2$ and $MoS_2$ have been identified as outstanding potential for applications in gas sensing and photodetector application. The chapter concludes with a summary of the latest advancements in 2D material-based photodetectors and gas sensors, underscoring the major challenges in their development. Eventually, it outlines the scope and objectives of a doctorate thesis, offering a contextual framework for the specified research.

## 1.1 Background

The Two-dimensional (2D) materials have received significant scrutiny as viable prospects for cutting-edge electronic devices, since the innovative separation of graphene by Novoselov and Geim in 2004 through a simple scotch tape approach, attributed to their remarkable electrical, mechanical, and chemical properties [Mas-Balleste et al., 2011]. These materials, distinguished by their nanosheet morphology, possess two dimensions—length and width—within the micrometer scale, while their thickness is inferior to 1 nm. In recent years, comprehensive investigations have shed light on the remarkable attributes of these atomically thin two-dimensional materials, facilitating the development of devices on both flexible and rigid substrates[Akinwande et al., 2014; Ansari et al., 2023; Novoselov et al., 2016]. Their low power consumption, higher charge carrier mobility, lightweight characteristics, considerable stretchability, formidable mechanical strength, outstanding optical transparency, and favorable stability to the environment render them exceptionally suitable for a broad spectrum of advanced applications[Zhao et al., 2015].

Recent studies have shown the capabilities of several 2D materials, such as TMDCs, graphene, and MXenes, in the fabrication of photodetectors, gas sensors, field-effect transistors, and supercapacitors[Baig, 2023]. The substantial surface-to-volume ratio and superior adsorption properties of 2D materials make them essential for smart sensing applications, including electronic skin (e-skin), photodetectors, home security, and air and health monitoring. TMDCs represent one of the oldest classes of 2D layered materials, encompassing a diverse range of electronic properties including semiconductors, metals, and insulators. The remarkable electronic, optical, and mechanical characteristics of graphene sparked considerable interest in TMDCs[Geim et al., 2007]. The distinctive characteristics of 2D materials, particularly TMDCs, arise from their atomically thin structure, which grants them exceptional electronic, mechanical, and thermal attributes[Nan et al., 2019; Zavabeti et al., 2020]. While graphene is known for its outstanding characteristics, its lack of a bandgap limits its application in switching devices[Geim, 2009]. To address this limitation, researchers have turned their focus toward other 2D semiconductors (2DSCs) with intrinsic bandgaps, such as TMDCs, which are notable for their stability, superior electronic performance, and strong spin-orbit coupling[Chhowalla et al., 2013; Mattheiss, 1973]. These characteristics open up numerous avenues for both fundamental and applied research across various fields, including electronics, sensing technologies, catalysis and energy storage[Jariwala et al., 2014; Wang et al., 2012].

The layered structure of TMDCs can be described by the $MX_2$ formula, where $M$ represents the transition metal ($M = Ti, Zr, Hf, Mo, W$) and $X$ signifies the chalcogen atoms ($X$ = S, Se, Te)[Chhowalla et al., 2013; Choi et al., 2017; Wilson et al., 1969]. The hexagonal lattice of the transition metal is positioned between two layers of chalcogen atoms, providing a unique

arrangement that facilitates diverse electronic behaviors. The filling of non-bonding d-orbitals in the transition metals contributes to this diversity, allowing for the classification of TMDCs into insulators, semiconductors, semi-metals, and metals[Chhowalla et al., 2013; Jariwala et al., 2014]. For instance, $HfS_2$ acts as an insulator, while $MoS_2$, $WS_2$, and $WSe_2$ are semiconductors; $WTe_2$ and $TiSe_2$ are semi-metals, and $NbS_2$ and $VSe_2$ function as metals[Kuc et al., 2011; Mattheiss, 1973]. The various combinations of transition metals and chalcogens have led to the discovery of over 40 distinct TMDC materials, most of which are synthesized, although some naturally occurring variants exist. Figure 1.1 (a), displays the periodic table, emphasizing the transition metals and chalcogen elements. The transition metals marked with solid violet colors are capable of forming layered 2D materials with all chalcogen elements, including Ti, Zr, Hf, V, Mo and Re.

A transition metal dichalcogenide (TMDC) monolayer consists of three atomic layers, with a chalcogen atom positioned between two covalently bonded transition metal atoms. Figure 1.1 (b), illustrates that the layers are interconnected by weak van der Waals forces, facilitating the transition from three-dimensional to two-dimensional structures. TMDCs can exist in three different polymorphs: 1T (trigonal), 2H (hexagonal), and 3R (rhombohedral), where the numbers indicate the number of layers per unit cell and the letters refer to the symmetry type. Each layer generally possesses a thickness of approximately 6-7 Å. The oxidation states of the metal (M) and chalcogen (X) in these materials are +4 and -2, respectively. The lone-pair electrons of chalcogen atoms establish a chemically stable surface on the basal planes of TMDCs, preventing dangling bonds, similarly to graphene. The M-M bond lengths in TMDCs range from 3.15 Å to 4.03 Å, approximately 15-25% larger than those in elemental transition metal solids, reflecting limited d orbital overlap[Chhowalla et al., 2013]. The coordination of the metal in multilayer TMDCs can be either trigonal prismatic ($D_{3h}$) or octahedral ($O_h$ or $D_{3d}$), contingent upon the most thermodynamically advantageous configuration, as shown in Figures 1.1 (c, d).

Recent advancements in the synthesis and characterization of TMDCs have further enhanced their appeal for integration into electronic circuits and devices. The ability to manipulate their properties through techniques such as chemical vapor deposition (CVD) allows for the fine-tuning of their electronic characteristics, making them suitable candidates for high-performance applications. The application of TMDCs in gas sensing and photodetection has attracted considerable attention owing to their extensive surface area and superior adsorption properties, enhancing their sensitivity and selectivity for detecting different gases. As the field of 2D materials continues to evolve, ongoing research into TMDCs aims to address challenges related to scalability and device fabrication[Alam et al., 2021]. Despite the promising attributes of these materials, achieving reliable large-scale production and integration into commercial applications remains a focus of investigation. The exploration of novel synthesis methods and the development of composite materials are critical for enhancing the performance and applicability of TMDCs in real-world scenarios.

$SnS_2$ and $MoS_2$ is a key member of the transition metal dichalcogenides (TMDs) family, attracting considerable attention due to its outstanding semiconductor characteristics. It features a direct bandgap, a high absorption coefficient, high carrier mobility, large growth surface area, rapid charge transportation, and a significant current on/off ratio, making it an ideal candidate for an innovative device application, including photodetectors, solar cells, sensors, and transistors.

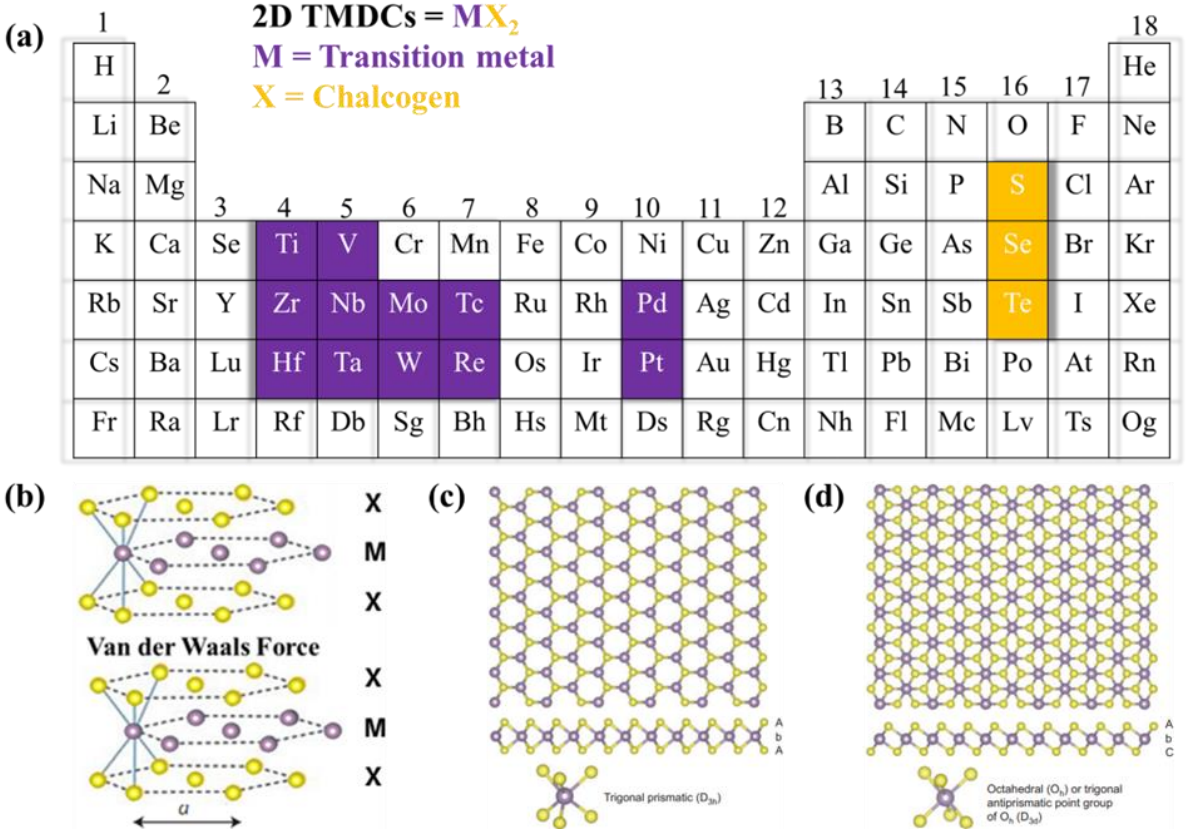



**Figure 1.1:** (a) Transition metal dichalcogenides materials in the periodic table that form layered materials and an example of 2D materials, (b) Stacking of hexagonally packed planes bounded by the van der Waals force. Possible coordination unit of layered TMDs, and (c) Trigonal prismatic (AbA) (d) Octahedron (AbC)[Chhowalla et al., 2013].

## 1.2 Molybdenum disulfide ($MoS_2$) and Tin disulfide ($SnS_2$)

### 1.2.1. Properties of $MoS_2$

#### 1.2.1.1 Basic crystalline structure

In its bulk form, $MoS_2$, characterized by its black powder or particle form, consists of layers arranged such that each Mo atom is surrounded by six S atoms, with a total thickness of three atomic layers. The adjacent layers are bonded by weak van der Waals forces, but strong covalent S-Mo-S bonds link the molybdenum (Mo) and sulfur (S) atoms. The shear strength of $MoS_2$ against normal loads has been measured at 24.6 MPa, highlighting its unique mechanical properties that make it suitable for solid lubricant applications. $MoS_2$ exhibits polytypism, with three distinct configurations i.e., 1T, 2H, and 3R. 1T, 2H, and 3R are associated with the point groups $D_{6d}$, $D_{6h}$, and $C_{3V}$, respectively, which are classified based on their atomic arrangements and layer stacking configurations, as depicted in Figure 1.2[Saha et al., 2020]. The first digit in the designation represents the number of layers, while the letters T, H, and R correspond to trigonal, hexagonal, and rhombohedral structures, respectively. The lattice parameters for each of these configurations are summarized in Table 1.1. By modifying the synthesis techniques, diverse allotropes and morphologies can be produced, encompassing 3D (e.g., snowflakes, flowers, and dandelions), 2D (e.g., nanostrips, nanosheets, and nanoribbons), 1D (e.g., nanowires and nanorods), and 0D (e.g., nanoplatelets). The thermodynamically stable and naturally occurring form of $MoS_2$ is the 2H phase, comprising approximately 3% of the 3R phase.

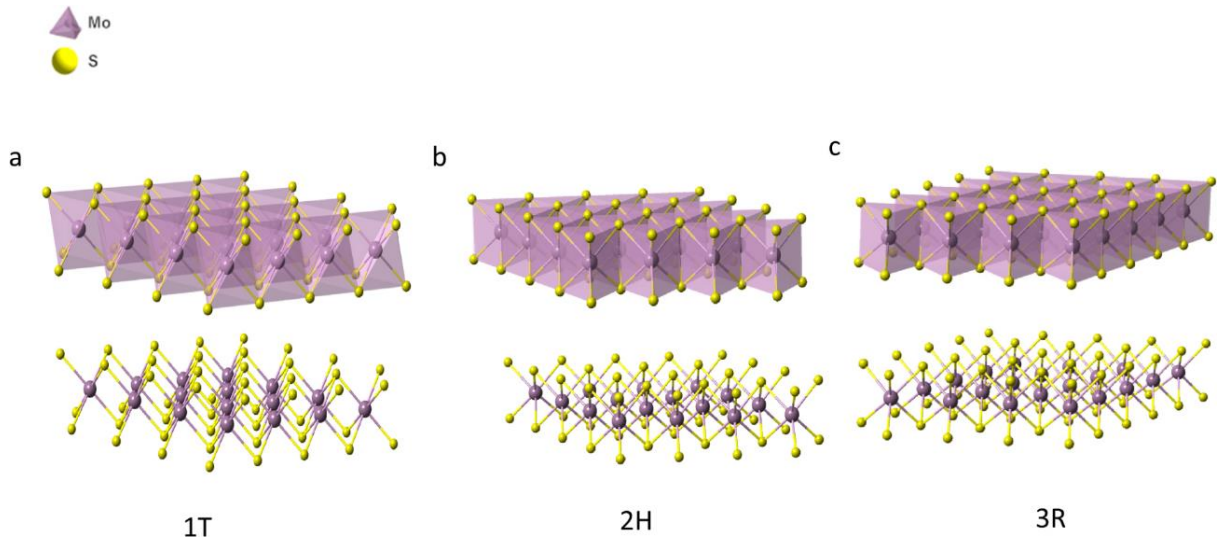



**Figure 1.1:** Crystal structures of $MoS_2$ polymorphs. (a) 1T phase (octahedral), (b) 2H phase (trigonal prismatic) and (c) 3R phase (trigonal prismatic)[Saha et al., 2020].

**Table 1.1:** Comparison among different structures of $MoS_2$

| Lattice Parameters (A°) | Lattice Parameters (A°) | Property | Space group | Carrier Mobility ($cm^2.V^{-1}.s^{-1}$) | Electrical Conductivity (s/m) | Adsorption Peak | Applications |
|---|---|---|---|---|---|---|---|
| 1T (Octahedral) | a = 5.60, c = 5.99 | Paramagnetic and metallic | P3m1 | 56 | 105 higher than 2H Phase | No peaks at 604 nm and 667 nm | Water decomposition, Intercalation chemistry |
| 2H (Trigonal Prismatics) | a = 3.15, c = 12.30 | Semiconducting | $P6_3/mmc$ | 24 | Low ( ~0.1s) | Showed peaks at 604nm and 667nm | Dry Lubricants, Dry Fuel |
| 3R (Trigonal Prismatics) | a = 3.17, c = 18.38 | Semiconducting | $P6_3/mmc$ | 100 | Low ( ~0.1) | Showed peaks at 604nm and 667nm | Dry Lubricants and nonlinear optical sensing |

The 2H-$MoS_2$ configuration is recognized as the most stable form, typically found in natural molybdenite, with lattice parameters a = 3.15 Å and c = 12.30 Å, as illustrated in Figure 1.3 (a). It belongs to the P63/mmc space group and displays a hexagonal Bravais lattice configuration[He et al., 2016]. As an n-type semiconductor, it possesses a charge carrier mobility of 100 $cm^2/(Vs)$ and remains thermodynamically stable up to approximately 1203 °C, at which point it transforms into $Mo_2S_3$. Its nonmagnetic semiconductor behavior arises from the antiparallel spin arrangement of its 4d electrons. Different synthesis techniques for 2H-$MoS_2$ encompass chemical vapor deposition, hydrothermal synthesis, and ball milling. When subjected

to temperatures over 800 °C and elevated pressure, 2H $MoS_2$ can undergo a transition from a semiconducting to a metallic state.

Another metastable phase of $MoS_2$ is the 1T (tetragonal) configuration that exhibits metallic and paramagnetic properties, characterized by lattice parameters a = 5.60 Å and c = 5.99 Å, as depicted in Figure 1.3 (b)[Acerce et al., 2015; Voiry et al., 2013]. This phase possesses a greater number of active sites and higher electrical conductivity compared to the more stable 2H phase, making it suitable for applications in intercalation chemistry and water splitting. The transformation of 1T-$MoS_2$ into the more stable 2H-$MoS_2$ can be achieved through methods such as annealing, electric doping, and the application of strain.

The 3R (rhombohedral) phase of $MoS_2$ is a stable form that demonstrates semiconductor characteristics and can obstruct $MoS_2$. The material is classified within the R3m space group, exhibiting lattice parameters of a = 3.17 Å and c = 18.38 Å[Saha et al., 2020]. Upon heating, the 3R phase may transform into the 2H phase. The absence of inversion symmetry in 3R-$MoS_2$ crystals results in remarkable nonlinear optical characteristics, potentially beneficial for nonlinear optical device applications.

The intriguing electrical properties of $MoS_2$ can be elucidated through Crystal Field Theory (CFT). The d-orbitals of the transition metal molybdenum (Mo) comprise five non-degenerate orbitals: $d_{x^2-y^2}$, $d_{z^2}$, $d_{xy}, d_{yz}, and\ d_{zx}$, which are situated between bonding (σ) and antibonding (σ*) states. In a trigonal prismatic (D3h) arrangement, these orbitals split into three distinct energy levels: $d_{z^2}\ (a1)$, $d_{x^2-y^2} + d_{xy}(e), and\ d_{yz} + d_{zx}$(e'). Conversely, in an octahedral ($D_{3d}$) environment, the orbitals divide into two levels: the $e_g$ level, comprising $d_{z^2}$, $d_{x^2-y^2}$ and the $t_{2g}$ level, which includes $d_{xy}, d_{yz}, and\ d_{zx}$. $MoS_2$ possesses a d-electron count of $d^2$, with the lowest energy level $d_{z^2}$, being fully occupied in the 2H-$MoS_2$ phase. The presence of partially filled higher orbitals in 1T-$MoS_2$ results in metallic conductivity, while complete filling of these orbitals in 2H-$MoS_2$ leads to semiconducting behavior. The filling of d-orbitals for both phases is depicted in Figures 1.3 (c) and 1.3 (d), illustrating the distinct electronic characteristics that arise from the different orbital configurations.

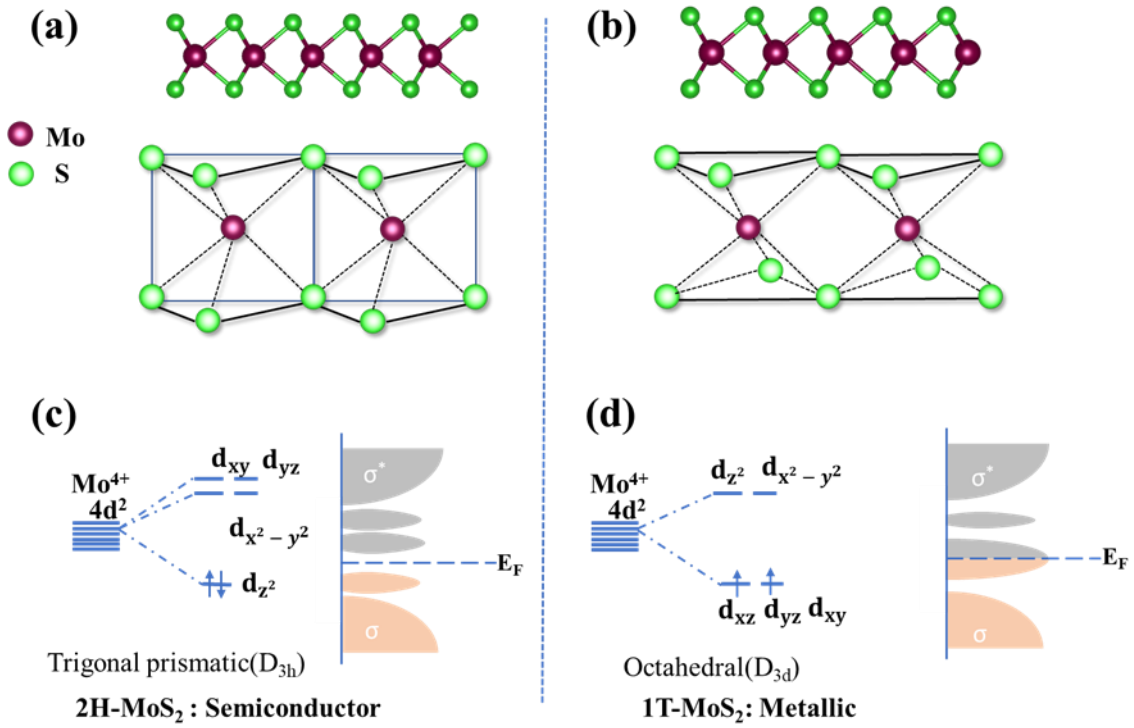



**Figure 1.2:** Crystal structure of $MoS_2$ (a) 2H phase (b) 1T phase, with a schematic representation of the gradual filling of d orbitals that are situated in the bandgap between bonding (σ) and anti-bonding states (σ*) [The chemistry of two-dimensional layered transition metal dichalcogenide nanosheets[Chhowalla et al., 2013; Jin et al., 2018].

### 1.2.1.2 Band Structure

$MoS_2$ is a semiconductor with a distinctive band structure that is significantly influenced by the number of layers in the crystal. The layers of $MoS_2$ are interconnected through weak van der Waals forces, resulting in a layered architecture. Upon reduction of bulk $MoS_2$ to a monolayer, the bandgap shifts from an indirect to a direct configuration, with the bandgap energy rising from 1.2 eV to 1.8 eV[Li et al., 2007; Mak et al., 2010a; Zhao et al., 2013a]. This alteration in band structure arises from the differing electronic states that contribute to the formation of the conduction and valence bands, which are primarily formed from a linear combination of sulfur (S) and molybdenum (Mo) orbitals.

The Brillouin zone of $MoS_2$ features three symmetry points: Γ, M, and K, as illustrated in Figure 1.4 (a, b). As the number of layers decreases, the theoretically calculated electronic band structure of $MoS_2$ shifts from indirect to direct semiconducting behavior. In bulk $MoS_2$, the conduction band minimum (CBM) is situated between the Γ and K points, whereas the valence band maximum (VBM) exists at the Γ point. As the layer count diminishes to bilayer and quadrilayer configurations, significant changes occur in the VBM at the Γ point and the CBM between the K and Γ points. This is attributed to the electronic states near the Γ and K points being composed of out-of-plane orbitals, which are strongly influenced by interlayer coupling. In contrast, the electronic states at the K point remain largely unchanged with respect to thickness, as both the CBM and VBM at this point are predominantly formed by localized in-plane orbitals of Mo (3d) and S (2p) atoms. The transition from an indirect to a direct bandgap in monolayer $MoS_2$ is mostly attributable to quantum confinement phenomena.

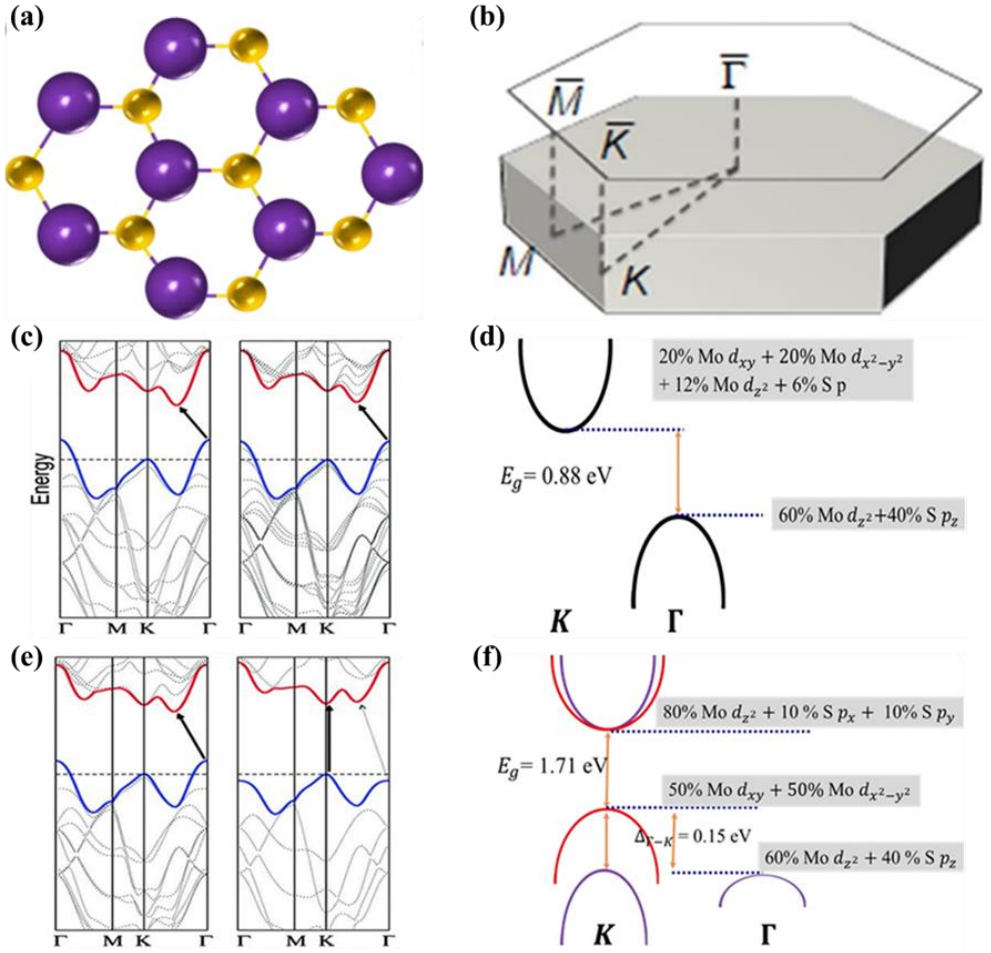



**Figure 1.3: (a)** Top view of the 2H-$MoS_2$ structure. (b) Corresponding Brillouin zones for the 2H-$MoS_2$[Kolobov et al., 2016]. Theoretically calculated band structures for the (c) Bulk $MoS_2$ and quadrilateral $MoS_2$. (d) Schematics of orbitals combinations of CBM and VBM electronic states and corresponding Mo and S orbitals for bulk $MoS_2$. Band structures for the (e) Bilayer $MoS_2$ and monolayer $MoS_2$. (f) Schematics of orbitals combinations of CBM and VBM electronic states and corresponding Mo and S orbitals for monolayer $MoS_2$ [Novoselov, 2011; Splendiani et al., 2010].

In bulk $MoS_2$ and up to four layers, the CBM is located between the Γ and K points, whereas the valence VBM is positioned at the Γ point (Figure 1.4 (c, d)). As the layer count diminishes, the electronic states at the VBM and CBM, situated between the Γ and K points, are notably influenced; conversely, the states at the K point exhibit less alteration. Additionally, the indirect bandgap increases monotonically with a reduction in layer number. In monolayer $MoS_2$, the CBM and VBM positions shift to the K point, resulting in a direct bandgap (Figure 1.4 (e)). These pronounced changes in band structure with decreasing layer count are directly linked to the nature of the orbitals involved in the formation of these electronic states. The CBM and VBM states between the Γ and K points are predominantly formed from a linear combination of the p orbitals of S atoms and the d orbitals of Mo atoms, as illustrated in Figures 1.4 (d) and Figure 1.4 (f). These out-of-plane orbitals are significantly affected by interlayer coupling, which in turn impacts the energy levels of these electronic states based on the thickness of the $MoS_2$ film. Conversely, the electronic states at the K point are primarily influenced by the in-plane Mo d orbitals and remain unaffected by the number of layers.

#### 1.2.1.3 Optical properties

This section discusses the fundamental optical properties of $MoS_2$, examining the transition from its bulk form to monolayer configurations, focusing on photoluminescence (PL), absorption, and Raman spectroscopy.

**(a) Raman spectra**

Raman spectroscopy serves as a crucial characterization and non-destructive method for elucidating the structural parameters of materials transitioning from a three-dimensional to a two-dimensional layered configuration. It is an effective technique for providing insights into lattice vibrations, doping levels, layer count, and strain within $MoS_2$ films. In contrast, monolayer and few-layer $MoS_2$ primarily identified two prominent Raman peaks: $E^1_{2g}$and $A_{1g}$, that correspond to the in-plane and out-of-plane vibrations of sulfur atoms, respectively (Figure 1.5(a)). Consequently, the intensity ratio of $E^1_{2g}/A_{1g}$ can be employed to characterize the growth structure and orientation of $MoS_2$ flakes, with this ratio being highly sensitive to strain and doping levels in $MoS_2$ films[Kukucska et al., 2017].

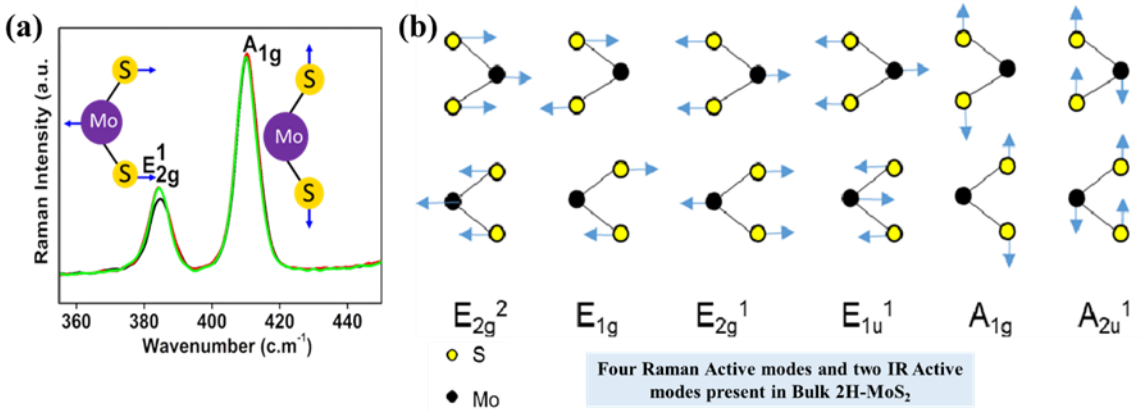



**Figure 1.4:** (a) Two Raman ($A_{1g}$ and $E_{2g}{}^1$) active mode in mono and few-layers $MoS_2$, and (b) All possible vibrational modes ($E_{2g}{}^2$ , $E_{1g}$, $E_{2g}{}^1$ , $A_{1g}$ and $E_{1u}{}^1$ , $A_{2u}{}^1$ ) in bulk $MoS_2$ [Lee et al., 2010; Ye et al., 2015].

For monolayer $MoS_2$, the Raman spectrum observed at a wavenumber at ~ 384 $cm^{-1}$ and 402 $cm^{-1}$, corresponding to the $E^1_{2g}$and $A_{1g}$modes, respectively. With an increase in the number of layers, the $E_{2g}{}^1$ mode exhibits a red shift, whereas the $A_{1g}$ mode displays a blue shift. The difference in wavenumber between these two modes increases with layer count, serving as a reliable indicator of $MoS_2$ thickness[Li et al., 2012b]. Although van der Waals interactions are responsible for the bonding between adjacent layers, leading to an increase in the restoring force on each atom with additional layers, experimental observations indicate a deviation from this

expectation. This suggests that the frequency shift is influenced by factors beyond van der Waals interlayer coupling, including surface reconstruction and long-range Coulomb interactions, which play a crucial role in diminishing the overall restoring force on the atoms[Lee et al., 2010].

Bulk $MoS_2$ exhibits four Raman active modes $E_{2g}^2$ , $E_{1g}$, $E_{2g}^1$ and $A_{1g}$ at 32, 286, 383 and 408 $cm^{-1}$ respectively, and two IR active modes ($E_{1u}^1$, and $A_{2u}^2$), as illustrated in Figure 1.5 (b). In Raman spectroscopy of $MoS_2$, the two prominent modes identified are $E_{2g}^1 and A_{1g}$, while the other modes, $E_{2g}^2$ and $E_{1g}$, are not detectable in monolayer samples due to the constraints imposed by the selection rules of the scattering geometry or limitations associated with Rayleigh scattered radiation[Lee et al., 2010]. The $E_{2g}^2$ mode is a low-frequency phonon mode, typically found in the range of 30 $cm^{-1}$ to 40 $cm^{-1}$, making it challenging to differentiate from the Rayleigh background scattering. To effectively identify such low-frequency phonon modes, specialized equipment, including a triple-grating Raman spectrometer and specific filters, is necessary to enhance detection capabilities[Zhao et al., 2013b].

**(b) Absorbance**

$MoS_2$ exhibits optical transparency of up to 85%, with an absorption efficiency of around 10% in the visible to near-infrared (NIR) spectrum for layers of a few nanometers in thickness. The absorbance spectra of $MoS_2$ show two prominent peaks at 660 and 605 nm (A- and B-exciton), as well as a stronger peak near 440 nm. The A and B peaks are connected with optical absorption due to band edge excitons from direct bandgap transitions at the Brillouin zone K point[Castellanos-Gomez et al., 2016]. Excitonic absorption from $MoS_2$ van Hove singularity causes the large C peak[Klots et al., 2014]. Although photoluminescence (PL) spectra normally use an excitation wavelength of 500 nm, recent reflectance and photocurrent spectroscopy research have shown this broad peak C. This broad peak C is attributed to strong intraband transitions resulting from significant mixing of d states and S p states[Liu et al., 2014c]. The absorbance of $MoS_2$ increases progressively with film thickness, becoming opaque after six to eight layers. Figure 1.6 (a), depicts the absorbance spectra of MoS2 as a function of excitation wavelength, dependent on thickness, varying from one to six layers. Figure 1.6 (b) shows that $MoS_2$ has a significant absorption coefficient throughout a wide spectral range. The absorbance spectra also indicate a redshift in the A-exciton peak position as the layer number increases, while the B-exciton peak remains relatively stable, in agreement with PL spectral observations. The inset of Figure 1.6 (a), highlights the thickness-dependent redshift of peaks A and C, while peak B remains nearly unchanged in position.

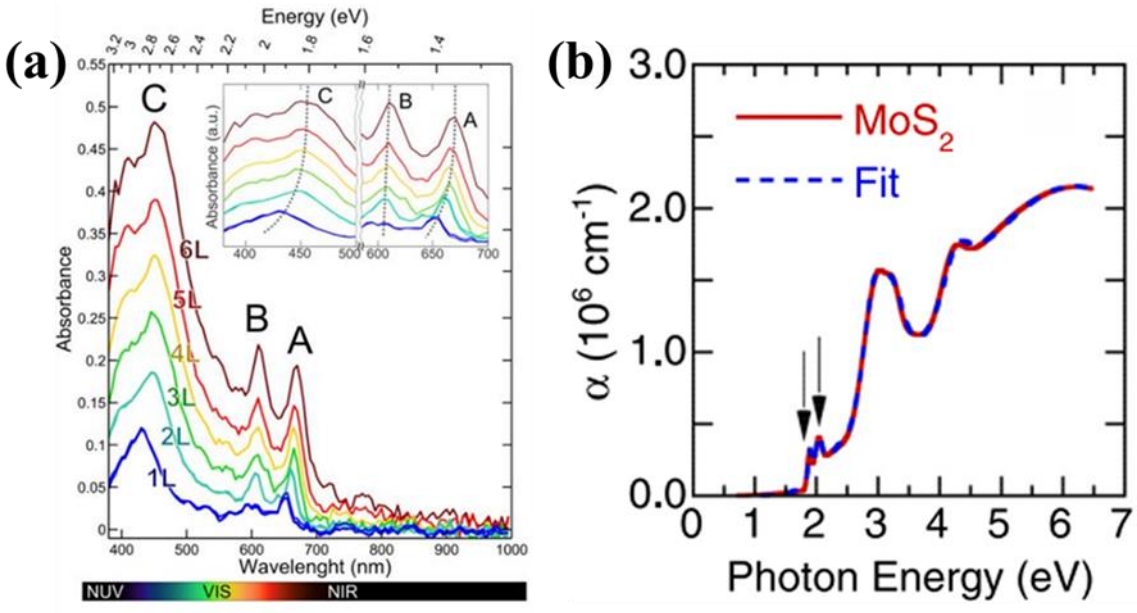



**Figure 1.5:** (a) Optical absorption spectra for $MoS_2$ from monolayer to six layers, and (b) The absorption coefficient was calculated for the $MoS_2$[Castellanos-Gomez et al., 2016; Liu et al., 2014c].

### (c) Photoluminescence spectra

$MoS_2$ exhibits thickness-dependent tunable photoluminescence (PL), characterized by two peaks, labelled 'A' and 'B', resulting from the splitting of the valence band into two energy levels (v1 and v2), as seen in Figure 1.7 (a)[Coehoorn et al., 1987; Splendiani et al., 2010]. The peak '*I*' is associated with indirect bandgap transitions observed in few-layer and bulk $MoS_2$. The mechanisms underlying valence band splitting differ between monolayer and few-layer $MoS_2$; in monolayer $MoS_2$, the splitting occurs due to spin-orbit coupling and the absence of inversion symmetry[Cheiwchanchamnangij et al., 2012; Mouri et al., 2013; Tongay et al., 2013], while in bilayer and few-layer $MoS_2$, it results from the combined effects of spin-orbit coupling and interlayer interactions[Zhu et al., 2011]. The peaks 'A' and 'B' represent direct excitonic transitions at the K symmetry point within the Brillouin zone[Mak et al., 2010a; Pei et al., 2015]. Additionally, the low-energy peak 'A' can be further resolved into two components: excitons and trions, with the presence of trions being influenced by electron doping[Cho et al., 2015a; Mak et al., 2013]. An exciton is defined as a bound electron-hole pair formed through Coulomb interactions, while a trion is a bound state comprising an electron and an exciton (Figure 1.7 (b)).

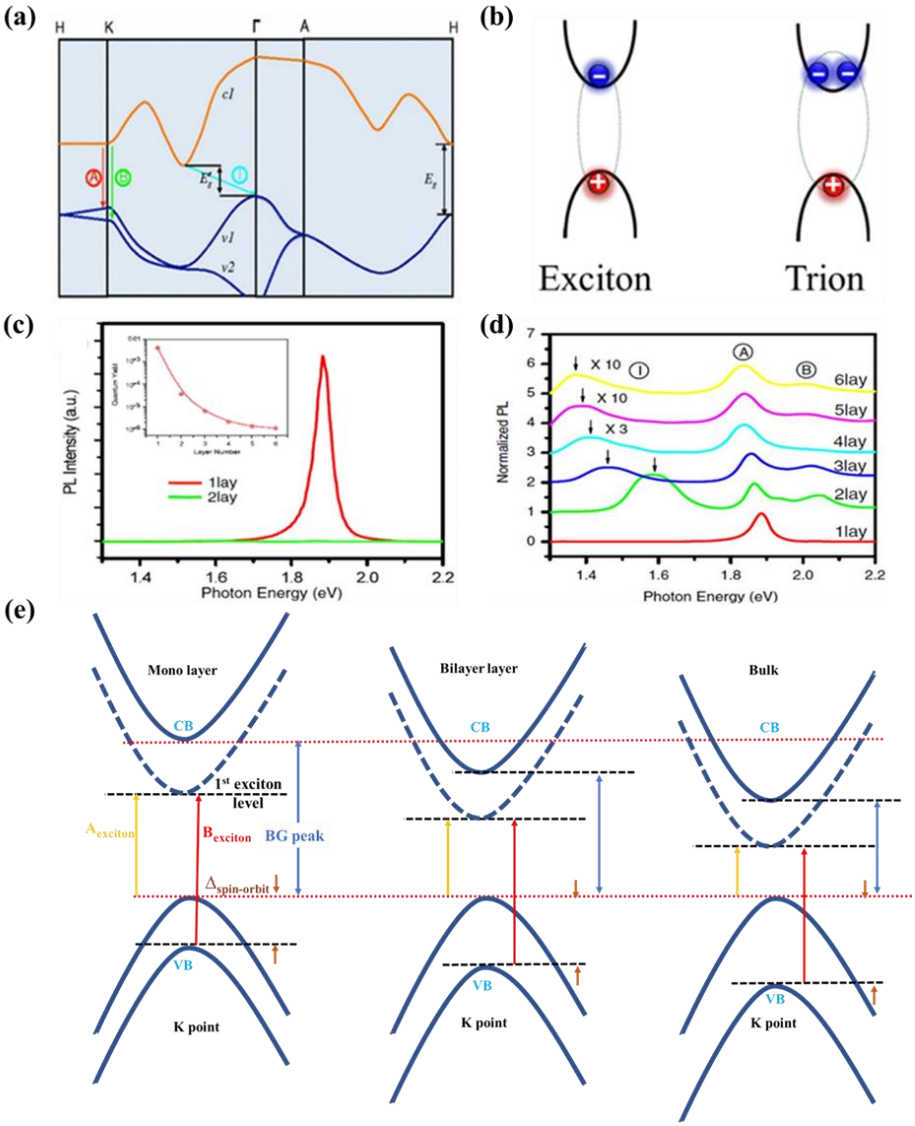



**Figure 1.6:** (a) Band structure of the bulk and monolayer $MoS_2$, where A and B indicate the direct-gap transitions, and I represent the indirect-gap transition. The indirect gap for the bulk is denoted by $E_g'$ and direct gap for the monolayer is indicated as $E_g$. (b) Schematic for excitons and trions. (c) PL spectra for mono and bilayer $MoS_2$, inset displaying the relative quantum yield of MoS2 as a function of layer number, (d) The normalized PL spectra with respect to layer number[Mak et al., 2010b]. (e) Schematic illustration of the optical transition occurring at the K-point of the Brillouin zone in different regions of $MoS_2$, including monolayer, bilayer, and bulk. The A exciton peak experiences a red shift due to the reduction of the first exciton level. The B-exciton peak position remains relatively the same because the decrease in the exciton level is balanced by an increase in the valence band splitting energy[Dhakal et al., 2014].

The PL intensity of $MoS_2$ significantly decreases as the number of layers increases, with bulk $MoS_2$ exhibiting the lowest PL intensity. In bulk $MoS_2$, the bandgap is indirect, whereas monolayer $MoS_2$ possesses a direct bandgap, resulting in a considerably higher PL intensity for monolayer samples, which diminishes with increasing layer thickness (Figure 1.7 (c-d))[Mak et al., 2010b]. The PL efficiency can be expressed as:

$$\eta = K_{rad}/(K_{rad} + K_{defect} + K_{relex} \quad (1.1)$$

where $K_{rad}$, $K_{defect}$, and $K_{relex}$ represent the rates of radiative recombination, defect trapping, and electron relaxation, respectively, within the conduction and valence bands[Splendiani et al., 2010]. The direct excitonic transitions at the K-point in both monolayer and bulk MoS2 occur at the same energy level, which results in minimal variation in the radiative recombination rate $K_{rad}$ with changes in thickness. In bulk $MoS_2$, the intraband relaxation rate $K_{relex}$ is relatively high, contributing to the low PL intensity. As the thickness of $MoS_2$ decreases, the indirect bandgap transitions shift toward a direct bandgap, resulting in increased PL intensity due to the reduction of $K_{relex}$ with decreasing layer number.

The A-exciton peak displays a redshift as the number of layers increases, attributed to a decrease in the energy gap between the band edges or a reduction in the first exciton level, or a combination of both effects. In contrast, the position of the B-exciton peak remains relatively stable with increasing layer number, as the decrease in exciton energy is counterbalanced by additional splitting in the valence band edge, as illustrated in Figure 1.7 (e). Consequently, a notable increase in photoluminescence (PL) intensity is observed, accompanied by a negligible defect-related recombination rate $K_{defect}$.

### 1.2.2. Properties of $SnS_2$

#### 1.2.2.1 Physical properties of $SnS_2$

Tin disulfide ($SnS_2$) is classified as *IV–VI* chalcogenide material, characterized by its golden-yellow color, resembling the configuration of transition metal dichalcogenide (TMDS)[Cao et al., 2018]. The atomic structure of $SnS_2$ features a tin (Sn) atom situated between two hexagonally close-packed sulfur (S) atoms[Sun et al., 2020b]. In its layered form, $SnS_2$ forms planar threefold layers (TLs) where strong covalent bonds are established within the plane, while weaker van der Waals interactions prevail between the layers, as depicted in Figure 1.8 (a). The crystal structure of $SnS_2$ is categorized under the $P\bar{3}m1$ (164) space group, with lattice parameters a = b = 0.3643 nm and c = 1.7683 nm. Similar to other TMDs, $SnS_2$ exhibits a layered architecture and possesses several notable properties, including a high optical absorption coefficient, a tunable bandgap, low toxicity, and natural abundance, making it a promising candidate for two-dimensional material applications such as photocatalysis, photodetector, and gas sensors. $SnS_2$ is identified as an n-type semiconductor with a narrow energy bandgap ranging from 2.0 to 2.4 eV[Chava et al., 2019]. The band positions were determined through linear extrapolation of the band edges and secondary electron cut-off, resulting in an ionization potential ($E_{vac} - E_{VBM}$) of 6.44 ± 0.07 eV and an electron affinity ($E_{vac} - E_{CBM}$) of 4.16 ± 0.17 eV. Consequently, the bandgap ($E_{CBM} - E_{VBM}$) was calculated to be 2.28 ± 0.15 eV, indicative of an indirect bandgap, as shown in Fig. 2(b). $SnS_2$ also demonstrates enhanced electron mobility (approximately 230 $cm^2\ V^{-1}\ s^{-1}$), high capacitance (645 $mA\ h\ g^{-1}$), and reduced environmental toxicity[Sun et al., 2019]. Furthermore, $SnS_2$ facilitates the operation of electronic devices at elevated temperatures, voltages, and frequencies, thereby enhancing system efficiency. Its layered $CdI_2$-type morphology contributes to its responsiveness to visible light and stability in acidic and neutral solutions, further promoting its application in effective environmental remediation. $SnS_2$ exhibits a range of unique and distinct properties that enhance its potential for various technological applications[Zhang et al., 2016].

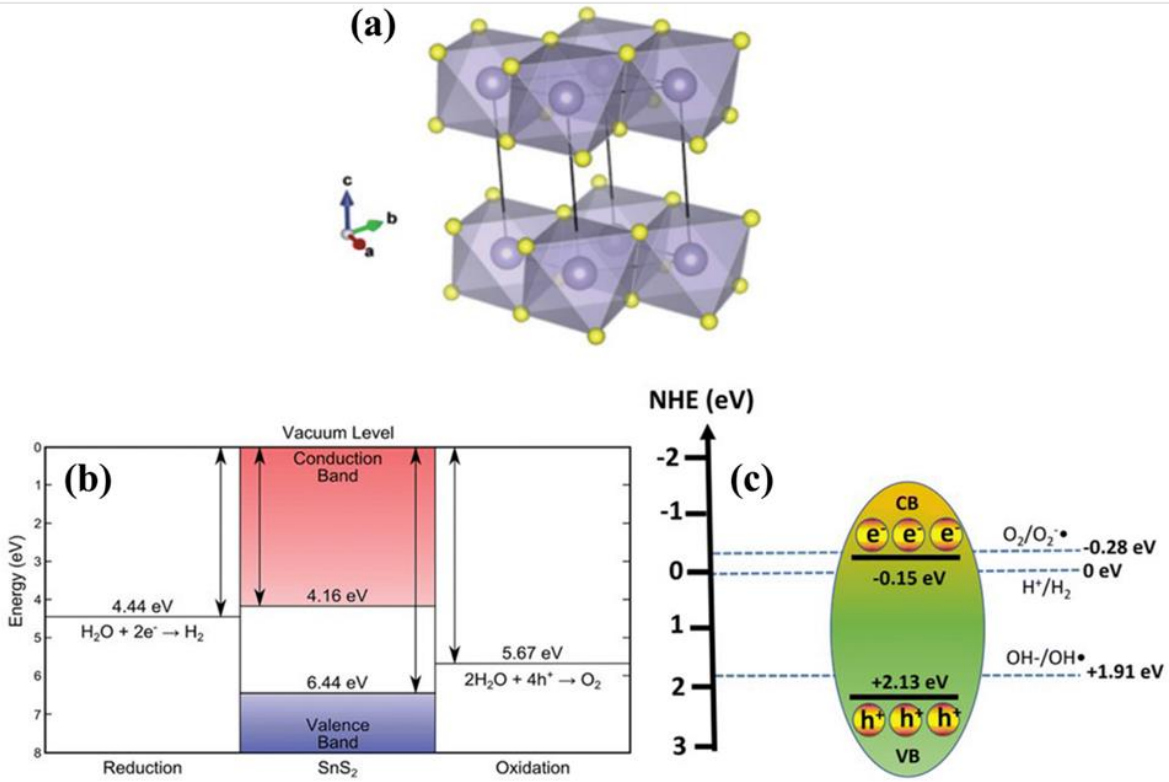



**Figure 1.7:** Properties of $SnS_2$. (a) Crystal structure, (b) band position, and (c) Band position of $SnS_2$ for photocatalytic reactions [Burton et al., 2016].

$SnS_2$ exhibits several unique and distinct properties, including:

- **Ultra-high Surface Area and Porosity:** The exceptionally high specific surface area of $SnS_2$ can be attributed to the effects of transition metal doping and the generation of vacancy defects. For instance, nickel (Ni) doping has been shown to enhance the surface area and produce diverse morphologies in both pure $SnS_2$ and Ni-doped $SnS_2$, as confirmed by scanning electron microscopy (SEM) analysis [Chen et al., 2018]. The pure $SnS_2$ nanosheets displayed hexagonal structures arranged in a spirally stacked configuration resembling a nanoflower, while the Ni-$SnS_2$ nanosheets exhibited a spherical stacking with numerous gaps between the nanoplates. Nitrogen ($N_2$) adsorption–desorption isotherms were employed to analyze the surface areas of various samples, revealing values of 79.90 $m^2\ g^{-1}$ for $SnS_2$-2, 72.25 $m^2\ g^{-1}$ for $SnS_2$-3, 78.40 $m^2\ g^{-1}$ for $SnS_2$-4, 86.14 $m^2\ g^{-1}$ for $SnS_2$-5, and 73.01 $m^2\ g^{-1}$ for $SnS_2$-6. Among these, $SnS_2$-5 exhibited the highest surface area, leading to an increased number of exposed active sites that further enhanced photocatalytic efficiency. Conversely, the reduced surface area of $SnS_2$-6 was attributed to an increased dosage of thioacetamide (TAA) [Qiang et al., 2020].
- **Broader Visible Light Absorption**: The efficient light-harvesting capability of $SnS_2$ is primarily due to the localized surface plasmon resonance (LSPR) effect, which arises from the collective oscillation of surface electrons in noble metals, such as gold (Au) [Mondal et al., 2021]. A significant increase in photo-absorption at 600 nm was observed, attributed to transitions within the intrinsic band gap, as confirmed by UV–vis diffuse reflectance spectroscopy (DRS) analysis. Furthermore, the broad-spectrum response to a 455 nm light source (LED lamp) indicates that $SnS_2$ nanoparticles possess excellent visible light responsiveness for the photodegradation of methyl orange (MO)[Park et al., 2015]. The synergistic effects of self-doping with sulfur, exciton transitions of adsorbed sulfide ions, and improved light trapping capabilities contribute to the enhanced visible light absorption.

Among these properties, the ultra-high surface area is particularly significant due to the increased availability of active sites. Additionally, the engineering of vacancy defects promotes accelerated

charge separation and enhances the absorption of reactants, resulting in improved performance of gas sensor.

#### 1.2.2.2 Structure of $SnS_2$

The theoretical simulations provided insights into the structural and electronic properties of the $SnS_2$ monolayer, which can exhibit both trigonal and hexagonal configurations. Typically, $SnS_2$ exists in two distinct phases: hexagonal (2H) and trigonal (1T), with the 1T phase being regarded as more thermodynamically stable than the 2H phase. Within the $SnS_2$ lattice, two sulfur (S) planes sandwich a tin (Sn) atom, forming strong covalent bonds, while the Sn atom is octahedrally coordinated by six sulfur atoms. This arrangement leads to a trilayer structure consisting of S-Sn-S atoms, corresponding to three atoms per unit cell. Cross-sectional and side views of the $SnS_2$ monolayer are illustrated in Figure 1.9 (a, b) [Sun et al., 2020b; Xia et al., 2015].

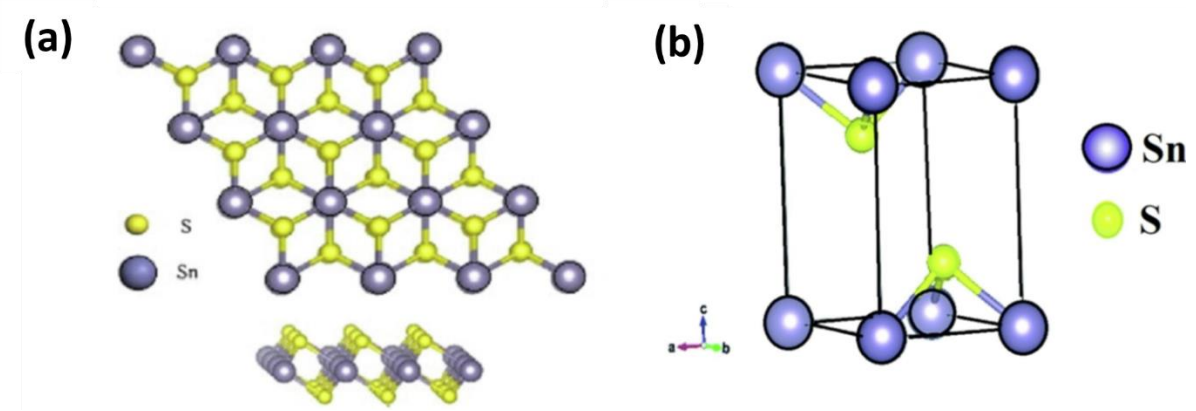



**Figure 1.8:** Side view and top view of ball and stick model schematic diagram of $SnS_2$[Xia et al., 2015]

#### 1.2.2.3 Optical properties

The optical properties of materials are crucial for enhancing their applications in photovoltaic devices, photoconductors, and near-infrared detectors. Semiconductors exhibit a sharp increase in absorption wavelength that corresponds to the energy of their bandgap, which results from the optical excitation of electrons across this energy bandgap [Mabiala-Poaty et al., 2018; Raizada et al., 2021]. The optical characteristics of $SnS_2$ have been investigated through various techniques, including optical absorbance measurements, Raman spectroscopy, and ultraviolet-visible (UV-vis) spectral analysis.

Burton and colleagues examined the optical absorption spectra, as well as the direct and indirect bandgaps of $SnS_2$, by plotting the absorption coefficient against photon energy (Figure 1.10 (a))) [Burton et al., 2016]. The resulting curves were derived from the linear regions, which were used to estimate the direct energy bandgap as a function of temperature. At room temperature (300 K), $SnS_2$ exhibits a direct bandgap of 2.38 ± 0.01 eV, while the indirect bandgap was determined by analyzing the square root of the absorption coefficient in relation to photon energy, along with the generalized linear portion of the curves at zero.

In a related study, Panda and co-researchers fabricated thin films of $SnS_2$ using cetyltrimethylammonium bromide (CTAB) and $SnCl_4 \cdot 5H_2O$ as precursors via a dip-coating method [Panda et al., 2007]. The Raman spectra indicated that the film surfaces were homogeneous with some localized variations, as depicted in Figure 1.10 (c). An intense peak at 314 $cm^{-1}$, corresponding to the $A_{1g}$ mode, was observed for the $SnS_2$ particles, while no distinct band for the $E_g$ modes was detected at 210 $cm^{-1}$. Additionally, the intensity of the Raman peak at 314 $cm^{-1}$ increased with higher annealing temperatures and longer annealing times. The full width at half maximum (FWHM) was also measured, and a Lorentzian fit was applied to the Raman peak, revealing a decrease in FWHM with increasing annealing temperature, which may indicate an improvement in the crystallinity of the films.

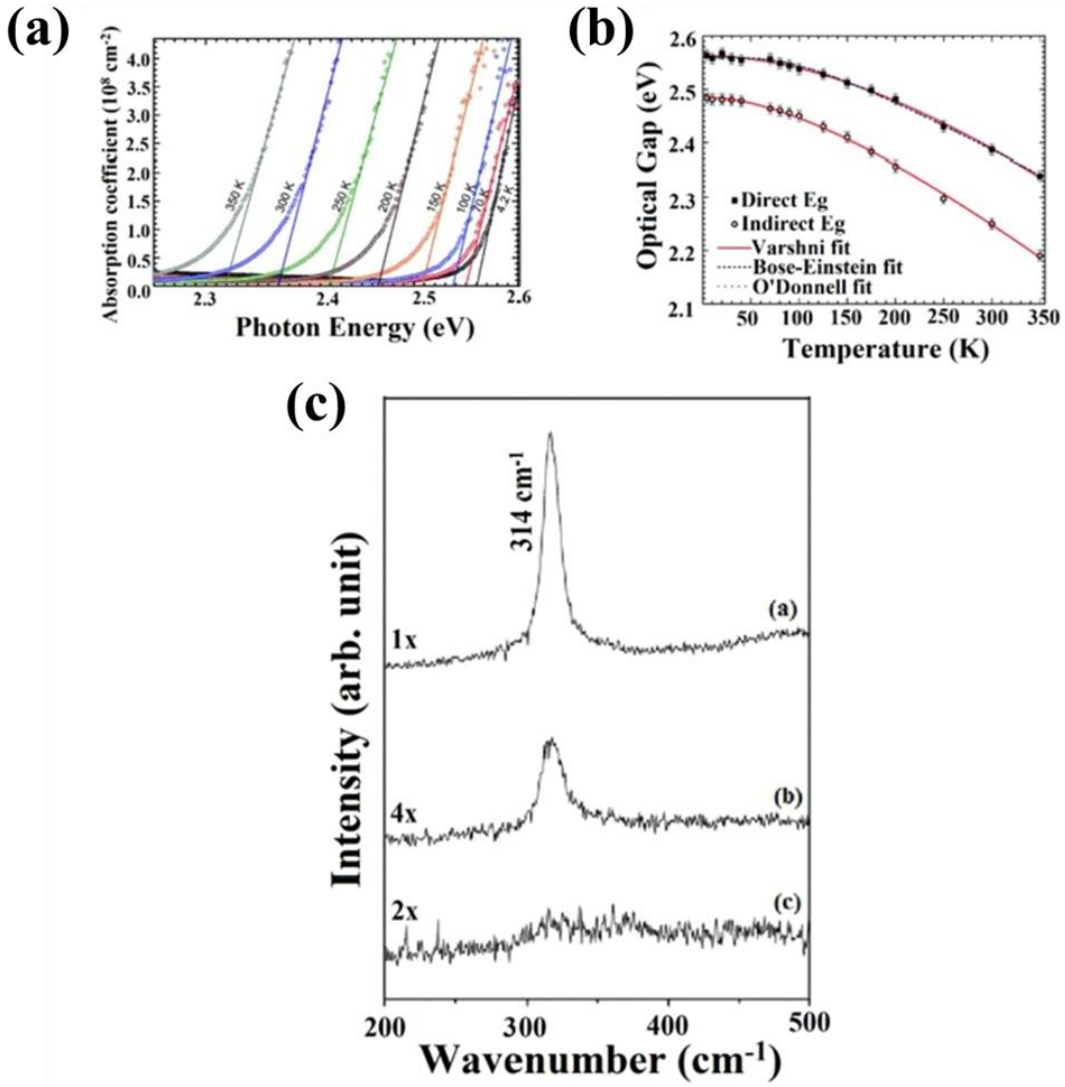



**Figure 1.9:** (a, b) Optical absorption spectra temperature corresponding to direct and indirect energy band gaps for a crystal structure of $SnS_2$. Reproduced with permission from ref.[Burton et al., 2016]. (c) Raman spectra of $SnS_2$ at varying temperature (150 °C for 1 h, 150 °C for 2 h, and 300 °C for 1 h). Reproduced with permission from ref. [Panda et al., 2007].

## 1.3 Synthesis of 2D materials

2D material exhibits distinctive properties and a wide variety of film structures during its growth, making it suitable for several applications. The characteristics of 2D material and the requirements for its applications are significantly influenced by the synthesis method employed. Consequently, it is essential to explore various synthesis techniques. 2D material can be synthesized using two primary approaches: (1) Top-down methods and (2) Bottom-up methods. The top-down technique entails the conversion of bulk materials into nanoscale particles through the etching of crystal planes from the substrate. The technique, although relatively simple, is constrained in its ability to generate shapes that are irregular and small particles, hence challenging the attainment of the necessary morphology and size. In contrast, the bottom-up approach assembles crystals on a substrate by growing atoms and molecules, which allows the production of nanoparticles with fine control over their morphology, sizes, and chemical composition. The top-down technique for producing single-layer or few-layer $SnS_2$ and $MoS_2$ nanoparticles relies on overcoming the interlayer van der Waals forces in bulk $SnS_2$ and $MoS_2$ using external forces, with primary methods including mechanical exfoliation, liquid-phase exfoliation, lithium-intercalated exfoliations or ultrasonication, and ion intercalation. The bottom-up approach typically utilizes $SnO_2$ or $MoO_3$ as starting materials, focusing on the nucleation and

growth of 2D crystals through chemical reactions. This method relies on the chemical reactions of precursors to generate nanoscale $SnS_2$ and $MoS_2$, with Chemical Vapor Deposition (CVD), pulsed laser deposition, wet chemical methods, Physical Vapor Deposition (PVD), and microwave-assisted technique being the primary methods of preparation. To achieve uniform and large-scale production of 2D materials, it is crucial to intensively research and optimize the synthesis and growth processes, as the performance of devices is contingent upon the quality of the synthesized 2D materials. Thus, it is essential to explore the different synthesis techniques available. This section provides an overview of the synthesis approaches for $SnS_2$ and $MoS_2$, along with their respective advantages and disadvantages.

### 1.3.1. Top-Down Approach

Nanofabrication utilizing the top-down approach is a prevalent technique for producing ultra-thin nanosheets of two-dimensional (2D) materials. The pioneering work by Novoselov and Geim demonstrated the use of micromechanical exfoliation to isolate graphene from bulk materials, achieving mono-layer graphene for the first time. This mechanical exfoliation method allows for the facile and cost-effective production of high-quality nanosheets, ranging from single to a few layers. For instance, the mechanical exfoliation of bulk graphite into few-layer or mono-layer graphene can be accomplished using simple Scotch tape[Novoselov et al., 2005]. This technique, known as mechanical stripping or micromechanical cleavage, utilizes the weak interlayer bonding in layered materials to systematically remove substantial crystals layer by layer with low-surface-tension tape, as shown in Figure 1.11 (a). The typical method involves attaching a valuable material like graphite to transparent tape's adhesive surface and delaminating it into sheets with consecutive sticky layers. The resultant flakes may be put onto a clean, flat substrate utilizing equipment such as plastic tweezers for subsequent processing. This technique has been effectively modified for the synthesis of diverse layered materials, such as transition metal dichalcogenides (TMDs) and hexagonal boron nitride (h-BN), as evidenced by the effective separation of few-layer $MoS_2$ nanosheets[Li et al., 2014] from bulk $MoS_2$ crystals. However, despite its simplicity and practicality, this technique has notable limitations, particularly concerning scalability, as it often yields low output and reproducibility. Consequently, it is primarily confined to laboratory-scale research rather than large-scale production. Controlling film quality is difficult, because substrate contamination during exfoliation, especially under high vacuum settings, might lower film quality. Mechanical stripping cannot meet industrial manufacturing requirements, making it unsuitable for nanosheets for gas sensors and photodetectors.

The liquid phase exfoliation technique is commonly utilized to separate bulk crystals into single-layer or few-layer 2D structures, employing water or organic solvents and external forces like ultrasonic or shear forces. This approach supports the production of large-scale solutions, making it suitable for industrial-scale applications and enabling the fabrication of sheets and composites with scalable potential. Solvent molecules are essential as they weaken the interlayer bonds within the material, promoting the separation of individual layers during ultrasonic treatment. The use of ultrasound further assists in breaking down these layers into nanoscale sheets. Acoustic radiation can effectively break the weak van der Waals contacts between $MoS_2$ layers, with two primary methods for exfoliating $MoS_2$ in solution. The initial approach encompasses mechanical procedures including ultrasonic treatment, grinding, bubbling, stirring, and shearing, which are predominantly physical but may incorporate some chemical additions. Surfactants such as sodium deoxycholate and chitosan can be employed to inhibit the re-aggregation of exfoliated. The liquid phase exfoliation method evolved from mechanical exfoliation techniques and was initially reported by [Coleman et al., 2011]. To create a suspension of $MoS_2$ thin layers, bulk $MoS_2$ is subjected to ultrasonic agitation in a suitable solvent, followed by separation via high-speed centrifugation. The resultant supernatant is then utilized to extract few-layer or monolayer $MoS_2$, often using N-Methylpyrrolidone (NMP) as a dispersing agent. Recently, the liquid-phase exfoliation technique has been employed for the production of few-layered InSe nanosheets, which possess a direct bandgap[Qi et al., 2021]. Photodetectors based

on these few-layered InSe materials demonstrate remarkable performance, exhibiting high photocurrent density, responsivity, and cyclic stability when tested in aqueous KOH solutions. The photodetection performance of these devices can be modified by changing the KOH concentration and the applied potential, demonstrating their promise as adjustable and effective photodetectors. An interesting application of liquid-phase exfoliation involves producing ultrathin nanosheets from the nonlayered material tellurium (Te), which has a chain-like structure with strong covalent bonds within the chains and weaker van der Waals interactions between them. This structural configuration facilitates the production of ultrathin sheets through liquid-phase exfoliation, resulting in materials that exhibit efficient photoresponsive properties. The nanosheets produced via this method exhibit excellent dispersion and stability in water, making them suitable for various applications. While this technique is more advantageous than mechanical stripping due to its higher yield, it does have drawbacks, including relatively low yield of single-layer $MoS_2$, the production of smaller nanosheets due to high ultrasonic energy, and the potential for sample and environmental contamination from organic solvents. Nevertheless, liquid phase exfoliation is considered a cost-effective and straightforward method for generating high-quality nanosheets, capable of producing both dry powders and wet suspensions, as well as macroscopic thin films. Overall, liquid phase exfoliation provides a viable alternative to micromechanical exfoliation, facilitating the large-scale production of single- or few-layer transition metal dichalcogenides (TMDs) for various applications.

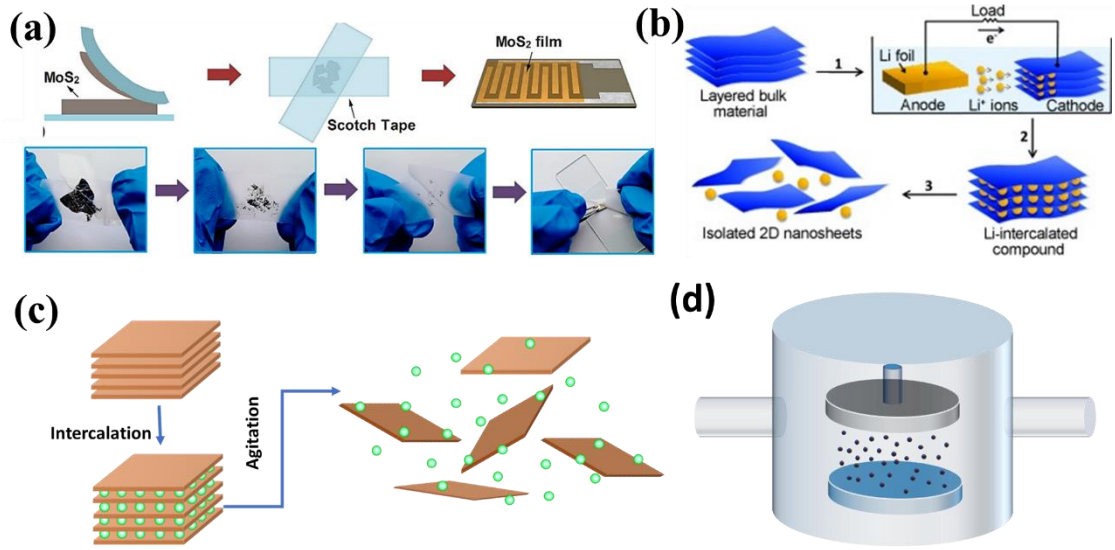



**Figure 1.10:** Schematic image of top-down approach for synthesis of 2D material (a) mechanically exfoliated $MoS_2$ (Scotch tape method), (b) Electrochemical lithiation process, (c) Liquid exfoliation method, and (d) Sputtering.

The ion intercalation method involves inserting small-radius cations, typically alkali metal ions such as $Li^+$, $Na^+$, and $K^+$, between the layers of bulk materials to form thin-layered structures. This process reduces interlayer interactions and overcomes the van der Waals forces that keep the layers intact[El Garah et al., 2018]. In these materials, covalent bonds hold individual layers together, while weaker van der Waals forces separate the layers, allowing suitable ions or molecules to be inserted into the interlayer spaces. For example, to create lithium-intercalated TMDs, layered TMDs are submerged in a solution of n-butyl lithium for an extended period, generally at least 48 hours, to ensure complete reaction. Subsequently, the intercalated material is exposed to water, which reacts with lithium to produce hydrogen gas, aiding in the exfoliation of the layers. This step enables the separation and purification of TMD layers[Zhao et al., 2024b]. However, this method presents risks, as ion intercalation can be somewhat unpredictable, and the use of organic intercalation compounds may pose explosion hazards. Despite its effectiveness, this method has limitations, such as challenges in producing large-area $MoS_2$ nanosheets and isolating single layers from multilayer structures. Additionally, the process can be time-consuming, sometimes taking days, and the removal of intercalated alkali ions can leave behind solvent residues, complicating large-scale production.

Also, Sputtering is a physical vapor deposition technique utilized for the fabrication of thin films, characterized by the generation of a gaseous plasma composed of inert gas ions, electrons, and the target material through the application of an electric field to the deposition material, as depicted in Figure 1.11(d). This method provides precise control over the thickness and uniformity of the resulting film. Recently, there has been increased interest in employing sputtering for the growth of high-quality $MoS_2$ films. The growth parameters, including growth pressure, base pressure, power, and substrate temperature, significantly influence the characteristics of the deposited $MoS_2$, necessitating the optimization of these parameters to achieve the desired film properties[Wadhwa et al., 2021a]. Controlling the substrate temperature is a common approach to enhancing film quality during sputtering; however, a more effective strategy involves initially growing $MoS_2$ layers at room temperature or low temperatures, followed by a post-annealing process at elevated temperatures. This method has demonstrated the ability to produce $MoS_2$ films with electrical conductivity comparable to those obtained through other popular techniques, such as chemical vapor deposition (CVD) and mechanical exfoliation. While direct sputtering from $MoS_2$ targets is a straightforward and widely used single-step growth technique, it often results in non-stoichiometric $MoS_2$ layers. To rectify this issue, reactive sputtering using $H_2S$ gas in conjunction with $MoS_2$ targets can be employed, allowing for the reaction of $H_2S$ with the $MoS_x$ target to yield stoichiometric $MoS_2$ films. Furthermore, sputtering from a molybdenum metal target in a sulfur vapor environment has been shown to produce high-quality, wafer-scale $MoS_2$ films. This approach enables the formation of large-area, uniform, and continuous layers that rival the quality of films produced by other preferred methods. Consequently, sputtering presents a promising option for large-scale industrial applications, with ongoing optimization of sputtering parameters anticipated to further enhance the quality of the resulting $MoS_2$ films.

In summary, each top-down stripping technique presents distinct advantages and limitations, allowing researchers to choose a method that aligns with their specific objectives. However, due to the inherent drawbacks associated with top-down methods, the bottom-up approach has been developed as an alternative. This technique is particularly notable for its capacity to produce large-area nanosheets, which has garnered significant interest in the scientific community. The bottom-up approach not only addresses some of the limitations of top-down methods but also offers promising pathways for the synthesis of high-quality nanoscale materials suitable for various applications.

### 1.3.2. Bottom-up Approach

As previously mentioned, the top-down strategy is employed to derive few-layer or monolayer materials from layered bulk substances through various exfoliation techniques. However, this approach is constrained to layered materials and typically yields a limited output. Consequently, there is a strong demand for the development of alternative strategies aimed at the mass production of 2D materials. In this regard, bottom-up methods offer efficient pathways for the large-scale synthesis of 2D materials by facilitating their growth or assembly from fundamental atomic or molecular constituents, as illustrated in Figure 1.12. These approaches not only improve scalability in production but also facilitate the fabrication of high-quality 2D materials with customizable properties for various applications.

One of the most productive bottom-up strategies for synthesizing two-dimensional (2D) materials is through wet chemical methods, which include hydrothermal and solvothermal synthesis as well as template synthesis. Hydro/solvothermal synthesis allows for the growth of desired crystalline materials at relatively low temperatures (below 240 °C)[Li et al., 2011]. By optimizing parameters such as reaction temperature, duration, and precursor ratios, ultrathin morphologies can be achieved. Conventionally, hydrothermal methods have utilized $(NH_4)_6Mo_7O_{24}\cdot 4H_2O$ and thiourea as catalysts for synthesizing $MoS_2$ nanoflakes, producing $MoS_2$ chips with numerous active surface sites.[Xie et al., 2013] Colloidal synthesis also serves as a

dependable method for creating transition metal dichalcogenides (TMDs). Traditional colloidal synthesis involves adding a cold chemical precursor solution to a hot solvent or heating the precursors in a vessel up to 320 °C. A more recent approach called "Diluted Chalcogen Continuous Inflow" (DCI) has been developed to generate monolayer TMDs such as $TiS_2$, $HfS_2$, and $ZrS_2$[Yoo et al., 2014]. Zhang *et al.*, effectively synthesized $MoS_2$ flower-like spheres through a hydrothermal process using hexaammonium heptamolybdate tetrahydrate ($(NH_4)_6Mo_7O_{24}$) and thiourea, producing nanospheres with high crystallinity and an approximate diameter of 4 µm[Zhang et al., 2015]. Similarly, Wang *et al.*, created three-dimensional flower-shaped $MoS_2$ microspheres made up of nanosheets by employing ammonium molybdate and thiourea in a hydrothermal synthesis method[Wang et al., 2018]. Additionally, template synthesis presents an innovative approach for fabricating nanostructures, wherein a template guides the growth of crystals to specific dimensions, which can subsequently be removed through thermal treatment or pH adjustments. This method is particularly effective for producing complex nanosheets (2D), nanowires (1D), and quantum dots (0D). The bottom-up approach inherent in wet chemical techniques could offer a notable improvement over exfoliation and chemical vapor deposition (CVD) methods, as they facilitate the integration of TMDs across a range of thicknesses, from monolayers to multilayers. The resulting materials exhibit high homogeneity and minimal thickness variation compared to those produced via CVD. Furthermore, wet chemical methods allow for the incorporation of dopants by introducing various chemicals during synthesis, and ligands can be utilized to modify or smooth the surface of the materials. Since it doesn't require specialized equipment, the hydrothermal method is easy to use for large-scale production. By using environmentally benign precursor chemicals, these solution-based methods can be adapted to conform with green chemistry and sustainable manufacturing practices.

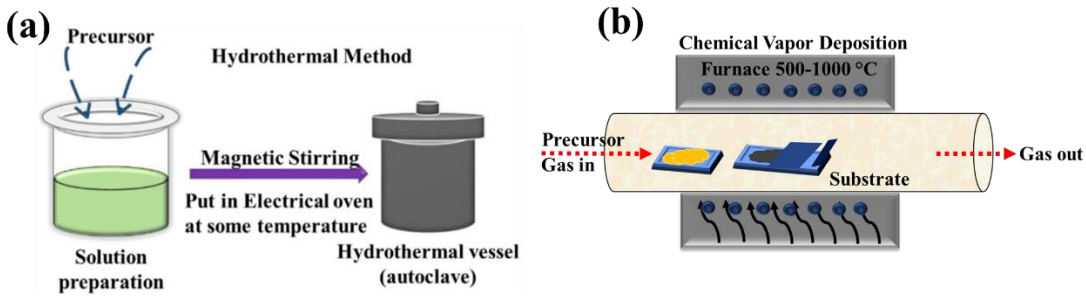



**Figure 1.11:** Schematic illustration of different bottom-up methods for the synthesis and growth of 2D material

Recently, microwave-assisted synthesis has garnered significant interest due to its time efficiency and high energy effectiveness. This method has been successfully employed to synthesize various two-dimensional (2D) nanomaterials, including $SnO_2$, α-$Ni(OH)_2$, $K_{0.17}MnO_2$, and CuSe.

Physical vapor deposition (PVD) uses vacuum evaporation and sputtering to evaporate solid or liquid source materials into gaseous atoms, molecules, or partially ionized species. Vaporized species are low-pressure deposited on a target substrate, encouraging nucleation and growth. PVD controls crystal formation by adjusting temperature, concentration, and gas flow in the system during a solid-gas-solid phase transition. The conventional PVD procedure for 2D TMDs involves placing a ceramic boat with the TMD powder source at the center of a quartz tube furnace and a clean substrate downstream to create a temperature differential. High-quality TMDs with few or single layers can be formed by changing temperature gradient, source evaporation temperature, and gas flow. Wu *et al.*, developed single-layer $MoS_2$ using $MoS_2$ powder and argon. The process involved maintaining 900 °C for evaporation and 650 °C for growth, resulting in 25 µm $MoS_2$ crystals with an equilateral triangle form on a $SiO_2$/Si substrate[Wu et al., 2013]. The PVD method's straightforward setup—vaporizing the source material—makes operational parameter management easy. The approach can only produce thin-layer $MoS_2$ due to the discrepancy between the tube furnace's heating temperature and the $MoS_2$ source's melting point.

Chemical vapor deposition (CVD), as a bottom-up approach, is recognized as one of the most effective techniques for synthesizing high-quality layered transition metal dichalcogenides (TMDs) with controlled dimensions on a large scale, making it particularly suitable for optoelectronic applications. CVD can be categorized into several variants, including atmospheric pressure CVD (APCVD), low-pressure CVD (LPCVD), plasma-enhanced CVD (PCVD), and metal-organic CVD (MOCVD), all following a similar growth procedure for 2D materials synthesis. The CVD process involves high-temperature synthesis, which can occur within or outside a tube furnace, allowing for the growth of desired 2D materials on substrates in thin film form or other specified morphologies. Due to its ability to produce high-purity materials with tunable properties, a variety of 2D materials, including graphene, $SnS_2$, $MoS_2$, and hexagonal boron nitride (h-BN), can be conveniently synthesized. However, this method requires high vacuum conditions, elevated temperatures, and specific substrates to facilitate the experimental procedure. This technique enables the development of a distinct class of 2D nanosheets and their composites through the use of diverse precursors. In CVD, chemical reactions involving vaporized precursors occur on the substrate, resulting in the formation of large-area thin films. The method, also referred to as vapor-solid growth, generates high-quality monolayers on the substrate, albeit with smaller quantities of flakes, often resulting in irregular 2D-$MoS_2$ films. During a typical CVD process, molybdenum source precursors such as molybdenum trioxide ($MoO_3$), ammonium thiomolybdate ($(NH_4)_2MoS_4$), and molybdenum pentachloride ($MoCl_5$), along with a sulfur source like sulfur powder or hydrogen sulfide ($H_2S$) gas, are injected into the reaction chamber. As the temperature increases, the precursors evaporate and are transported through the gas flow, where they react and deposit onto the substrate, often producing volatile by-products that are subsequently removed by the gas stream. The growth dynamics of 2D $SnS_2$ and $MoS_2$ are influenced by critical parameters, including carrier gas flow rate, growth temperature, precursor quantity, substrate positioning, and the presence of promoters, all of which affect the nucleation and growth mechanisms. Nonetheless, the CVD technique faces challenges in controlling deposition properties, such as precursor vapor rates, which can lead to compositional gradients across the same wafer. Additionally, the need for high precision and monitoring at elevated temperatures, along with the generation of toxic by-products, limits the feasibility of producing large-area, single-domain materials. To address these challenges, various modifications can be implemented, such as optimizing growth parameters, employing catalysts or promoters, or exploring alternative synthesis methods. One promising approach involves a two-step process, where a thin layer of $MoO_3$ or molybdenum is first deposited onto the substrate via techniques like sputtering or thermal evaporation. The pre-deposited layer is then annealed in an inert gas atmosphere at high temperatures to convert it into a uniform $MoO_x$ layer, which serves as a precursor for subsequent sulfurization. In the final step, the $MoO_x$ layer is exposed to sulfur-containing gases or materials, such as $H_2S$ or sulfur powder, leading to the formation of $MoS_2$, thus enhancing the uniformity and reproducibility of the resulting films.

In conclusion, the three primary bottom-up synthesis methods—hydrothermal/solvothermal, CVD, and PVD—facilitate the production of few-layer or single-layer nanosheets while offering significant advantages in the control of material morphology and structure. The bottom-up approach allows for effective management of layer formation and defect density, making it applicable for the synthesis of nearly all types of 2D materials. Nevertheless, challenges persist in achieving the deposition of large, uniform monolayers of molybdenum disulfide over extensive areas, compounded by issues related to time efficiency and high production costs.

## 1.4 Gas Sensor

Gas sensors are electronic devices that serve as transducers, converting chemical information into electrical signals. They can be categorized in two main ways: by their operational principles and by the materials used in their sensing layers. Enhancing the performance of gas sensors can be achieved by altering the structures and morphologies of the sensing layers.

Functioning as electronic noses, gas sensors are capable of detecting specific target gases in the environment. Each gas sensor comprises two fundamental components: a receptor unit that interacts with gas molecules to generate chemical information and a transducer unit that transforms this information into an electrical signal. This signal is subsequently processed by various electrical components within the gas detection system, as depicted in Figure 1.13. The timely detection of toxic gases is crucial in contemporary society, and chemiresistive gas sensors have emerged as a leading type due to their ease of integration, efficient manufacturing processes, scalability, real-time monitoring capabilities, low power requirements, and long-term stability in challenging conditions. The operational principle of chemiresistive gas sensors relies on changes in the resistance of the sensing film upon exposure to gas molecules, facilitating charge transfer between the gas and the sensing material. These sensors have found extensive applications in detecting a range of gases, including $NH_3$, $NO_2$, $H_2$, $H_2S$, and $CO_2$. Gas sensors are essential in numerous areas such as industrial process control, air quality monitoring, and the detection of gas leaks in hazardous settings. Their use is crucial for preventing accidents and ensuring the safety of both individuals and the environment.

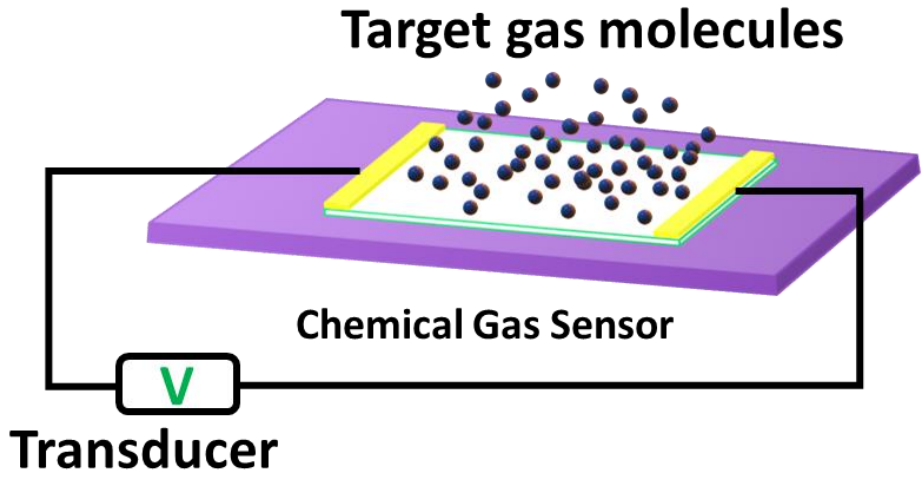



**Figure 1.12:** Schematic representation of a gas sensor.

### 1.4.1. $NO_2$ Gas Sensor

The detection of hazardous combustible gases such as $NO_2$, $H_2S$, $CO_2$, $SO_2$, and volatile organic compounds (VOCs) is crucial for tackling global issues like environmental pollution and hazardous industrial work environments that threaten human health [Yamazoe, 2005]. Nitrogen dioxide ($NO_2$) stands out as a major air pollutant, primarily emitted through the burning of fossil fuels, power plants, nuclear activities, and vehicle emissions. Even at low concentrations, $NO_2$ poses significant health risks, leading to throat irritation, shortness of breath, and pulmonary edema, while long-term exposure to higher levels is associated with carcinogenic effects [Abbas et al., 2015; Pyeon et al., 2020a]. $NO_2$ also contributes to environmental issues such as acid rain and photochemical smog, highlighting the importance of its detection for environmental health. Monitoring $NO_2$ at parts per million (ppm) levels is critical for protecting both the environment and public health. However, detecting low concentrations of $NO_2$ in complex gas mixtures remains challenging. This challenge underscores the need for advanced sensors that can selectively and quickly detect $NO_2$ with high accuracy under ambient conditions. Recent studies have explored metal oxide nanostructures and 1D semiconductors like carbon nanotubes and silicon nanowires to improve gas sensor performance [Snow et al., 2006; Strand et al., 1997]. Yet, the requirement for high operating temperatures (>200 °C) in metal oxide sensors and the limited surface area of 1D semiconductors have driven research toward new materials. 2D materials, including graphene, phosphorene, $SnS_2$, $WSe_2$, $MoSe_2$, $WS_2$, and $MoS_2$, have emerged as promising candidates for gas sensing due to their ability to operate at room temperature without additional heating or UV sources. Among these, graphene is noted for its remarkable sensitivity,

with the capacity to detect individual gas molecules due to its high surface-to-volume ratio, low electrical noise, and excellent conductivity. However, pristine graphene sensors often face issues with selectivity, which is particularly problematic in environments containing multiple toxic gases. Although sensor advancements often require balancing selectivity, sensitivity, and reversibility, achieving high selectivity remains essential for practical gas sensor applications.

### 1.4.2. Classification of gas sensors

Gas sensors are a type of chemical sensor that detect gases by exhibiting changes in physical properties such as conductance, resistance, absorbance, frequency, or temperature upon exposure. Several techniques are used for gas detection, including electrochemical sensors, metal oxide semiconductor sensors, capacitance sensors, acoustic sensors, optical sensors, and calorimetric sensors. Figure 1.16, shows the classification of gas sensors according to their operating principles[Tang et al., 2017]. The selection of a gas sensor technology depends on the surrounding gas environment, which influences the sensor materials' optical, electrical, chemical, and physical properties. This thesis specifically addresses sensors that rely on variations in electrical resistance when exposed to gases. Each type of sensor technology comes with distinct advantages and limitations; for instance, the fabrication of resistive sensors is relatively straightforward and cost-effective compared to optical and electrochemical sensor technologies. The sensing layer can be constructed from various materials, with conductometric gas sensors commonly made from metal oxide semiconductors such as $SnO_2$, ZnO, and $TiO_2$, which are also utilized in commercial applications. However, these materials typically require elevated temperatures (>250 °C) to exhibit gas responses, necessitating additional microheaters, which limits their functionality at room temperature. Conducting polymers can respond to gases at room temperature, but their longevity is often compromised due to degradation in ambient air and humidity. As a result, there is a growing demand for new materials capable of providing stable gas detection at room temperature. The groundbreaking discovery of room-temperature detection of individual gas molecules using graphene sensors in 2007 has fueled interest in two-dimensional (2D) materials for gas sensing applications. These 2D materials are highly promising due to their large surface-to-volume ratios, numerous active adsorption sites, and exceptional physicochemical properties. Their effectiveness in room-temperature gas detection is largely due to charge transfer mechanisms facilitated by the electronic interactions between gas molecules and the adsorption sites on their surfaces. This advantage removes the need for microheaters typically required in traditional solid-state gas sensor technologies, paving the way for compact, battery-operated gas sensors that support advanced Internet of Things (IoT) applications.

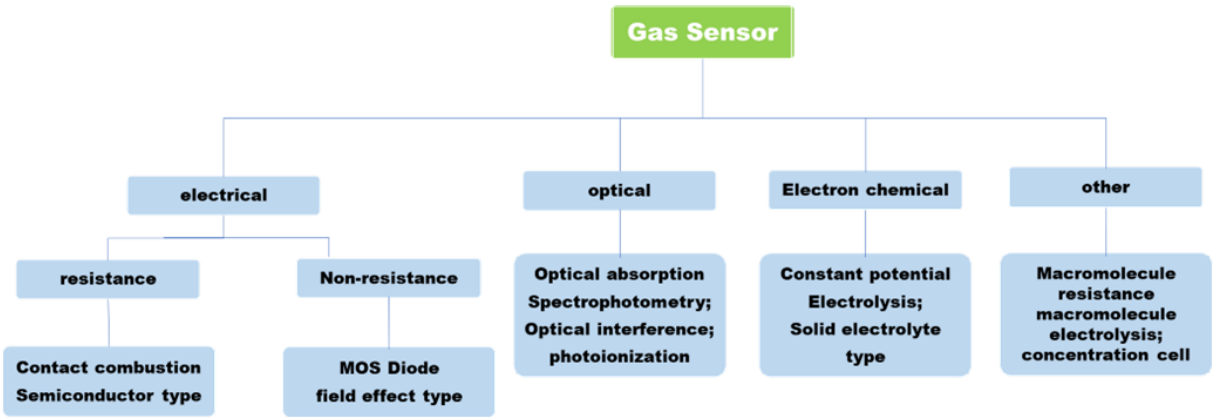



**Figure 1.13:** Classification of the gas sensor based on sensing operation principles. Reproduced with permission from ref. [Tang et al., 2017].

### 1.4.3. Characteristics of Gas Sensor

The performance of gas sensors is often evaluated based on a number of vital factors that characterize their gas sensing capabilities. The criteria are vital for comparing and characterizing the performance of conductometric gas sensors, the focus of this research. To assess the performance of gas sensors, the following essential parameters are commonly employed: stability, detection limit, response time, recovery time, sensitivity, and selectivity. These criteria comprehensively elucidate the gas sensor's ability to accurately detect and measure particular gases, along with its durability and reliability in diverse operational environments. By evaluating these parameters for performance, researchers and developers may improve the development and production of gas sensors to achieve superior performance, reliability, and flexibility across diverse applications.

***(a) Sensor Response*** $(\Delta R)$

The capability of a sensor to detect variations in gas concentration is quantified as its Sensor response. It is defined as the ratio of the change in sensor resistance due to the presence of gas molecules, relative to its baseline resistance in air. This concept can be represented by various equations[Ramirez-Torres et al., 2014; Zhang et al., 2014a, 2014b]:

$$\Delta R = \frac{R_g - R_o}{R_o} \quad (1.2)$$

$$\Delta R = \frac{V_g - V_o}{V_o} \quad (1.3)$$

$$\Delta R = \frac{I_g - I_o}{I_o} \quad (1.4)$$

$$\Delta R = \frac{R_o - R_g}{R_o} \quad (1.5)$$

$$\Delta R = \frac{R_g}{R_o} \quad (1.6)$$

$$\Delta R = \frac{R_o}{R_g} \quad (1.7)$$

where, $R_g$, $V_g$, $I_g$, $R_o$, $V_o$, and $I_o$ represent resistance, current, and voltage, respectively, in the presence of gas molecules and represent these parameters in air or prior to gas exposure. A higher sensor response indicates a more significant change in resistance when the sensor is exposed to gas molecules.

***(b) Response and Recovery Time***

The response time of a gas sensor is defined as the duration required the sensor can reach a response that ranges from 10% to 90% of its maximum response, when exposed to the target gas. Conversely, recovery time refers to the interval needed for the sensor's response to revert from 90% to 10% of its baseline response during the desorption phase after the gas has been removed. Ideally, a gas sensor characterized by fast response and recovery times to enhance sensor performance.

***(c) Selectivity***

The selectivity of a gas sensor refers to its ability to demonstrate the highest sensitivity to a specific gas, while minimizing responses to other gases present in the environment. This characteristic is vital for ensuring that the sensor accurately detects the target gas without interference from surrounding gases, thereby reducing the likelihood of false readings. Selectivity is essential for the sensor to effectively identify the gas of interest amidst various interfering gases. Consequently, a gas sensor must be highly selective to reliably distinguish the target gas from other gases, ensuring accurate and dependable measurements.

***(d) Limit of Detection (LOD)***

LOD serves as an important indicator of the gas sensor and refers to the minimal concentration of the target gas that can be reliably sensing by the device. A low detection limit is crucial for applications that require the detection of very low gas concentrations.

***(e) Operating Temperature***

In the field of gas sensor applications, the operational temperature serves as a fundamental parameter that considerably impacts device performance, especially in real-time monitoring situations, where sensors are obligated to operate steadily amidst adverse environmental factors. It is essential for gas sensors to demonstrate a broad operational temperature range, while preserving optimal sensitivity and stability at room temperature (RT). At RT, sensors should demonstrate a high response to target gases, thereby enhancing the detection of trace concentrations with remarkable accuracy. Consequently, the reduction of the operating temperature proves beneficial, as it augments the overall reliability and efficiency of the sensor across various applications, thus fulfilling the requirements for accurate gas monitoring in diverse environments.

***(f) Stability***

Stability refers to a gas sensor's potential to keep its performance over time while responding to various conditions in the environment. Sensors demonstrating strong stability are essential for providing highly accurate and reliable measurements over long periods of time, which is crucial for the dependability of monitoring systems. Consistent performance is crucial for applications subjected to extended exposure to fluctuating temperatures, humidity, and other external factors, as it greatly impacts the sensor's ability to provide accurate data and maintain reliable functionality over its operational life.

## 1.5 Gas Sensing Mechanism of 2D Materials

The performance of gas sensors is closely tied to their underlying sensing mechanisms. In traditional metal oxide gas sensors, this mechanism mainly involves surface reactions between target gas molecules and pre-adsorbed oxygen species on the metal oxide's surface. These interactions lead to the formation of oxygen ions ($O^{2-}$, $O^{-}$, and $O_2^{-}$) as electrons are drawn from the metal oxide's conduction band, facilitated by atmospheric oxygen adsorption at various operating temperatures[Han et al., 2018]. On the other hand, gas sensors that employ two-dimensional (2D) materials operate based on the interaction between gas molecules and the 2D material film. These interactions can be classified into two primary mechanisms: physisorption and chemisorption. Physisorption occurs in pristine 2D materials films, where gas molecules exhibit weak adsorption energies and longer adsorption distances, resulting in minimal charge transfer and an almost unchanged electronic structure. In contrast, chemisorption takes place in defective 2D materials layers, such as those formed during the synthesis of $MoS_2$, where gas molecules engage in stronger chemical interactions. This process is characterized by reduced adsorption distances, leading to significant charge transfer, enhanced adsorption energies, and notable alterations in the electronic states of the material. As a result, the presence of defects in 2D materials films significantly improves their gas sensing performance. Also, the directionality of charge transfer is contingent upon the oxidizing or reducing nature of the target gas analytes. Specifically, oxidizing gases, such as nitrogen dioxide ($NO_2$), accept electrons due to the presence of an unpaired electron on the nitrogen atom, whereas reducing gases, such as ammonia ($NH_3$), donate electrons to the material due to their lone pair of electrons.

The electronic interactions between gas molecules and the reactive sites on the surface of 2D materials significantly influence charge carrier concentration, leading to variations in conductivity (or resistivity) of these materials. This charge transfer process has been substantiated through theoretical calculations using density functional theory (DFT) and in-situ photoluminescence studies. Specifically, Yue *et al.,* conducted a theoretical analysis of the adsorption of various molecules, including $H_2$, $O_2$, $H_2O$, $NH_3$, NO, $NO_2$, and CO on $MoS_2$, employing DFT calculations executed with the Vienna Ab-Initio Simulation Package (VASP)[Yue

et al., 2013]. They utilized a 4×4 supercell of $MoS_2$ with a lattice constant of 3.12 Å for their simulations. The gas adsorption behavior is governed by several parameters, including favorable adsorption sites on $MoS_2$ for specific gas molecules, the distance between the gas molecules and the $MoS_2$ layer, the adsorption energy, charge transfer dynamics, and the directionality of charge transfer. For effective gas adsorption on the sensing surface, a strong interaction—either physisorption or chemisorption—between the gas molecules and $MoS_2$ flakes is essential. The strength of this interaction is quantitatively assessed through the calculation of adsorption energy, by the following equation:

$$E_{ads} = E_{MoS_2+Molecules} - (E_{MoS_2} + E_{Molecules}) \quad (1.8)$$

where, $E_{ads}$ is the adsorption energy, $E_{MoS_2} + E_{Molecules}$ is the total energy of $MoS_2$ and the adsorbed gas molecule, $E_{MoS_2}$ and $E_{Molecules}$ are the energy of the $MoS_2$ film and single gas molecule, respectively. For effective gas adsorption, it is essential that the adsorption energy is negative, indicating a strong interaction characterized by an exothermic process. Additionally, the charge transfer dynamics play a critical role in determining gas adsorption behavior. This charge transfer is affected by the relative positions of the highest occupied molecular orbitals (HOMO) and the lowest unoccupied molecular orbitals (LUMO) of the gas molecules. When the Fermi level is situated below the HOMO, charge is transferred from the gas molecule to the sensing surface, designating the gas as an electron donor. Conversely, if the Fermi level is positioned above the LUMO, charge transfer occurs from the sensing surface to the gas molecule, classifying the gas as an electron acceptor[Leenaerts et al., 2008].

Optimizing the Schottky barrier and built-in potential at the sensing material-metal electrode interfaces improves sensor performance beyond direct charge transfer between gas molecules and reactive sites[Wei et al., 2009]. The nature of the contact—whether Schottky or ohmic—depends on the work function of the metal and the electron affinity of the material. For instance, n-type $MoS_2$, with an electron affinity of approximately 4.2 eV[Fontana et al., 2013; Gong et al., 2013], forms a Schottky junction with gold (Au), which has a work function around 5.1 eV[Sze et al., 2021]. Upon exposure to $NO_2$, the Fermi level of n-type $MoS_2$ shifts towards the valence band due to electron extraction by the $NO_2$ molecules, resulting in an increased Schottky barrier and a decreased built-in potential, which consequently reduces the device conductivity. Conversely, the interaction with $NH_3$ leads to opposite effects[Liu et al., 2014a]. The incorporation of additional materials into 2D sensing platforms, such as in hybrid structures or van der Waals heterostructures, complicates the sensing mechanism but can enhance performance by tuning the barrier height at the heterointerfaces through gas adsorption[Lee et al., 2018]. For example, Han *et al.*, proposed a sensing mechanism that involves modulation of the heterojunction barrier potential at the ZnO/$MoS_2$ interface in response to gas exposure, where a depletion region forms due to electron-hole diffusion aimed at equilibrating the differing Fermi levels[Han et al., 2018]. Typically, noble metals are deposited on the surfaces of sensing materials, and their higher work functions lead to electron transfer from the sensing material to the noble metal upon contact in air, resulting in the formation of an electric double layer (EDL) and associated Schottky barriers. When exposed to oxidizing gases like $NO_2$, additional electrons are extracted from the interface, further increasing the Schottky barrier height and expanding the EDL, thereby modulating the resistance of the n-type sensing material. Furthermore, the electronic sensitization effect of noble metals, which arises from changes in their oxidation states, also plays a significant role in resistance modulation. In catalytic sensitization, noble metals facilitate the dissociation of target gases, such as $H_2$, into atomic species that spill over to the adjacent sensing layer, where they can react with adsorbed oxygen species, leading to electron release and resistance changes. Composite formation enhances sensor response by increasing the contact area between different materials, allowing for the formation of various heterojunctions, including p-n, n-n, and p-p junctions. These heterojunctions lead to band bending and charge depletion layers, which are responsive to gas exposure, resulting in significant resistance changes and enhanced sensing signals.

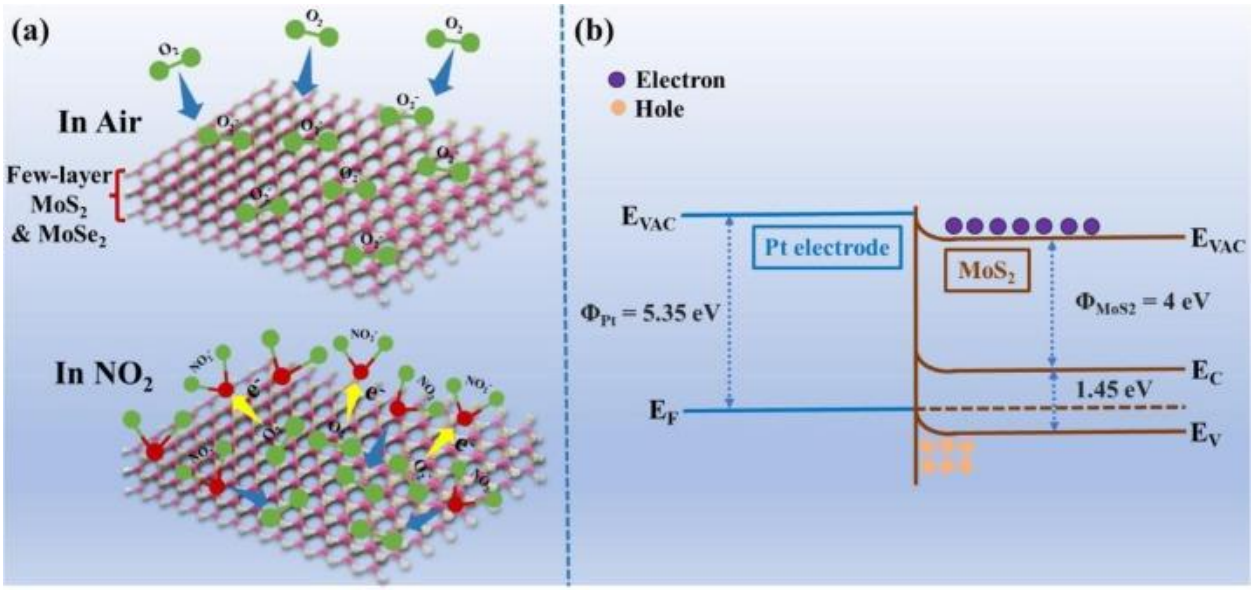



**Figure 1.14:** Schematics of gas sensing mechanism of in 2D material-based gas sensors.

The mechanisms underlying gas sensing in various mixed-dimensional heterostructures involving transition metal dichalcogenides (TMDCs) are extensively examined in [Lee et al., 2018], with attention to both electronic and chemical sensitization processes. Validated gas sensing mechanisms for sensors based on 2D materials have shown performance improvements through individual and combined effects. Additionally, the following sections delve into the factors that affect the gas sensing properties of $SnS_2$ and $MoS_2$, offering a detailed exploration of the complex interactions that enhance the performance of TMDC-based gas sensors, particularly focusing on $SnS_2$ and $MoS_2$.

## 1.6 Literature Review on $MoS_2$ and $SnS_2$ Gas Sensor

In recent years, advancements in gas sensing technologies have heavily relied on materials like metal oxides, conducting polymers, and carbon-based materials. Carbon materials offer advantages like low cost and the ability to function at room temperature, making them favorable alternatives to traditional metal oxides and polymers[Mirzaei et al., 2019; Wang et al., 2019]. However, their limitations, such as low selectivity, extended recovery times, and limited gas-molecule interaction, have spurred research into other materials. Transition metal dichalcogenides (TMDs), particularly 2D materials like $MoS_2$ and $MoSe_2$, are emerging as strong candidates for gas sensing due to their impressive electron transport properties, adjustable electronic structures, and high chemical stability[Hien et al., 2020; Kumar et al., 2024b]. $MoS_2$, with its large surface area and high electron mobility, has gained particular attention. It exhibits excellent adsorption properties due to its expansive surface sites and defect structures, which enhance chemical interactions with gas molecules. When exposed to gases such as $NO_2$ and $NH_3$, $MoS_2$-based sensors display distinct charge transfer responses, which alter their electrical conductivity. The material's sensitivity is further influenced by the number of layers, with thicker $MoS_2$ layers showing enhanced stability and sensitivity. Additionally, morphological engineering, such as vertically aligned $MoS_2$ flakes, has been shown to increase the density of active sites, improving sensitivity. Various synthesis techniques, including CVD and chemical methods, enable large-area $MoS_2$ production, essential for practical sensor applications. Functionalizing $MoS_2$ with nanoparticles, particularly noble metals, has further refined its selectivity and sensitivity due to effects like enhanced charge modulation and the spillover effect. This functionalization facilitates selective gas detection, as specific gases cause different doping effects in $MoS_2$. Future improvements are likely to focus on optimizing sensor response times and stability at room temperature, as well as enhancing the material's selectivity through metal nanoparticle doping and ligand conjugation.

In recent studies, Afroozeh *et al.,* explored the latest developments in transition metal dichalcogenides (TMDs) for gas sensing applications[Afroozeh et al., 2019]. Filipovic *et al.,* investigated the integration of two-dimensional (2D) materials, including $MoS_2$, with CMOS technology for gas sensor applications, noting their potential as channel materials for field-effect transistors (FETs) due to their broad band gap[Filipovic et al., 2022]. Aftab *et al.,* further contributed by introducing novel 2D architectural configurations that enhance gas sensing capabilities[Aftab et al., 2023]. Li *et al.,* conducted a pivotal study on gas and $MoS_2$ interactions by fabricating field-effect transistor (FET) gas sensors using single-layer, bilayer, tri-layer, and four-layer $MoS_2$, each obtained through mechanical exfoliation[Li et al., 2012a]. The sensors, when exposed to NO gas, demonstrated a decrease in current attributed to charge transfer between the gas molecules and $MoS_2$, effectively causing p-type doping in the inherently n-type $MoS_2$. Among these, the bilayer $MoS_2$ sensor provided the highest current response, with a detection limit of 0.8 ppm for NO gas, comparable to that observed in tri-layer and four-layer devices, although single-layer $MoS_2$ exhibited unstable current behavior over time.

Expanding on gas sensitivity, Liu *et al.,* (2014), discovered that modulating Schottky contacts between $MoS_2$ and Ti/Au electrodes in CVD-grown monolayer devices significantly enhanced gas-sensing capabilities[Liu et al., 2014a]. They observed that $NO_2$ adsorbed onto $MoS_2$ formed $NO_2^-$, which increased the Schottky barrier height and reduced built-in potential, enabling detection as low as 20 ppb $NO_2$ and 1 ppm $NH_3$. However, achieving full baseline resistance recovery at room temperature remains challenging due to strong binding energies between $MoS_2$ and gas molecules; thermal or optical desorption assistance may be necessary for practical application, although sensitivity could decrease at elevated temperatures. Theoretical density functional theory (DFT) studies showed that charge transfer interactions are stronger at $MoS_2$ edge sites, which have higher adsorption energies than the terrace sites of the basal plane. Cho et al., harnessed these findings by developing vertically aligned $MoS_2$ via rapid CVD sulfurization, which exhibited a five-fold increase in sensitivity to $NO_2$ compared to horizontally aligned structures due to a higher density of exposed edge sites[Cho et al., 2015c]. Further, Agrawal *et al.,* fabricated a three-dimensional $MoS_2$ network using a "tube-in-tube" CVD method, where interconnected edge sites rapidly responded to hydrogen gas[Agrawal et al., 2017]. Additionally, Li *et al.,* produced smooth, solid, and hollow $MoS_2$ spheres through a hydrothermal method, finding that the hollow sphere structure—owing to its large surface area and accessible edge sites—exhibited 3.1 times the $NO_2$ sensitivity of solid spheres and facilitated deeper $NO_2$ diffusion, reducing operating temperatures while enhancing adsorption rates at increased $NO_2$ concentrations[Li et al., 2019b].

Additionally, Wadhwa *et al.*, introduced active and sensitive $H_2$ sensor based on vertically aligned (VA) $MoS_2$ flakes functionalized with Pt NPs[Wadhwa et al., 2022b]. The Pt@$MoS_2$ sensor achieved a sensitivity of 23% with excellent repeatability, rapid response, and full recovery at RT. Selectivity tests indicated robust responses to $H_2$ compared to gases like $NO_2$, $NH_3$, $H_2S$, $SO_2$, and $CO_2$. The improved sensor response was attributed to the Pt spillover effect and the distribution of adsorption sites at the Pt-$MoS_2$ interface. Density functional theory calculations supported the experimental findings, revealing that Pt@$MoS_2$ has a high $H_2$ adsorption capacity, leading to superior and accurate $H_2$ detection Repeatability tests of Pt@$MoS_2$ at 50 ppm $H_2$ at RT further confirmed the sensor's stability.

Nonetheless, these approaches result in heightened complexity and increased costs associated with the fabrication of the devices [Dey et al., 2013]. Moreover, it was noted that operating the device at elevated temperatures led to a reduction in both response and recovery times, albeit at the expense of diminished sensitivity. The introduction of heteroatoms into $MoS_2$ holds considerable research potential for elucidating its gas-sensitive performance[Tang et al., 2018]. Recently, plasma processing has been demonstrated as a rapid, convenient, straightforward, and efficient technique for altering the surface chemical properties of materials, particularly suitable for the treatment of two-dimensional materials without any contamination

from solvents. Furthermore, plasma treatment of $MoS_2$ may lead to an increase in edge sites and the introduction of heteroatoms, thereby enhancing their charge carrier mobility as well as their catalytic and optoelectronic properties.

Nitrogen incorporation within TMDs is recognized as a common technique to alter their intrinsic physical and chemical attributes for ion retention, oxygen reduction, gas sensor, and hydrogen evolution processes [Ren et al., 2018; Tao et al., 2019; Zhao et al., 2024a]. In recent developments, the employment of nitrogen plasma has been recognized as a powerful approach to effectively insert N atoms within TMDs. The introduction of nitrogen atoms alters the surface electronic characteristics, facilitating a narrower bandgap, expedited charge mobility, and a wealth of active sites for catalytic engagement, while potentially enhancing the robustness of atomic linkages. With respect to gas sensors, remarkable adsorption capacity and selective affinity for $CO_2$, which generally displays a minimal response, have been theoretically predicted in nitrogen-doped $MoSe_2$ utilizing density functional theory (DFT) [Enujekwu et al., 2021]. This research unveils a direction towards the realization of controllable selectivity; however, tangible experimental validations have proven to be elusive until now. Azcatl *et al.*, demonstrated a method to control nitrogen substitutional doping concentration in $MoS_2$ through remote $N_2$ plasma treatment[Azcatl et al., 2016]. Following this work, Zhao *et al.*, investigated the influence of nitrogen doping on the gas sensing properties of 2D $MoS_2$. The N-doped $MoS_2$ nanosheets, created by plasma treatment, introduced nitrogen as an additional active site within the material[Zhao et al., 2024a]. This modification effectively lowered the Fermi level of $MoS_2$, resulting in a reduced band gap and increased conductivity. The nitrogen doping notably enhanced the material's detection capabilities, responsiveness, and response time to $NO_2$, showcasing a marked improvement in gas recognition performance.

Tin disulfide ($SnS_2$) has emerged as a highly significant two-dimensional (2D) semiconductor nanomaterial, particularly noted for its exceptional photoelectric, mechanical, and electrical properties. As a member of the IV-VI semiconductor family often referred to as "gold powder," $SnS_2$ has attracted considerable attention over the past decade[Cao et al., 2018]. This non-toxic, n-type semiconductor possesses a direct optical band gap in the range of 2.2 to 3.2 eV, a high excitonic binding energy of 170 meV, and favorable electronegativity[Das Mahapatra et al., 2021]. The material features a substantial lattice spacing of 0.59 nm, which facilitates the adsorption and desorption of gas molecules on its surface and within its active lattice sites. Furthermore, $SnS_2$ exhibits a high optical absorption coefficient ($10^4$ to $10^5$ $cm^{-1}$), impressive electronic mobility of 230 $cm^2$ $V^{-1}$ $s^{-1,}$ and adequate oxidation resistance, with a density of 4.14 $g/cm^3$ and a melting point of 882 °C[Sun et al., 2019; Zhan et al., 2020]. The advantageous properties of 2D materials, including $SnS_2$, such as chemical, physical, and thermal stability, along with their planar crystal structures and large surface-to-volume ratios, have made them particularly effective for sensing applications. These characteristics enable superior sensing capabilities, including ultra-sensitivity at the molecular level, rapid response times, and low power consumption. $SnS_2$ has demonstrated outstanding performance in electrocatalytic reduction, optoelectronic devices, photocatalytic generation, and notably in gas sensing due to its unique structural features. The layered structure of $SnS_2$, akin to that of graphene, allows for the fabrication of various nanostructures, including nanotubes, nanowires, and both vertically and horizontally aligned flakes, enhancing its applicability in gas sensing technologies. The surface morphology of vertically aligned $SnS_2$ flakes is crucial for improving gas sensor sensitivity by maximizing the active surface area available for interaction. Ou *et al.*, demonstrated that multilayer $SnS_2$ flakes exhibit remarkable sensitivity and selectivity towards $NO_2$ at operating temperatures below 160 °C[Ou et al., 2015]. Similarly, Giberti *et al.*, developed $SnS_2$ nanorod-based materials that displayed good selectivity for acetone and acetaldehyde at a working temperature of 300 °C[Qin et al., 2018]. Xiong *et al.*, reported the synthesis of $SnS_2$ nanoflowers, which effectively detect ammonia ($NH_3$) concentrations ranging from 0.5 to 100 ppm at 200 °C[Xiong et al., 2018].

In recent years, mono- or few-layer 2D materials have garnered significant interest as a novel class of room-temperature gas-sensitive materials due to their outstanding physical and chemical properties, including a large active surface area, low electrical noise and high electrical

conductivity[Yang et al., 2017a]. Exfoliated black phosphorus exhibits rapid responses to ammonia ($NH_3$), with detection sensitivity reaching as low as 10 ppm at room temperature[Donarelli et al., 2016]. Likewise, few-layer reduced graphene oxide has a rapid sensitivity to $NH_3$ concentrations as low as 1 ppb[Hu et al., 2014]. Ultrathin $SnS_2$ nanosheets exhibit significant potential for nanoelectronic applications. Zhou *et al.,* documented the creation of a high-performance flexible photodetector employing chemical vapor deposition (CVD)-grown $SnS_2$ nanosheets, attaining an exceptional responsivity of 34.6 A/W[Zhou et al., 2016].

$SnS_2$ is identified as a viable material for chemosensor applications at room temperature, largely attributable to the low electronegativity of sulfur atoms. Nonetheless, its efficacy in gas detection is constrained by various limitations, such as low selectivity, extended response and recovery times, and inadequate stability. Researchers have investigated multiple strategies to improve the optical and electrical properties of $SnS_2$, including doping, the formation of nanocomposites, and heterostructure engineering[Mishra et al., 2024]. The modifications enhance the gas sensing capabilities of $SnS_2$ by modifying its band structure, charge transfer mechanisms, physisorption characteristics, and surface reactivity, which collectively increase its gas adsorption capacity. Engineering heterostructures enhances sensitivity, accelerates response and recovery times, improves stability, and enables more efficient detection across a broader range of gases, attributed to increased surface area and enhanced electron mobility[Bag et al., 2019]. Wu *et al.,* reported that the $SnS_2/SnSe_2$ heterostructure demonstrates improved interfacial charge transfer for $NO_2$ sensing[Wu et al., 2023]. The well-defined atomic interface between the two materials creates a lateral built-in electric field, which significantly enhances the adsorption of $NO_2$ molecules and accelerates charge transport across the heterostructure's 2D plane. Different morphologies of $SnS_2$ and its heterostructures or nanocomposites, such as nanowires, nanotubes, 2D layers, nanoflowers, nanoplates, quantum dots, and core-shell structures, have been synthesized to enhance sensor performance by promoting rapid electron transport and facilitating interactions with oxygen molecules, thereby creating active chemisorbed sites on the sensor surface. The synthesis of $SnS_2$ and its heterostructures/nanocomposites has been accomplished using various physical and chemical techniques, such as hydrothermal synthesis, chemical vapor deposition, solvothermal processes, successive ionic layer adsorption and reaction (SILAR), vacuum evaporation, hot injection, thermal evaporation, RF-magnetron sputtering, and DC magnetron sputtering.

Vacancy defects, which significantly influence the properties of materials, are often an unavoidable consequence of the exfoliation process. Interestingly, these defects can enhance gas adsorption capabilities. Zhao *et al.,* utilized first-principles density functional theory (DFT) calculations to show that monolayer $SnS_2$ with sulfur vacancies displays increased sensitivity to nitrogen-based molecules, including $NH_3$, NO, and $NO_2$[Zhao et al., 2017a]. This indicates that mono- or few-layer $SnS_2$ with vacancies can be produced through lithium intercalation and exfoliation techniques, which may enhance the gas-sensing performance of 2D $SnS_2$ nanosheets. In addition to heterostructure development, alternative strategies are available for modifying electronic properties and increasing the active surface area. Vacancy engineering, which incorporates anion vacancies into the catalyst lattice, enhances electronic conductivity and creates additional active sites for adsorption[Kunstmann et al., 2017]. The incorporation of sulfur (S) vacancies effectively reduces the band gap of $SnS_2$, enhancing its sodium storage capabilities. Vacancies are frequently perceived as constraints that may impede a material's performance; however, they can also lead to interesting phenomena resulting from alterations in the intrinsic properties of the materials. Although numerous strategies have been employed to improve gas sensing performance via defect engineering, only a limited number of defects have resulted in substantial enhancements. The localization of electron density at defect sites significantly enhances gas sensing activity via orbital mixing and charge transfer. Theoretical studies demonstrate that $SnS_2$ monolayers with sulfur vacancies exhibit enhanced sensitivity to $NO_2$ in comparison to other molecules, including NO, $NH_3$, $H_2O$, and CO. Hu *et al.,* successfully introduced sulfur vacancies and created an in-plane $SnS_2/SnO_2$ heterojunction within $SnS_2$

nanosheets through a high-energy ball milling technique, resulting in shallow electronic traps near the valence band maximum[Hu et al., 2020].

## 1.7 Photodetector

A photodetector (PD) is an electronic device that transforms optical signals into electrical signals, enabling the detection of incident photons across a broad spectrum of the solar range. The operational capabilities of a photodetector are contingent upon the bandgap of the semiconductor material employed in its construction, allowing it to function in various regions, including X-ray, ultraviolet (UV), visible (VIS), infrared (IR), and terahertz (THz) ranges. The detection process involves the absorption of photons, which generates free electron-hole pairs within the semiconductor when the energy of the incident photons exceeds the material's bandgap. These charge carriers are subsequently driven by either a built-in electric field or an externally applied bias voltage, resulting in the generation of a photocurrent that can be amplified, processed, and analyzed. Photodetectors are utilized in a wide array of applications, including imaging, flame detection, optical communication, biomedical devices, motion sensing, air purification, night vision, missile tracking, security systems, ozone sensing, and space technology. The schematic representation of a photodetector device is illustrated in Figure 1.16.

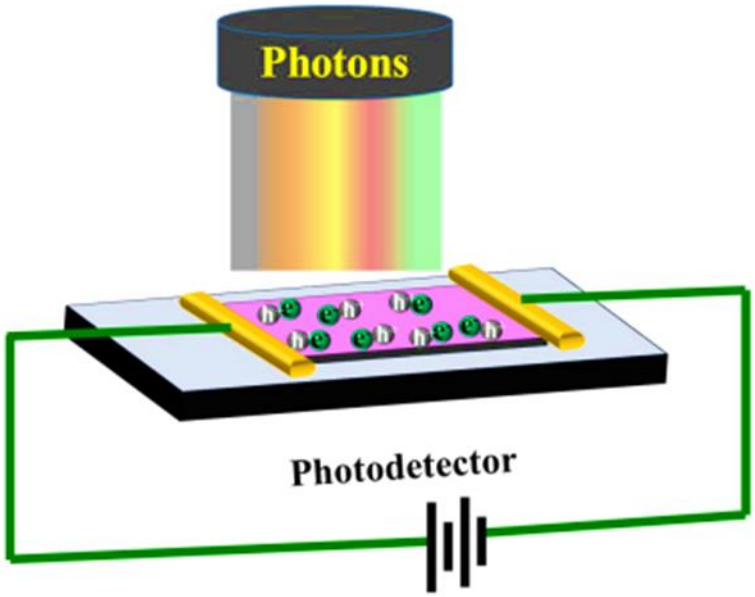



**Figure 1.15:** Schematic of a photodetector device

### 1.7.1. The Figure of Merits of a Photodetector

The performance of photodetectors is defined by numerous critical metrics, including responsivity, rise time, decay time, detectivity, and external quantum efficiency (EQE). These measurements are crucial for evaluating the performance of photodetectors under diverse operating situations and dimensions.

#### (a) Responsivity (R)

It is a crucial parameter that greatly affects the performance of a photodetector. It quantifies the efficiency with which the device converts incident optical power into a generated photocurrent and is defined as the ratio of the photocurrent produced ($I_{photo}$), to the incident optical power ($P_o$)[Liu et al., 2014b]. Responsivity is typically measured in amperes per watt (A/W). This metric serves as a crucial indicator of the input-output gain of a photodetector system, reflecting its capability to transform incoming photons into electrical current. The responsivity is expressed by following equation:

$$R = \frac{I_{Photo} - I_{dark}}{P_o.S} \quad (1.9)$$

Where, $I_{Photo}$ denotes the photocurrent generated, when the photodetector is exposed to light, $I_{dark}$ refers to the current measured in the absence of illumination (A), $P_o$ signifies the power density of the incident light (watts per unit area), and S represents the effective active area of the photodetector that is illuminated.

An increase in demonstrates a more efficient conversion of optical energy into an electrical signal, which subsequently enhances the generation of photocurrent.

**(b) Specific detectivity ($D^*$)**

Detectivity is a critical metric that evaluates the ability of photodetectors to detect weaker light signals. It serves as a fundamental indicator of the sensitivity of an optical detector, quantifying its capability to discern weak optical signals in presence of the noise. The detectivity is inversely related to the noise equivalent power (NEP) and is mathematically represented by equation (1.5). A higher detectivity value signifies a more effective detector, capable of detecting weaker signals.

$$D^* = \frac{\sqrt{AB}}{NEP} = \frac{R\sqrt{A}}{\sqrt{2.q.I_{dark}}} \quad (1.10)$$

Here, A, B, R, q, $I_{dark}$ are the active area, detector bandwidth, responsivity, a charge of the electrons, and dark current, respectively. A low dark current is essential for achieving high detectivity in photodetectors, as it minimizes the background noise that can obscure weak optical signals. The unit of detectivity is expressed in Jones ($cm\sqrt{Hz}/W$).

**(c) External quantum efficiency (EQE)**

The EQE quantifies how effectively incident photons generate electron-hole pairs that contribute to the photocurrent of the device. The expression is generally represented as the ratio of the number of electron-hole pairs effectively collected by the device to the number of incident photons. This relationship emphasizes how effectively incident photons aid in generating the photocurrent that external circuits collect. In certain cases, the EQE can exceed 100%, indicating that a single photon can produce multiple electron-hole pairs. This phenomenon may occur when the lifetime of the photogenerated charge carriers is longer than their transit time, which can be attributed to charge trapping and differences in mobility between electrons and holes. It is given by following equation:

$$EQE = \frac{R.h.c}{q.\lambda} \quad (1.11)$$

Where, R represents responsivity, h denotes the Planck constant, c signifies the speed of light, q indicates the electron charge, and λ refers to the wavelength of the incident light.

A high EQE signifies that a device can effectively convert incident photons into electrical current, successfully collecting a substantial proportion of the generated electron-hole pairs.

**(d) Response time (t)**

The response time of a photodetector (PD) is an essential performance metric, characterized as the time taken for the PD output to adjust in reaction to changes in incident light intensity. The response time consists of two elements: the rise time ($\tau_{rise}$) and the decay time ($\tau_{decay}$). These are usually measured as the duration it takes for the photocurrent to rise from 10% to 90% of its peak value, while the decay time indicates the time needed for it to fall from 90% to 10%, respectively. An expedited response time is crucial for guaranteeing the effective and timely functioning of the device, thereby improving the precision and dependability of its detection abilities.

**(e) Broadband Range**

The detection range is a critical parameter for any photodetector device, as it defines the ability of the detector to efficiently absorb incident light across a broad spectrum and

transforming into an electrical output. This broadband detection is influenced by both the intrinsic material properties, such as the bandgap, and the design characteristics of the detector itself. The absorption edge of the material specifies the longest wavelength that can be effectively absorbed. A broader spectral range allows a photodetector to capture light across a wider array of wavelengths, which is particularly advantageous for applications like remote sensing and spectroscopy, where the ability to detect a diverse range of wavelengths is crucial.

### 1.7.2. Photodetector Mechanism

The conversion of light signals into electrical signals predominantly occurs through two main processes: the first is associated with the electric field generated by optical radiation, encompassing the photovoltaic, photoconductive, and photogating effects; the second involves thermal processes, which include the photo-thermoelectric and photo-bolometric effects. This discussion will provide an overview of all relevant photo-conversion mechanisms.

#### (a) Photoconductive effect

The photoconductive effect involves the absorption of photons, leading to the generation of excess free charge carriers that influence the electrical resistance of the semiconductor material. The generation of excess carriers holds less importance for photoconductivity compared to the alterations in space-charge resulting from deep-level photoionization. An electron, which is a majority carrier, is emitted from a deep level within the surface depletion region and is subsequently driven into the quasineutral region. This process leads to a positive photoconductive response by facilitating the receding of the surface depletion layer. Conversely, for minority carrier holes, photoemission decreases space charge, thereby extending the surface depletion region. Under an applied bias without illumination, a small current flows between the electrodes, as illustrated in Figure 1.17 (a).

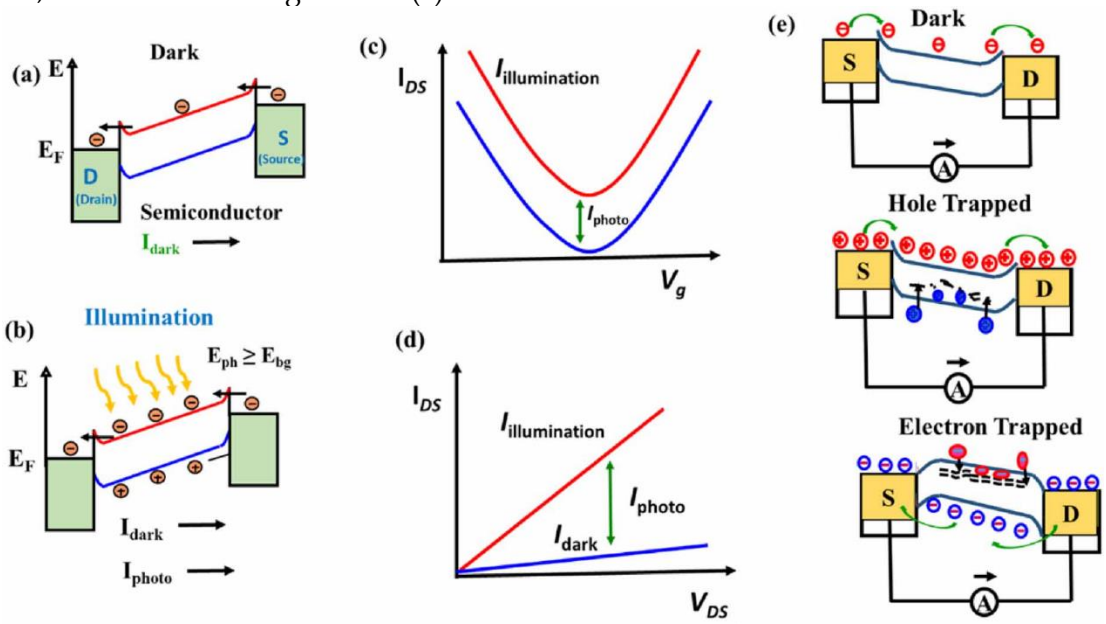



**Figure 1.16:** Schematic diagram of photoconductive effect (a) without illumination and under external bias, (b) under illumination with energy of photons ($E_{ph}$), (c) $I_{DS}$ – $V_g$ curves under light (solid red line) and in the dark (solid blue line), (d) traces of $I_{DS}$ – $V_{DS}$ in the dark (solid blue line) and when illuminated (solid red line). (e) Schematic view of photogating effect[Kumar et al., 2021a].

When light with energy exceeding the bandgap ($E_p > E_g$) strikes the device, it results in the generation of electron-hole pairs (excitons), which are then separated by the applied bias voltage, as illustrated in Figure 1.17 (b). The application of bias voltage promotes the separation of these pairs, leading to the movement of free electrons and holes towards the metal electrodes in opposite directions[Furchi et al., 2014]. This leads to an increase in the total photocurrent ($I_{photo}$), which subsequently combined with the dark current, and increases the device's conductivity, as

shown in Figure 1.17 (c, d). To effectively observe the photoconductive effect, an applied bias voltage ($V_{ds}$) is essential. For optimal separation of electron-hole pairs, Ohmic contacts are preferred. In photoconductive applications, two critical parameters are the photoconductive gain and relaxation rate. Higher electron mobility allows electrons to move more rapidly than holes, contributing significantly to the photocurrent. A single photon can generate multiple electrons, enhancing efficiency.

**(b) Photovoltaic effect**

The photovoltaic effect generates voltage and electric current, when a material is subjected to light of sufficient energy ($h\upsilon \geq E_g$), with the internal electric field from the p-n junction or Schottky barrier facilitating the separation of electron-hole pairs via photon absorption, as depicted in Figure 1.18 (a, b)[Kumar et al., 2021a]. In the dark, photovoltaic devices exhibit non-Ohmic current-voltage (*I-V*) characteristic[Rehman et al., 2016]. The forward source-drain current ($I_{DS}$) in a p-n junction being exponentially related to the applied bias voltage ($V_{DS}$) i.e. $I_{DS} \propto \exp(V_{DS}) - 1$, while the reverse current remains negligible until the junction reaches breakdown. When the device is illuminated with zero bias voltage ($V_{bias} = 0$), the internal electric field facilitates the separation of excited charge carriers, resulting in high short-circuit photocurrent ($I_{sc}$). Conversely, when the circuit is open, the accumulation of opposite charge carriers (electron-hole pairs) at the terminals produces an open-circuit voltage ($V_{oc}$). Typically, these detectors operate in self-bias or reverse bias modes. In photovoltaic operation, the dark current is minimized, enhancing the detectivity of the device. Various phototransistors and photodiode types, such as PN, PIN, and Schottky photodiodes, are designed based on the principles of the photovoltaic effect, where the built-in field separates the photogenerated electron-hole pairs.

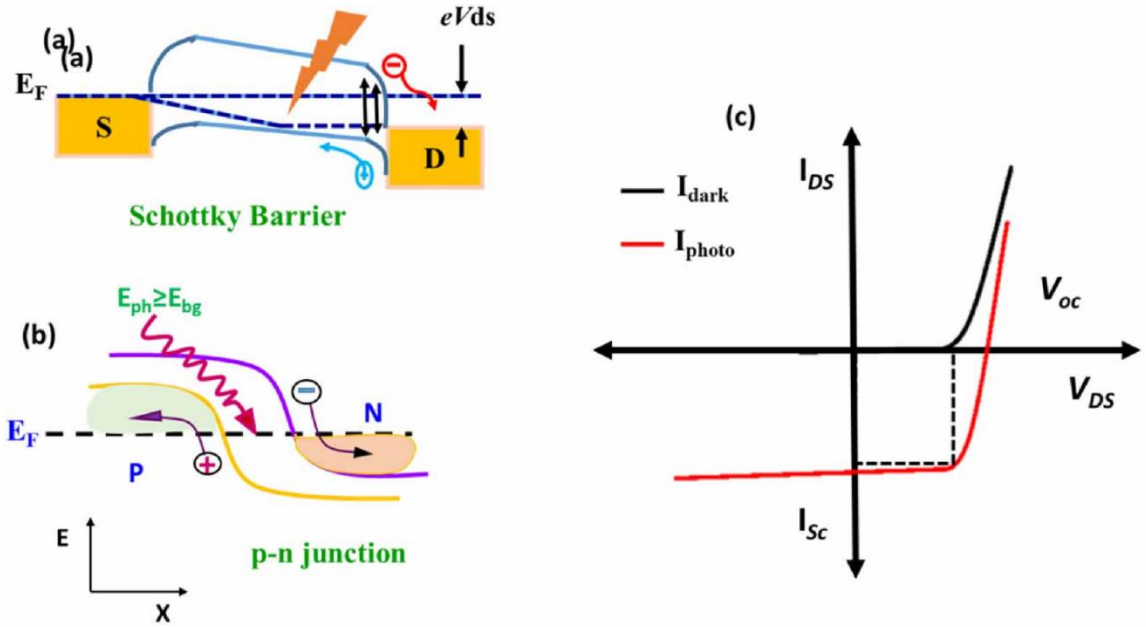



**Figure 1.17:** (a), (b) Schematic view of photovoltaic effect arising from a metal–semiconductor Schottky barrier and p–n junction, and (c) $I_{DS}$ – $V_{DS}$ traces in the dark (solid black line) and under illumination (solid red line), reprinted with permission[Kumar et al., 2021a].

The rise in reverse current is due to the internal electric field directing photogenerated carriers in the opposite direction when reverse bias and illumination are applied. In specific scenarios, like when a substantial reverse bias is applied to a heavily doped p-n junction, the photogenerated carriers can gain speed due to the intense electric field, leading to increased photoconductive gain via impact ionization. The I-V characteristics of the PN junction, illustrated in Figure 1.18 (c), indicate that when illuminated, the I-V curve shifts downward in comparison to the dark curve, attributed to the analogous polarity of photocurrent and reverse current. The majority of photodetectors function as PN diodes, operating in either reverse bias (photoconductive mode) or at zero bias (photovoltaic mode). The minimum dark current is

observed at zero voltage, enhancing the detectivity of the photodetector. However, the photo responsivity is generally lower compared to devices that employ photoconductive mechanisms, primarily due to the absence of internal gain. The photoconductive mode, defined by reverse-bias operation, enhances photodiode speed through minimized junction capacitance, resulting in a significant internal gain that facilitates the detection of low-power light signals.

**(c) Photogating effect**

The photogating effect is a specialized class of the photoconducting phenomenon arising from the presence of localized or trapped energy levels, such as surface states, defects, hybrid compositions, or impurities within the semiconductor's band gap, as depicted in Figure 1.17 (e). In this phenomenon, one type of photogenerated charge carrier becomes trapped in localized states that do not contribute to photocurrent generation, while the remaining carriers are free to move within the channel material, thereby modulating its conductance and facilitating the formation of photocurrent[Fang et al., 2017; Kumar et al., 2021a]. For instance, in an n-type semiconductor with hole trap states, generated holes are captured by these defect states, while the electrons contribute to photocurrent generation. In the second scenario, electron-hole pairs are generated in surface adsorbates, with one type of charge subsequently transferred into the host semiconductor. In both cases, the trapped charges create an additional gate voltage for the channel, effectively modulating the conductivity of the semiconductor. The longer lifetime of the trapped charge carriers, results in significant photoconductive gain. These trapped carriers can induce an additional local gate voltage, which shifts the transfer characteristics horizontally from the dark state ($\Delta V_g$), allowing for an increase or decrease in photocurrent, which effectively modulating the conductivity of the semiconductor.

**(d) Bolometric effect**

The photo-bolometric effect is characterized by the modulation of the resistivity of materials as a result of uniform heating from photon absorption. Depending on the nature of thermal irradiation, the resistance of the temperature-sensitive material may either increase or decrease of the material, leading to corresponding changes in photocurrent, while maintaining a fixed bias voltage[Richards, 1994]. This effect is directly related to the change in conductance of the material with temperature (dG/dT), with the uniform temperature rise (ΔT) being attributed to laser-induced heating. To enhance the precision of conductance change measurements, detectors utilizing this principle typically employ a four-wire configuration. Over the past decade, 2D materials such as graphene, 1T-$TaS_2$, $MoS_2$, and single-walled carbon nanotube films have exhibited exceptional bolometric performance, functioning effectively as bolometric detectors. Due to their remarkable properties, 2D materials are increasingly recognized as promising candidates for next-generation bolometers.

## 1.8 Literature survey on photodetectors based on $MoS_2$

Traditionally, photodetectors composed of silicon (Si), indium antimonide (InSb), and indium gallium arsenide (InGaAs) have dominated the commercial sector for several decades, owing to their extensive availability, exceptional performance characteristics, ease of incorporation into prevailing systems, and capability for mass production[Casalino et al., 2010; Fang et al., 2012; Soref, 1993]. Yet, silicon possesses an indirect bandgap of 1.1 eV, which restricts its light absorption prowess mainly to the visible and near-infrared spectral domains, ultimately curtailing its functional efficiency. Furthermore, the inherent brittleness, rigidity, and opacity of silicon render it unsuitable for applications involving wearable, flexible, and bendable devices. On the other hand, compounds like mercury cadmium telluride (HgCdTe), gallium antimonide (GaSb), and indium antimonide (InSb) have proven effective as photodetectors within the mid-wave and long-wave infrared spectrum; however, their operational dependence on cryogenic temperatures renders them unsuitable for a wide array of applications[Fong et al., 1999; Rogalski, 2005]. Hence, it is necessary to innovate a new suite of optoelectronic materials that tackle the challenges presented by traditional photodetectors. These innovative materials are required to exhibit broad-spectrum UV-Visible-NIR light absorption, rapid on/off switching characteristics,

robust light-matter interaction properties, and compatibility with current complementary metal-oxide-semiconductor (CMOS) technologies. Fortunately, two-dimensional (2D) materials encompass all of these requisite attributes, positioning them as a potentially optimal solution to circumvent the limitations posed by conventional photodetectors. Additionally, 2D materials are characterized by their flexibility, transparency, and lightweight nature, rendering them particularly suitable for integration into wearable and flexible device applications [Mas-Balleste et al., 2011]. Their facile compatibility with extant technologies facilitates seamless incorporation into contemporary systems.

The landmark discovery of single-layer graphene from graphite in 2004 captivated the research community due to graphene's exceptional properties, such as its ultra-high carrier mobility ($2\times10^5 cm^2/V\cdot s$), remarkable mechanical strength (130 GPa), and impressive broadband optical absorption coefficient ($7\times10^5\ cm^{-1}$)[Mak et al., 2010a; Wadhwa et al., 2021a]. However, despite these advantageous properties, graphene's lack of an intrinsic bandgap limits its utility in switching devices. Silicene, a 2D silicon allotrope similar to graphene, offers a narrow but finite bandgap, though its practical applications are restricted by challenges in synthesis and device fabrication[Liu et al., 2018b]. Phosphorene, or black phosphorus (BP), has also garnered attention due to its large and tunable bandgap (0.3–2 eV), high carrier mobility, and moderate on-off current ratio[Liu et al., 2014d]. With these properties, phosphorene occupies a unique position, bridging the gap between the mobility and current on-off ratios found in transition metal dichalcogenides (TMDs) and group 4 semiconductor allotropes. However, the instability of phosphorene in ambient conditions presents a significant hurdle for its application in semiconductor devices[Island et al., 2015].

TMD materials, known for their broad range of bandgaps and excellent physical and chemical properties, are widely used in low-power electronics. While TMDs exhibit lower mobility than graphene and phosphorene, they achieve higher on-off current ratios, making them promising candidates for photodetectors[Liu et al., 2018b]. $MoS_2$, in particular, has emerged as the primary focus for researchers developing 2D TMD-based photodetectors, with recent advances bringing it closer to commercial viability[Wadhwa et al., 2021a]. This section will provide a concise overview of the latest developments in $MoS_2$-based photodetectors.

$MoS_2$ photodetectors are primarily constructed as field-effect transistors (FETs), with the pioneering device fabricated by Radisavljevic *et al*., using a monolayer of $MoS_2$ obtained through mechanical exfoliation[Lopez-Sanchez et al., 2013]. This FET demonstrated a responsivity of 7.5 mA/W and a response time of 50 ms under 80 μW optical power and a 50 V gate voltage. Zhang *et al*., achieved a superior responsivity of 2200 A/W in vacuum and 780 A/W in ambient air for a CVD-grown monolayer $MoS_2$ film[Zhang et al., 2013]. Responsivity variations in monolayer $MoS_2$ are influenced by factors like device resistance, geometry, interdigitated electrode configurations, bias and gate voltages, light source characteristics, laser spot area, and setup limitations, all impacting device performance[Yin et al., 2012]. Although monolayer $MoS_2$ photodetectors show improvements over graphene detectors, they suffer from low absorption, leading to research on high-performance multilayer $MoS_2$ (ML $MoS_2$) devices[Lee et al., 2012a]. In 2013, Yu *et al*., introduced the first vertical $MoS_2$ heterostructure for enhanced photon capture, paving the way for further studies of 2D heterostructures for photodetection[Yu et al., 2013]. Lee *et al*., developed a vertical p-n junction utilizing p-type $WSe_2$ and n-type $MoS_2$. The differences in bandgap and work function establish a distinct type-II interface that facilitates charge carrier separation, thereby extending the photodetection range via interlayer excitation[Lee et al., 2014].

The establishment of a type-II band alignment in $MoS_2/MoTe_2$ heterostructures results in a reduced energy gap of 0.657 eV between the valence band maximum (VBM) of $MoTe_2$ and the conduction band minimum (CBM) of $MoS_2$, corresponding to 1.8 μm, which is less than the bandgap of each individual material. This hybrid structure exhibits a photoresponse to illumination at wavelengths extending to 1.5 μm, thereby effectively expanding the photodetection range possible with 2D heterostructures. Colloidal quantum dots (CQDs) are photosensitive materials characterized by adjustable bandgaps achieved via size quantization. This property allows for spectral tuning across a broad range, from UV-visible to mid-infrared,

rendering them suitable for light-detection applications[Generation, 2009; Keuleyan et al., 2011]. A substantial enhancement in photoresponsivity has been observed in hybrid photodetectors that integrate $MoS_2$ with CQDs[Huo et al., 2017; Kufer et al., 2014; Ra et al., 2016]. For example, Kufer *et al.,* presented a $MoS_2$/PbS quantum dot hybrid photodetector that achieved an extended spectral response up to 1.5 µm with high responsivity[Kufer et al., 2014]. Recent developments in $MoS_2$ synthesis and film-transfer methods facilitate the integration of $MoS_2$ with conventional 3D bulk materials, including Si, GaAs, and GaN[Wang et al., 2015a; Xu et al., 2016]. In $MoS_2$/3D heterostructures, p-n or n-n junctions enable efficient separation of photogenerated electron-hole pairs owing to the strong electric field present in the depletion region. Consequently, $MoS_2$/3D hybrid detectors demonstrate elevated detectivity and rapid response times. The spatial photocurrent map at the vertical p-n junction of $MoS_2$/Si, indicates that photocurrent generation is predominantly localized at the junction, highlighting its essential function in facilitating effective charge separation and collection in the device.

Plasmonic nanostructures, including metal nanoparticles, nanoantennas, and nanodiscs, have been combined with 2D $MoS_2$ to enhance light-matter interaction. Surface plasmons (SPs) are characterized by coherent oscillations of free electrons confined at the interface of two media, typically a metal and a dielectric, which possess opposite signs in the real part of their dielectric constants. The oscillations create an electromagnetic field adjacent to the metal surface, and the charge movement on the surface, in conjunction with this electromagnetic field, results in the formation of surface plasmon polaritons (SPPs). Surface plasmon polaritons (SPPs) exhibit a higher frequency compared to incident photons, leading to enhanced spatial confinement and intensified localized fields. The plasmon-enhanced optical field markedly amplifies the interaction between light and matter. Miao *et al.,* integrated 4 nm thick Au nanoparticles onto $MoS_2$, resulting in a two-fold increase in photocurrent[Miao et al., 2015]. This enhancement is linked to improved absorption in $MoS_2$, which is attributed to the augmented optical field and light trapping around the Au nanoparticles. Rahmati *et al.,* similarly decorated CVD-grown vertical $MoS_2$ with Au NPs, resulting in a 20-fold enhancement in photocurrent attributed to the plasmonic effect and increased light scattering[Rahmati et al., 2019]. Plasmonic nanostructures can generate hot electrons via surface plasmon decay, facilitating photodetection in 2D materials that exceeds their intrinsic bandgap. Hot electrons can be directly injected into $MoS_2$ through the metal-semiconductor Schottky barrier, resulting in photocurrent that exceeds the bandgap limit. Wang *et al.,* utilized this method to develop a near-infrared (NIR) $MoS_2$ photodetector using bilayer $MoS_2$ with an asymmetric Au nanoantenna array[Wang et al., 2015b]. This device demonstrates a significant photoresponse beyond the bandgap, which is ascribed to hot carrier injection into $MoS_2$ via surface plasmon-induced non-radiative decay under illumination. Furthermore, it attains a significant infrared photo gain of $10^5$ at 1070 nm, attributed to a high responsivity of 5.2 A/W. Enhanced absorption in 2D films via plasmonic nanostructures results in a significant improvement in the device's photoresponse.

## 1.9 Challenges and Motivation

This thesis focuses on synthesizing high-quality $SnS_2$ and $MoS_2$ films with controlled morphology, alongside the fabrication of $SnS_2$ and $MoS_2$-based gas sensors and photodetectors.

Several challenges exist in synthesizing $SnS_2$ and $MoS_2$ films, particularly through chemical vapor deposition (CVD), which, despite its potential, faces limitations in achieving large-scale, uniform, and reproducible growth. Key issues with CVD include precise control over growth parameters, film morphology, uniformity, and repeatability. An additional challenge lies in synthesizing vertically aligned $SnS_2$ and $MoS_2$ flakes, as in-plane $SnS_2$ and $MoS_2$ growth is thermodynamically more favorable, making large-scale vertical alignment particularly complex. Although progress has been made, establishing a reproducible and scalable process for high-quality, uniformly aligned $SnS_2$ and $MoS_2$ via CVD remains an open challenge.

The increasing industrial and transportation activities linked to population growth have led to a rise in atmospheric toxic gases, resulting in cognitive impairments and decision-making

challenges in affected populations [Zhang et al., 2018c; Zivin et al., 2012]. According to the World Health Organization, millions of annual deaths are attributable to air pollution, prompting heightened attention to air quality monitoring as a means to protect both human health and the environment. Nitrogen dioxide ($NO_2$), an acidic and hazardous gas, is continuously released into the atmosphere due to anthropogenic activities. Gas sensors are essential devices for detecting harmful inorganic gases (such as $NO_2$, NO, $NH_3$, $H_2$, and $CO_2$) and organic gases (including methane, triethylamine, and benzene) [Binions et al., 2013; Hübert et al., 2011; Korotcenkov et al., 2009; Liu et al., 2017; Timmer et al., 2005]. They are widely used across various sectors, including industrial processes, agriculture, aerospace, military, and medical diagnostics [Arshak et al., 2004; Kohl, 2001; Yamazoe, 1991; Yunusa et al., 2014] . Traditional $NO_2$ sensors have notable limitations, including high-temperature operation, slow recovery rates, and performance degradation in adverse environmental conditions. Recent studies have identified $SnS_2$ and $MoS_2$ as promising candidates for the development of next-generation $NO_2$ sensors. However, these materials face significant challenges, including incomplete recovery at room temperature, attributed to the strong adsorption of $NO_2$ molecules on their surfaces. While thermal heating could facilitate recovery, it compromises the overall sensing performance. To better understand these dynamics, we analyzed $NO_2$ sensing data from various $SnS_2$ and $MoS_2$ sensor configurations, including bare, morphology-optimized, and hybrid structures.

Future advancements in sensor performance should focus on improving selectivity, lowering detection limits, stabilizing materials, and eliminating unwanted impurities. Significant scientific progress has been made to tackle these challenges through advanced synthesis methods, defect engineering, novel 2D materials, noble metal doping, surface functionalization, heterostructure fabrication, film thickness reduction, and light illumination techniques. The defect density and doping concentration in two-dimensional (2D) materials can be precisely controlled through methods such as chemical functionalization, molecular doping, and ion irradiation. By manipulating the electrical and chemical properties of these materials through defect introduction and doping, researchers can significantly enhance their sensing performance, including sensitivity, selectivity, and stability. For example, Kumar *et al.,* investigated the gas sensing properties of sulfur-vacancy $SnS_2$ ($V_S$-$SnS_2$) flakes created using a direct chemical vapor deposition (CVD) method followed by plasma treatment[Kumar et al., 2023a]. Treatment with nitrogen ($N_2$) plasma resulted in the formation of sulfur vacancies, as illustrated in their findings. Additionally, Patel *et al.,* developed vanadium-doped $MoO_3$ nanostructures, which served as precursors for the atmospheric pressure CVD growth of $MoS_2$[Patel et al., 2024]. Their experiments demonstrated that doping $MoS_2$ with vanadium significantly enhanced its gas-sensing capabilities. Specifically, V-doped $MoS_2$ exhibited a markedly improved response to ammonia ($NH_3$) at room temperature, with response and recovery times of 29.5 and 39.5 seconds, respectively. Furthermore, the incorporation of heteroatoms, such as sulfur, nitrogen, boron, and silicon, into 2D materials can effectively modify their defect concentrations. Both bare and tungsten (W)-doped $MoS_2$ have been successfully synthesized using hydrothermal techniques, and the influence of W doping on response and recovery times in the presence of $NO_2$ has been shown to be significant. Notably, doping $MoS_2$ with W at a 1:2 ratio with molybdenum dramatically increased the response speed, reducing the reaction and recovery times from hundreds of seconds to mere tens of seconds.

Despite significant advancements in the performance of $MoS_2$ photodetectors, the intrinsic limitations of utilizing a single material restrict their photodetection capabilities. The atomically thin structure of $MoS_2$ (a few nanometers thick) results in low optical absorbance, which hampers its efficiency in light detection. Additionally, the lack of high-quality p-n junctions leads to a high recombination rate of charge carriers in bare MoS2, which negatively impacts photodetector performance. The active wavelength detection range of these devices is constrained by the bandgap of $MoS_2$, further restricting their effectiveness for broadband photodetection.

A promising strategy to address these challenges involves the integration of multiple high-absorbing materials with complementary bandgaps, which can significantly enhance light absorption across a broader spectral range and improve device performance. By constructing heterostructures with other optically efficient materials, the optical absorption of $MoS_2$ can be

augmented, facilitating more effective light detection. Heterostructure photodetectors typically demonstrate superior photoresponse compared to their individual components, thereby increasing functionality. The surfaces of 2D materials, being free from dangling bonds, allow for seamless integration without concerns related to lattice mismatch, enabling a wide variety of heterostructure combinations due to interlayer coupling. Consequently, heterostructures present a viable pathway for fabricating high-performance photodetectors, offering benefits such as enhanced responsivity, reduced response times, and an extended operational bandwidth. Additionally, understanding charge carrier dynamics at the heterostructure interface is crucial, as device performance is significantly influenced by band alignment and charge extraction processes. The characteristics of the junction and charge transport are interrelated, and optimizing the interface is essential for improving device efficiency. Thus, comprehensive studies of the interface are necessary to elucidate the mechanisms that govern device performance.
Numerous studies have documented the performance of various materials, including graphene and III-V group nitrides, in photodetectors. These materials exhibit a broad spectrum of performance characteristics in terms of responsivity and response time. Notably, a trend has emerged wherein materials demonstrating higher responsivity tend to experience slower response times. For instance, while graphene-based photodetectors are known for their rapid response, they exhibit lower responsivity compared to other materials. Conversely, photodetector devices based on GaTe, $TiS_2$, and $MoS_2$ demonstrate high responsivity, yet they are hindered by prolonged response times. This disparity indicates a critical need for researchers to develop photodetector devices that combine high responsivity with fast response times, ultimately optimizing performance across both metrics.

## 1.10 Objective of the present thesis work

The primary goal of this research thesis is to develop a simple and effective method for synthesizing uniform, reproducible, and large-area $SnS_2$ and $MoS_2$ intended for use in gas sensing and photodetector applications.
In this thesis work, the author aims to:

- Develop a robust and scalable method for synthesizing high-quality 2D materials such as $SnS_2$ and $MoS_2$ using CVD.
- Optimize the CVD process to achieve uniform and defect-free material growth, which is essential for reliable sensor performance.
- Spectroscopic and microscopic characterizations of CVD grown different nanostructures or morphologies of $SnS_2$ and $MoS_2$ at room temperature.
- Design and fabricate gas sensors incorporating the grown $SnS_2$ and $MoS_2$.
- Systematically optimize sensor performance parameters, including sensitivity, selectivity, and response time, to enhance detection capabilities and operational reliability.
- Investigate the effect of plasma treatment techniques and surface functionalization using nobel nanoparticle in gas sensing field after fabricating a gas sensor.
- Fabrications of highly responsive, fast response and broadband $MoS_2$-based heterostructures

## 1.11 Outline of Thesis

Outline of this thesis is described below.

**Chapter 1:** This chapter provides an overview of the physical properties of transition metal dichalcogenides (TMDs), with a particular emphasis on $MoS_2$ and $SnS_2$, highlighting their potential for device applications. A comprehensive review of recent advancements in this field is included to contextualize the research presented in this thesis. The discussion addresses key challenges in the large-area synthesis of uniform and highly reproducible $MoS_2$ flakes and vertically aligned $SnS_2$ flakes, emphasizing their relevance for scalable applications. Furthermore, the chapter examines the limitations of conventional gas sensing materials, underscoring the advantages of $MoS_2$ and $SnS_2$ in achieving selective $NO_2$ detection. The potential of these materials for developing high-performance broadband photodetectors is also explored, along with the challenges that must be overcome to establish them as next-generation photodetector materials. The chapter concludes by summarizing the objectives and aims of this thesis, which seeks to address these challenges and advance the understanding and application of $MoS_2$ and $SnS_2$ in gas sensing and optoelectronic devices.

**Chapter 2:** This chapter provides an overview of the synthesis and characterization techniques utilized in this study, with a focus on understanding the structural, morphological, and optical properties of $MoS_2$ and $SnS_2$ and its interfaces. The deposition methods employed for material synthesis are discussed, along with various characterization techniques used to examine the morphology and structure of the synthesized materials. Furthermore, the chapter elaborates on the gas and light-sensing characterization systems integral to this research, emphasizing their role in assessing the performance of $MoS_2$ and $SnS_2$-based devices for gas sensing and photodetection applications.

**Chapter 3:** This chapter explores the large-area growth of highly uniform $MoS_2$ and $SnS_2$ using thermal chemical vapor deposition (CVD) technique, providing a comprehensive understanding of the growth mechanisms and the influence of various parameters on optimizing the synthesis process. It systematically demonstrates the controlled transition from in-plane to vertically aligned $MoS_2$ and $SnS_2$ flakes, emphasizing the critical role of gas flow rate in determining the density and uniformity of vertically aligned structures. Additionally, the chapter introduces an innovative method for fabricating Au/Cr interdigitated electrodes (IDEs), which are crucial components for gas sensor and photodetector platforms based on 2D materials.

**Chapter 4:** This chapter begins by examining the changes in morphology and semiconducting properties of $MoS_2$ following defect introduction and functionalization with noble metal nanoparticles. It then delves into the effects of defect and surface engineering on the gas sensing performance of CVD-grown $MoS_2$, accompanied by a proposed gas sensing mechanism.

**Chapter 5:** This chapter explores the gas sensing behavior of vertically aligned $SnS_2$ flakes subjected to nitrogen plasma treatment. It provides a comprehensive analysis of the enhanced gas sensing performance achieved through plasma treatment and introduces a comparative study of the gas sensing characteristics of $SnS_2$ before and after nitrogen plasma modification. A proposed sensing mechanism is also discussed, offering insights into the underlying processes driving the improved response.

**Chapter 6:** This chapter examines the application of density functional theory (DFT) calculations to elucidate the adsorption mechanisms of $NO_2$ gas molecules on the surfaces of $MoS_2$ and $SnS_2$ flakes synthesized via CVD. Additionally, it investigates the adsorption kinetics of $NO_2$ gas on $SnS_2$ nanoflake-based chemiresistor sensors by employing the Lee and Strano model. This model effectively interprets the sensor response curves, enabling the determination of the irreversible reaction rate across various $NO_2$ concentrations.

**Chapter 7:** In this chapter, the light-sensing behavior of 2D $MoS_2$ in the visible to near-infrared wavelength range was explored through the fabrication of a vertical out-of-plane van der Waals heterojunction composed of $MoS_2$ and $WS_2$. The heterostructure demonstrated enhanced

photodetection performance, attributed to mechanisms involving photoexcited enhanced carrier density and photogating effects. These effects facilitate efficient charge carrier generation and separation under illumination, resulting in a stronger photoresponse. Additionally, the self-powered behavior of the photodetectors was discussed, the $MoS_2$-$WS_2$ heterojunction exhibited superior self-powered performance, leveraging the built-in potential at the heterointerface for efficient charge separation without requiring an external bias.

**Chapter 8:** In the final chapter of this thesis, a comprehensive summary of the research work was presented, encapsulating the findings and contributions made toward the advancement of $MoS_2$ and $SnS_2$-based sensing applications. This chapter also outlined the challenges encountered during the study and provided insights into the future scope of this research, particularly in the context of 2D materials like $MoS_2$ and $SnS_2$. Key aspects of the emerging research directions were discussed, including the need for scalable and high-quality growth techniques, enhanced device performance, and integration strategies for practical applications.

# 2
# Fabrication and Characterisation of Materials and Devices

This chapter provides a concise overview of the fabrication and characterization methods employed for the deposition and analysis of two-dimensional (2D) $SnS_2$ and $MoS_2$. Various characterization techniques are utilized to assess the structural, morphological, and optical properties of $SnS_2$ and $MoS_2$. In this study, $SnS_2$ and $MoS_2$ are synthesized using chemical vapor deposition (CVD) methods. An RF plasma chamber is utilized to create vacancies and introduce nitrogen doping in both $MoS_2$ and $SnS_2$ by employing nitrogen gas, enhancing their electronic properties. Additionally, RF magnetron sputtering is employed for the functionalization of noble nanoparticles on the surface of $MoS_2$, which is expected to improve its gas sensing capabilities. Furthermore, the chapter discusses the hydrothermal method for synthesizing $WS_2$ nanostructures, highlighting its advantages in producing high-quality materials with controlled morphology. The structural, morphological, and compositional characteristics of the synthesized $SnS_2$ and $MoS_2$ are examined through X-ray diffraction (XRD), scanning electron microscopy (SEM), and energy dispersive X-ray spectroscopy (EDS). The optical properties are investigated using Raman spectroscopy, photoluminescence (PL), and UV-Vis-NIR spectroscopy. Additionally, the chemical, elemental, and electronic properties of $MoS_2$ are analyzed using X-ray photoelectron spectroscopy (XPS) and ultraviolet photoelectron spectroscopy (UPS). The device fabrication and measurement techniques used to evaluate the performance of photodetectors and gas sensors are also covered. The chapter concludes with a detailed examination of the experimental setup and methodologies employed for gas sensing and light detection experiments, providing a thorough understanding of the synthesis and characterization processes for these advanced materials.

## 2.1 Deposition techniques

### 2.1.1. Chemical Vapor Deposition (CVD)

CVD is a widely recognized method for the synthesis of two-dimensional materials and thin films, enables chemical reactions of gaseous reactants near or on the heated substrate, resulting in the formation of stable materials or thin films[Sun et al., 2021].. Historically, CVD has evolved from early examples, such as soot formation from incomplete combustion, to industrial applications like tungsten deposition on carbon lamps through the reduction of $WCl_6$ with $H_2$ in 1983. Since then, CVD has gained significant traction for thin film deposition, becoming a popular method for producing crystalline, polycrystalline, and amorphous films. The advantages of CVD include the ability to synthesize highly dense, large-area films with excellent uniformity and strong adhesion to substrates when deposition parameters are optimized. This technique also allows for precise control over the crystal structure, orientation, and morphology of the films, utilizing a diverse array of chemical precursors to grow various materials, including hydrides, halides, and oxides. CVD is capable of synthesizing a wide range of materials, including carbides, metals, nitrides, oxides, sulfides, and more. However, several challenges are associated with this technique. One significant issue is reproducibility, which can hinder the consistent fabrication of materials using CVD. Additionally, the process generates toxic gases and material waste due to the use of corrosive, flammable, and hazardous precursors. Essential features for an effective CVD system include the rapid delivery and precise calibration of reactant gases, as well as the necessity for proper substrate annealing to facilitate optimal growth and synthesis. Furthermore, the system must efficiently remove any by-products or residual materials to avoid contamination and ensure the production of high-quality films.

In this thesis, we employed the atmospheric pressure chemical vapor deposition (APCVD) technique to synthesize $SnS_2$ and $MoS_2$, which operates at atmospheric pressure without

necessitating a vacuum environment. The APCVD method is not only cost-effective but also enables the growth of large-area, highly uniform materials while allowing for controlled synthesis following appropriate optimization.

#### 2.1.1.1 Atmospheric Chemical Vapor Deposition Method

APCVD method is conducted at elevated temperatures and atmospheric pressure, making it particularly advantageous for the synthesis of transition metal dichalcogenides (TMDCs). This method is widely utilized to precisely control various characteristics of the grown materials, including the number of layers, flake size, orientation, morphology, heterostructure formation, dopant incorporation, and defect density. These parameters significantly impact the electrical, optical, and catalytic properties of TMDC materials. The manipulation of CVD growth parameters—such as the amount of precursor, growth duration, precursor temperature, distance between precursors, distance from precursor to substrate, and variations between substrates—is crucial for achieving the desired material properties. Consequently, a thorough understanding of these parameters is essential for optimizing the CVD process. Although various CVD techniques exist, the underlying process remains consistent, comprising a series of fundamental steps.

As illustrated in Figure 2.1(a), the initial step in the CVD process involves generating gaseous reactants within the chamber, which is achieved by heating the precursors beyond their melting points. For the synthesis of $MoS_2$, molybdenum trioxide ($MoO_3$) and sulfur (S) powders are utilized as precursors and are subjected to high temperatures that exceed their melting points. These gases can then take one of two pathways: they may either diffuse directly through the boundary layer to adsorb onto the substrate, facilitated by inert carrier gases such as nitrogen or argon (step 2 and step 3) or undergo homogeneous gas-phase reactions that yield intermediate reactants (green spheres) and gaseous by-products (pink spheres) (step 4). In both scenarios, the reactant gases and intermediates adhere to the heated substrate surface and diffuse along it. In the fifth step, the absorbed species diffuse across the heated substrate, initiating surface processes such as surface migration, nucleation, and the formation of crystalline centers. Following this, the sixth step involves the removal of by-products and any unreacted gaseous species from the substrate through convection or diffusion. Finally, in the seventh step, these by-products and unreacted gases are expelled from the CVD chamber via an outlet, completing the deposition process.

The APCVD system features three independent heating zones, each with a distinct temperature profile regulated by a PID controller, capable of achieving temperatures up to 1100 °C., as shown in Figure 2.1 (b). A large quartz tube, measuring 65 mm in diameter and 1200 mm in length, serves as the reaction chamber for the deposition of $SnS_2$ and $MoS_2$ in this thesis.

#### 2.1.1.2 Key Parameters in APCVD Responsible for the Growth of 2D Materials

In this discussion, we examine several critical parameters influencing the growth of $MoS_2$ flakes, including growth temperature, substrate-to-precursor distance, growth time, and carrier gas flow rate. Growth temperature plays a pivotal role in the CVD process, as it significantly affects both the thermodynamics and kinetics of growth. Optimizing the growth temperature is essential for facilitating the precursor reactions on the substrate surface, as even minor fluctuations in temperature can disrupt the interactions between the reactants. The growth temperature also influences the ability of gaseous reactants to reach the substrate and affects the diffusion of these species at the substrate interface. Higher temperatures can enhance the feeding rate at the substrate, resulting in an accelerated growth rate.

The substrate-to-precursor distance is another crucial parameter that must be maintained under consistent growth conditions, such as temperature, gas flow rate, and growth duration. The morphology and dimensions of the resulting film are strongly influenced by this distance. A shorter distance typically leads to a higher nucleation rate, which may result in smaller film sizes. Conversely, an optimized distance can yield larger films with desirable shapes. Therefore, careful optimization of the substrate-precursor distance is necessary.

Growth time is a determining factor for both the thickness and area of the deposited film. Initially, nucleation sites form on the substrate, and as time progresses, these sites grow and

develop into larger film domains. These domains can merge, resulting in the formation of a continuous surface film, while the film's thickness also increases with extended growth time. Consequently, it is vital to optimize growth time to achieve the desired film thickness.

Carrier gas flow rate serves two essential functions during the growth process. Typically inert in nature, carrier gases create a pure inert environment within the CVD chamber, which is crucial for the growth process. Additionally, they facilitate the transport of gaseous species toward the substrate. Therefore, precise control of the gas flow rate is important, as a higher flow rate can enhance growth dynamics by accelerating the transport of gaseous species to the substrate.

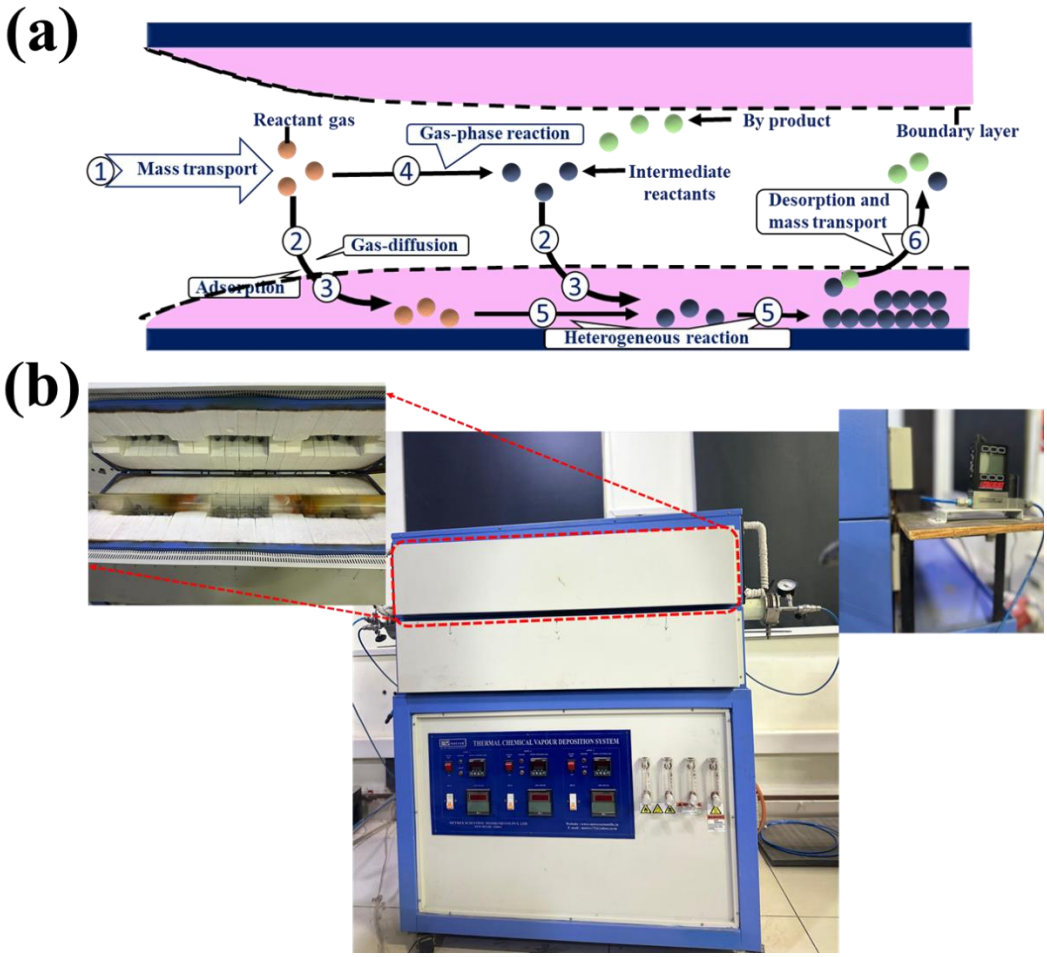



**Figure 2.1:** (a) Schematic illustration of the CVD steps, and (b) Optical images of thermal chemical vapor deposition (CVD) system which is used for this thesis work

### 2.1.2. Magnetron sputtering

Sputtering is a physical vapor deposition (PVD) technique that facilitates the ejection of atoms from a target material through the bombardment of energetic ions. This method is extensively employed for the scalable deposition of thin films onto various substrates. This technique offers several advantages over other physical vapor deposition (PVD) methods, including the capability for large-area growth, uniform film thickness, low-temperature processing, and reduced operational costs. Unlike other PVD techniques, RF sputtering is conducted in a high vacuum environment. A typical sputtering system consists of a process chamber connected to a high vacuum system, an RF power supply, a matching network, a process gas valve, and sample heaters. The RF sputtering system utilizes a 13.56 MHz RF power supply to couple plasma to the insulating material target. For continuous plasma generation, the system frequency must exceed the effective RC time constant, which is adjusted using an impedance matching network. RF power is delivered to the target material through this matching network.

A cleaned substrate is introduced into the process chamber via a load lock assembly, and the vacuum system is activated to minimize contamination risks during the deposition process. To

achieve high vacuum conditions, the system typically employs a turbo molecular pump system, which is supported by a roughing rotary pump. Initially, the rotary pump establishes a rough vacuum of approximately $10^{-2}$ mbar, subsequently serving as a backing source for the turbo molecular pump to reach high vacuum levels around $10^{-7}$ mbar. Once high vacuum is attained, a controlled flow of inert argon (Ar) gas is introduced into the chamber using a mass flow controller (MFC) and a high negative voltage is applied to the target, as illustrated in Figure 2.2 (a). The stray electrons present in the chamber are accelerated and collide with the Ar gas, resulting in the ionization of gas atoms and the formation of plasma. The positively charged Ar ions are then accelerated toward the cathode (target), where they collide with target atoms, leading to the ejection or sputtering of these atoms through momentum transfer. The ejected atoms possess sufficient kinetic energy to traverse the chamber and deposit onto the substrate, thereby forming a thin film[Mattox, 2010]. Additionally, the electrons emitted during the bombardment contribute to sustaining the plasma. A substrate heater and rotation assembly are incorporated to ensure uniform deposition across the sample.

Magnetron sputtering enhances plasma confinement through the application of strong magnetic and electric fields. In this configuration, electrons follow a helical trajectory around the magnetic field lines, which increases the ionization of gas neutrals near the target surface, resulting in a higher plasma density and deposition rate. Sputtering techniques can be categorized into two types: direct current (DC) sputtering and radio frequency (RF) sputtering. In DC sputtering, the target is connected to a direct current power supply, generating a static electric field that accelerates electrons away from the target (cathode). These accelerated electrons ionize the inert gas atoms, and the resulting positive ions erode the target material, with the sputtered atoms subsequently depositing onto the substrate. However, DC sputtering is limited in its ability to deposit insulating and ceramic materials due to the formation of space charge regions that repel incoming Ar ions, leading to plasma loss.

Figure 2.2 (b). depicts the RF sputtering system (Excel Instruments), utilized by the nanosensors research group at IIT Jodhpur, which was employed to deposit nanoparticle of Nobel metal like Au, Ag, Pd, Pt etc., discussed in this thesis. Various depositions were conducted by adjusting parameters such as argon flow, RF power, deposition time, and temperature to optimize the size of nanoparticle for desired device performance. The optical, morphological, and structural properties of the nanoparticle can be influenced by these deposition parameters.

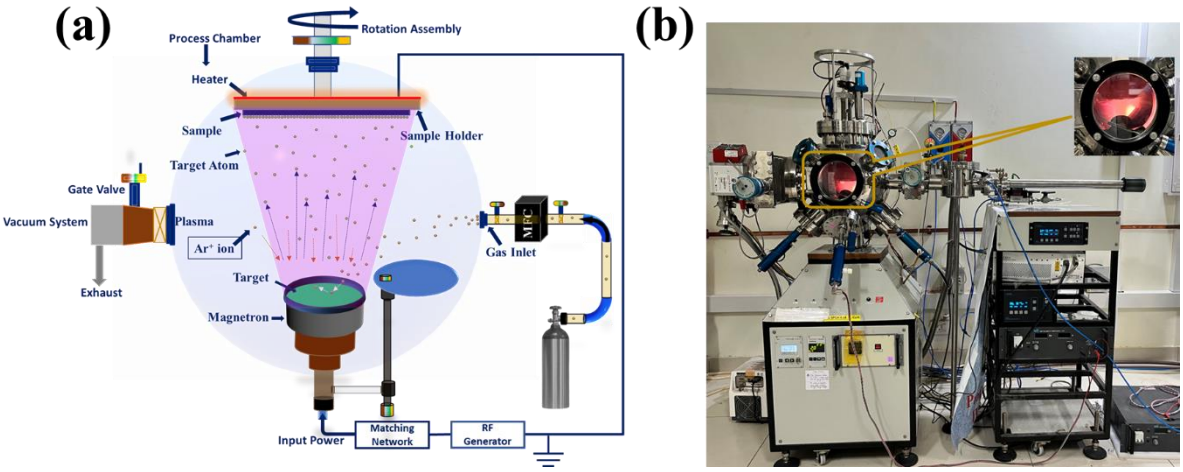



**Figure 2.2:** (a) Schematic representation of the RF sputtering system, and (b) Optical images of sputtering system at the microfabrication lab, IIT Jodhpur.

### 2.1.3. Thermal Evaporation

Thermal evaporation is a prevalent physical vapor deposition (PVD) technique utilized for the deposition of metallic thin films in microfabrication, as well as for semiconductor materials with low melting points. This process occurs in a high vacuum environment, typically exceeding $10^{-6}$ mbar, which enhances the mean free path of material particles, allowing them to deposit on the substrate without colliding and subsequently condensing to form a thin film. The quality of

metal contacts is crucial for the performance of microelectronic devices, and thermal evaporation is an effective method for achieving high-quality metal contacts. The operational principle of the thermal evaporation system, illustrated in Figure 2.3 (a), relies on resistive heating, where a resistive metal filament or boat is powered by an external electrical source to melt the metal chunks intended for evaporation. These boats are typically constructed from materials with high melting points and low reactivity, such as tungsten and molybdenum. A high current is passed through the boats to facilitate the evaporation of the metal in a vacuum, allowing the vaporized particles to travel freely to the substrate and form a thin film. To monitor the thickness of the deposited films, thermal evaporation systems are generally equipped with a quartz crystal thickness monitor. To achieve uniform thickness across large surfaces, a sample rotation assembly is employed. The thermal evaporation technique offers several advantages, including large-area deposition, film uniformity, and minimal contamination during the deposition process.

Thermal evaporation is extensively employed for depositing thin films of metals and metal oxides on various substrates at a wafer scale, with film thicknesses ranging from nm to µm. The process involves heating the material in a heated boat via resistive heating until it vaporizes, with the vapor traveling upward to deposit on the substrate. The high vacuum chamber enhances the mean free path of vapor molecules, ensuring efficient deposition. In this thesis work, the thermal evaporation system was exclusively used for metal deposition to fabricate device electrodes. In the deposition process, the control of metal thickness on the substrate was achieved by adjusting both the current and the deposition duration, where an increase in current led to a corresponding rise in the deposition rate. To ensure uniform metal deposition, substrate rotation was implemented throughout the process. Figure 2.3(b), presents a photographic depiction of the thermal evaporation system utilized for depositing metal contacts in the devices discussed in this thesis. This system is part of the in-house fabrication facility of the nanosensors research group at IIT Jodhpur and is capable of depositing three different materials without breaking the vacuum, facilitating the growth of multilayer structures without exposing the sample to atmospheric conditions. Additionally, a load lock chamber is integrated into the system to reduce processing time. The vacuum system comprises a dry rotary pump coupled with a turbo-molecular pump, and it includes provisions for substrate heating, rotation, and a chiller unit.

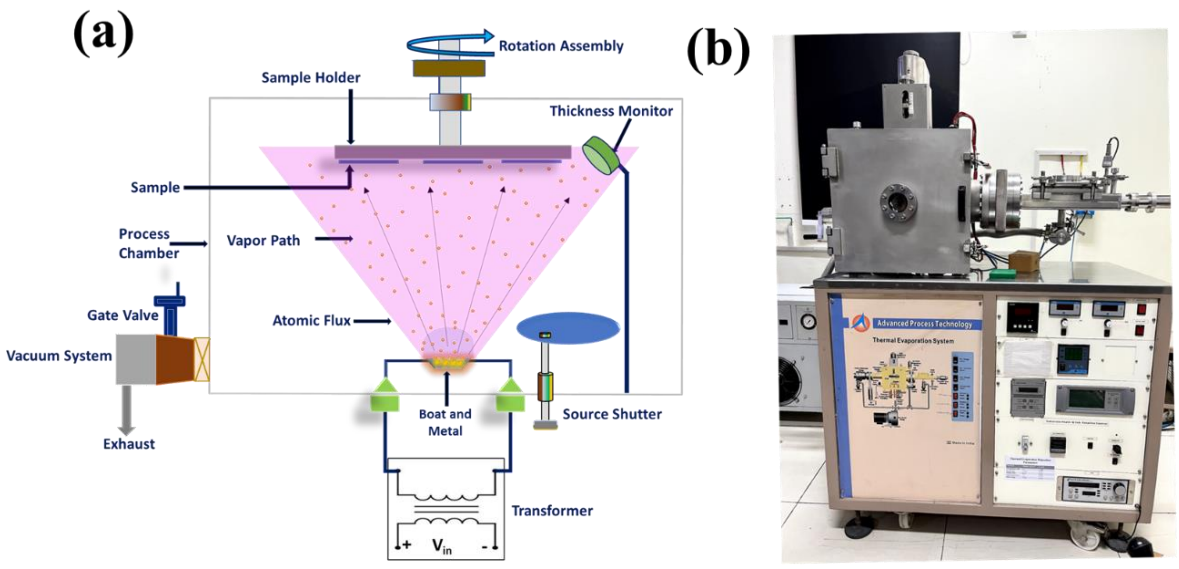



***Figure 2.3:*** *(a) Schematic illustration of the thermal evaporation system, and (b) Optical images of Thermal evaporation system at Microfabrication lab, IIT Jodhpur.*

## 2.2 Characterization Techniques

### 2.2.1. Field Emission Scanning Electron Microscopy (FESEM)

Field Emission Scanning Electron Microscopy (FESEM) is a highly effective surface imaging technique and widely utilized technique for analysing surface morphology, particle size, nanostructure shapes, and the thickness of nanometric thin films. The operational principles of FESEM and Scanning Electron Microscopy (SEM) are largely similar, with the primary distinction being the method of electron emission. SEM employs a thermionic emission gun to generate electrons, whereas FESEM utilizes a field emission electron gun, which produces a focused electron beam across a broad energy range, enabling the acquisition of detailed, high-resolution images of surface features. One notable advantage of FESEM over SEM is its capability to perform imaging at lower potentials, which minimizes charging effects and allows for the examination of non-conductive samples.

In the FESEM process, incident electrons interact with the sample surface, resulting in the emission of backscattered and secondary electrons. These emitted electrons are captured by detectors, which generate surface images. Backscattered electrons provide insights into surface defects and variations within the sample, while secondary electrons contribute to the topographic and morphological characterization of the samples[Dehm et al., 2012]. The schematic representation of FESEM illustrates its operational mechanism, where the field emission gun generates electrons in an ultra-high vacuum environment, as shown in Figure 2.4 (a). The field gradient accelerates these electrons through various electromagnetic lenses, focusing them onto the sample surface. The interaction of the electrons with the sample surface leads to the emission of backscattered and secondary electrons, which are then detected and processed to yield high-resolution images containing detailed sample information.

In this study, the SEM (EVO 18, Zeiss), and FESEM (Apreo-2, Thermo Scientific) available at the central facility of IIT Jodhpur was employed to obtain morphological details of the deposited 2D material. Figure 2.4 (b, c), presents a pictorial representation of the FESEM utilized for the research conducted in this work.

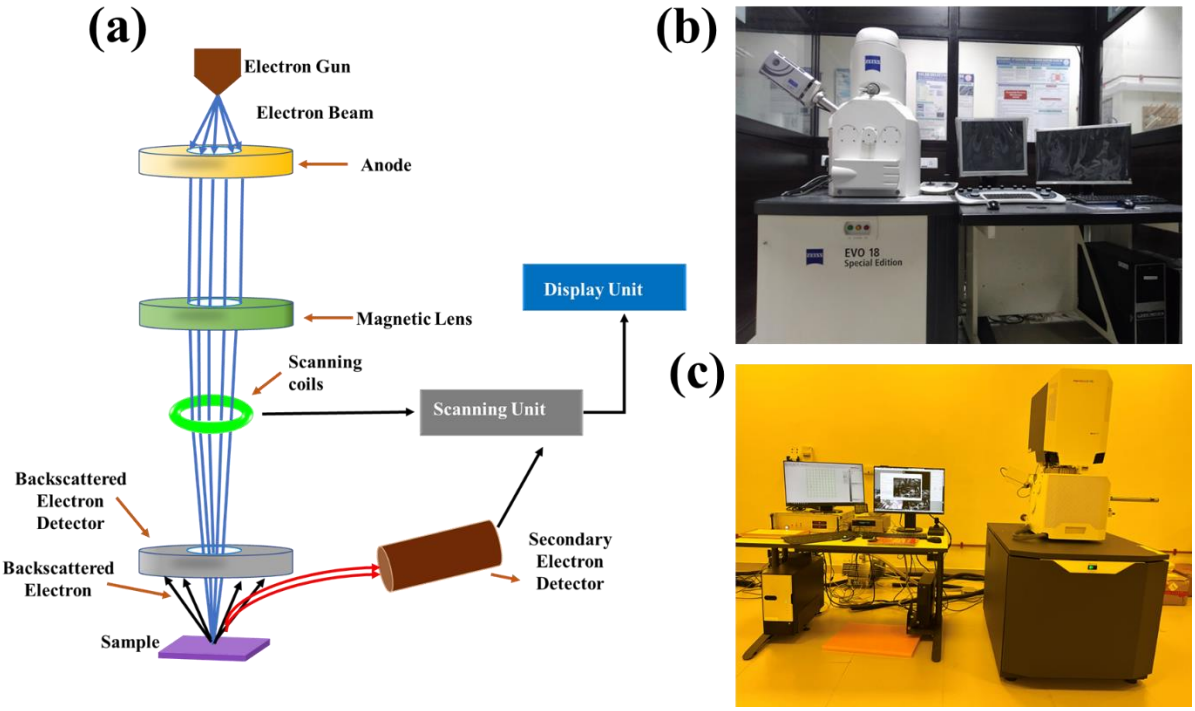



***Figure 2.4:*** *(a) Schematic representation of working of FESEM, and (b) Optical images of SEM and FESEM in central facility IIT Jodhpur.*

### 2.2.2. Energy Dispersive X-Ray Analysis Spectroscopy (EDX)

Energy-Dispersive X-ray Spectroscopy (EDX) is a widely utilized analytical technique for the identification and mapping of individual elements within a sample. Each element possesses a unique atomic structure, resulting in distinct elemental peaks in EDX spectra that serve as a fingerprint for the respective elements. The electron beam, generated by an electron gun, provides surface information about the sample. When the accelerated electrons collide with the sample, they can eject inner-shell electrons from the atoms. Electrons from higher energy states then transition to fill these vacancies, resulting in the emission of characteristic X-rays. These emitted X-rays serve as signatures for specific elemental atoms.

To characterize the elemental composition of the target sample, the energy or wavelength of the emitted X-rays is analyzed. The emitted X-rays are detected by a highly sensitive detector, which generates a charge pulse proportional to the energy of the X-rays. This charge pulse is subsequently converted into a voltage pulse by a charge-sensitive preamplifier, followed by processing through a multichannel analyzer. The voltage measurements correspond to the energy of each emitted X-ray from specific elements, and this data is then transmitted to a computer system for further analysis and evaluation.

### 2.2.3. Raman Spectroscopy

Raman spectroscopy has emerged as a prominent non-destructive technique for investigating two-dimensional materials, providing insights into their vibrational modes, rotational dynamics, and low-frequency behaviors. This spectroscopic method assesses the changes in the polarizability of molecules, which are influenced by factors such as size, shape, and the orientation of the electron cloud.

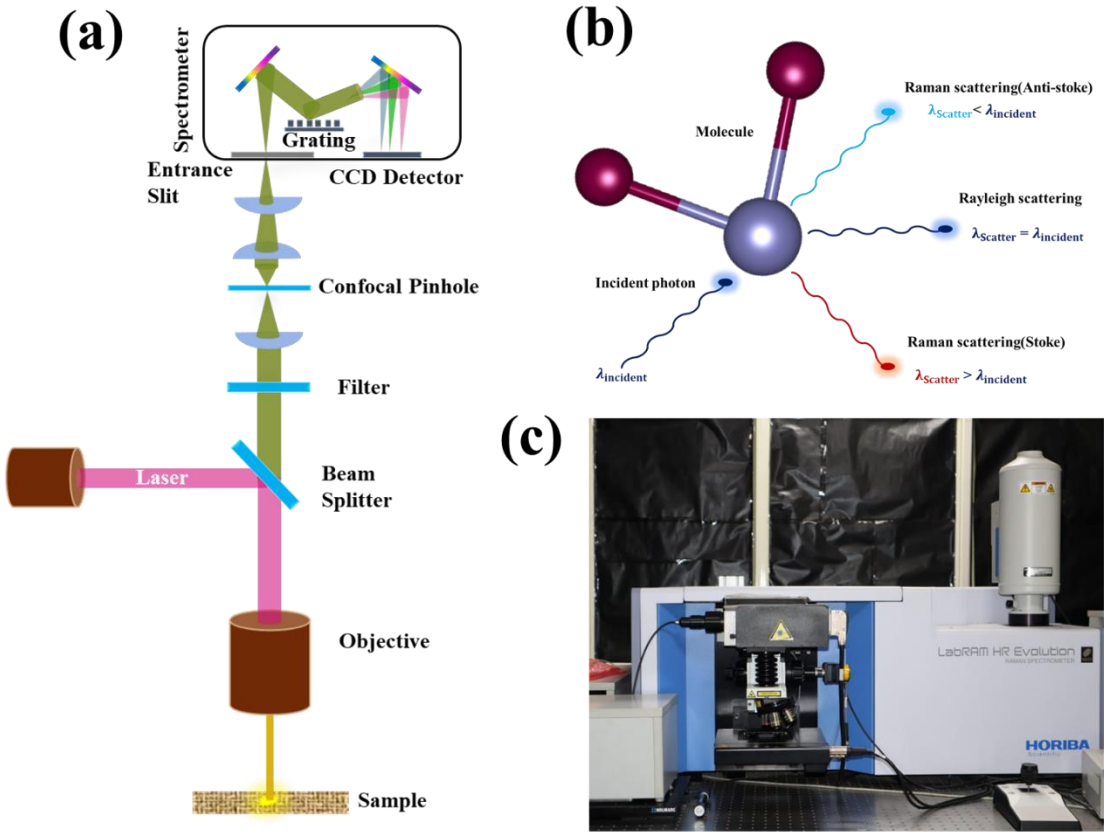



***Figure 2.5:*** *(a) Schematic representation of Working of Raman spectroscopy, (b) Schematic view of the light interaction with the molecule depicting Rayleigh and Raman scattering, and (c) Optical images of Raman Microscope, IIT Mandi.*

When monochromatic visible light interacts with the sample, the majority of the energy is absorbed, while a small fraction experiences a frequency shift due to molecular vibrations. The resulting frequency-modulated signals are detected, yielding information about the vibrational modes present in the sample's molecular structure. During the interaction of incident light with the material, most photons undergo Rayleigh (elastic) scattering, retaining the same wavelength as the incident light[Perkowitz, 2012]. However, a minority of photons scatter at different wavelengths, a phenomenon known as Raman (inelastic) scattering. The energy difference between the incident and scattered photons, termed the Raman shift, provides critical information regarding the vibrational modes and energies of the atoms and molecules within the sample. Stokes scattering occurs when the scattered photons possess lower energy than the incident photons, while anti-Stokes scattering is observed when the scattered photons have higher energy, as shown in Figure 2.5 (b). The schematic representation of the Raman setup, depicted in Figure 2.5 (a), illustrates the focused laser beam directed onto the sample surface through an objective microscope lens, which also collects the backscattered light. A charge-coupled device (CCD) is employed to detect the wavenumbers within the selected spectral range, facilitating comprehensive analysis of the material's molecular vibrations.

As illustrated in Figure 2.5 (c), the Raman spectroscopy apparatus utilized in this study enables detailed analysis of the chemical composition, structure, phases, and polymorphs of the material under investigation.

### 2.2.4. X-ray Photoelectron Spectroscopy (XPS)

XPS is a crucial surface-sensitive quantitative analytical technique employed to assess the elemental composition, chemical and electronic states, and empirical formulas of material surfaces up to a thickness of approximately 10 nm. In this method, X-rays are directed onto the sample's surface, resulting in the ejection of electrons from the material. The kinetic energy of these emitted electrons is subsequently measured by a detector, allowing for the calculation of their binding energy using the following equation:

$$B.E. = h\nu - (K.E. + \emptyset) \tag{2.1}$$

where, B.E. represents the binding energy of the electron, $h\nu$ is the energy of the X-ray photons, $K.E.$ is the kinetic energy of the emitted electrons, and $\emptyset$ is the work function, which varies depending on both the spectrometer and the material[Chastain et al., 1992; Stevie et al., 2020].

XPS operates on the principles of the photoelectric effect, wherein a sample is irradiated with soft X-rays, leading to the emission of photoelectrons from its surface. These emitted electrons are collected and analyzed using an electron energy analyzer to determine their kinetic energy and intensity. The emission of photoelectrons results from the complete transfer of X-ray energy to core-level electrons, and the kinetic energy of these electrons is indicative of the chemical states of the elements present in the sample, facilitating both identification and quantification. The binding energy of the ejected photoelectrons is derived from the aforementioned equation. Given that the average penetration depth for XPS is around 5-10 nm, argon ion etching is often employed to clean the sample surface and eliminate any surface contaminants prior to analysis. This etching process, combined with a series of cycles, allows for the generation of XPS depth profiles, providing chemical information from the top layers down to the substrate. The ejected photoelectrons are directed through a hemispherical electron energy analyzer, which sorts them based on their kinetic energy, yielding elemental and chemical information about the surrounding atoms. The standard XPS penetration depth is approximately 5 nm, utilizing a monochromatic X-ray beam with a diameter ranging from 20 to 500 μm, as illustrated in the schematic representation in Figure 2.6 (a).

In this investigation, X-ray Photoelectron Spectroscopy (XPS) measurements were conducted utilizing a ThermoFisher Scientific Nexsa system, which employs Al Kα X-rays (hν = 1486.86 eV) within an ultrahigh vacuum environment, with the anode operating at 12 kV and 150 W. Prior to conducting elemental scans, survey scans were performed on each sample at a pass energy of 100

eV to obtain a comprehensive overview of the elemental composition. As depicted in Figure 2.6 (b), the XPS apparatus utilized in this research enables detailed analysis of the chemical composition of materials.

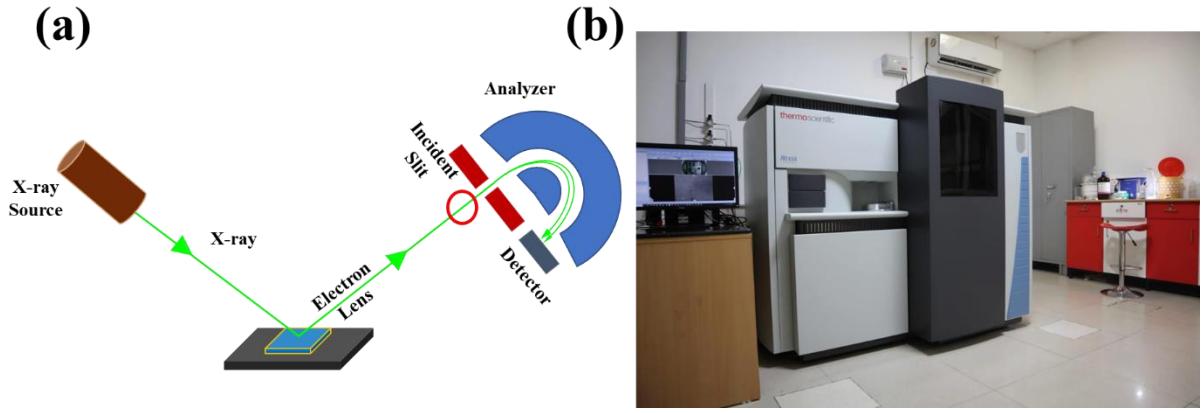



***Figure 2.6:*** *(a) Schematic of the XPS setup, which provides both elemental and chemical detail, and (b) Optical images of XPS system, IIT Mandi.*

### 2.2.5. Photoluminescence Spectroscopy (PL)

Photoluminescence (PL) spectroscopy is a widely utilized, non-contact, and non-destructive technique for examining the optical properties of materials[Perkowitz, 2012]. When incident light with energy exceeding the material's bandgap is directed onto the sample, it is absorbed by electrons, promoting them to excited states. These excited electrons subsequently return to their ground states, releasing energy through either radiative transition, resulting in photon emission, or non-radiative transitions, which generate phonons. The energy emitted during these band-to-band transitions provides critical information regarding the material's bandgap. As illustrated in Figure 2.7, an exciton monochromator is employed to produce monochromatic light, selectively allowing only the desired wavelengths to pass while blocking unwanted light. In this study, PL spectra were recorded at room temperature using a home-built micro-PL/Raman system, which includes a HORIBA iHR 320 Spectrometer equipped with a Synapse CCD, a 532 nm continuous-wave laser, and a 100× objective lens. The excitation was achieved with a 532 nm laser, and the emitted signals were collected in reflection mode, enabling the acquisition of valuable insights into the electronic and luminescent properties of the materials while minimizing sample damage.

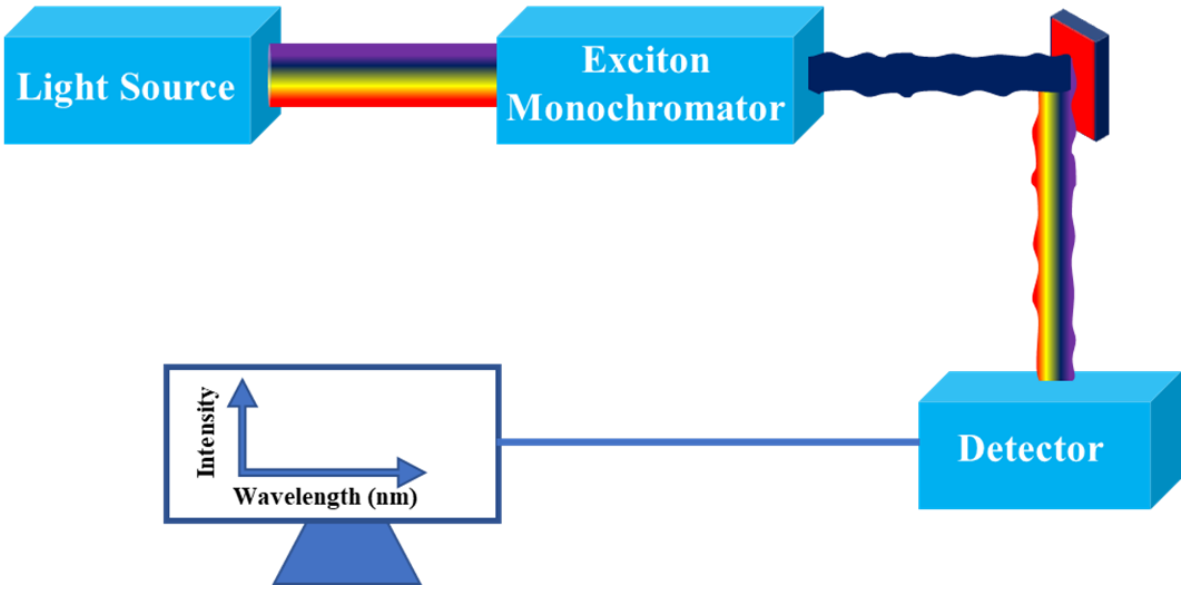



**Figure 2.7:** Schematic of a PL spectroscopy.

### 2.2.6. Ultraviolet-Visible (UV-VIS) Spectroscopy

Ultraviolet-Visible (UV-Vis) spectroscopy is a fundamental and highly effective characterization technique employed to investigate the chemical properties and nature of materials. This method utilizes high-energy light waves within the wavelength range of 200 nm to 800 nm to analyze the interaction between light and matter. When incident light interacts with the sample molecules, electrons transition from lower energy levels to higher energy levels. UV-Vis Diffuse Reflectance Spectroscopy (DRS) is particularly advantageous for obtaining spectra from powder and opaque samples with minimal sample preparation. To facilitate the collection of reflection spectra, an integrating sphere—an optical accessory designed as a hollow enclosure with an internal surface coated with a diffusely reflective material—is employed. This sphere enhances the collection of surface-reflected electromagnetic radiation as a function of frequency, allowing for the generation of reflectance spectra. The analysis of these spectra is performed using the Kubelka-Munk function, which provides insights into the sample's properties. As depicted in Figure 2.8 (a), UV-Vis spectroscopy is utilized for various optical characterizations, including transmittance, absorption, and reflectivity, by measuring the light intensity after it passes through the sample. The UV-Vis setup typically includes a tungsten lamp and a deuterium (D2) lamp as sources for visible and UV light, respectively, along with filters, diffraction gratings, beam splitters, photodiodes, guided mirrors, and a data acquisition system. The diffraction grating and filters effectively separate the incident light into distinct regions: UV, visible, and near-infrared (NIR). A beam splitter directs 50% of the incident light to mirror 3, while the remaining light is directed to mirror 4.

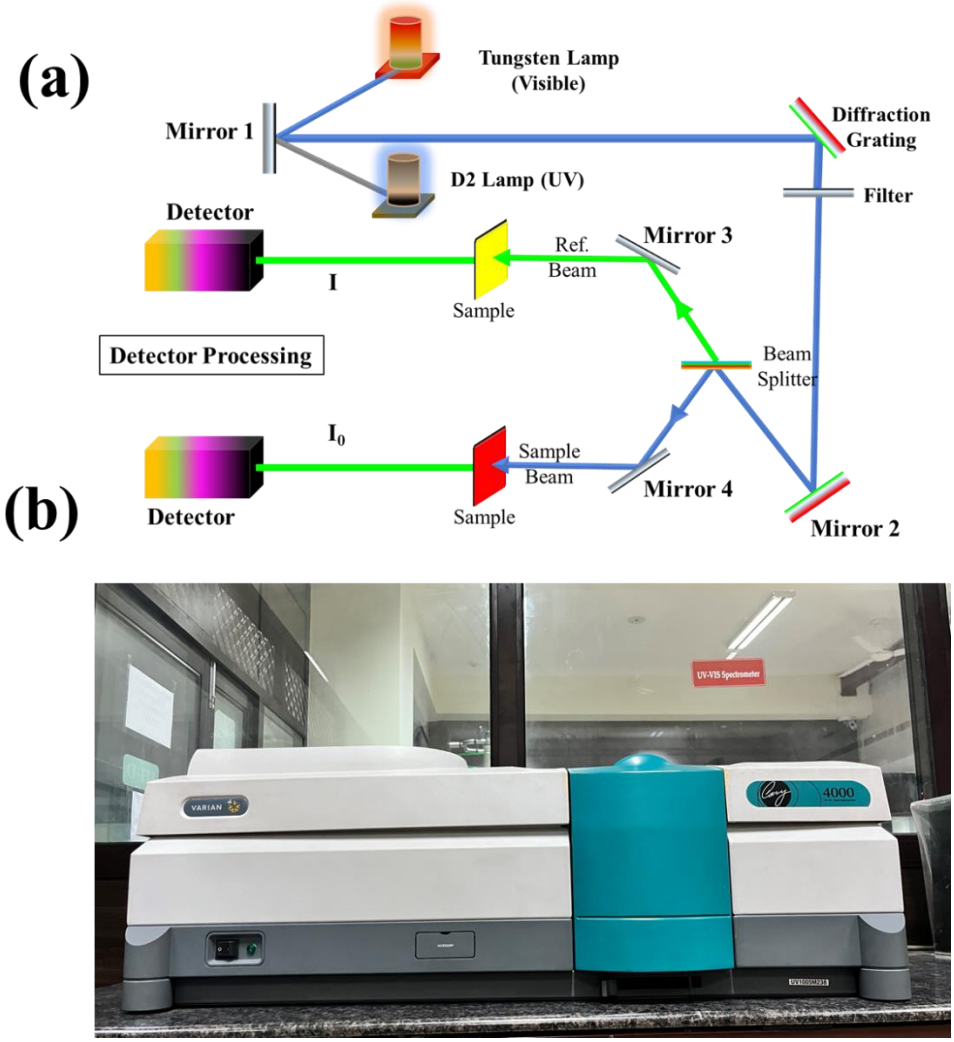



**Figure 2.8:** (a)Schematic representation of a UV-VIS spectrometer, and (b) Optical images of UV-VIS spectrometer, IIT Jodhpur.

In the UV-Vis spectroscopy setup, one portion of the light beam is directed through a reference sample, while the other portion is transmitted through the target sample. The transmitted light intensities for the reference and target samples are denoted as ($I_0$) and ($I$), respectively[Perkampus, 2013]. Photodetectors are employed to capture the transmitted beams, facilitating subsequent data acquisition. The absorption coefficient for a thin film, characterized by its thickness (t) and transmission (T), can be determined using specific equations mentioned below:

$$\alpha = \frac{1}{\tau}\ln\{\frac{1}{T}\} \quad (2.2)$$

The bandgap ($E_g$) can be calculated using equation:

$$(\alpha h\nu)^2 = A\,(h\nu - E_g) \quad (2.3)$$

Here, h, $h\nu$ represent a Planck's constant and is the photon energy.

In this study, we utilized a UV-Vis spectrometer (Cary 4000, Varian) integrated with a Diffuse Reflectance Spectroscopy (DRS) assembly to characterize the powder samples. The UV-Vis spectra of the synthesized materials were obtained across a wavelength range of 200 nm to 800 nm to evaluate the bandgap of the materials. The Figure 2.8 (b), presented illustrates the UV-Vis spectrometer employed during the experimental work, offering a visual representation of the instrumentation used for spectral analysis.

### 2.2.7. X-ray Diffraction (XRD)

X-ray diffraction (XRD) is a fundamental technique employed to ascertain the crystal structure and lattice parameters of crystalline solids and thin films. In addition to these primary functions, XRD yields critical insights into the stress/strain, phase composition, and crystallite size of the materials under examination. A typical XRD system comprises three essential components: an X-ray source, a sample holder, and a detector[Cullity et al., n.d.]. When X-rays are directed at a crystalline material, the electrons within the crystal lattice interact with the incident radiation, resulting in constructive interference at specific angles, known as the Bragg condition. The X-ray source generates both Cu $K_\alpha$ (λ= (0.1504 nm) and Cu $K_\beta$ radiation, with a nickel filter positioned at the X-ray tube opening to block unwanted Cu $K_\beta$ radiation. The detector is maneuvered around the sample at varying 2θ angles to capture the diffracted X-rays, as shown in Figure 2.9 (a).

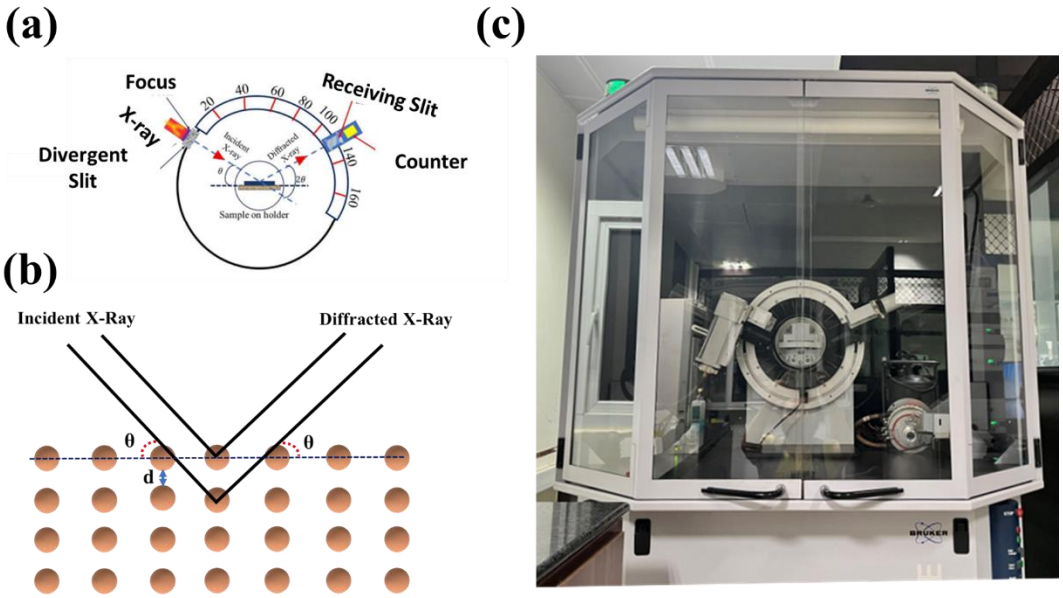



**Figure 2.9:** (a) Schematic for the X-ray diffraction used to study the crystal structure of the film, (b) Diagram of Bragg's law for X-ray diffraction, and (c) Optical images of X-ray diffraction system (D8 Advance, Bruker) at IIT Jodhpur.

The incident X-rays interact with the sample, leading to constructive interference, which is fundamental to the analysis. Bragg's equation serves as the essential criterion for achieving constructive interference in X-ray diffraction, is expressed as follows:

$$n\lambda = 2dsin\theta \qquad (2.4)$$

where d is the lattice spacing, n is the order of diffraction, λ is the wavelength of the X-ray, and θ is the angle of diffraction with respect to the crystal planes, respectively.

The condition for constructive interference is defined by the integer n=1 (Pillai (2015)). Figure 2.9 (b), illustrates the law of diffraction, which aids in the comprehension of Bragg's law and facilitates the determination of lattice spacing (d) by utilizing known parameters from the equation. In this thesis, the X-ray diffraction system employed to analyze the structural properties of the synthesized $SnS_2$ and $MoS_2$ films is the D-8 Advanced model from Bruker, as shown in Figure 2.9 (c). This system is part of the central facility at IIT Jodhpur and utilizes a copper source to generate X-rays with a wavelength of Cu $K_\alpha$ = 1.54 Å.

### 2.2.8. Kelvin probe force microscopy (KPFM)

KPFM is a sophisticated scanning probe microscopy technique that enables high-precision measurements of local variations in a material's work function with nanometer-scale resolution. This technique operates in a non-contact mode and is capable of quantifying the contact potential difference (CPD) between the probe tip and the sample. The local contact potential difference (LCPD) is influenced by short-range interactions between the tip and the sample [Melitz et al., 2011]. KPFM effectively detects and maps these LCPD variations, yielding critical insights into the electrical properties of the material. The operation of KPFM involves aligning the Fermi levels of the sample and the tip as they approach each other, which leads to electron transfer between the two materials. This electron flow results in a shift in the vacuum levels and generates a CPD between the sample and the tip. Figure 2.10 (a), depicts the energy level alignment between the tip and the sample in the absence of electrical contact, while the alignment of the Fermi levels and the resulting vacuum level offset following electrical contact. The contact potential difference ($V_{CPD}$) is determined using equation (2.5).

$$V_{CPD} = \frac{\emptyset_t - \emptyset_s}{q} \qquad (2.5)$$

where, q, $\emptyset_t$ and $\emptyset_s$ are the elementary charge and work function of the tip and sample, respectively.

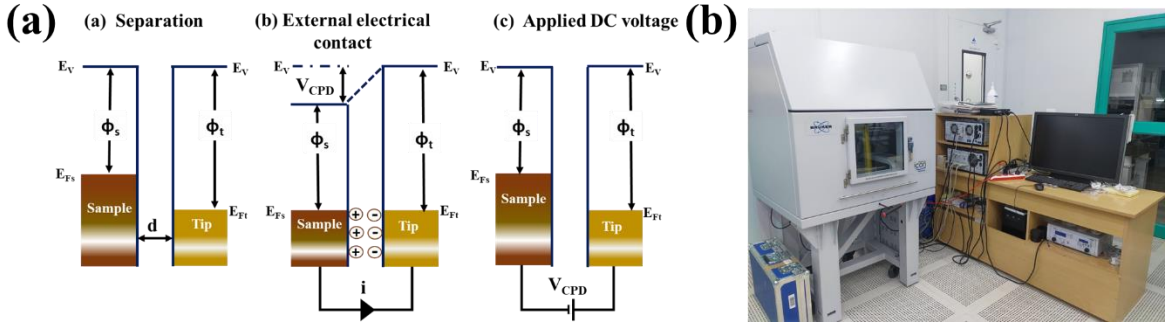



**Figure 2.10:** (a) Schematic view of band alignment between the sample and the tip in a typical KPFM set-up under different conditions: Non-contact, External electrical contact, Applied DC voltage, and (b) Optical images of KPFM system at IIT Mandi.

The induced contact potential difference ($V_{CPD}$) generates an electrical force that can be counteracted by applying a DC voltage of opposite polarity between the tip and the sample. This counteracting voltage corresponds to the difference in work function between the tip and the sample, enabling the determination of the sample's work function when the work function of the

tip is known [12]. In this study, atomic force microscopy (AFM) images were acquired using an Agilent 5500 scanning probe microscope. KPFM measurements were conducted through amplitude modulation with a Budget Sensors Cr/Pt-coated Multi 75-EG tip, which has a force constant of 3 N/m and a resonance frequency of 75 kHz. The electrostatic force between the tip and the sample was generated by the electrical oscillation of the tip, which was nullified by applying a DC offset to the scanning tip. Additionally, a Dolan-Jenner MI-150 Fiber Optic Illuminator was utilized to provide illumination during the KPFM measurements.

The Figure 2.10 (b), presented illustrates the KPFM system employed during the experimental work, offering a visual representation of the instrumentation used for spectral analysis.

## 2.3 Plasma treatment

The behavior of plasma is profoundly influenced by electric and magnetic fields because of its charged characteristics. To create this plasma environment, a gas may be energized through the application of electrical energy and magnetic fields, or it can be heated to a temperature high enough to detach at least one valence electron from its atoms. This ionization process is distinct from ion beam sources, in which charged ions are extracted from discharge plasma to form an accelerated beam. Nonetheless, the overall energy input from the charged and excited species in the plasma can be controlled based on various factors, including the plasma source type, its configuration, and process parameters such as power input, the range of applied fields (e.g., microwave, radio frequency (RF), or direct current (DC)), gas flow rate, the type of process gas utilized, and treatment duration. In recent decades, a variety of gases including argon, oxygen, nitrogen, fluorine, carbon dioxide, and water vapor have been employed as process gases for plasma generation in numerous applications, due to their ability to introduce distinct reactive species, ions, and radicals to surfaces.




**Figure 2.11:** (a) Optical images of RF Plasma chamber.

In this thesis, plasma treatment was conducted within the stainless-steel sample preparation chamber (with a base pressure of $<10^{-2}$ mbar) at room temperature, as seen in Figure 2.11 The apparatus was constructed utilizing two parallel plate electrodes. The sample designated for treatment was placed inside a standard Pyrex enclosure, allowing the working gas to flow through the area between the electrodes, facilitated by a mass flow controller (MFC). The electrodes were linked to a power supply, and the exhaust gas was channeled through plastic tubing to a fume hood. The chamber underwent evacuation through the utilization of a double storage rotary vacuum pump. The RF generator functioned at the conventional industrial frequency of 13.56 MHz. The sample was positioned between the electrodes, and a glow discharge plasma was generated at a pressure of $3 \times 10^{-2}$ mbar utilizing nitrogen gas within the laboratory batch reactor. After treatment, the sample was transferred to the analysis chamber without exposure to ambient air.

## 2.4 Device fabrication and characterization

### 2.4.1. Deposition of Metal Contact Using Thermal Evaporation

Thermal evaporation is a widely utilized physical vapor deposition technique for the deposition of metal contacts. In this process, the substrate is positioned upside down within the sample holder of the evaporation chamber, while alumina-coated molybdenum boats are employed to evaporate the metal. The boats are heated by passing a high current through them via a step-down transformer, which facilitates the evaporation of the metal and its subsequent deposition onto the substrate to form electrodes. Achieving a high vacuum environment, typically in the range of $10^{-6}$ to $10^{-7}$ mbar, is crucial for ensuring high-quality electrode deposition. This vacuum minimizes contamination from background gases and moisture, providing a large mean free path that reduces molecular collisions and allows for direct impacts of metal atoms on the substrate. The geometry and dimensions of the deposited electrodes are defined by the shadow mask utilized during the deposition process. In this thesis, two distinct physical shadow masks were employed, as illustrated in Figure 2.12.

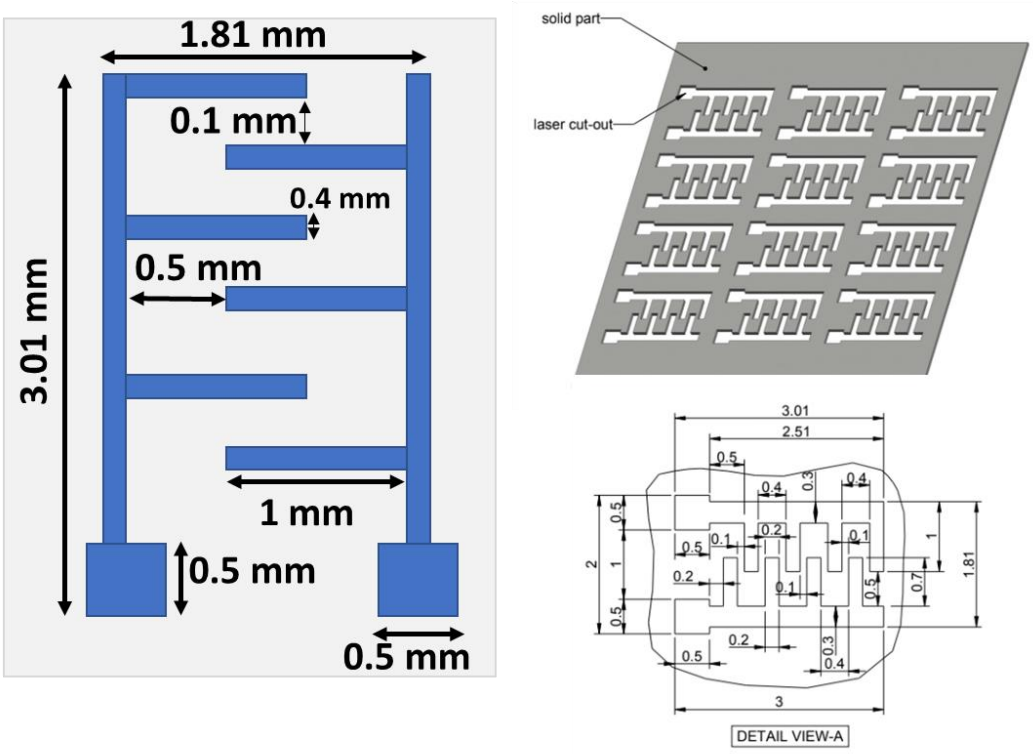



**Figure 2.12:** Interdigitated electrode physical shadow mask used for electrode deposition.

### 2.4.2. Gas Sensing Measurement

Gas-sensing measurements were conducted within a vacuum-sealed chamber to prevent interference from external gases. Figure 2.13, illustrates the gas sensing setup utilized in this thesis. Following the fabrication of the sensor devices, all units were positioned within this setup to conduct gas sensing experiments. There are two primary methodologies for assessing the gas sensing properties of any device: (1) Dynamic gas sensing and (2) Static gas sensing. In dynamic gas sensing, the device is continuously exposed to a specific gas concentration, which is then evacuated from the opposite side of the gas chamber. Conversely, static gas sensing involves placing the device in a sealed gas chamber, where the target gas concentration is introduced, allowing the gas to saturate the device before being expelled from the chamber. The gases investigated, including $NO_2$, $NH_3$, $CO_2$, CO, $H_2$, $CH_4$, and $H_2S$, were diluted with pure Ar gas, and the desired concentration was achieved by mixing $N_2$ with the target gas. The fabricated sensing device was positioned on a sample stage inside the chamber, with two probes facilitating electrical measurements. The sample stage's temperature was regulated using a PID controller to ensure a constant temperature during the experiment. The sensor's performance was assessed with a computer-controlled Keithley 2636 B. A micro-syringe was employed to introduce the target gas into the sensing chamber, which had a volume of 3.5 liters, allowing for precise injection of a known volume of the target gas (in milliliters) into the chamber. The gas concentration was determined using equation (2.6).

$$Gas\ concentration\ in\ (ppm) = \frac{Gas\ taken\ in\ Syringe\ (ml)}{Volume\ of\ sensing\ chamber\ (ml)}\ X\ Gas\ in\ cylinder\ (ppm) \qquad (2.6)$$

Gas sensing experiments were performed across a wide temperature spectrum, extending from 0 to 200 °C, while ensuring that relative humidity remained constant. A high-accuracy humidity sensor (SHT31-APR, Sensirion AG, Switzerland) was utilized to continuously monitor the relative humidity throughout the duration of the experiments. This experimental configuration facilitated meticulous regulation of both temperature and humidity parameters during the sensing evaluations, thereby allowing for a thorough and accurate assessment of the sensor's performance.

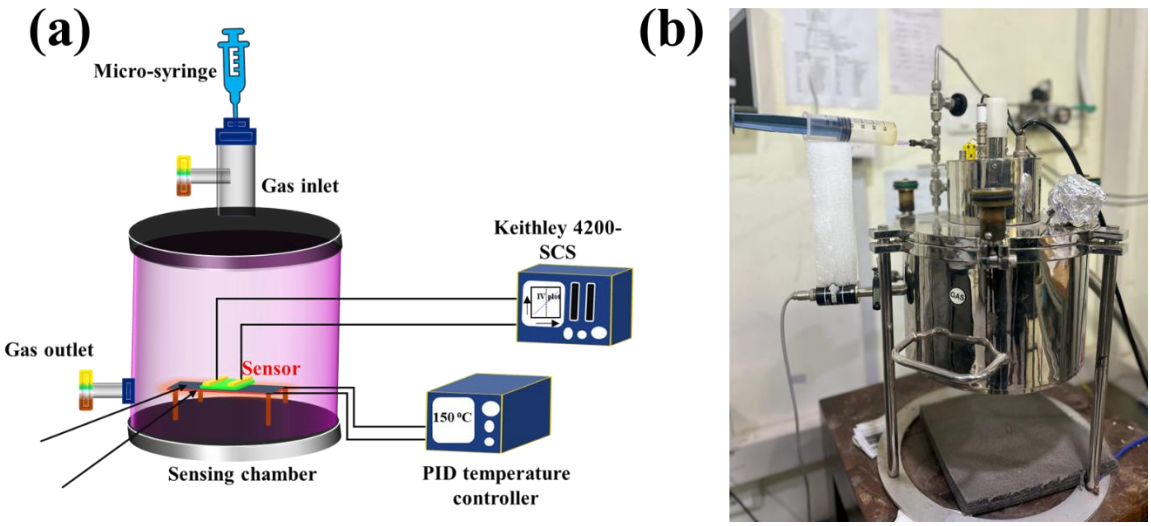



**Figure 2.13:** (a) Schematic illustration of gas sensing setup, and (b) Optical Image of the gas sensing system, which is used for this thesis work.

### 2.4.3. Photodetector measurement

The evaluation of the performance of the $MoS_2$-based photodetectors was conducted through photoresponse testing, employing the Holmarc Photodetector setup (SQR200F). This setup features a monochromator equipped with a 180 W xenon arc lamp, a lock-in amplifier, and a chopper connected to a sub-femtoamp sensitive Keithley-6430 Source Measure Unit (SMU).

Figure 2.14 presents the schematic representation of the monochromator configuration. The monochromator was utilized to assess the photodetector responses across a wavelength spectrum of 400 to 2500 nm. The optical power for various incident wavelengths was calibrated using a standard silicon photodiode (UV-VIS-NIR, 250-1100 nm), featuring a precisely sized square photosensitive area of 5.8 x 5.8 mm². This calibration was essential for ensuring accurate measurements of the photodetector devices. Measurements within the ultraviolet range were performed using surface-mounted light-emitting diodes (LEDs) emitting at wavelengths of 254 nm and 365 nm, delivering an intensity of 1 mW/cm². All device measurements were conducted under ambient conditions within an optically sealed chamber to eliminate interference from external light sources. All measurements were conducted at room temperature.

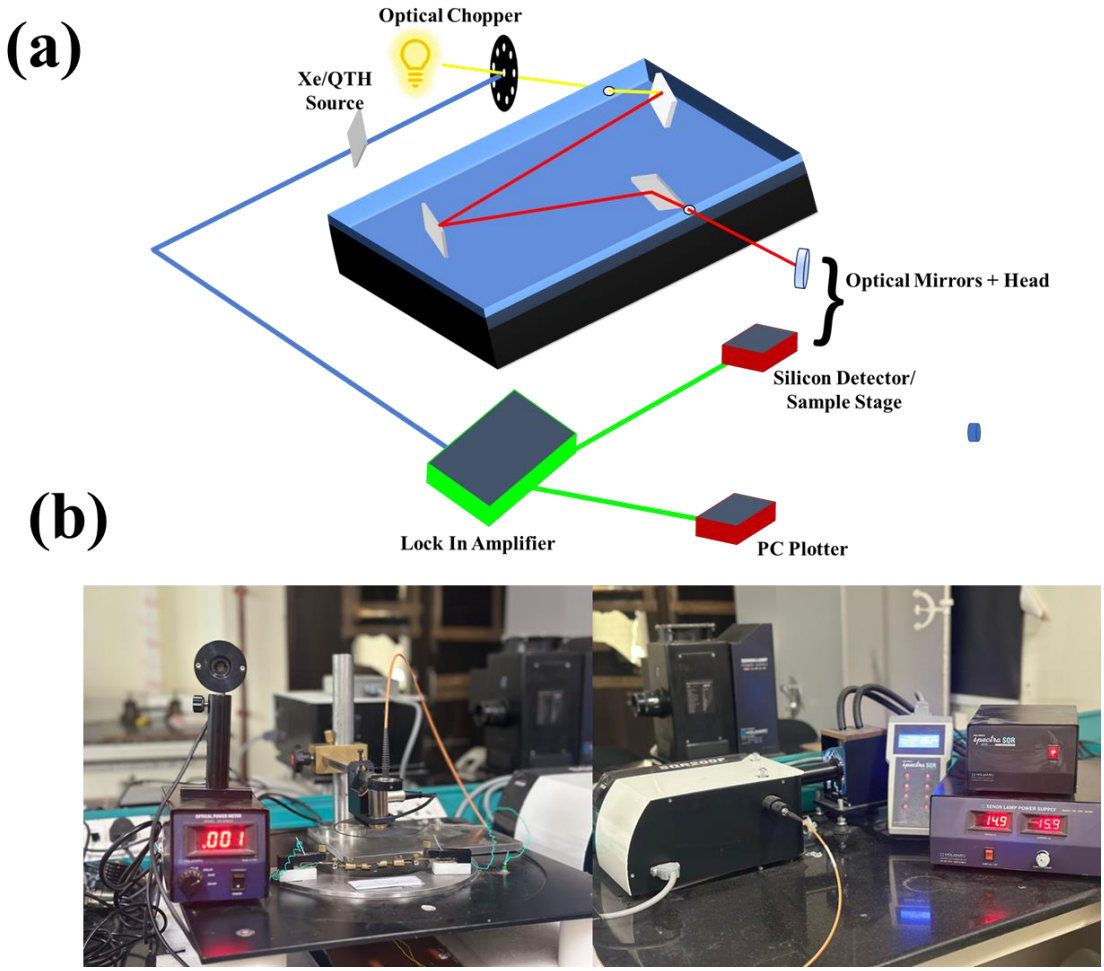



**Figure 2.14:** (a) Schematic representation of the experimental setup used to measure spectral response of $MoS_2$ based photodetectors, and (b) Optical Image of the photodetector system, which is used for this thesis work.

# 3
# Growth and characterization of $MoS_2$ and $SnS_2$ flakes

This chapter explores the controlled growth of $MoS_2$ and $SnS_2$ flakes, transitioning from in-plane structures to vertically aligned, edge-enriched flakes through a thermal chemical vapor deposition (CVD) technique. This controlled and tunable growth of chemically active edge sites is crucial for enhancing the catalytic activities of these materials across a wide range of applications. From a thermodynamic perspective, the formation of inert in-plane $MoS_2$ and $SnS_2$ is typically favored due to their limited active sites compared to edge sites. This study demonstrates that by varying the gas flow rate during the CVD process, it is possible to achieve a transition from in-plane flakes to a dense, electrically connected 3-D network of $MoS_2$ and $SnS_2$ flakes. The results indicate that increasing the gas flow rate leads to a higher density of these vertically aligned structures. Raman spectroscopy analysis confirms that the synthesized $MoS_2$ and $SnS_2$ flakes consist of a few layers. The proposed growth mechanism suggests that in-plane $MoS_2$ and $SnS_2$ serve as seed layers for the initial growth of vertically aligned flakes, which ultimately results in the formation of an interconnected 3D network. Additionally, the chapter presents a novel method for fabricating Au/Cr interdigitated electrodes (IDE), which are essential components for gas sensors and photodetector platforms that utilize 2D materials. These IDEs were fabricated using a thermal evaporation system combined with a physical mask, showcasing an innovative approach to integrating these materials into functional device

## 3.1 Necessity and Challenges for Controlled growth of $MoS_2$ and $SnS_2$ Flakes

The atomically thin monolayer transition-metal dichalcogenides (TMDCs), specifically $MoS_2$ and $SnS_2$, have garnered significant attention in scientific research due to their exceptional electronic, optical, and chemical characteristics, which distinctly contrast with those of their bulk materials and other 2D materials. For example, $MoS_2$ is well-suited for use in solar cells, optoelectronics, gas sensor, and high-performance nano-electronic devices due to its direct band gap of 1.8 eV. Furthermore, $MoS_2$ exhibits potential in catalytic roles, such as ultra-sensitive sensors, hydrogen generation, and electrochemical catalysis. Its promise as a noble-metal-free electrocatalyst for gas sensor and photodetector, as boosting its catalytic prowess hinges on maximizing the presence of active edge sites. Nonetheless, the thermodynamic inclination for in-plane growth restricts the availability of these active sites, creating a demand for controlled growth techniques to amplify the density of vertically oriented $MoS_2$ flakes.

In a similar vein, $SnS_2$, another noteworthy 2D material, reveals immense potential across varied applications, including gas sensors and photodetectors. With an indirect bandgap spanning from 2.18 to 2.44 eV and impressive carrier mobility, $SnS_2$ stands as an eco-friendly n-type semiconductor. Its elevated optical absorption coefficient in the visible spectrum further bolsters its applicability in light detection technologies. The fabrication of high-quality, large-scale 2D $SnS_2$ is crucial for its industrial viability; however, obstacles persist in managing the dimensions, uniformity, and crystallinity of the nanoflakes.

Both $MoS_2$ and $SnS_2$ can be produced through an array of methods, with chemical vapor deposition (CVD) emerging as the most promising for attaining high-quality nanoflakes. CVD permits meticulous control over growth parameters, which is vital for fine-tuning the morphology and structural attributes of the materials. While considerable strides have been made in the CVD synthesis of ultrathin MoS2 and $SnS_2$ nanoflakes, challenges remain. For $MoS_2$, the transition from in-plane to vertically aligned structures have not been extensively documented, constraining the comprehension of their growth processes and potential roles in gas sensing and photodetection. In the case of $SnS_2$, achieving selective synthesis of pure phases proves intricate due to the varying sensitivities of distinct crystal phases to growth conditions.

Furthermore, the performance of $MoS_2$ and $SnS_2$-based gas sensor frequently suffers from inadequate responsivity and sluggish response times, which impede their real-world

applicability. Thus, a unified effort is essential to devise controlled growth methodologies for both $MoS_2$ and $SnS_2$ that yield high-quality, pure-phase nanoflakes. Tackling these challenges will be vital for unlocking the full spectrum of possibilities presented by these materials in gas sensing, light detection, and beyond. By honing in on the controlled synthesis of $MoS_2$ and $SnS_2$, researchers can illuminate pathways for pioneering applications that capitalize on the extraordinary properties of these 2D materials, ultimately fostering advancements in environmental monitoring, energy conversion, and the next wave of electronic devices.

## 3.2 Growth of $MoS_2$ and $SnS_2$ Flakes by CVD Method

### 3.2.1. Synthesis of $MoS_2$ Flakes

In this research endeavor, 2D $MoS_2$ flakes were synthesized utilizing two solid precursors, specifically molybdenum trioxide ($MoO_3$) and sulfur (S), via a three-zone chemical vapor deposition (CVD) technique facilitated by a two-inch diameter apparatus, as shown in Figure 3.1 (a). Prior to the growth phase, the $SiO_2$/Si substrates underwent a rigorous chemical cleaning process. Within this conventional synthesis framework, an alumina boat containing 1 grams of sulfur powder (99.99%, Sigma-Aldrich) was positioned in the first zone, while a separate alumina boat containing 0.03 grams of $MoO_3$ powder (99.9%, Sigma-Aldrich) was strategically placed in the second zone (central), situated 15 cm away from the first zone. Initially, the tube was evacuated to a base pressure of 10 mTorr and subsequently purged two to three times with ultra-high-purity argon gas (200 sccm) to eliminate oxygen and other potential contaminants from the system. Following this purging process, the rotary pump was deactivated, and purging with argon (200 sccm) continued until atmospheric pressure was attained. During this interval, the temperatures in the second and first zones were maintained at a constant 100 °C and 30 °C, respectively. Thereafter, the temperature was elevated at a heating rate of 16 °C per minute until it reached 650 °C, after which the rate of increase was adjusted to 25 °C per minute from 650 °C to 850 °C for $MoO_3$. The temperature of sulfur was sustained at 30 °C until the temperature of $MoO_3$ attained 700 °C, at which point the temperature was rapidly escalated to 200 °C, are presented in figure 3.1 (b). During the growth period, the temperature in zone 3 ascended to 350 °C as a result of thermal conduction from zone 2 to zone 3. High-quality $MoS_2$ was synthesized by annealing $MoO_3$ at 850 °C for 45 minutes under atmospheric pressure with an argon flow rate of 80 sccm, with the $SiO_2$/Si substrate positioned face down on the $MoO_3$. Ultimately, the furnace was switch off, and the tube was permitted to cool naturally to ambient temperature.

To enhance the growth parameters of $MoS_2$, we methodically altered both the evaporation temperature of $MoO_3$ and the flow rate of argon gas. The nomenclature associated with the synthesized samples is illustrated in figure 3.1 (c, d). Initially, the temperature was fine-tuned by performing experiments at 750°C ($MoS_2$-750), 800°C ($MoS_2$-800), 850°C ($MoS_2$-850), and 900°C ($MoS_2$-900), while maintaining a constant argon gas flow rate of 80 sccm. After determining the optimal temperature, the influence of the argon gas flow on the growth of $MoS_2$ was examined by adjusting the flow rates to 60 sccm ($MoS_2$-60), 80 sccm ($MoS_2$-80), 100 sccm ($MoS_2$-100), and 120 sccm ($MoS_2$-120), while maintaining fixed temperatures of 850 °C for zone 1 and 200 °C for zone 2, respectively. This methodology enabled us to explore the interaction between temperature and gas flow, yielding valuable insights into the parameters that facilitate the controlled growth of high-quality $MoS_2$.

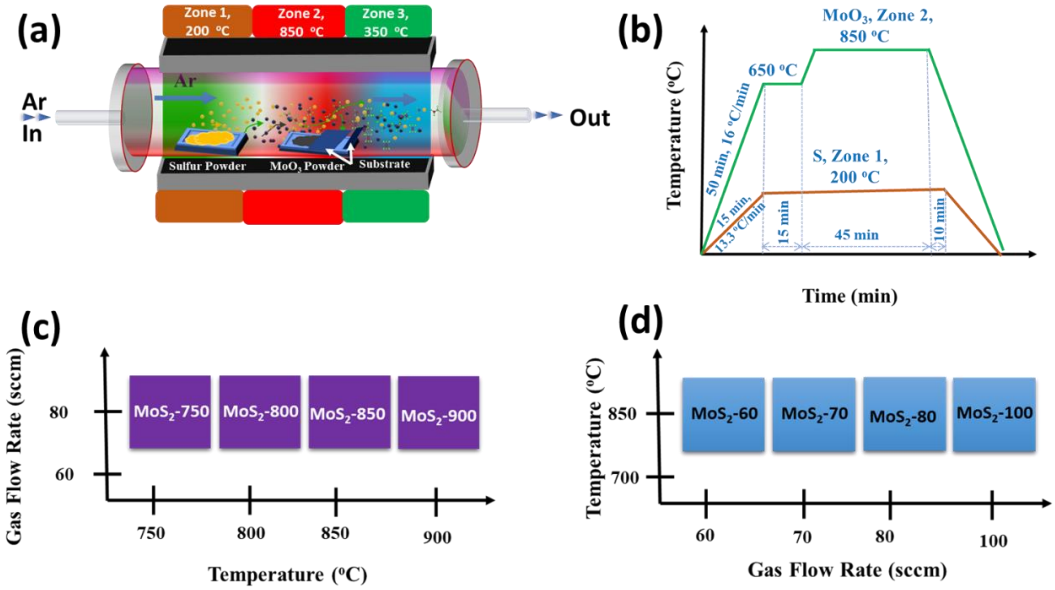



**Figure 3.1:** (a) Schematic of thermal chemical vapor deposition (CVD) technique used to grow $MoS_2$ flakes. $SiO_2$/Si substrate was placed on top of $MoO_3$ powder in zone 1, (b) temperature profile for $MoO_3$ and S powders in Zone 1, Zone 2, respectively and (c, d) Show the different growth conditions and nomenclatures of synthesized samples.

### 3.2.2. Characterizations of $MoS_2$ Flakes

We systematically optimized the growth parameters for $MoS_2$ flakes produced via a chemical vapor deposition (CVD) method, emphasizing the interplay between growth temperature and argon flow rate. The results obtained from scanning electron microscopy (SEM) demonstrated pronounced morphological variations in the $MoS_2$ flakes contingent upon these specific variables. At an argon flow rate of 80 sccm and a growth temperature of 850 °C, isolated $MoS_2$ flakes enriched at the edges were discerned, signifying optimal conditions for the establishment of active sites. Subsequent examination of the growth temperature, as illustrated in Figure 2, revealed that an incremental increase in temperature from 750 °C to 900 °C in intervals of 16 °C elicited a significant transformation in the morphology of the $MoS_2$ flakes. At lower thermal conditions (750 °C and 800 °C), the flakes manifested a dendritic structure, reflective of sulfur-rich growth environments, characterized by diminutive domain sizes and elevated nucleation densities. Conversely, upon elevating the temperature to 850 °C, a substantial enlargement in domain size accompanied by a reduction in nucleation density was noted, thereby facilitating the generation of larger, more continuous films with distinctly defined grain boundaries.

To further elucidate the impact of growth temperature on nucleation density and flake dimensions, we undertook experiments at 750 °C, 800 °C, 850 °C, and 900 °C, intentionally excluding sulfur from the synthesis protocol, as shown in Figure 3.2. The findings revealed that at 750 °C, a paucity of nucleation sites was evident, while at 800 °C, a significantly high nucleation density was recorded alongside exceedingly small seed sizes. As the temperature ascended to 850 °C, a decline in nucleation density was observed, accompanied by an increase in seed sizes, which culminated in the formation of larger $MoS_2$ regions. This observed trend was substantiated by SEM image, which indicated that the $MoS_2$ flakes synthesized at 850 °C exhibited a more uniform distribution and interconnectedness, thereby constituting a 3-D network. In stark contrast, the $MoS_2$ flakes cultivated at 900 °C displayed larger dimensions yet a diminished density, thereby underscoring the inherent trade-off between flake size and density.

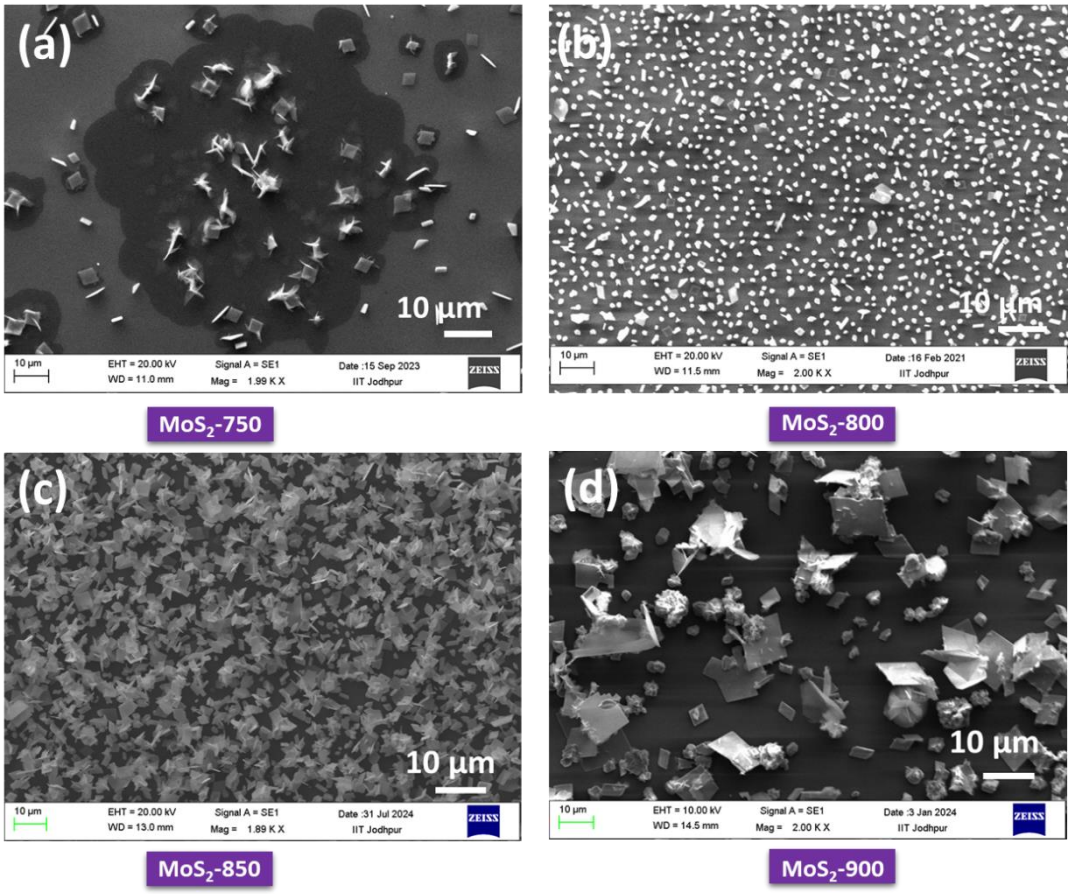



**Figure 3.2:** SEM images of $MoS_2$ flakes grow at different deposition temperature (a) 750 °C, (b) 800 °C, (c) 850 °C, and (d) 900 °C. The flow of argon of 80 sccm keep constant during the growth.

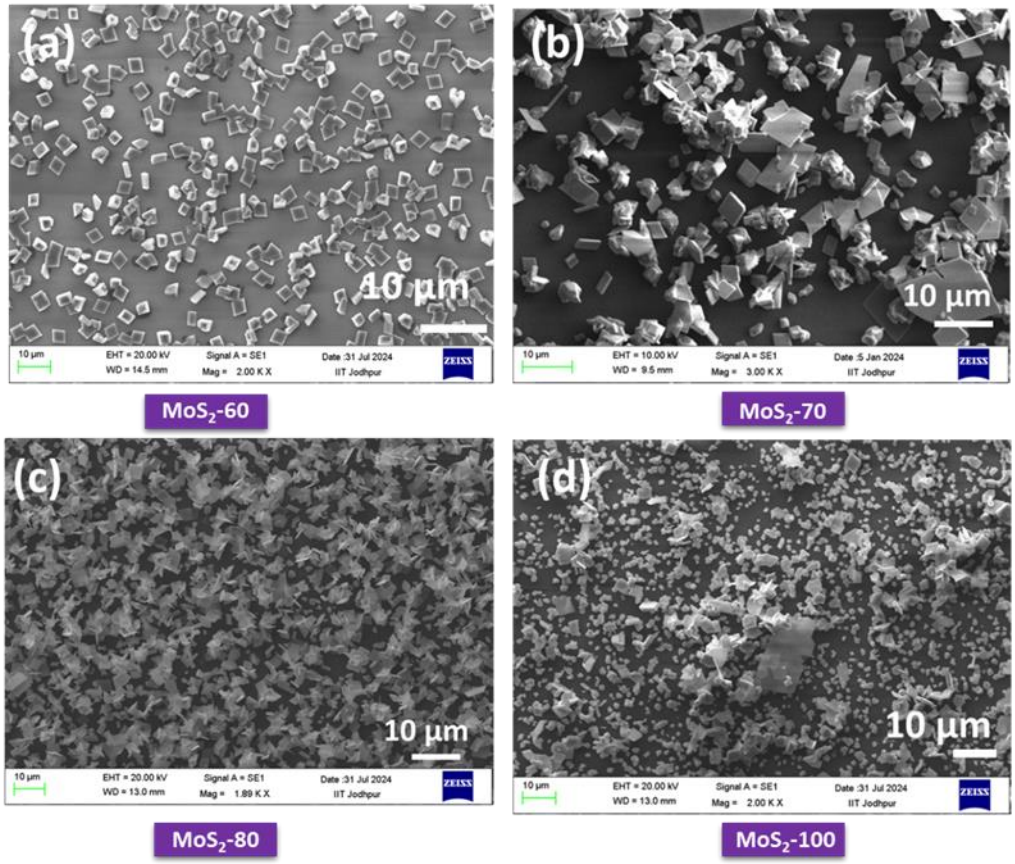



**Figure 3.3:** SEM images of $MoS_2$ flakes grow at different gas flow rates (a) 60 sccm, (b) 70 sccm, (c) 80 sccm and (d) 100 sccm. The growth temperature for all these samples was fixed at 850°C.

Moreover, we investigated the effect of varying argon flow rates, while maintaining a constant growth temperature of 850 °C and a sulfur temperature of 200 °C. As the argon flow rate was incremented from 60 sccm to 100 sccm, a notable enhancement in the lateral dimensions of the flakes was observed, alongside the activation of additional nucleation sites, as seen in Figure 3.3. However, beyond a particular flow rate threshold, no substantial augmentation in lateral growth was recorded, implying that excessively elevated argon flow rates may induce kinetic growth conditions at the expense of thermodynamic ones. This phenomenon resulted in irregular, dendritic morphologies, which are suboptimal for the generation of high-quality two-dimensional crystals. Cumulatively, our findings accentuate the critical importance of fine-tuning both growth temperature and argon flow rate to realize high-quality $MoS_2$ flakes with advantageous morphological attributes for prospective applications in catalysis and sensing.

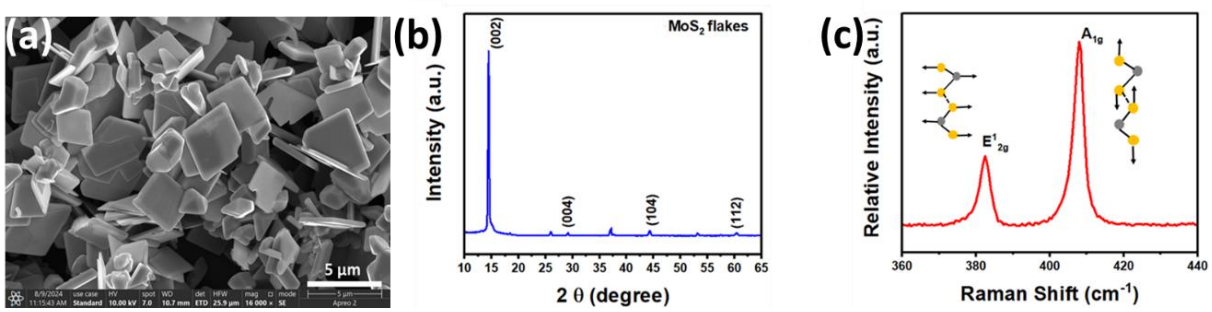



**Figure 3.4:** (a) High-resolution FE-SEM images of CVD grown $MoS_2$ on $SiO_2$/Si substrate, (b) XRD spectra of optimized MoS2 flakes, the peaks become sharper, highly intense and with more planes of $MoS_2$, and (c) Raman spectra of the optimized $MoS_2$ flakes. Raman spectra consist of two strong peaks that corresponds to in-plane, $E^1_{2g}$, and out-of-plane, $A_{1g}$, vibrations of S- Mo-S atoms.

Furthermore, we performed XRD and Raman spectroscopy to investigate the orientation of optimized $MoS_2$ on $SiO_2$ substrate. From figure 3.4 (b), it is observed that $MoS_2$ grown on $SiO_2$ shows (002), (004), (104) and (112) peaks in $MoS_2$-80 and $MoS_2$-800 with an additional (002) peak having high intensity in $MoS_2$ ($MoS_2$, JCPDS #.37-1492) [Kumar et al., 2018b]. The high intensity of the (002) peaks indicates that the basal planes. The orientation of $MoS_2$ flakes is also confirmed by Raman spectroscopy, which is a standard nondestructive technique to determine the number of layers, crystallinity and orientation of 2D materials. Figure 3.4 (c) clearly indicates that two vibrational modes $E^1_{2g}$ (**in-plane vibrational mode**) and $A_{1g}$ (**out-of-plane vibrational mode)** of 2H-$MoS_2$ are positioned at ~383 and ~407 $cm^{-1}$, respectively, confirming few-layer $MoS_2$ [Lee et al., 2012b].

### 3.2.3. Synthesis of vertically Aligned $SnS_2$ flakes

The synthesis of Vertically Aligned $SnS_2$ (VA-$SnS_2$) flakes was accomplished via a three-zone chemical vapor deposition (CVD), grown on SiO2/Si substrate, as shown in Figure 3.5 (a). Prior to the deposition process, the substrates underwent a thorough cleaning protocol based on the RCA-1 method to ensure the elimination of both organic and inorganic impurities, thereby providing a pristine surface conducive to homogeneous growth. Sulfur (S) powder and $SnO_2$ powder were employed as precursors in the growth of $SnS_2$, with their spatial configuration within the CVD apparatus meticulously designed to enhance the reaction kinetics.

The experimental configuration encompassed three distinct thermal zones within the CVD reactor. The precursor of SnO2 (0.05 gm) and sulfur (1gm) was kept in alumina boat in Zone-2 and Zone-1 of CVD respectively. The substrate was placed inclined at 45° on the heighted substrate holder in the Zone-3 of CVD at 450 °C temperature. Prior to the commencement of the growth procedure, the quartz tube of the CVD apparatus was purged with argon (Ar) gas at a flow rate of 500 sccm for a duration of 10 minutes to eradicate any residual oxygen and impurities. During the reaction phase, Zone 1, containing the sulfur source, was regulated at a temperature of 200 °C, while Zone 2, housing the SnO2 precursor, was elevated to 1000 °C at a heating ramp

rate of 16 °C/min, as seen in Figure 3.5 (b). Continuous argon gas flow was maintained at 80 sccm, and the reaction was allowed to proceed for a duration of 90 minutes. Upon completion of the deposition process, the system was permitted to cool naturally to ambient temperature.

To elucidate the impact of growth parameters on the morphology and quality of the $SnS_2$ flakes, a systematic investigation was conducted regarding the effects of temperature and argon gas flow rate. Initially, the temperature in Zone 2 was altered, while maintaining a constant argon flow rate of 80 sccm. Growth temperatures of 800 °C, 900 °C, 950 °C, and 1000 °C were examined, with the respective samples designated as $SnS_2$-800, $SnS_2$-900, $SnS_2$-950, and $SnS_2$-1000, as illustrate in Figure 3.5 (c). The findings indicated substantial disparities in flake morphology and crystallinity, underscoring the pivotal influence of temperature within the growth mechanism. Furthermore, the impact of argon gas flow rate was scrutinized by varying it from 60 sccm to 120 sccm in increments of 20 sccm, while sustaining the growth temperature at 1000 °C. The resultant samples, labeled $SnS_2$-60, $SnS_2$-80, $SnS_2$-100, and $SnS_2$-120, demonstrated variations in growth uniformity and flake dimensions as a function of the gas flow rate, as seen in Figure 3.5 (d). The $SnS_2$ flakes were developed under kinetic circumstances due to turbulent gas flow, and traditional thermodynamics did not play a major role.

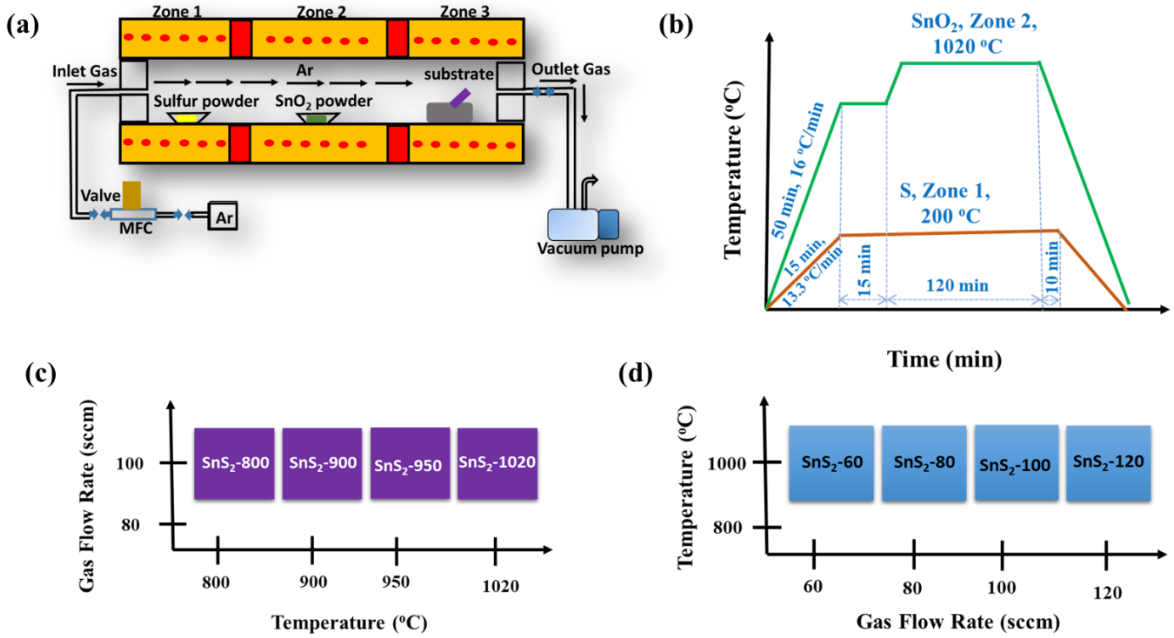



**Figure 3.5:** (a) Schematic of the thermal chemical vapour deposition (CVD) technique used in growing $SnS_2$ flakes. $SiO_2$/Si substrate place in in zone 3. (b)The temperature profiles of S and SnO2 powders in zones 1 and 2, respectively and (c, d) illustrate the various growth circumstances (Temperature, gas flow) and grown sample names.

### 3.2.4. Characterizations of $SnS_2$ Flakes

We employed Scanning Electron Microscopy (SEM) to elucidate the growth dynamics of $SnS_2$ on $SiO_2$/Si substrates under a spectrum of experimental conditions, which included variations in growth temperature and argon gas flow rates. The findings indicated that the $SnS_2$ samples synthesized at growth temperatures of 800 °C, 900 °C and 950 °C comprised clusters characterized by grains that exhibited random orientation, lacking parallel alignment to the substrate surface, as shown in Figure 3.6 (a-c). Conversely, the synthesis conducted at 1000 °C yielded a continuous $SnS_2$ film exhibiting a uniform morphological profile, as seen in Figure 3.6 (d). Moreover, we investigated the influence of argon flow rate, while maintaining a constant growth temperature of 1000 °C and a sulfur source temperature of 200 °C. The increment of argon flow from 60 sccm to 120 sccm, resulted in an enhancement of the lateral dimensions of the $SnS_2$ flakes and facilitated the activation of additional nucleation sites. Nonetheless, excessively elevated flow rates disrupted the thermodynamic growth parameters, culminating in irregular dendritic morphologies that are not conducive to the production of high-quality two-dimensional crystals.

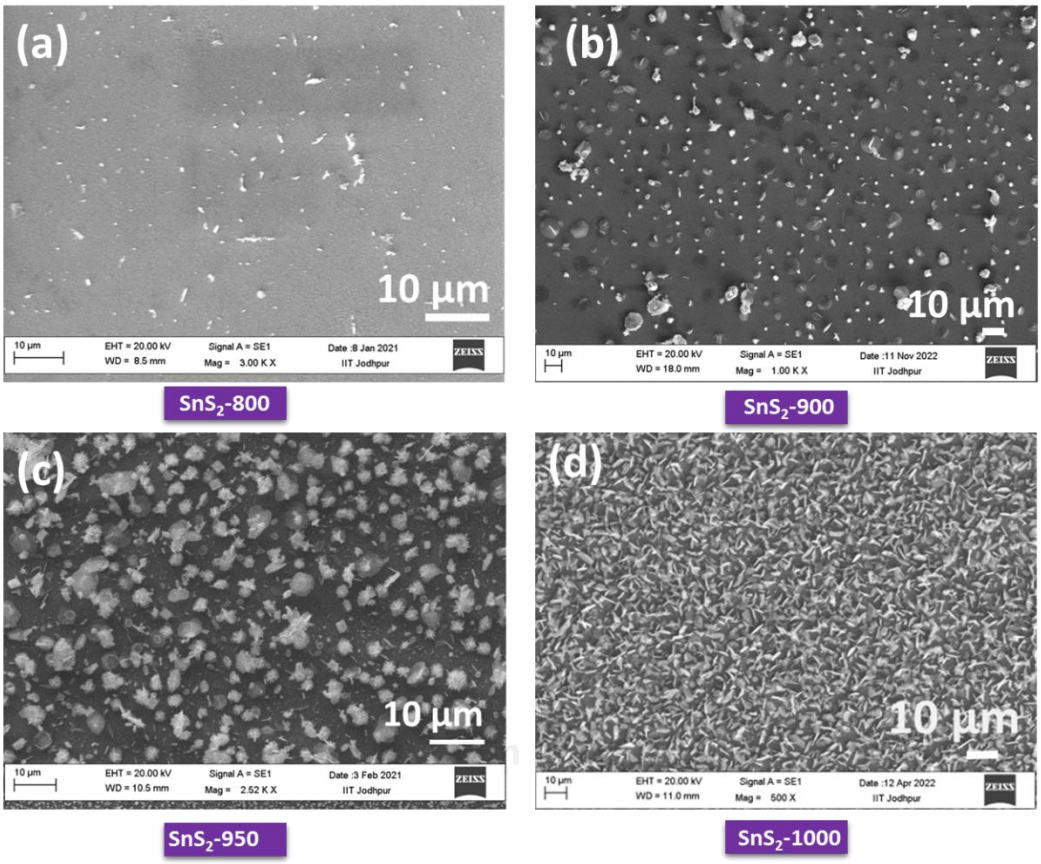



**Figure 3.6**: SEM images of $SnS_2$ flakes grow at different deposition temperature (a) 800 °C, (b) 900 °C, (c) 950 °C, and (d) 1000 °C. The flow of argon gas (100 sccm) keep constant during the growth.

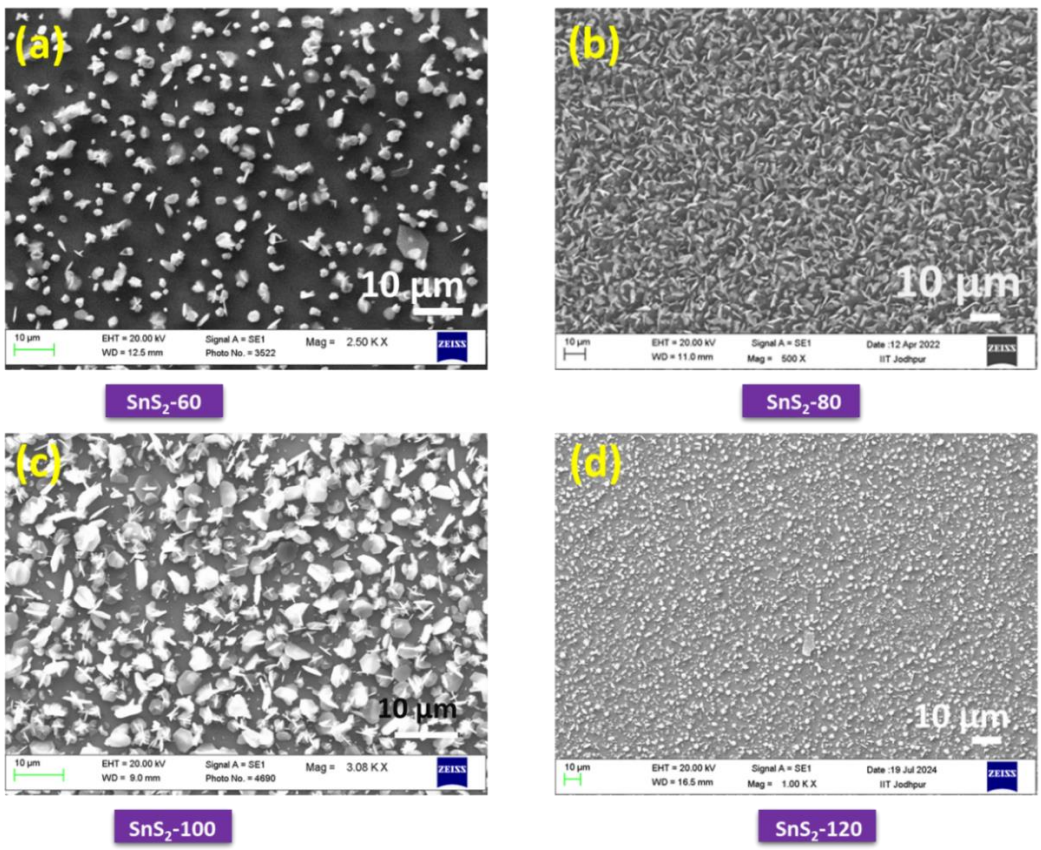



**Figure 3.7:** SEM images of $SnS_2$ flakes grow at different gas flow rates (a) 60 sccm, (b) 80 sccm, (c) 100 sccm and (d) 120 sccm. The growth temperature for all these samples was fixed at 1000°C.

The optimal synthesis conditions were determined to be a growth temperature of 1000 °C combined with an argon flow rate of 80 sccm, which produced the most uniform and densely populated vertical $SnS_2$ flakes, as shown in Figure 3.8 (a). SEM analysis corroborated the vertically aligned architecture of these flakes, which were uniformly dispersed across the $SiO_2$/Si substrate. This vertical alignment is particularly advantageous for gas sensing applications, as it amplifies the number of available adsorption sites, thereby improving sensitivity.

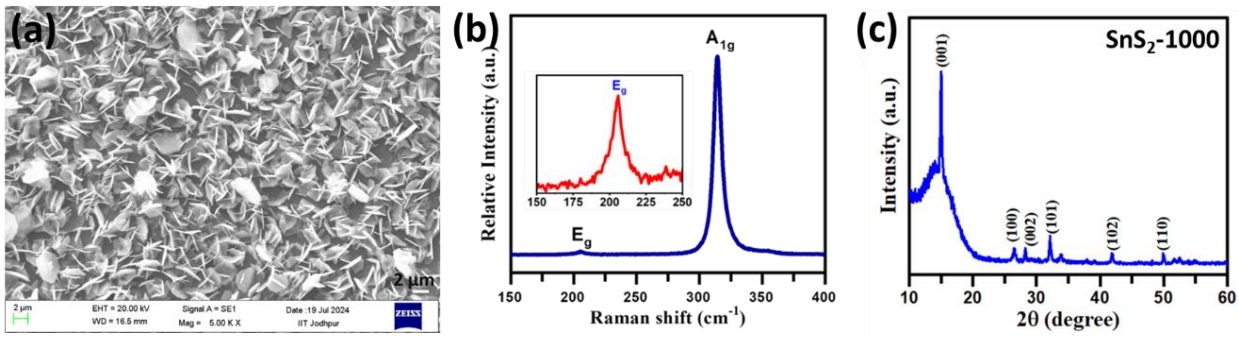



**Figure 3.8.** (a) High-resolution SEM images of CVD grown vertically aligned $SnS_2$ flakes on $SiO_2$/Si substrate, (b) Raman spectra of the optimized $SnS_2$ flakes. Raman spectra consist of two strong peaks that corresponds to in-plane, $E_g$, and out-of-plane, $A_{1g}$, vibrations of S- Sn-S atoms, **(c)** XRD spectra of optimized $SnS_2$ flakes, the peaks become sharper, highly intense and with more planes of $SnS_2$.

To further characterize the optimized samples, we conducted Raman spectroscopy and X-ray Diffractometry (XRD) analyses. Raman spectroscopy identified two distinctive vibrational modes: the in-plane vibrational mode ($E_g$) at approximately 205 $cm^{-1}$ and the out-of-plane vibrational mode ($A_{1g}$) at around 314 $cm^{-1}$. The prominent intensity of the $A_{1g}$ mode signified robust Raman activity and high crystallinity, while the comparatively diminished $E_9$ mode indicated a reduction in scattering centers in the in-plane direction, as seen in Figure 3.8 (b). XRD analysis validated the phase purity and hexagonal crystalline structure of the $SnS_2$ layers, with well-defined diffraction peaks discerned at angles of 15.0°, 28.4°, 30°, 32.3°, 42.1°, and 50.2°, correlating with the (001), (100), (002), (101), (102), and (110) crystallographic planes, respectively, as depicted in Figure 3.8 (c). These findings correspond with the JCPDS #23–0677 standard pattern, affirming the material's high crystallinity and phase purity.

In summary, the integration of SEM, Raman, and XRD analytical techniques substantiates that the optimized growth conditions yield high-quality $SnS_2$ flakes characterized by favorable morphological and structural attributes, rendering them appropriate for applications in sensing and catalysis.

## 3.3 Proposed Growth Mechanism

The growth of $MoS_2$ and $SnS_2$ flakes employing the chemical vapor deposition (CVD) technique entails a vapor-phase interaction between metallic precursors and sulfur vapor under meticulously regulated parameters. Consequently, the growth mechanism encompasses a sequence of distinct phases: diffusion and absorption, nucleation and chemical reaction, and ultimately, the growth phase, as shown in Figure 3.9. In the diffusion and absorption phase (precursor stage), the CVD apparatus typically incorporates metal oxide precursors such as $MoO_3$ for $MoS_2$, and $SnO_2$ for $SnS_2$. This methodology facilitates the generation of high-quality two-dimensional (2D) crystals with precise regulation over morphology and thickness.

For $MoS_2$, the growth process commonly utilizes molybdenum-based precursors, specifically $MoO_3$, alongside sulfur powder serving as the sulfur source. Throughout this procedure, $MoO_3$ undergoes decomposition into volatile constituents, which migrate through the reaction chamber towards the heated substrate. The precursor molecules are propelled by the flow of inert gases (such as Ar or $N_2$) into the reaction zone, where adsorption onto the substrate surface initiates. The adsorption process of these precursor molecules is modulated by the temperature and flow

rate, which subsequently governs the uniformity and concentration of the adhered species on the substrate.

In the nucleation and chemical reaction phase, the adsorbed precursor molecules engage in chemical transformations on the heated substrate surface. For $MoS_2$, $MoO_3$ reacts with sulfur vapor to yield $MoS_2$. These chemical reactions can be articulated as:

$$2MOO_3 + S \rightarrow 2MoO_2 + SO_2 \tag{3.1}$$

$$MoO_3 + 3S \rightarrow MoS_2 + SO_2 \tag{3.2}$$

Similarly, the synthesis of $SnS_2$ encompasses tin-based precursors, including $SnO_2$, in conjunction with sulfur vapor. The tin precursor undergoes vaporization at elevated temperatures, resulting in the formation of Sn-containing species, which are subsequently conveyed to the substrate. Sulfur vapor, produced from thermally treated sulfur powder, interacts with the tin species to yield $SnS_2$ on the substrate. Upon the adsorption of the precursors onto the substrate, the nucleation phase initiates. The $SnO_2$ vapor engages in a reaction with the sulfur vapor at the substrate interface, leading to the formation of $SnS_2$ through the subsequent reaction:

$$SnO_2 + S_2 \rightarrow SnS_2 + SO_2 \tag{3.3}$$

During this phase, the initial nucleation of monolayers or few-layered flakes commences, propelled by the supersaturation of precursor species at the substrate surface. Nucleation serves as a pivotal determinant for regulating both the lateral dimensions and density of the flakes, as it establishes the quantity of nuclei that will act as initiators for subsequent growth. The nucleation rate is contingent upon temperature, precursor concentration, and the partial pressure of sulfur vapor, all of which must be judiciously optimized to facilitate controlled layer development.

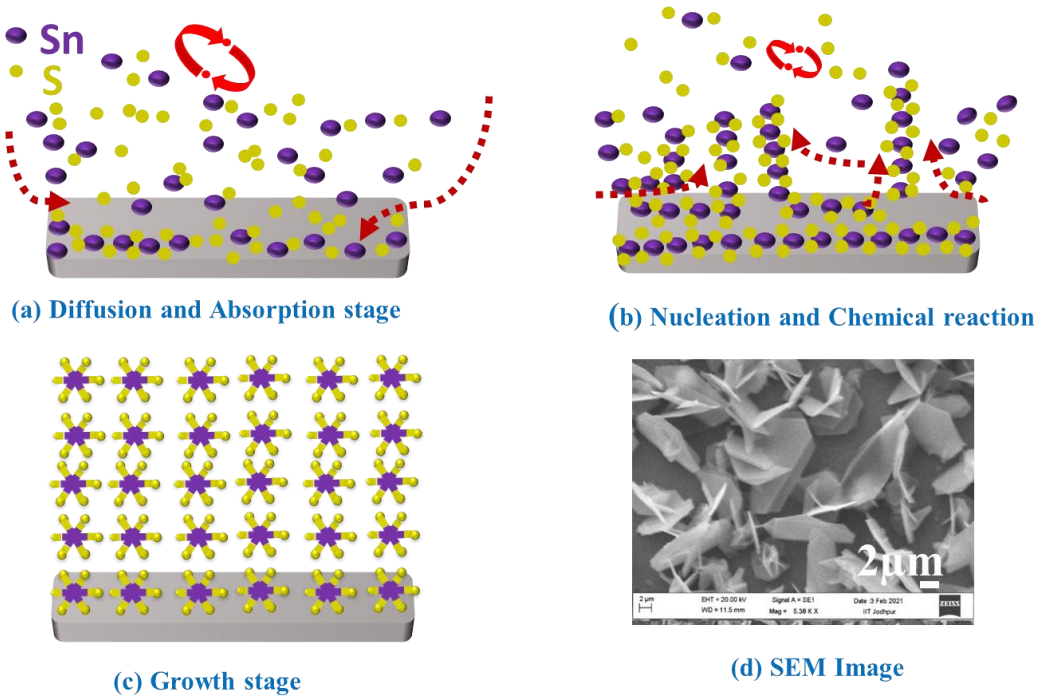



**Figure 3.9** The suggested growth mechanism for edge-enriched $MoS_2$ and $SnS_2$ flakes. (a) Represents the diffusion and absorption stage of in-plane $MoS_2$ and $SnS_2$ formation. In this phase, in-plane $MoS_2$ and $SnS_2$ development is more rapid, resulting in the production of monolayer to multilayer flakes on the substrate, (b) Growth of edge-enriched flakes at the nucleation and chemical reaction stage. The incoming S and Mo, Sn atoms adsorb on the substrate and $MoS_2$ and $SnS_2$ flakes, causing edge-enriched flakes to develop, (c) Schematic illustration the growth stage for finally as grown interconnected $MoS_2$ and $SnS_2$ flakes, and (d) SEM image of the $MoS_2$ and $SnS_2$ flakes.

Ultimately, in the growth phase, the newly established nuclei on the substrate initiate expansion into larger, continuous films or flakes. As the reaction advances, additional precursor material decomposes and migrates to the surface, where it is absorbed and reacts with the pre-existing nuclei. This progression results in the lateral expansion of the flakes. The growth process typically adheres to a layer-by-layer (epitaxial) mechanism, wherein the newly formed atoms or molecules are deposited atop previously synthesized layers, thereby preserving the crystallinity of the material. The growth rate is influenced by variables such as temperature, the flux of precursor molecules, and sulfur availability.

The growth mechanism is highly sensitive to both kinetic and thermodynamic parameters, which include sulfur flow rate and the velocity of the carrier gas. Elevated flow rates may induce irregular, dendritic morphologies as a consequence of rapid kinetics, whereas diminished flow rates might restrict precursor availability, thereby impeding growth. Under meticulously optimized conditions, the $MoS_2$ and $SnS_2$ flakes exhibit a uniform thickness, hexagonal geometries, and pronounced crystallinity. The meticulous balancing of diffusion, nucleation, and growth phenomena is essential to ensure the synthesis of high-quality $MoS_2$ and $SnS_2$ flakes endowed with favourable morphological and structural characteristics, rendering them particularly advantageous for applications in catalysis, sensing, and optoelectronics.

In summary, the chemical vapor deposition (CVD) growth of $MoS_2$ and $SnS_2$ flakes represents a multifaceted, multi-stage process that incorporates precursor diffusion and adsorption, nucleation alongside chemical reactions on the substrate, and the subsequent proliferation of the flakes. By meticulously regulating the parameters during each stage—namely precursor flux, temperature, and sulfur vapor concentration—high-quality, large-area monolayer or few-layer flakes of $MoS_2$ and $SnS_2$ can be effectively synthesized.

## 3.4 Synthesis of $WS_2$

The $WS_2$ was prepared via a simple hydrothermal method. At room temperature, Sodium tungstate dihydrate ($Na_2WO_4 \cdot 2H_2O$), thiourea ($CH_4N_2S$), and oxalic acid ($H_2C_2O_4$) were typically added to 40 mL of deionized water while stirring constantly for 60 minutes. Next, a 50 mL Teflon-lined stainless-steel autoclave was used to keep the reaction mixture at 200 °C for 24 hours and cooled to room temperature naturally. Finally, the precipitate was centrifuged at 5000 rpm for 20 min and washed three or more times with ethanol and DI water and dried the collected black powder at 60 °C for 12 hours, as shown in Figure 3.10 (a).

Following the hydrothermal synthesis of $WS_2$ nanoparticles, the morphology of the produced material was meticulously examined FE-SEM. The FE-SEM image, disclosed the emergence of well-defined $WS_2$ nanoparticles, thereby affirming the successful synthesis of the material as illustrated in Figure 3.10 (b). To further substantiate the composition and structural characteristics of the synthesized $WS_2$, Raman spectroscopy was employed. The Raman spectra displayed two prominent characteristic peaks of $WS_2$ at 353 $cm^{-1}$ and 416 $cm^{-1}$, which are associated with the in-plane vibrational mode ($E^1_{2g}$) and the out-of-plane vibrational mode ($A_{1g}$), respectively, as seen in Figure 3.10 (c). These findings corroborate the high purity and crystallinity of the $WS_2$ nanoparticles, thereby illustrating that the hydrothermal method constitutes an efficacious approach for the synthesis of high-quality $WS_2$ for prospective applications in electronic and optoelectronic devices.

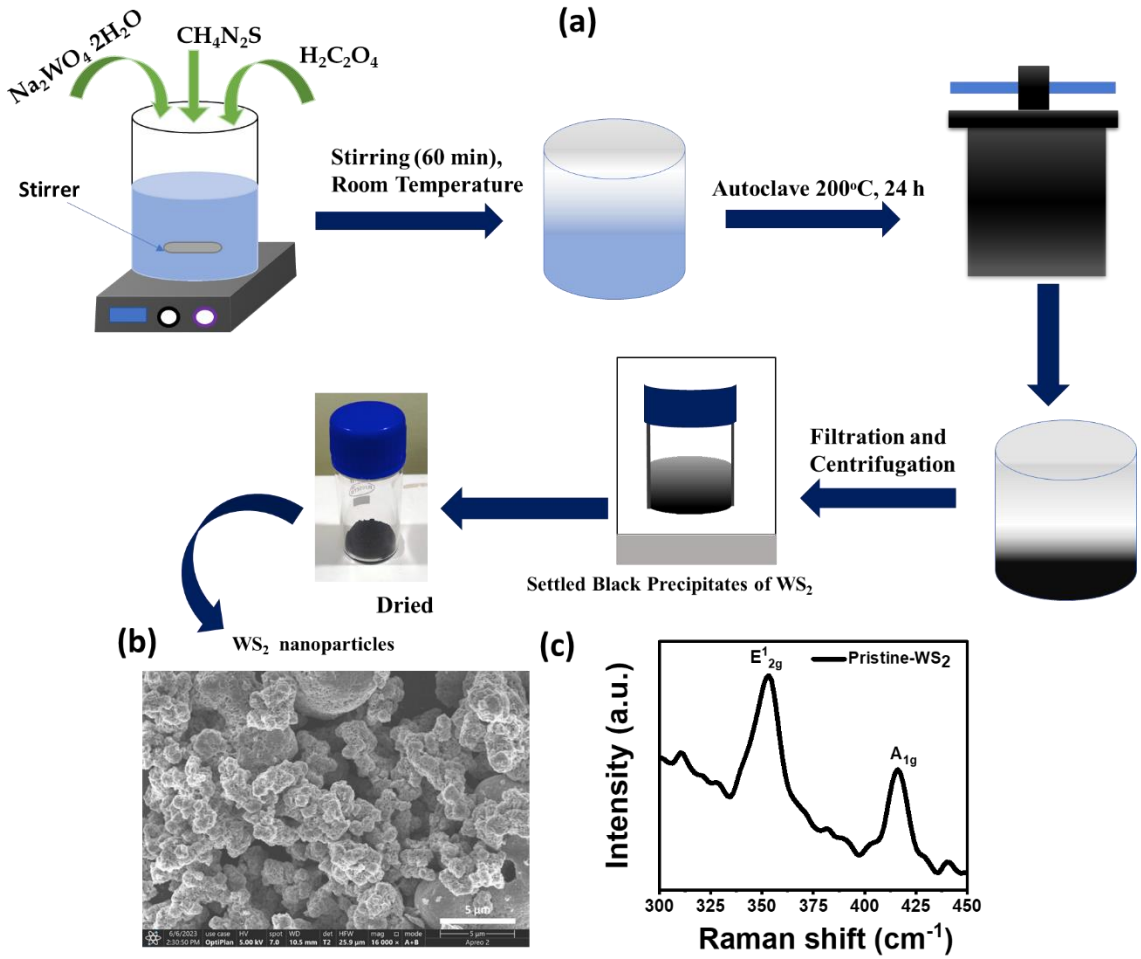



**Figure 3.10.** (a) Schematic illustration of $WS_2$ nanoparticle synthesis using the hydrothermal method, (b) FE-SEM image showing the morphology of the synthesized $WS_2$ nanoparticles, and (c) Raman spectra confirming the characteristic vibrational modes of $WS_2$.

## 3.5 Nitrogen Plasma Treatment

To thoroughly investigate the effects of nitrogen plasma treatment on the properties of two unique materials, specifically $MoS_2$ and $SnS_2$, films of each material were carefully crafted and then divided into smaller pieces to facilitate precise plasma exposure. The $MoS_2$ specimens underwent nitrogen plasma treatment at a radio frequency (RF) power of 10 W and a nitrogen flow rate of 0.5 sccm, with the duration of treatment varied across 0, 1, 5, and 8 minutes, resulting in the formation of nitrogen-doped $MoS_2$ as depicted in Figure 3.11 (a). In a similar manner, vertically aligned $SnS_2$ samples were exposed to nitrogen plasma treatment under equivalent RF power and environmental parameters, albeit with treatment durations of 0, 4, 8, 12, and 16 minutes. These samples were designated as N0, N4, N8, N12, and N16, respectively, as shown in Figure 3.11 (b).

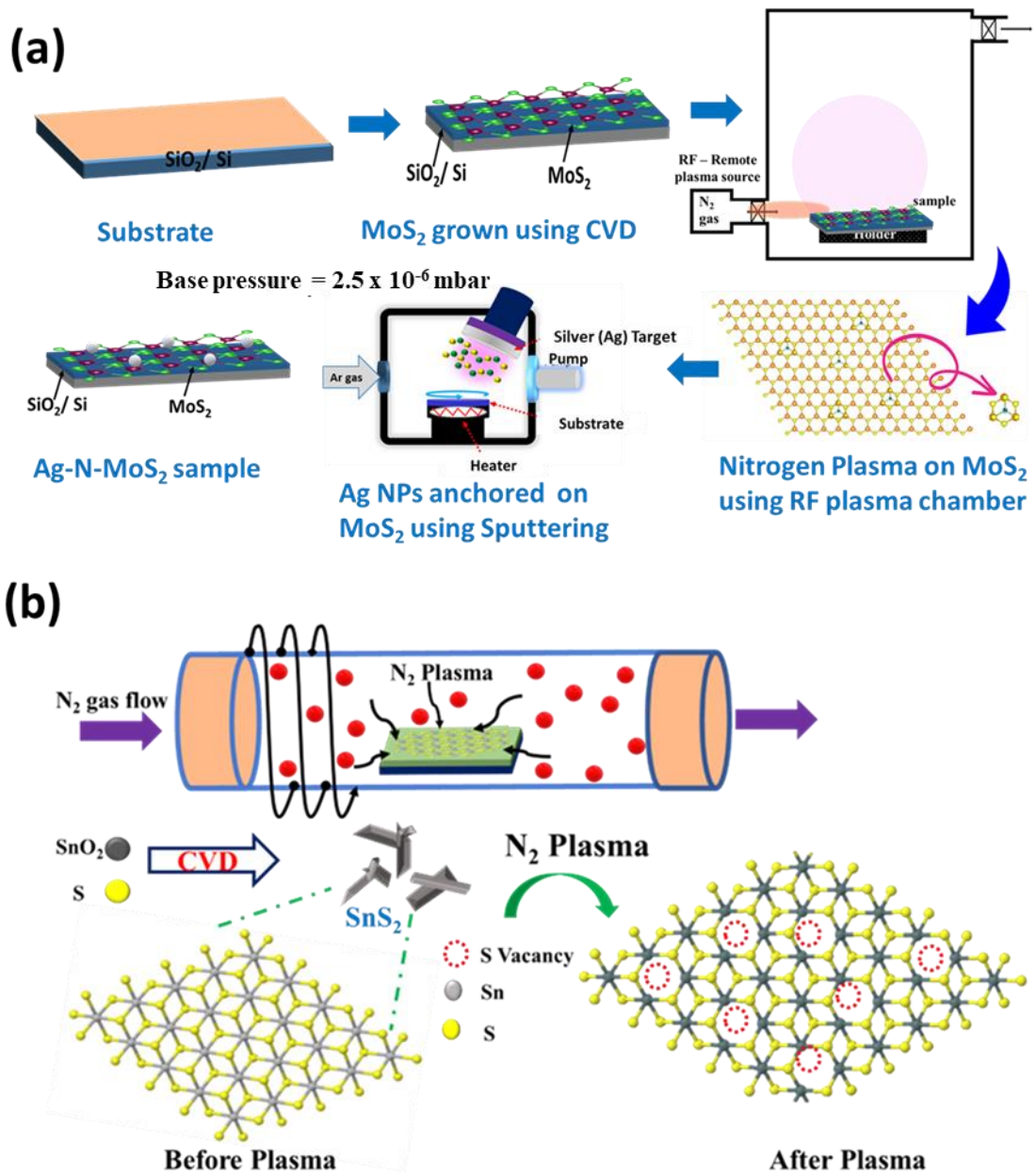



**Figure 3.11** Schematic illustration of (a) nitrogen plasma treatment and subsequent functionalization with silver (Ag) nanoparticles on CVD-grown $MoS_2$ flakes, and (b) nitrogen plasma treatment on CVD-grown $SnS_2$ flakes, showcasing the process of sulfur vacancy creation, nitrogen doping, and nanoparticle deposition to enhance material properties.

## 3.6 Synthesis of Silver Nanoparticles Using DC Sputtering Technique

Silver (Ag) nanoparticles were synthesized via a DC sputtering method, with a high-purity Ag target under controlled environments. The deposition process was carried out at room temperature (RT) with an argon (Ar) gas flow rate of 30 sccm, confirming a stable sputtering atmosphere. The working pressure during the process was kept at $2\times10^{-2}$ mbar to help effective plasma generation and uniform deposition, as seen in Figure 3.11 (a).

A DC power supply was used to create plasma, where a voltage of 0.34 V and a current of 0.24 kA were applied, resulting in a deposition power of ~81.6 W. The controlled sputtering parameters facilitated the expulsion of Ag atoms from the target by energetic Ar ions, which subsequently condensed upon the substrate, resulting in the formation of nanoparticles. The deposition time and conditions were optimized to achieve uniform size distribution and morphology of the Ag nanoparticles. The deposition duration and conditions were meticulously optimized to attain a uniform size distribution and morphology of the Ag nanoparticles. These synthesized nanoparticles manifest advantageous properties for a multitude of applications,

including catalysis, plasmonic, and sensing technologies, thereby illustrating the efficacy of DC sputtering as a precise and scalable fabrication technique.

## 3.7 Device Fabrication Process

To enable accurate and reproducible sensing performance, interdigitated electrode (IDE) structures with a gap of 100 μm between fringes were fabricated on $MoS_2$ and $SnS_2$ flakes grown through chemical vapor deposition (CVD). The IDE fabrication process involved the use of a shadow mask for pattern definition and thermal evaporation of Au/Cr as the electrode material, as shown in Figure 3.12. Below are the detailed steps:

---

**Step 1: Substrate Preparation**

1. **Cleaning Protocol**:
   - A clean substrate is critical to ensure proper growth of thin films and reliable electrode adhesion.
   - The substrate $Si/SiO_2$ was ultrasonicated sequentially in acetone and isopropanol (IPA) for 10 minutes each, followed by rinsing with deionized (DI) water and nitrogen blow drying.
   - An optional oxygen plasma cleaning step (5–10 minutes) was used to remove residual organic contaminants and improve surface hydrophilicity.

---

**Step 2: Growth of $MoS_2$ and $SnS_2$ Flakes**

- High-quality $SnS_2$ and $MoS_2$ flakes were synthesized using a thermal CVD method with optimized growth conditions to ensure uniformity, desirable crystal orientation, and minimal defects.
- The quality of the films was characterized using SEM, Raman spectroscopy, and X-ray diffraction (XRD) to confirm their structural and morphological properties.

---

**Step 3: Preparation and Alignment of Shadow Mask**

1. **Shadow Mask Design**:
   - The IDE pattern was designed with interdigitated fingers featuring a **100 μm gap** between the fringes, tailored for sensing applications.
   - A precision laser cutter or photolithography was used to fabricate the shadow mask from a durable material, ensuring minimal dimensional deviation.
2. **Mask Alignment**:
   - The shadow mask was carefully aligned over the $SnS_2$ and $MoS_2$ thin films, ensuring proper coverage of the active sensing region.

---

**Step 4: Electrode Deposition Using Thermal Evaporation**

**Thermal Evaporation Setup:**

- The substrate with the aligned shadow mask was loaded into a thermal evaporation system, and the chamber was evacuated to a vacuum level of ~$10^{-6}$ Torr to prevent contamination.

**Deposition of Chromium (Cr) Adhesion Layer:**

- A 30 nm Cr layer was deposited as an adhesion layer to enhance the bonding between the gold electrode and the TMD surface.

**Deposition of Gold (Au) Electrode Layer:**

- A 200–300 nm Au layer was deposited on top of the Cr layer to form the interdigitated electrodes.
- The thickness of the layers was monitored in real time using a quartz crystal microbalance (QCM).

**Mask Removal**:

- After deposition, the shadow mask was gently removed to reveal the interdigitated electrode pattern.

---

**Step 5: Post-Processing (Optional)**

- The fabricated devices were subjected to mild annealing at 200–300°C in an inert atmosphere (Ar or $N_2$) to improve the metal-semiconductor interface, reduce contact resistance, and stabilize the electrode material.

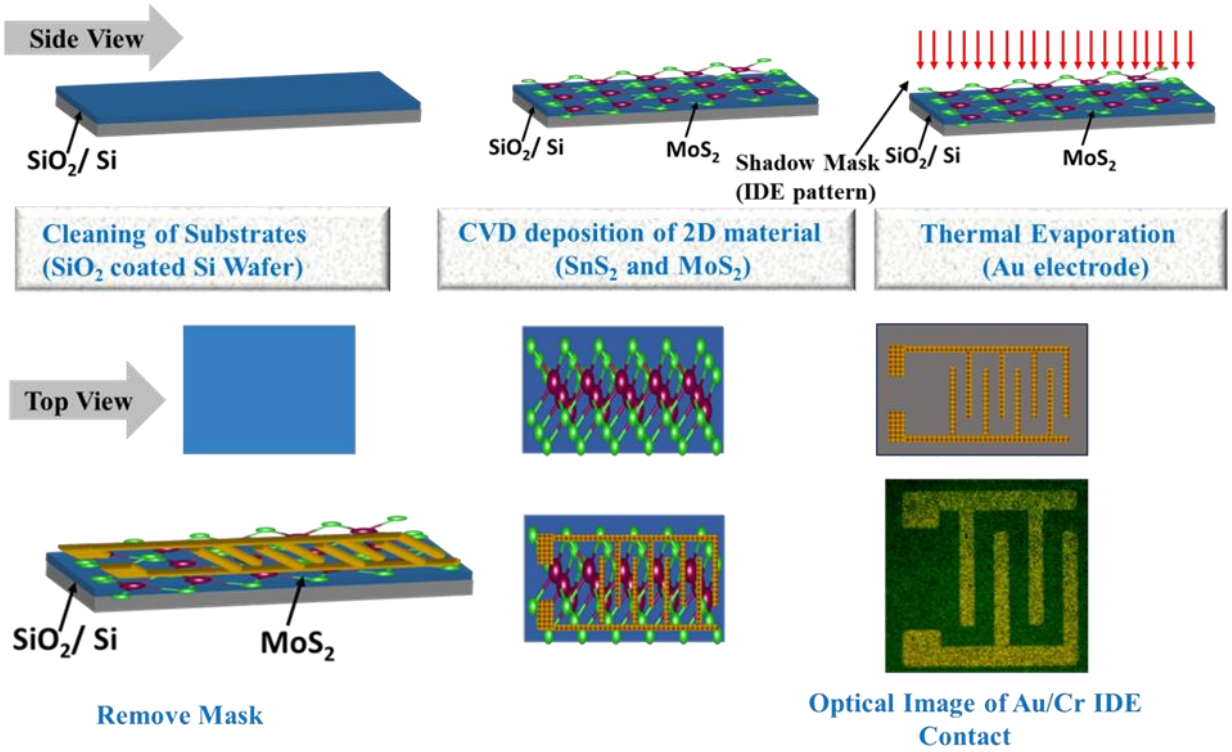



**Figure 3.12** Device Fabrication Process for Interdigitated Electrode (IDE) Structures on CVD-grown $SnS_2$ and $MoS_2$.

## 3.8 Summary

In summary, this chapter focuses on the controlled and tunable growth of interconnected $MoS_2$ and $SnS_2$ flakes using a three-zone thermal CVD technique. The growth was systematically optimized by varying growth temperatures and gas flow rates to modulate the density of the flakes, transitioning from standalone $MoS_2$ and $SnS_2$ flakes to a well-connected three-dimensional network of these flakes. Morphological, structural, and optical analyses of the synthesized materials revealed that the growth initiates with in-plane $MoS_2$ and $SnS_2$ flakes. With increasing gas flow rates, a gradual transition to vertically aligned flakes was observed, resulting in a denser and interconnected network.

The controlled synthesis and proposed growth mechanism for vertically aligned $MoS_2$ and $SnS_2$ flakes offer valuable insights for tailoring the structural and functional properties of transition metal dichalcogenides (TMDCs). These insights are crucial for designing TMDC-based materials with desirable characteristics for advanced applications. Furthermore, nitrogen plasma treatment was utilized to introduce sulfur vacancies and nitrogen doping in $MoS_2$ and $SnS_2$, effectively modifying their electronic and optical properties. Additionally, Ag nanoparticles were synthesized using a DC sputtering technique to further enhance the performance of $MoS_2$ flakes.

Hydrothermal synthesis was employed to produce $WS_2$ nanoparticles, providing another avenue to explore the tunability of TMDC materials. Devices were then fabricated using the synthesized $MoS_2$ and $SnS_2$ flakes for gas sensing and photodetection applications. Interdigitated electrode (IDE) patterns were employed to facilitate electrical measurements of the devices, leveraging the tailored properties of $MoS_2$ and $SnS_2$ flakes. This chapter highlights the comprehensive approach to material synthesis, property tuning, and device fabrication, paving the way for future innovations in gas sensing and optoelectronic technologies.

# 4

# Effects on Gas Sensing Characteristics of $MoS_2$ flakes using Surface and Structural Modifications

In this chapter, we present an innovative methodology for achieving selective nitrogen dioxide ($NO_2$) gas sensing through the utilization of nitrogen-doped molybdenum disulfide (N-$MoS_2$) that has been functionalized with silver nanoparticles (Ag NPs). We conduct a thorough investigation into the functionalization of N-$MoS_2$ with Ag NPs to enhance its performance in detecting $NO_2$ gas. $MoS_2$ flakes were synthesized via chemical vapor deposition (CVD) and were subsequently treated with nitrogen plasma to facilitate the doping process. We systematically assess the gas sensing capabilities of pristine $MoS_2$, nitrogen-doped $MoS_2$ (N-$MoS_2$), and Ag-decorated nitrogen-doped $MoS_2$ (Ag-N-$MoS_2$), specifically focusing on their performance in $NO_2$ gas sensing. Our results reveal that the Ag NPs functionalized N-$MoS_2$ sensor demonstrates remarkable response, rapid response times, and complete recovery. The detailed gas sensing mechanism is proposed in light of the plasma treatment create vacancy or doping and surface functionalization of noble metal nanoparticle (Ag NPs), which plays a crucial role in enhancing the interaction between the gas molecules and the sensing material. Our investigation indicates that Ag NPs functionalized nitrogen-doped $MoS_2$ represents a promising candidate $NO_2$ gas sensing. Furthermore, our results contribute substantially to the progress of gas sensing technology by providing enhanced response and selectivity through innovative modifications of materials.

## 4.1 Requirement of Fast highly response $NO_2$ Gas Sensor and Challenges

In the last few years, the importance of hazardous gases sensing has increased across several industries, including air quality monitoring, workplace safety, and healthcare diagnostics [Freddi et al., 2020; Walsh, 1996; Zhang et al., 2019]. Nitrogen dioxide ($NO_2$) is classified as one of the corrosive gaseous substances that poses significant threats to both environmental integrity and human health. The inhalation of $NO_2$ has the potential to inflict considerable damage upon the human respiratory system, emphysema, ocular structures, chronic bronchitis, and mucosal tissues [de la Hoz et al., 1996; Hashemzadeh et al., 2019; Kumar et al., 2024a]. Even small exposure to $NO_2$ increases the risk of acquiring health problems. The National Institute for Occupational Safety and Health (NIOSH) has set a nitrogen dioxide ($NO_2$) exposure limit of 1 ppm. In pursuit of this aim, an extensive range of sensors, featuring electrochemical cells and metal oxide chemiresistive, have been designed for the commercial identification of $NO_2$ gas [Dey, 2018; Khan et al., 2019]. Still, numerous critical technical challenges endure, such as the extensive response and recovery intervals, poor selectivity, high temperature conditions needed for operation, and insufficient selectivity of metal oxide semiconductors have restricted their role in the prompt detection of nitrogen dioxide ($NO_2$) gas [Lou et al., 2021]. Therefore, there is an urgent requirement to explore alternative materials that exhibit equivalent or superior sensitive, selective, and efficient performance towards $NO_2$ gas.

Transition metal dichalcogenides (TMDs), characterized by their distinctive two-dimensional (2D) attributes, have garnered significant interest within the domain of sensor technology owing to their remarkable chemical and physical characteristics. The electrical properties exhibited by TMDs demonstrate a heightened sensitivity to external stimuli induced by surface or interface interactions, thereby presenting substantial potential for the detection of hazardous nitrogen dioxide ($NO_2$) [Liu et al., 2017; Nasir et al., 2017][11-12]. Among all emerging two-dimensional materials, $MoS_2$ is being thoroughly explored for its prospective applications in hazardous gas sensing, owing to their tunable band gap that varies with thickness, distinctive electronic attributes, high surface-to-volume ratio, adept charge transport functionalities and

superior on/off switching efficiency, which provides numerous active sites for electronic interaction with gas molecules [Bollinger et al., 2001; Kim et al., 2014; Kumar et al., 2018b; Tong et al., 2015]. Recent reports have documented the efficacy of $MoS_2$ gas sensors for detecting gases such as $H_2$, $NH_3$, $H_2S$, $NO_2$, and $CO_2$ [Agrawal et al., 2017; Cho et al., 2015c; Liu et al., 2014a]. However, pristine $MoS_2$-based $NO_2$ gas sensors continue to exhibit prolonged response speed, low gas response coupled with a lack of selectivity, and recovery characteristics remain inadequate, presenting significant challenges for practical applications [Cho et al., 2015c; He et al., 2012]. These challenges were addressed through the heteroatom doping, such as the incorporation of nitrogen and platinum (Pt), palladium (Pd), silver (Ag) etc., fabrication of a composite structure of $MoS_2$ with reduced graphene oxide (rGO), and a $MoS_2$/graphene hybrid aerogel, proves to be highly beneficial for modifying the chemical and electronic properties of $MoS_2$, to amplify the synergy between the target gas and the sensing layer[Cho et al., 2015b; Long et al., 2016a]. Nonetheless, these approaches result in heightened complexity and increased costs associated with the fabrication of the devices [Dey et al., 2013]. Moreover, it was noted that operating the device at elevated temperatures led to a reduction in both response and recovery times, albeit at the expense of diminished sensitivity. The introduction of heteroatoms into $MoS_2$ holds considerable research potential for elucidating its gas-sensitive performance [Tang et al., 2018]. Recently, plasma processing has been demonstrated as a rapid, convenient, straightforward, and efficient technique for altering the surface chemical properties of materials, particularly suitable for the treatment of two-dimensional materials without any contamination from solvents.

Nitrogen incorporation within TMDs is recognized as a common technique to alter their intrinsic physical and chemical attributes for ion retention, oxygen reduction, gas sensor, and hydrogen evolution processes [Deng et al., 2017, 2018; Kumar et al., 2023a; Liu et al., 2016; Ren et al., 2018; Tao et al., 2019; Zhao et al., 2023a]. In recent developments, the employment of nitrogen plasma has been recognized as a powerful approach to effectively insert N atoms within TMDs. The introduction of nitrogen atoms alters the surface electronic characteristics, facilitating a narrower bandgap, expedited charge mobility, and a wealth of active sites for catalytic engagement, while potentially enhancing the robustness of atomic linkages. With respect to gas sensors, remarkable adsorption capacity and selective affinity for $CO_2$, which generally displays a minimal response, have been theoretically predicted in nitrogen-doped $MoSe_2$ utilizing density functional theory (DFT)[Enujekwu et al., 2021]. This research unveils a direction towards the realization of controllable selectivity; however, tangible experimental validations have proven to be elusive until now.

For additional improvement in gas sensing performance, the integration of noble metal catalysts is also a favored approach to effectively lower the energy threshold necessary for gas sensing reactions. Furthermore, the catalytic phenomena involved, such as the spillover effect, electron sensitization, and chemical sensitization, not only deliver supplementary electrons for gas adsorption and desorption but also significantly quicken the rate of chemical reactions. Recently, the amalgamation of $MoS_2$ with metal nanoparticles, metal oxide semiconductors, and other two-dimensional materials has unveiled innovative pathways to elevate sensing performance through both chemical and electronic sensitization. For instance, Kuru *et al.* disclosed that a sensor based on a $MoS_2$ nanosheet–Pd nanoparticle composite exhibits remarkable sensitivity to $H_2$, attributable to the modulation of the work function by Pd nanoparticles[Kuru et al., 2015].Park *et al.,* demonstrated that $MoS_2$ gas sensors adorned with Pd nanoparticles exhibited sensitivity enhancements of 5.58 and 4.25 for $NH_3$ and $H_2S$ gases, respectively, in comparison to their undecorated $MoS_2$ gas sensor counterparts [Park et al., 2018]. In order to augment the performance of nitrogen plasma-treated $MoS_2$ in sensing of $NO_2$, contemporary research has examined the addition of silver (Ag) nanoparticles. Enhanced charge transfer kinetics and an increase in active sites can lead to a dramatic improvement in the sensor's response, when decorated with Ag nanoparticles on $MoS_2$. These nanoparticles are known for their exceptional catalytic efficiency and ability to enhance electron transport. The synergistic impact of Ag nanoparticles alongside nitrogen-doped $MoS_2$ culminates in a sensor that boasts heightened sensitivity and selectivity.

## 4.2 Synthesis and Fabrication of Ag NPs anchored-nitrogen plasma treated $MoS_2$ flakes

In Chapter 3, the synthesis of $MoS_2$ flakes utilising a three-zone CVD approach had been discussed in depth. Molybdenum trioxide ($MoO_3$) and sulphur (S) were used as precursors in the synthesis of $MoS_2$ flakes, which were meticulously optimised. The sulphur and $MoO_3$ temperatures were kept at 200 °C and 850 °C, respectively, for 45 minutes while an argon flow of 80 sccm was in place. The next step was to use thermal evaporation to create interdigital elecrode (IDE) of Au/Cr contact with a precise 100 μm spacing. In order to further improve the characteristics, nitrogen doping and surface vacancies were introduced into the $MoS_2$ flakes using nitrogen plasma treatment, which was carried out for 1, 5, and 8 minutes at an RF power of 10 W and a nitrogen flow rate of 0.5 sccm. Subsequently, the functionalisation of Ag nanoparticles was performed by RF sputtering for 10 seconds. When the fabricated devices were examined for different $NO_2$ concentrations, their gas sensing the ability demonstrated significant enhancement as a result of the combined impacts of Ag functionalisation and nitrogen plasma treatment.

## 4.3 Results and Discussion

### 4.3.1. Structure and chemical properties

Field emission scanning electron microscopy (FE-SEM) is utilized for the morphological examination of the mixed $MoS_2$ films. Figure 4.1, illustrates the FESEM image of highly homogeneous interconnected $MoS_2$ films, adorned with silver nanoparticles (Ag NPs) on their surface. The synthesized $MoS_2$ films exhibit a considerable surface-to-volume ratio, resulting in an increased number of accessible active sites, as depicted in Figure 4.1 (a). The Ag NPs are uniformly dispersed across the $MoS_2$ films, and possess a spherical morphology, with an average diameter of ~ 50 nm, as seen in Figure 4.1(d). Ag NPs were uniformly distributed over pristine $MoS_2$ and N-$MoS_2$, which is confirmed by elemental mapping using energy-dispersive spectroscopy (EDX), as shown in Figure 4.2.

The orientation of the pristine $MoS_2$, N-$MoS_2$, Ag-$MoS_2$, and Ag-N-$MoS_2$ are further confirmed by Raman spectroscopy, a recognized non-destructive approach utilized to identify the layer number, crystallinity, and orientation of 2D materials. Figure 4.3 (a), displays the Raman spectra for pristine $MoS_2$ situated on a $SiO_2$/Si substrate. The in-plane ($E^1_{2g}$) and out-of-plane ($A_{1g}$) vibrational modes are the two prominent peaks in the Raman spectra of $MoS_2$ at 380.42 and 406.62 $cm^{-1}$, and the peak shifts to 381.92 and 407.96 $cm^{-1}$ for N-$MoS_2$, after 5 min nitrogen plasma treatment. The observed peak separation between the $A_{1g}$ and $E^1_{2g}$ vibrational modes measures 26.20 $cm^{-1}$, is indicative few layers of $MoS_2$, according to existing literature [Lee et al., 2010]. Following a 5-minute treatment with $N_2$ plasma, the $E^1_{2g}$ peak associated with an in-plane vibrational mode exhibited a blue shift. The observed blue shift of the $E_{2g}{}^1$ peak has been associated with the symmetry breaking of this vibrational mode, which arises from the application of strain within the $MoS_2$ layered structure [Conley et al., 2013]. The blue shift of the pristine $MoS_2$ mode relative to the initially pristine $MoS_2$ implies that the strain induced by the presence of Mo–N bonding is compressive, suggesting a contraction of the $MoS_2$ lattice due to nitrogen being introduced as a dopant [Azcatl et al., 2016; Hui et al., 2013]. This phenomenon is reminiscent of silicon, wherein compressive strain is instigated by the doping with boron or carbon atoms [Tillack et al., 1995]. Moreover, in addition to the compressive strain effects in the N-doped $MoS_2$ system, charge doping effects are likely to influence the observed in Raman signal, which is manifested as a shift in the out-of-plane vibrational mode $A_{1g}$ [Chakraborty et al., 2012]. In alignment with the p-type doping of $MoS_2$ facilitated by substitutional nitrogen, the $A_{1g}$ peak exhibited a blue shift of 1.35 ± 0.07 $cm^{-1}$ subsequent to 5 minutes of exposure to $N_2$ plasma. The Raman spectra of Ag decorated $MoS_2$ and N-$MoS_2$ are depicted in Figure 1(b). It is abundantly clear from the spectra that the Raman intensity experiences a remarkable amplification in the Ag-$MoS_2$, when compared to the pristine $MoS_2$ [Mukherjee et al., 2021; Wadhwa et al., 2023]. This

enhancement is attributable to the captivating SERS (surface enhanced resonance scattering) effect [Wadhwa et al., 2022a; Wang et al., 2022].

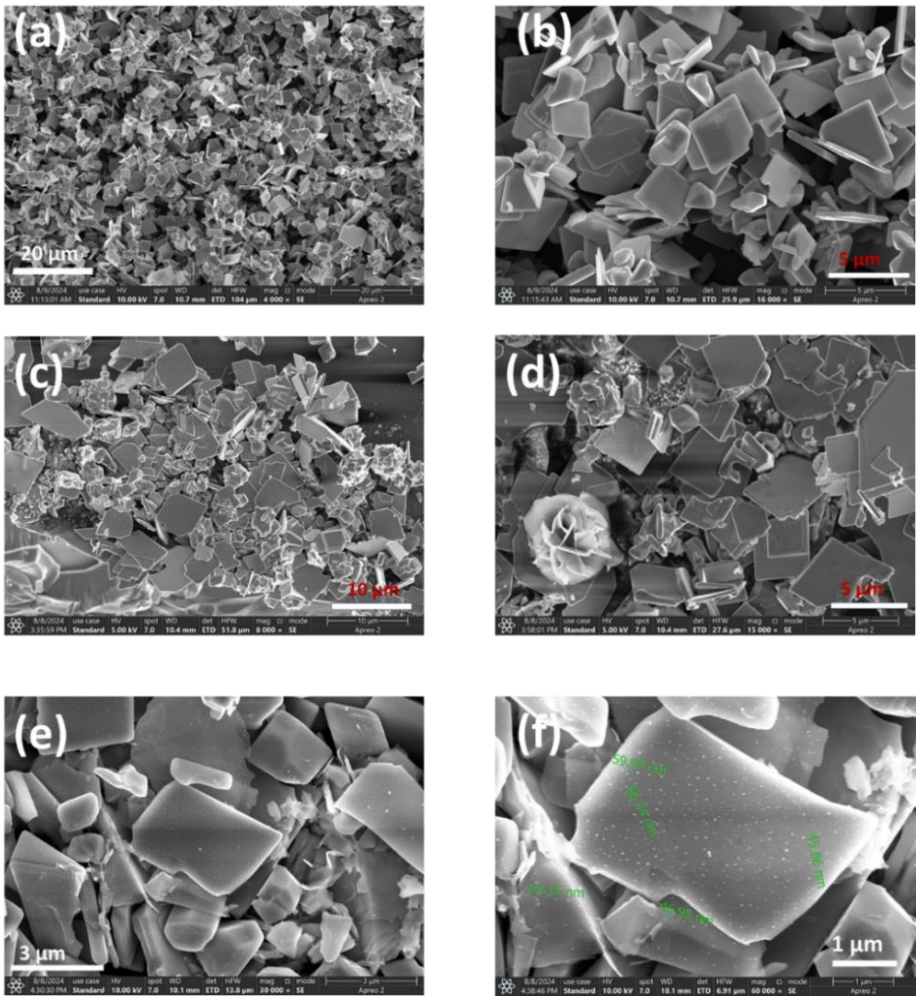



**Figure 4.1:** FE-SEM images of (a) Grown $MoS_2$ flakes, (b) High-resolution image of $MoS_2$ flakes, (c) Nitrogen plasma treated $MoS_2$ ($N\text{-}MoS_2$) flakes, (d) High magnification view of $N\text{-}MoS_2$, (e) Ag NPs anchored $N\text{-}MoS_2$ ($Ag\text{-}N\text{-}MoS_2$) flakes, and (f) High-resolution image of $Ag\text{-}N\text{-}MoS_2$ flakes. The average size of Ag NPs is 50nm.

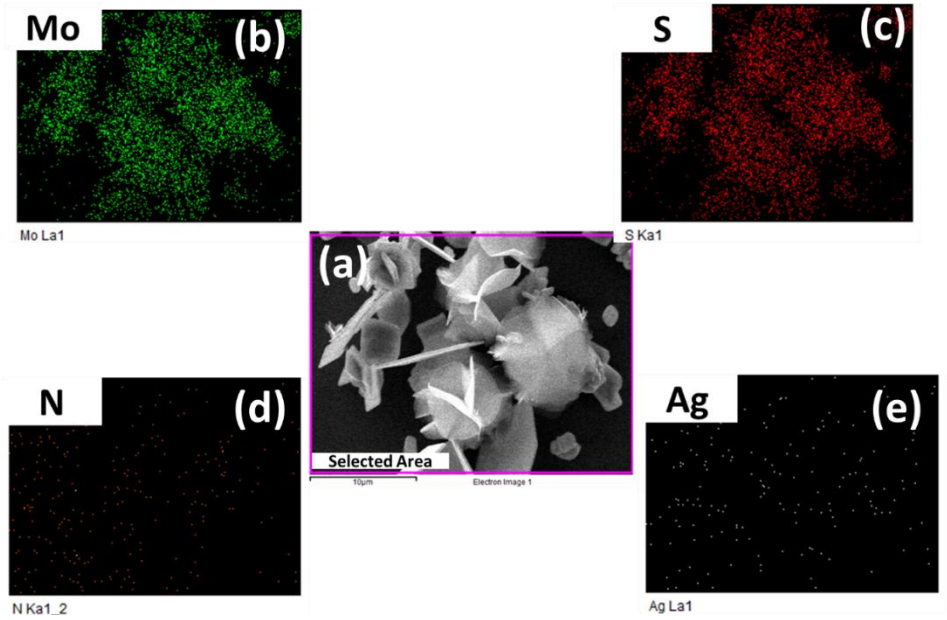



**Figure 4.2** Energy dispersive spectroscopy (EDX) elemental mapping of $Ag\text{-}N\text{-}MoS_2$ sample (a) Area selected, Elemental mapping of (b) Molybdenum (Mo), (c) sulfur (S), (d) Nitrogen (N), and (e) Silver (Ag).

The intricate methodology of integrating N as a dopant via nitrogen plasma within the crystalline architecture of pristine $MoS_2$ alongside the careful deposition of Ag NPs on their surfaces, which culminated in the fabrication of hybrids such as Ag-$MoS_2$, and Ag-N-$MoS_2$, X-ray photoelectron spectroscopy (XPS) was performed on samples, as depicted in Figure 4.3 (b-e). The spectral signals corresponding to Mo 3d, S 2p, Mo 3p, and Ag 3d were discernible. Within the framework of Pristine $MoS_2$, the Mo 3d core level distinctly bifurcates into two peaks, namely Mo $3d_{5/2}$ and Mo $3d3_{/2}$, corresponding to $Mo^{+4}$, located at binding energy positions of 229.62 and 232.75 eV, respectively. The S 2p core level also splits into two doublets, S $2p_{3/2}$ and S $2p_{1/2}$, harmoniously centered at 162.5 and 163.72 eV, respectively, linked to divalent sulfide ($S^{-2}$). These binding energy positions for Mo 3d and S 2p core levels resonate perfectly with the reported $MoS_2$ [Amin et al., 2018; Kumar et al., 2018a; Wadhwa et al., 2023]. The peaks attributed to $Mo^{+6}$ is located at 235.68 eV, respectively [Zhao et al., 2024a]. This phenomenon can be attributed to the oxidation processes occurring on the surface of $MoS_2$. Additionally, a Mo-S peak centred at a binding energy of 226.74 eV was also detected. An intriguing comparative XPS investigation of pristine, and 5-minute plasma-enhanced $MoS_2$ samples discloses a nuanced red shift of 0.43eV in the Mo 3d and S 2p peaks present in the treated sample, as shown in Figure 4.3 (b, c) [Azcatl et al., 2016]. N-Mo bond formation is further supported by the presence of N 1s core-level spectra, as seen in XPS analysis (Figure 4.3 (d)). The N 1s spectrum of N-$MoS_2$ is deconstructed into two peaks: one associated with Mo $3p_{3/2}$ at 395.24 eV, and peak at 398.22 eV corresponding to the characteristic signal of the N-Mo bond [Hu et al., 2018; Tan et al., 2021]. It is crucial to note that the Mo $3p_{3/2}$ region overlaps with the N 1s region, as illustrated by the peak attributed to $MoS_2$ at 395.24 eV. Furthermore, N displayed no reactivity with S, as the S 2p region revealed no evidence of S–N bonding [Azcatl et al., 2016]. Thus, the favorable formation of a covalent bond between Mo and N is distinctly highlighted, indicating that N preferentially replaces S atoms within the $MoS_2$ structure [Azcatl et al., 2016]. Overall, a tunable N concentration could be achieved under the specified plasma exposure conditions. The shifts in peak positions within the treated sample fundamentally reflect a change in the electronic band architecture. It is highly probable that the Fermi level has descended toward the valence band, a consequence of S-vacancy creation and the nitrogen atom engages with molybdenum to establish a novel bond [Ma et al., 2013]. These S-vacancies could very well convert the $MoS_2$ from n-type to p-type [Azcatl et al., 2016; McDonnell et al., 2014]. Conversely, the emergence of a doublet of peaks at 374.15 eV and 368.15 eV, linked to Ag 3d states arising from the $3d_{3/2}$ and $3d_{5/2}$ orbitals respectively, substantiates the successful deposition of Ag NPs on the surface of the Ag-$MoS_2$ and Ag-N-$MoS_2$, as illustrated in Figure 4.3 (e) [Ansari et al., 2022; Yin et al., 2020]. However, following the integration of Ag NPS onto $MoS_2$, a striking redshift of 0.74 eV is detected in both the Mo 3d and S 2p core levels. This observed redshift in the core-level positions of Mo 3d and S 2p in Ag-$MoS_2$ strongly suggests the phenomenon of strain effect [Richter et al., 2004]. Hence, X-ray photoelectron spectroscopy (XPS) analyse is complementary and illustrate the p-doping in $MoS_2$ subsequent to the incorporation of nitrogen through the plasma treatment.

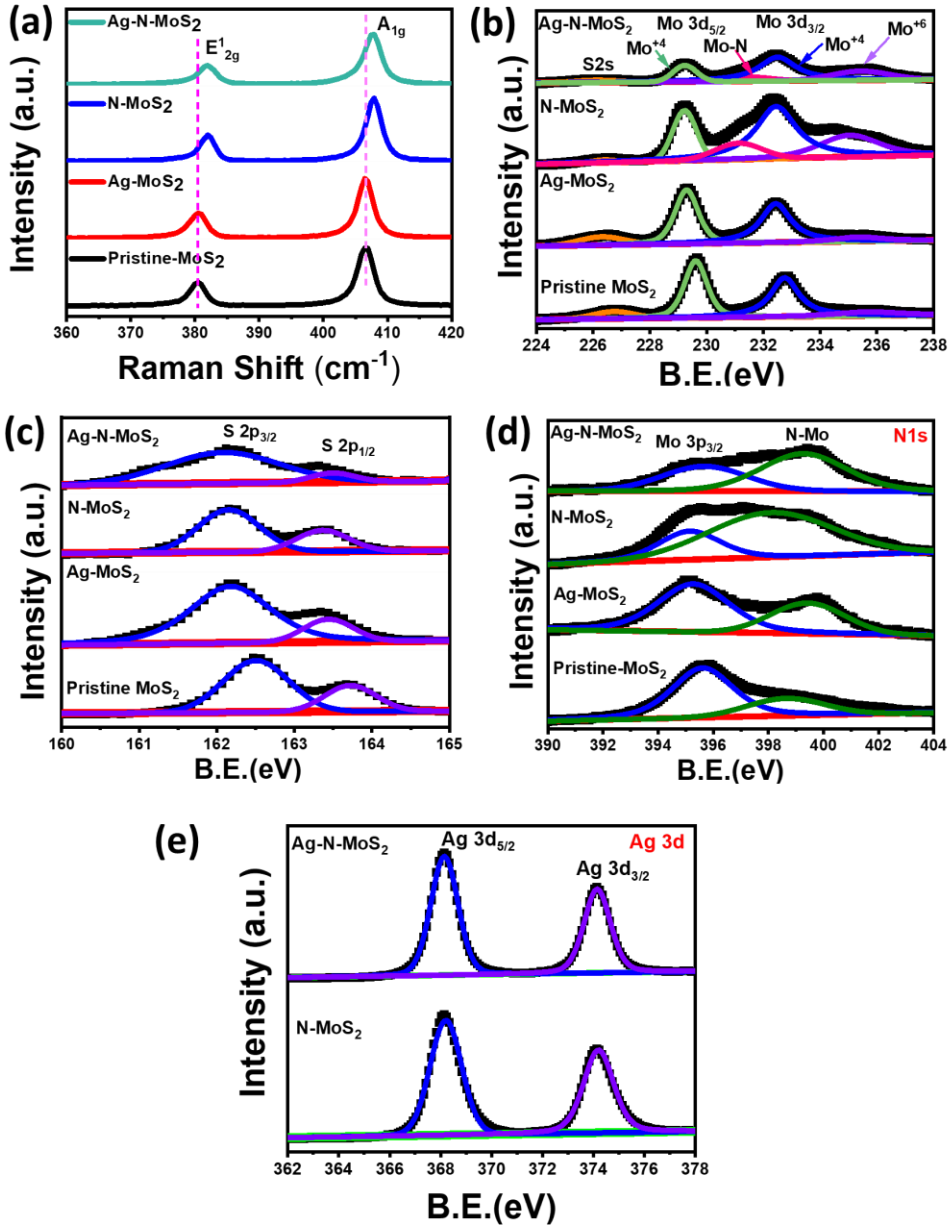



**Figure 4.3:** Raman spectra of the pristine $MoS_2$, Ag-$MoS_2$, N-$MoS_2$ and Ag-N-$MoS_2$.**(a)** High-resolution XPS spectra for the N pristine $MoS_2$, Ag-$MoS_2$, N-$MoS_2$ and Ag-N-$MoS_2$, **(b)** Mo 3d, **(c)** S 2p, **(d)** N1s, and **(e)** Ag 3d.

### 4.3.2. $NO_2$ Gas Sensing Performance of $MoS_2$ Flakes

The $MoS_2$ flakes were then examined for the presence of 1% $NO_2$ at various temperatures. The 1% concentration is equivalent to 10,000 ppm. The phenomena of gas molecular absorption and desorption on the surfaces of $MoS_2$, within the theoretical paradigms of semiconductor gas sensing, can be significantly influenced by temperature variations. The $MoS_2$-based gas sensors were developed on $SiO_2$/Si substrates, as depicted schematically in Figure 4.4 (a). Initially, the sensing characteristics of the pristine $MoS_2$ device were meticulously investigated for its interaction with $NO_2$ gas across a range of concentrations from 50 to 1 ppm at RT to 125 °C. Upon the introduction of $NO_2$ gas, a reduction in the sensor's resistance was observed, as illustrate in Figure 4.4 (b). The relative sensitivity of the sensor exhibits an enhancement corresponding to the elevation in $NO_2$ concentration. The following formula was used to determine the device's relative response:

$$(\Delta R/R_a) \times 100\% = (R_g - R_a)/R_a \times 100\% \qquad (4.1)$$

where $R_a$ is the device's initial resistance in air and $R_g$ is its resistance in the gas environment. As illustrated in Figure 4.4 (b), the relative response of the $MoS_2$ gas sensor exhibits a positive correlation with increasing temperature, achieving an optimal operational temperature of 100 °C, which corresponds to a peak response of 23%. Figure 4.4 (c-f) demonstrates the dynamic resistance and relative response of pristine $MoS_2$ under different concentration of $NO_2$ gas at operating temperature RT and 100 °C. It is evident that the relative response escalates with the augmentation of $NO_2$ concentration. Figure 4.5, shows the resistance and relative response analysis of pristine $MoS_2$ towards $NO_2$ gas at temperature 50 °C, 75 °C and 125 °C. The mechanism underlying gas sensing is fundamentally predicated on the charge transfer phenomena between the gas molecules and $MoS_2$. Due to the presence of an unpaired electron in the nitrogen atom, $NO_2$ functions as an electron acceptor, thereby facilitating the extraction of an electron from $MoS_2$. The observed reduction in resistance subsequent to $NO_2$ exposure indicates the p-type semiconductor behavior of $MoS_2$. Thus, the augmented sensing response indicates that the initial elevation of the operating temperature promotes the adsorption and charge transfer processes. However, a further increase in temperature beyond 100 °C resulted in a pronounced decline in the sensing response, likely attributable to the dominance of the $NO_2$ desorption process at elevated temperatures.

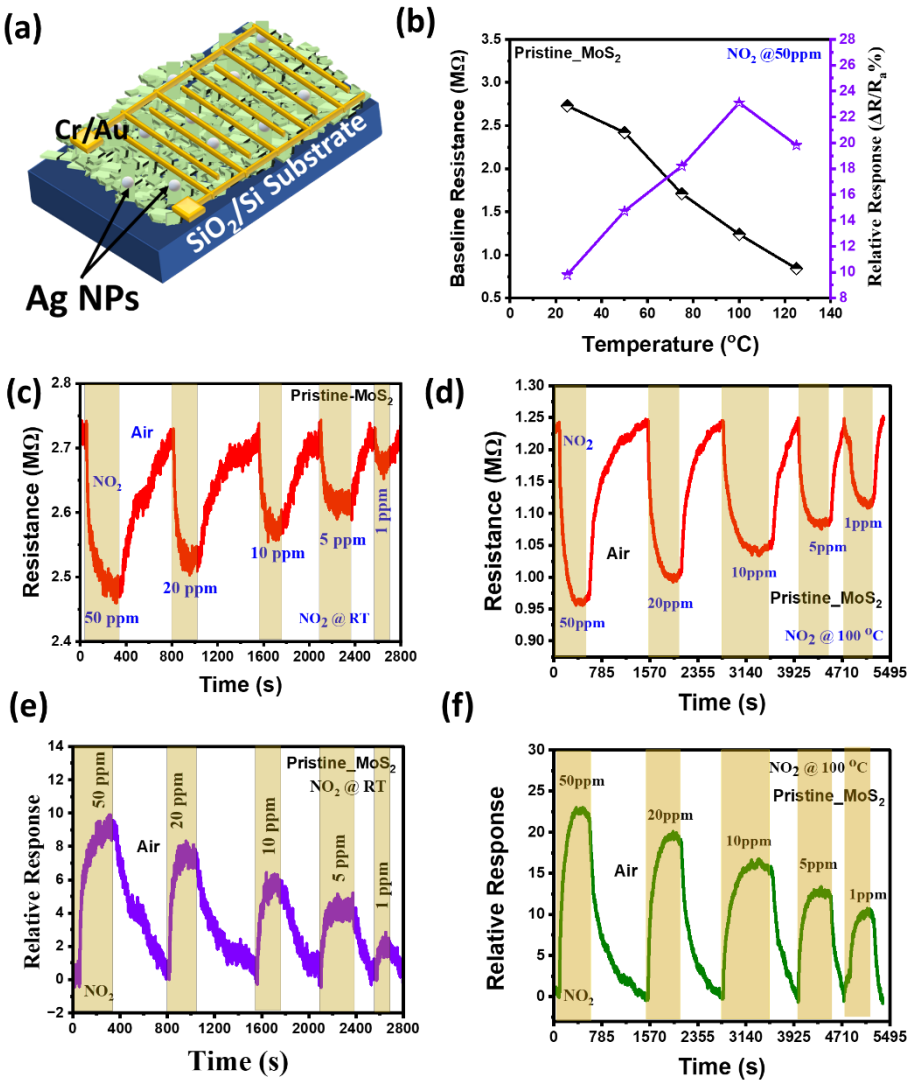



**Figure 4.4:** (a) Schematic of the Ag NPs-decorated N-$MoS_2$ sensor, (b) Comparison of variation in baseline resistance (absence of gas) and relative response of the pristine-$MoS_2$ sensor with temperature, (c) Resistance versus time plot of the pristine-$MoS_2$ under exposure to NO2 gas ranging from 50 to 1 ppm at RT, (d) Relative response characteristics of the pristine-$MoS_2$ sensor at RT, (e) Resistance versus time plot of the pristine-$MoS_2$ under exposure to $NO_2$ gas ranging from 50 to 1 ppm at 100 °C, (f) Relative response characteristics of the pristine-$MoS_2$ sensor at 100 °C.

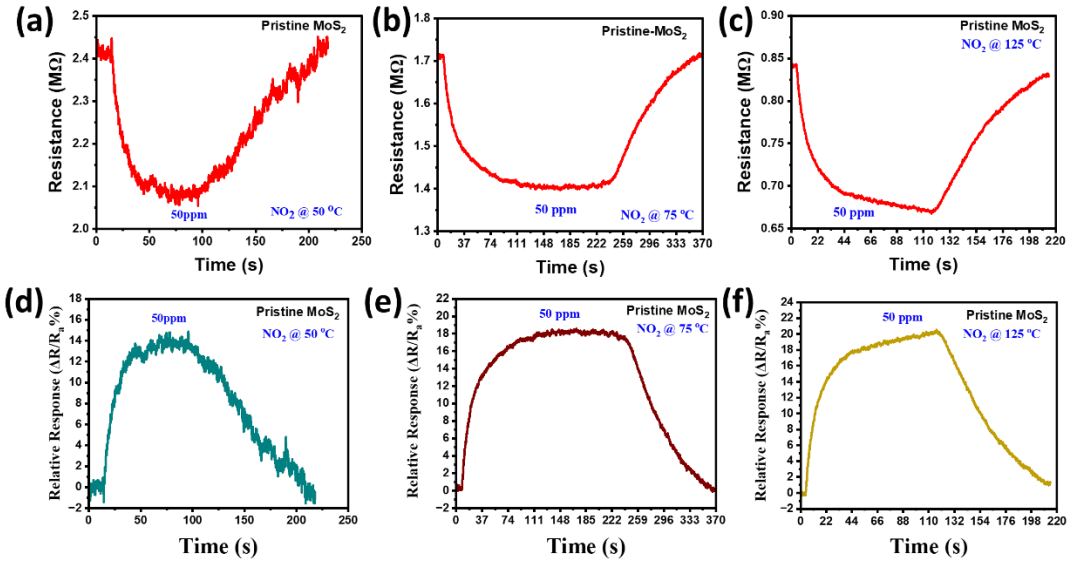



**Figure 4.5:** Real time change in resistance at temperature (a) 50 °C, (b) 75 °C, (c) 125 °C, and Real time change in response at temperature (d) 50 °C, (e) 75 °C, (f) 125 °C, of pristine MoS2 as function of 50 ppm $NO_2$ concentration.

### 4.3.3. Effect of nitrogen plasma treatment on $MoS_2$ (N-$MoS_2$) Flakes toward $NO_2$ Gas Sensing Performance

To enhance the relative response of the device, nitrogen was induced on the surface of $MoS_2$ via $N_2$ plasma treatment of the $MoS_2$ sample (details provided in chapter 3).

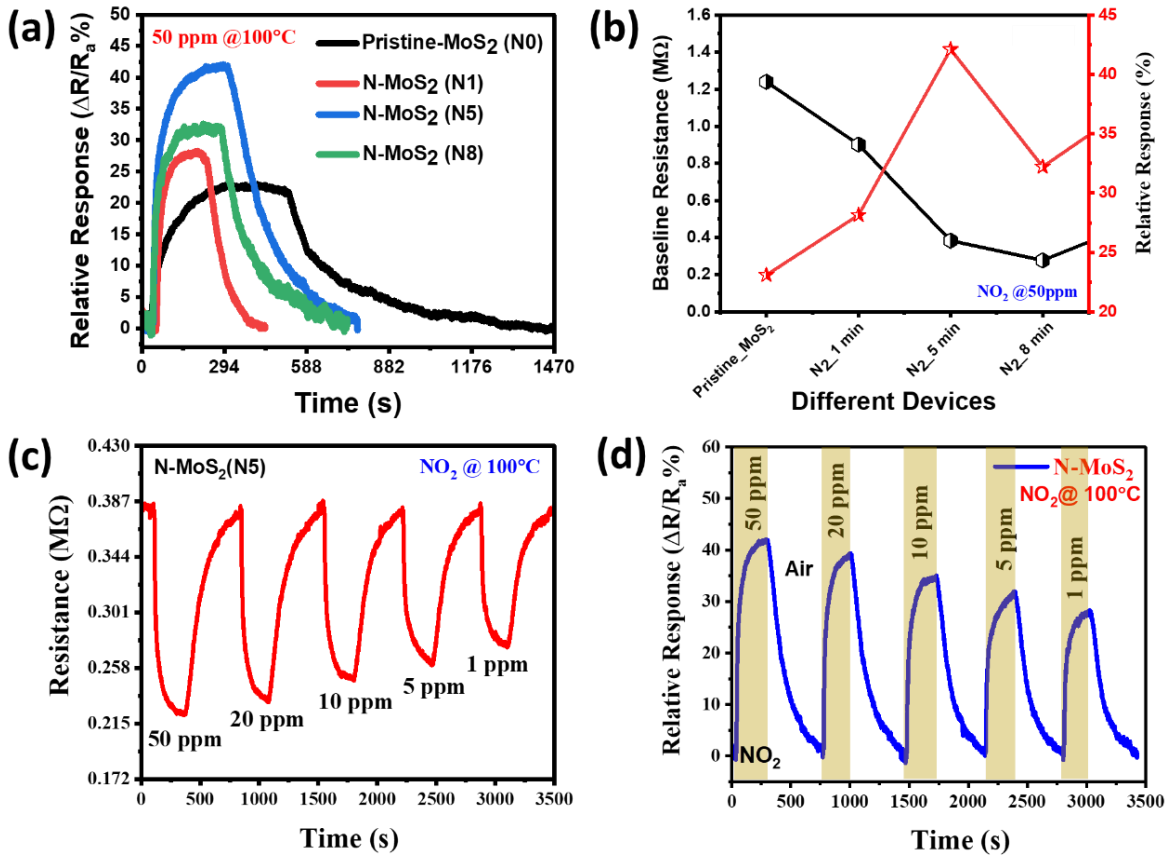



**Figure 4.6:** (a) Comparison of response of N0, N1, N5, and $N_8$ sensors for 50 ppm of $NO_2$, respectively, (b) Comparison of baseline resistance and response of N0, N1, N5, and N8 sensors for 50 ppm of $NO_2$, respectively, (c) Real time change in resistance, and (d) Transient relative response of N-$MoS_2$ device for different concentration of $NO_2$ at 100 °C.

The sensing response of the N-$MoS_2$ device was monitored for different duration of plasma treatment at 100 °C at different concentration of $NO_2$ gas. The calibration response graph for both untreated and plasma-treated $MoS_2$-based sensors (N0, N1, N5, and N8 samples) pertaining to a concentration of 50 ppm $NO_2$ gas at 100 °C is illustrated in Figure 4.6 (a) As depicted in Figure 4.6 (b), it was noted that the N-$MoS_2$ (N5) device displayed an enhanced response of approximately 42.09% to 50 ppm $NO_2$ at 100 °C, surpassing that of all other devices and exhibiting a response ~1.8 times greater than that of the pristine $MoS_2$ device (N0). It is evident that the sensor current reduces as the concentration of $NO_2$ gas increase. Figure 4.6 (c, d) shows N-$MoS_2$ (N5) sensor resistance as well response vs time profile for different concentration of $NO_2$ gas ranges from 5-50 ppm at 100 °C. In Figure 4.4 (c) and Figure 4.6 (c), both N-$MoS_2$ and $MoS_2$ are characterized by p-type semiconductor attributes, with the resistance decrease upon exposure to $NO_2$ gas. Upon a transition of the surrounding environment from $NO_2$ to atmospheric conditions, the resistance values of both sensors gradually increase, returning to their original states. The initial resistance of N-$MoS_2$ is lower than that of $MoS_2$, attributable to the band gap narrowing induced by N-doping in $MoS_2$.

### 4.3.4. Effect of surface functionalization of silver nanoparticles (Ag NPs) on pristine-$MoS_2$ and N-$MoS_2$ Flakes toward $NO_2$ Gas Sensing Performance

To achieve improved gas sensor response and selectivity, we have conducted the functionalization of the Ag NPs for 10 s on N-$MoS_2$ and pristine $MoS_2$ sensor, and investigated the in the sensing properties after decoration of Ag NPs. Figure 4.7 (a, b), illustrates the variations in sensing response and baseline resistance after decoration of Ag NPs for N-$MoS_2$ and pristine $MoS_2$ for 50 ppm of $NO_2$ gas at 100 °C. We noted an increase in the sensing response from 42.09% to 71.02% after Ag NPs decoration for a concentration of 50 ppm of $NO_2$ gas molecules. Figure 4.7 (c), demonstrates the sensor response curves of pristine $MoS_2$, Ag-$MoS_2$, N-$MoS_2$, and Ag-N-$MoS_2$ sensors to $NO_2$ gas at different concentrations ranging between 1 and 50 ppm. The responses of each sensor exhibit a positive correlation with the increasing concentrations of $NO_2$ gas. Furthermore, in comparison to the other sensors, the Ag-N-$MoS_2$ reveals the most pronounced response towards $NO_2$.

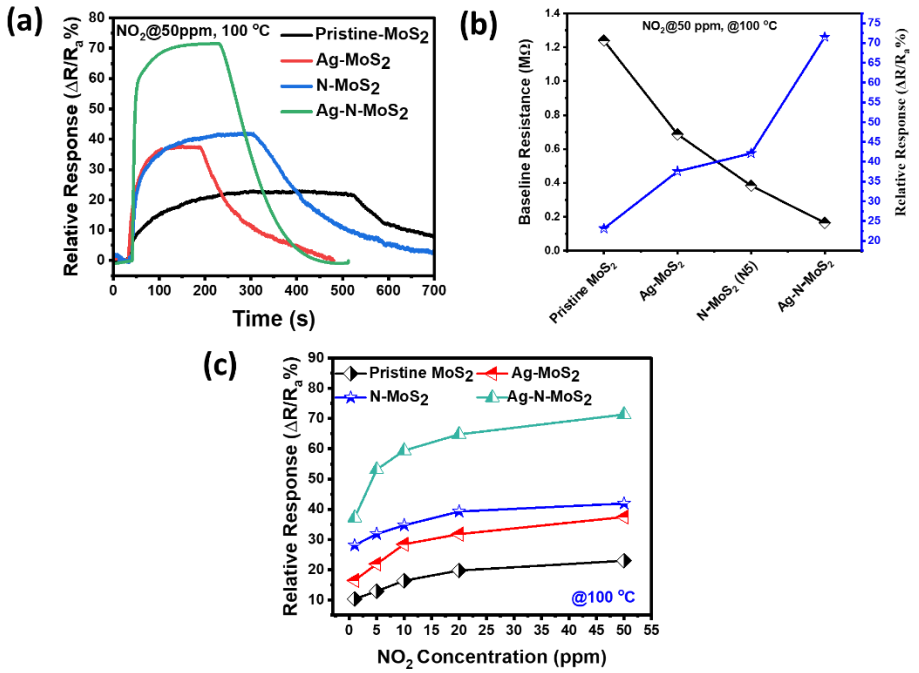



**Figure 4.7:** (a) Comparison of the relative response for pristine $MoS_2$, nitrogen plasma treated $MoS_2$ (N-$MoS_2$), Ag functionalized sensor (Ag-$MoS_2$, and Ag-N-$MoS_2$) for 50 ppm of $NO_2$, (b) Baseline resistance and relative response curve of the pristine $MoS_2$, Ag-$MoS_2$, N-$MoS_2$, and Ag-N-$MoS_2$ sensors for 50 ppm of NO2, and (c) Relative response versus different concentration of NO2 gas curve of the pristine $MoS_2$, Ag-$MoS_2$, N-$MoS_2$, and Ag-N-$MoS_2$ sensors for 50 ppm of $NO_2$ at 100 °C, respectively.

Figure 4.8 (a-d) depicts the transient relative resistance and response of Ag-$MoS_2$, and Ag-N-$MoS_2$ sensor devices for different concentration of $NO_2$ at 100 °C. The observed increase in sensor response following functionalization can be elucidated through the mechanisms of spillover and the chemical sensitization effect of the Ag nanoparticles on the surface of the $MoS_2$ film.

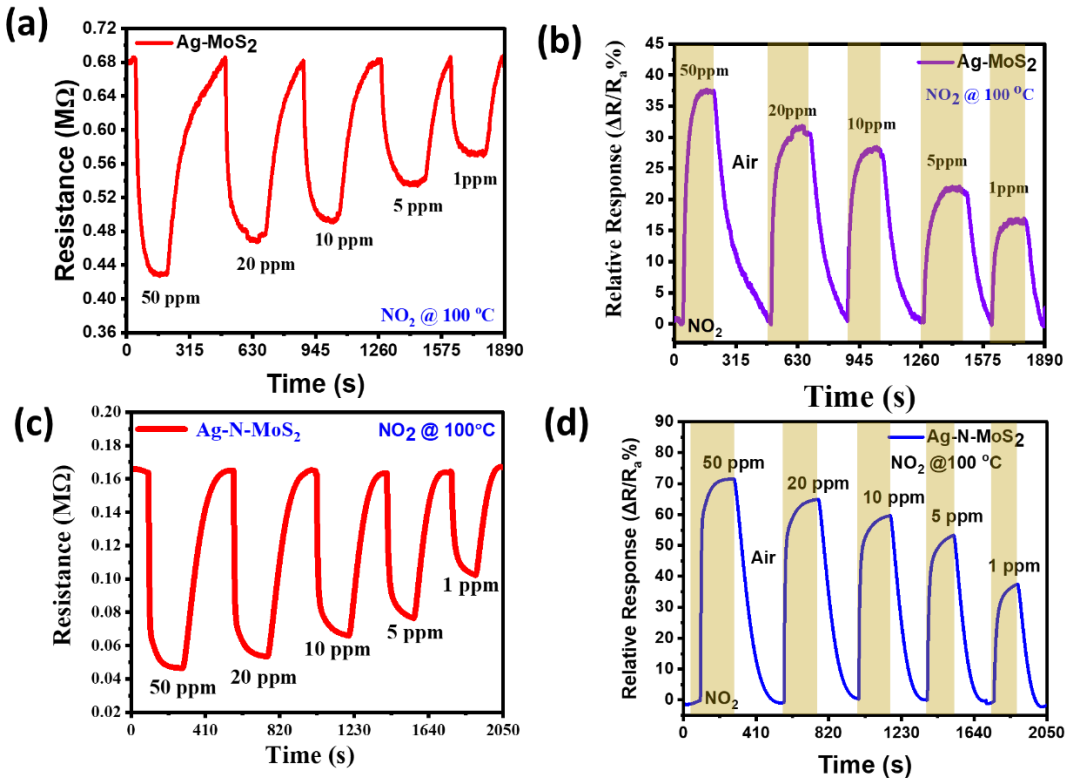



**Figure 4.8:** Transient relative resistance and response for different concentration of NO2 at 100 °C (a, b) Ag-$MoS_2$, and (c, d) Ag-N-$MoS_2$.

### 4.3.5. Response and recovery time of the pristine-$MoS_2$, Ag-$MoS_2$, N-$MoS_2$ and Ag-N-$MoS_2$ sensors

In order to determine the 2D-material-based sensors response ($\tau_{rise}$) and recovery time ($\tau_{fall}$), the pristine-$MoS_2$, Ag-$MoS_2$, N-$MoS_2$ and Ag-N-$MoS_2$ sensors static responses have been studied. In order to accomplish this, the sensor response change over time under a fixed $NO_2$ gas concentration was observed. Figure 4.9, illustrates the response and recovery times for the pristine $MoS_2$, Ag-$MoS_2$, N-$MoS_2$, and Ag-N-$MoS_2$ devices. The response time of a sensor is defined as the duration required to achieve 90% of the saturation level from the baseline value, whereas the recovery time is defined as the interval required to revert to 90% of the baseline value from the saturated sensing level. From Figure S5, we deduced that the response and recovery times were calculated to be 151.62 s, 45.68 s, 71.07 s and 352.27 s, 199.349ss, 256.84 s, for the pristine $MoS_2$, Ag-$MoS_2$, N-$MoS_2$ sensors, respectively. Conversely, the Ag-N-$MoS_2$ sensor demonstrated improvements in both response and recovery times, recorded at 27.17 s and 132.24 s, respectively.

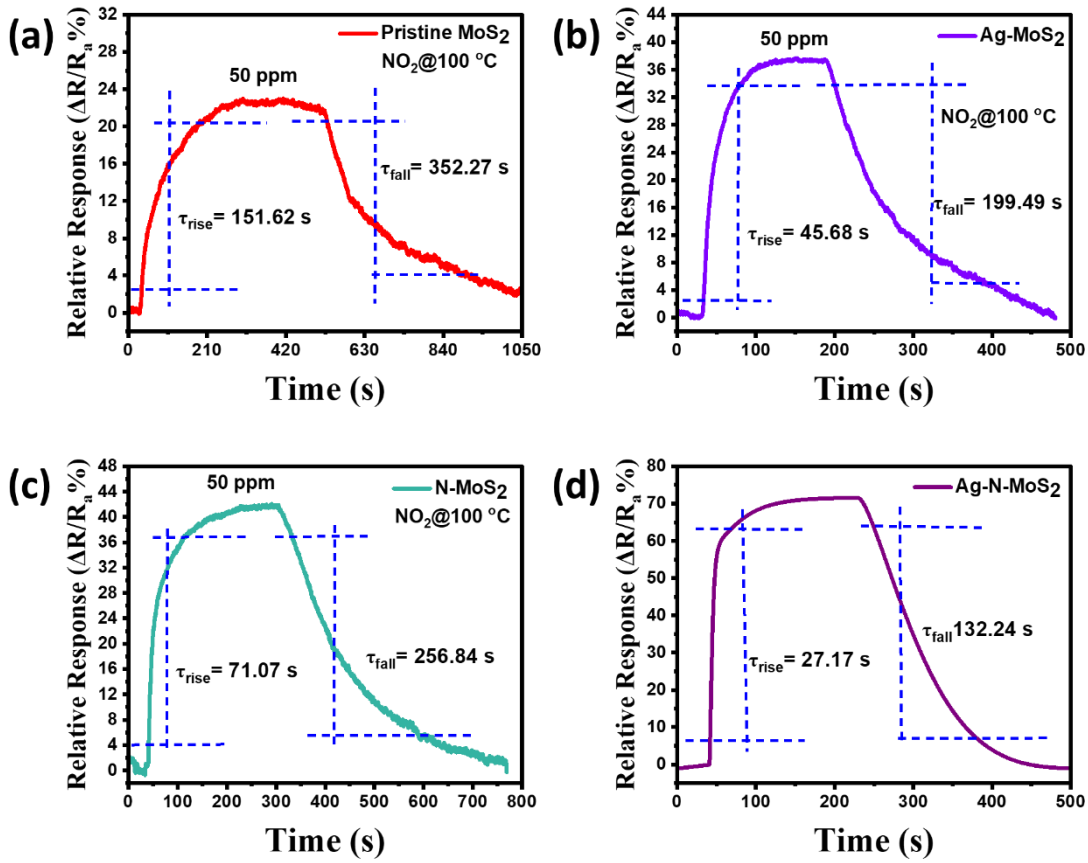



**Figure 4.9:** Response time and Recovery time of sensor under a 50 ppm NO2 concentration at 100 °C. (a) pristine $MoS_2$, (b) Ag-$MoS_2$, (c) N-$MoS_2$, and (d) Ag-N-$MoS_2$.

## 4.4 Long-term stability, Effect of Humidity, Short-term repeatability, and Selectivity of $MoS_2$ sensors

In the context of devices intended for practical applications, it is essential to investigate the influence of ambient parameters, such as long-term stability, humidity, repeatability and selectivity, which significantly impacts the performance of gas sensors based on 2D materials. Figure 4.10 (a), illustrates the long-term stability of the pristine $MoS_2$, Ag-$MoS_2$, N-$MoS_2$, and Ag-N-$MoS_2$ devices, when exposed to 50 ppm of $NO_2$ gas at 100 °C. The sensor's relative response was systematically evaluated on a weekly basis over a duration of 11 weeks, confirming the assertion that the developed Ag-N-$MoS_2$ sensor showcases considerable long-term stability. Also, all sensor i.e., pristine $MoS_2$, Ag-$MoS_2$, N-$MoS_2$, and Ag-N-$MoS_2$ were subjected to testing under varying humidity conditions (relative humidity ranging from 20% to 80%) at a temperature of 100 °C, revealing a marginal reduction in base resistance even at elevated humidity levels of 80%, as seen in Figure 4.10 (b). The concept of repeatability is a fundamental prerequisite for the assessment of sensor reliability. The repeatability of the Ag-N-$MoS_2$ sensor was systematically examined under conditions of 50 ppm $NO_2$ gas at 100 °C. The repetitive dynamic response, encompassing 12 consecutive cycles of the Ag-N-$MoS_2$ sensor, is illustrated in Figure 4.10 (c). Notably, no significant variation was detected in the sensor's response throughout the repeated cycles of $NO_2$ gas exposure and removal, thereby indicating that the sensor maintains its initial response characteristics and demonstrates exceptional repeatability. Furthermore, the sensing characteristics of pristine $MoS_2$, Ag-$MoS_2$, N-$MoS_2$, and Ag-N-$MoS_2$ were explored in the context of various ambient gases like $H_2$, $H_2S$, $NH_3$, $CO_2$, $CH_4$, and CO. The selectivity curve validates that Ag-N-$MoS_2$ sensor become more selective as compare N-$MoS_2$ Ag-$MoS_2$ and pristine $MoS_2$ for $NO_2$ gas, as shown in Fig 4.10 (d). Additionally, the performance characteristics of the Ag-N-$MoS_2$ sensor were compared with previously reported $MoS_2$ material-based $NO_2$ sensors, as presented in Table 4.1.

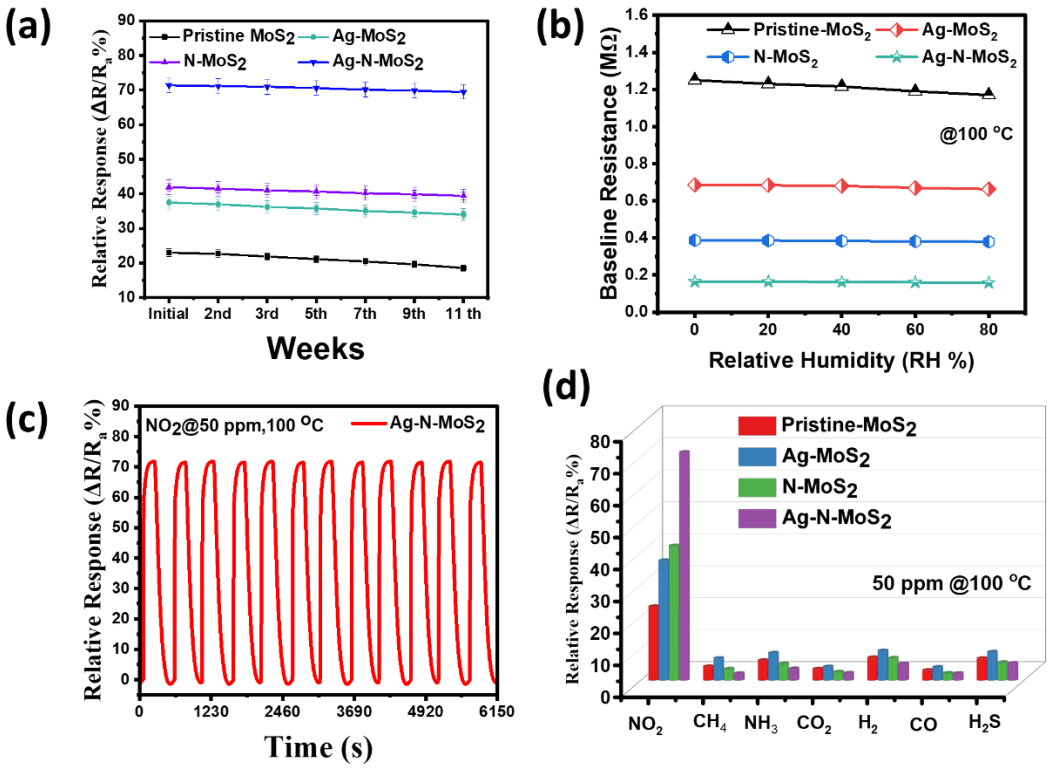



**Figure 4.10:** (a) The long-term stability of the pristine $MoS_2$, Ag-$MoS_2$, N-$MoS_2$, and Ag-N-$MoS_2$ devices to 50 ppm $NO_2$ gas at 100 °C, **(b)** Baseline resistance versus different relative humidity (RH %) of pristine $MoS_2$, Ag-$MoS_2$, N-$MoS_2$, and Ag-N-$MoS_2$ devices to $NO_2$ gas at 100 °C, **(c)** Repeatability of Ag-N-$MoS_2$ toward 50 ppm of $NO_2$ gas at 100 °C, and **(d)** Selectivity performance of pristine $MoS_2$, Ag-$MoS_2$, N-$MoS_2$, and Ag-N-$MoS_2$ devices to 50 ppm of various gases at 100 °C.

**Table 4.1:** Comparison of Various $MoS_2$ materials based $NO_2$ gas sensor

| Sensing materials | Operating Temperature (°C) | $NO_2$ (ppm) | Response | Rise/Fall Time (s) | Ref. |
|---|---|---|---|---|---|
| **$MoS_2$ flakes** | 100 | 100 | ~21.6[a] | 71/310 | [Kumar et al., 2017] |
| **$MoS_2$ hollow spheres** | 150 | 200 | 40.3[a] | 79/255 | [Li et al., 2019b] |
| **Ag–$Fe_2O_3$@$MoS_2$ nanocomposite** | 120 | 10 | 230.1[a] | 140/332 | [Yin et al., 2020] |
| **$MoS_2$/Graphene** | 200 | 0.5 | ~9[a] | 21.6/29.4 | [Long et al., 2016a] |
| **Pt-$MoS_2$ flakes** | 157 | 32 | 2.86[b] | 35/210 | [Zhao et al., 2023b] |
| **$MoS_2$@$SnO_2$** | RT | 100 | 34.67[b] | 2.2/10.54 | [Bai et al., 2021] |
| **$MoS_2$:2D-QC** | 100 | 100 | 66 | -/- | [Kumar et al., 2023b] |
| **$MoS_2$/$MoO_3$** | RT | 1 | 18.9 | 20/30 | [Yan et al., 2024] |
| **Nb-$MoS_2$** | 100 | 5 | 44 | 30/85 | [Ramaraj et al., 2022] |
| **Ag-N-$MoS_2$** | 100 | 50 | 71.02 | 27.17/132.24 | This work |

# [a]($\Delta R/R_a$ ), # [b]($R_a/R_g$)

## 4.5 Gas sensing mechanism

The gas-sensing mechanism associated with the pristine $MoS_2$ gas sensor relies on the change in resistance of the sensing devices due to the adsorption and desorption of target gas molecules at the surface of the sensing materials. This phenomenon constitutes the fundamental operational principle of the pristine $MoS_2$ sensors. When $MoS_2$ is exposed to ambient air, oxygen molecules adhere to the exposed surface, resulting in the formation of chemisorbed oxygen species $O^{\delta-}$ ($O_2$, $O^{2-}$, and $O^-$) through the extract an electron from the valence band of p-type $MoS_2$, thereby facilitating the development of a hole accumulation layer (HAL) in proximity to the surface, which results in an increase in resistance [Choi et al., 2015][75]. Upon interaction of the $NO_2$ molecule with the $MoS_2$ sensing layer, a weak interaction occurs at the active site of the sensing material. Given that $NO_2$ functions as an oxidizing agent and electron-withdrawing gas, electrons migrate from the $MoS_2$ surface to the $NO_2$ molecules, thereby inducing a modification in the resistance of the sensing material, as demonstrated in equations 4.2 and 4.3[Kumar et al., 2023a; Wadhwa et al., 2023].

$$O_2\ (gas) + e^- \rightarrow\ O_2^- \tag{4.2}$$

$$NO_2(gas) + e^- \rightarrow NO_2^- \tag{4.3}$$

In order to enhance the sensing abilities of the pristine $MoS_2$ sensor, we performed nitrogen plasma treatment for different time interval, as it has been reported that its change the electronics structure, higher absorption activity and more edge sites for catalytic reaction towards $NO_2$ gas molecules. We used density-functional theory (DFT) calculations to predict the relevant interaction parameters and compared the $NO_2$ oxidation energy with the full energy band diagrams of $MoS_2$ samples in order to uncover the surface impact of doped N atoms in $MoS_2$ (in chapter 6). Following the adsorption of $NO_2$, the energy bands of both $MoS_2$ and N-$MoS_2$ exhibit a negative displacement towards the valence band. Consequently, the electrical conductivities of both $MoS_2$ and N-$MoS_2$ are improved and decreased resistance, suggesting that they are p-type semiconductors. Nevertheless, as the conductivity of N-$MoS_2$ experiences an enhancement, the mobility of holes concurrently escalates, leading to a more rapid decrement in the resistance of N-$MoS_2$ as compared to pristine $MoS_2$.

To improve the performance of N-$MoS_2$, we also functionalized the surface of N-$MoS_2$ using the Ag NPs, as it serves as a catalyst by lowering the activation energy associated with reaction of $NO_2$. Silver decorated nitrogen doped $MoS_2$ monolayer increases $NO_2$ adsorption energy further to -1.33 eV. The phenomena of chemical sensitization and electronic sensitization represent two distinct methodologies employed to elucidate the improved sensing response. The proposed gas-sensing mechanism for the N-$MoS_2$-based gas sensor incorporating Ag NPs is represented in Figure 4.11. In the context of chemical sensitization, the Ag NPs situated on the surface of the N-$MoS_2$ sensing layer function as a catalytic agent, thereby facilitating the dissociation of molecular oxygen ($O_2$). Consequently, there will be a transfer of electrons from Ag to N-$MoS_2$, thereby enhancing the gas adsorption capacity of the gas sensor. Furthermore, the incorporation of Ag NPs will induce a chemical sensitization effect, facilitating the dissociation of analyte gases, which in turn significantly decreases both the response and recovery times of the sensor. Also, the uniform distribution of Ag NPs across the N-$MoS_2$ layer promotes the dissociation of $O_2$ through interactions with the Ag surface, which subsequently leads to an increased spillover of oxygen anions ($O^-$), resulting in a decrease of the resistance of the N-$MoS_2$ layer following the functionalization with Ag NPs. Moreover, during the exposure to $NO_2$, the presence of large $O^-$ anions significantly elevates the sensing response in comparison to the pristine $MoS_2$ sensor.

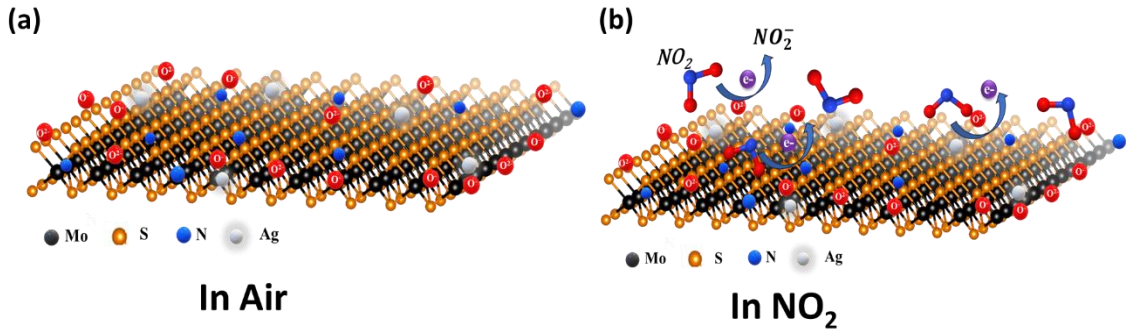



**Figure 4.11:** Schematic diagram proposed sensing mechanism.

## 4.6 Summary

In summary, we demonstrate that the sensing performance of CVD grown $MoS_2$-based $NO_2$ gas sensors can be significantly improved through the nitrogen doped and defect-selective surface functionalization of Ag NPs. Utilizing a combination of Raman spectroscopy and X-ray photoelectron spectroscopy, we validated the effective p-doping of $MoS_2$ through nitrogen plasma treatment and established beneficial band alignment, which is integral to the dynamics of charge carriers. Our comparative evaluation of the sensing responses from pristine $MoS_2$, N-$MoS_2$, Ag-$MoS_2$, and Ag-N-$MoS_2$ devices at an elevated temperature of 100 °C reveals that the Ag-N-$MoS_2$ configuration displays the most pronounced sensitivity to $NO_2$, thereby highlighting the synergistic interactions between silver nanoparticles and nitrogen doping. The Ag-N-$MoS_2$ sensor exhibited a remarkable response to $NO_2$ achieving 71.02% at 50 ppm at at 100 °C, with fast response (27.17 s) and recovery times (132.24 s). DFT calculations supported the strong adsorption of $NO_2$ on Ag-N-$MoS_2$ sensor. These results imply that Ag-N-$MoS_2$ possesses significant promise for the development of highly sensitive and efficient gas sensors, thereby facilitating future progress in environmental monitoring and detection methodologies.

# 5
# Improved Gas Sensing Performance of $SnS_2$ via Defect Engineering

In this chapter, we elucidate a highly selective and sensitive nitrogen dioxide ($NO_2$) gas sensor employing vertically aligned $SnS_2$ (VA-$SnS_2$) flakes. In the previous chapter 3, we already discussed about the synthesis process of VA-$SnS_2$ via a chemical vapor deposition (CVD) technique under meticulously controlled gas flow conditions. The morphology of the vertically aligned $SnS_2$ flakes was validated through scanning electron microscopy (SEM), Raman spectroscopy, and X-ray diffraction (XRD) analyses. The sensing behavior of these VA-$SnS_2$ structures was rigorously investigated for various concentrations of $NO_2$ at distinct temperature settings. Also, we study the various gas sensing performance parameters like response, selectivity, reliability of the fabricated n VA-$SnS_2$ sensor towards $NO_2$ gas. Although the device displayed excellent sensing response at room temperature (RT), it encountered challenges regarding high response time and recovery at RT. To augment the sensing characteristics, we implemented nitrogen plasma treatment on the VA-$SnS_2$ flakes, which resulted in a significant generation of surface vacancies. The duration of exposure during the plasma treatment was judiciously regulated, leading to considerable enhancements in the $NO_2$ sensing efficacy. Then, we examined the sensing properties of S-vacancy $SnS_2$ ($V_S$-$SnS_2$) flakes device to various concentration of $NO_2$ gas. After conducting a repeatability and selectivity test for the optimised $V_S$-$SnS_2$ flakes device, a highly $NO_2$ selective conventional sensor was fabricated. The findings suggest that the fabricated SnS2 sensor possesses substantial potential for utilization in the air purification and monitoring sectors. Additionally, this investigation lays the groundwork for forthcoming studies and innovative fabrication methodologies for 2D material-based gas sensors, aspiring for enhanced sensitivity and efficacy in the detection of toxic gases.

## 5.1 Requirement of highly selective and high response $NO_2$ Gas Sensor and Challenges

Sensors, as fundamental devices for acquiring and transmitting external data, play a critical role in our lives [Swan, 2012]. A gas sensor is a type of sensor that can detect gaseous pollutants in the environment, thus assisting in enhancing human health and productivity. It may be used in environmental monitoring [Walters et al., 2018], personal healthcare [Iitani et al., 2018], and production management. The concentration of hazardous and toxic gases such as $NO_2$, $H_2S$, $CO_2$, $SO_2$, and volatile organic compound (VOC) rapidly increases in environment due to continuous advancement in industrialization [Abbas et al., 2015; Liu et al., 2014a]. $NO_2$ is the most toxic and hazardous gas, and even at low concentration, it is dangerous to human health, which may cause throat irritation, dyspnea, and pulmonary edema, whereas prolonged exposure to a high concentration of $NO_2$ has carcinoma, which can cause cancer disease [Pyeon et al., 2020a; Yang et al., 2019]. Furthermore, since $NO_2$ gas can cause air pollution such as acid rain and photochemical smog, its detection is important for maintaining a healthy environment and helps human health. As a result, designing and fabricating a gas sensor with excellent sensitivity and selectivity for real-time detecting $NO_2$ gas in the atmosphere and in our immediate surrounds is awfully important.

Two-dimensional (2D) materials have received significant interest due to their atomically layered structures and excellent physical, optical, chemical, and mechanical characteristics and have wide applications in optoelectronics [Lin et al., 2015], flexible devices [Tsai et al., 2015], sensors [Nourbakhsh et al., 2016], tunneling field-effect transistors [Sarkar et al., 2015; Shao et al., 2020], and energy storage [David et al., 2014]. Graphene is the first-generation two-dimensional material, consisting of a single layer of carbon atoms that have $sp^2$ hybridization creating a honeycomb crystal structure [Zhang et al., 2018a]. The use of graphene in $NO_2$ sensing has been

a huge success because of its carrier mobility, good chemical stability, and large specific surface area [Zhang et al., 2018b].

Tin disulfide ($SnS_2$), a promising 2D layered nanomaterial, has received huge interest because of its earth-abundant, nontoxic, easy surface modification, and heavy metal-free properties [Kwon et al., 2019]. $SnS_2$ has shown exceptional performance in electrocatalytic reduction[Chu et al., 2020], optoelectronic devices [Gao et al., 2020], photocatalytic generation [Barba-Nieto et al., 2020], and particularly gas sensing [Huang et al., 2019], due to its distinctive structures and features. The $SnS_2$ nanostructure, which is similar to the graphene nanosheet, offers new possibilities for the manufacturing of nanotubes, nanowires (NWs), and vertically or horizontally aligned $SnS_2$ flakes for desired device applications [Kumar et al., 2022]. Xu *et al.,* [Xu et al., 2022], investigated the fabrication of a room temperature, all-optical, high-performance $NO_2$ sensor using a simple D-shaped optical fiber with ultrathin 2D $SnS_2$. When exposed to $NO_2$ gas at a low concentration of 50 ppb, this all-optical sensor shows an optical power change of up to 7 W. With an extraordinarily low limit of detection (LOD) of 0.464 ppb, this process is totally reversible. Ou *et al.,* [Ou et al., 2015], developed a novel gas sensor based on 2D $SnS_2$ flakes with a very high selectivity to $NO_2$ molecules, and this was accomplished at the optimal temperature of 120 °C, attaining detection limits of 30 ppb and demonstrating an amazing response factor of 36, when subjected to a concentration of 10 ppm of $NO_2$.

Furthermore, the physisorption of $NO_2$ on $SnS_2$ has been demonstrated to be based on intermolecular interactions, viz., van der Waals forces. The activation energy required for physisorption is much lower than that of chemisorption, and gaseous molecule physisorption can occur at low temperatures [Ou et al., 2015]. However, there are several barriers to the actual use of the material. To begin with, pristine $SnS_2$ has a poor gas sensing performance due to the low absorption of $NO_2$ and poor intrinsic conductivity [Shafiei et al., 2018]. Second, the resistance of $SnS_2$ in the atmosphere is high at low temperatures, but as the temperature goes up, there is a possibility of oxidation to $SnO_2$. Many recent studies have focused on the development of $SnS_2$-based heterostructures, such as $SnS_2$/SnS [Sun et al., 2019], $SnS_2$/$MoS_2$[Liu et al., 2020], g-$C_3N_4$/$SnS_2$ [Sun et al., 2020a], and $SnS_2$/$SnO_2$ [Hao et al., 2018] to improve the sensing response and lower the operating temperature. As is evident from these studies, the improved $SnS_2$ electronic structure and more active sites for $NO_2$ adsorption are responsible for the better $NO_2$ sensing capabilities.

There are other effective ways for modifying the electronic properties and improving the active surface area in addition to heterostructure development. For example, by incorporating anion vacancies into the catalyst lattice, vacancy engineering offers a way to increase electronic conductivity and create active surface area for adsorption. The presence of sulfur (S) vacancies has been shown to effectively reduce the band gap of $SnS_2$ and result in improved sodium storage performance [Wang et al., 2020a]. Several fascinating phenomena can emerge as a result of the changes in the intrinsic characteristics of materials when deficiencies are present. Despite several ways to enhance the gas sensing performance of $SnS_2$ by defect engineering [He et al., 2012], a few defects have resulted in significant improvements. The localization of electron density at the defect site, which greatly enhances sensing activity through orbital mixing and charge transfer, is a fundamental feature that governs the gas sensing capability. A theoretical investigation has shown that the $SnS_2$ monolayer with a S vacancy exhibits more sensitivity to $NO_2$ in comparison to NO, $NH_3$, $H_2O$, and CO molecules [Zhao et al., 2017b]. Hu *et al.,* used a high-energy ball milling technique to successfully introduce S vacancies and an in-plane $SnS_2$/$SnO_2$ heterojunction into $SnS_2$ nanosheets. Near the valence band maximum, the S vacancies in the $SnS_2$ structure introduce shallow electronic traps [Hu et al., 2020]. Zhang *et al.,* developed a defective nanosheet of $SnS_2$ using Ar plasma treatment and used it for $NH_3$ gas sensing applications [Zhang et al., 2020a]. Plasma treatment created a high number of surface defects on $SnS_2$ nanosheets, which were controlled with the exposure period to change the electronic configuration.

## 5.2 Synthesis, and nitrogen plasma treatment of Vertically Aligned $SnS_2$ flakes

In Chapter 3, the synthesis of Vertically Aligned $SnS_2$ (VA-$SnS_2$) flakes via a three-zone CVD approach had been discussed in depth. Tin dioxide ($SnO_2$) and sulfur (S) were used as precursors in the synthesis of VA-$SnS_2$ flakes, which were meticulously optimized. The sulfur and $SnO_2$ temperatures were kept at 200 °C and 1000 °C, respectively, for 90 minutes while an argon flow of 80 sccm. The next step was to use thermal evaporation to create interdigital electrode (IDE) of Au/Cr contact with a precise 100 µm spacing. In order to further improve the characteristics, surface vacancies were introduced into the VA-$SnS_2$ flakes using nitrogen plasma treatment, which was carried out for 4, 8, 12, and 16 minutes at an RF power of 10 W. Then, the fabricated devices were examined for different $NO_2$ concentrations, their gas sensing the ability demonstrated significant enhancement as a result of occurrence of S vacancies in materials through the nitrogen plasma treatment.

## 5.3 Characterization

### 5.3.1. Structure and chemical properties of $SnS_2$ flakes

The SEM images show that the $SnS_2$ flakes are vertically aligned and uniformly grown over the $SiO_2$/Si substrate as shown in Figure 5.1 (a) and (b). Vertically aligned surfaces are more sensitive as they have more adsorption site, which is required to get good sensitivity of the gas sensors. Raman spectroscopy was used to determine the orientation, crystallinity and vibration characteristics of the $SnS_2$ flakes. Figure 5.1 (c) shows, the Raman spectra of 2D $SnS_2$ having two active vibrational modes which are in-plane vibration ($E_g$) and out-of-plane vibration mode ($A_{1g}$) at ~205 $cm^{-1}$ and ~314 $cm^{-1}$, respectively. The out of plane mode $A_{1g}$ is strong peak and the in-plane mode $E_g$ is very less detectable, this might be due to the pruning in the scattering centers of in-plane mode of scattering. Mode $A_{1g}$ has no change in dipole moment and infra-red inactive and hence Raman active and vice versa for $E_g$.

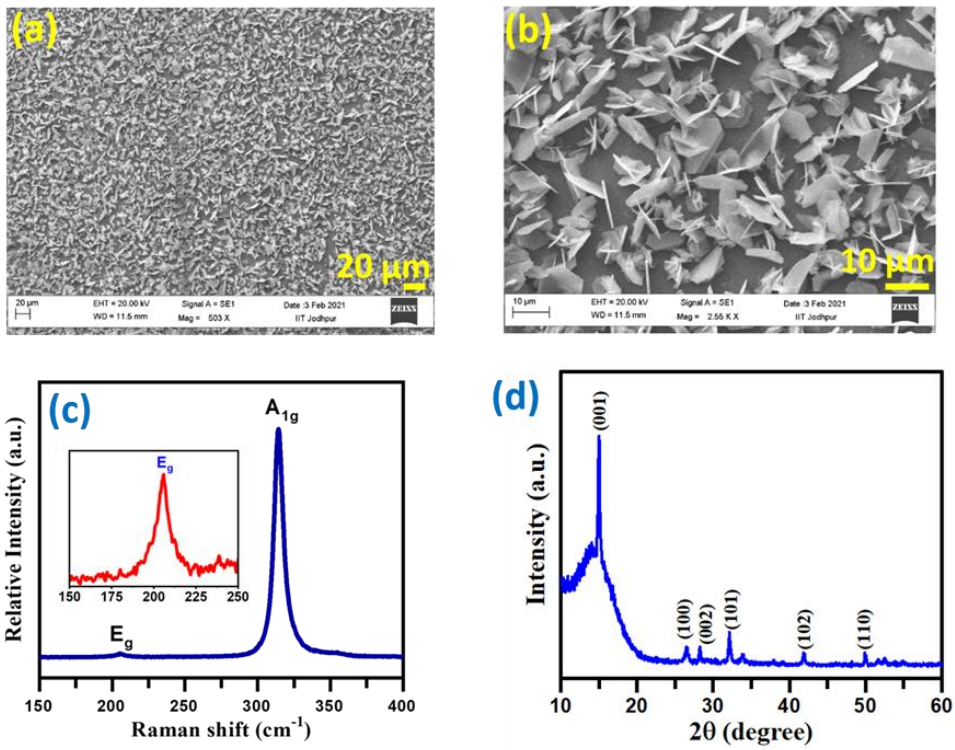



**Figure 5.1:** (a) SEM images of the vertically aligned $SnS_2$, (b) a magnified view of the flakes network, **(c)** Raman spectra of the vertically aligned $SnS_2$ flakes at 532 nm laser, and **(d)** X-Ray diffraction pattern of vertically aligned $SnS_2$ flakes.

Furthermore, X-ray diffraction (XRD) was used to confirm the purity and phase structure of the $SnS_2$. In Figure 5.1 (d), the diffraction peaks were observed at 15.0°, 28.4°, 30°, 32.3°, 42.1° and

50.2° corresponds to (001), (100), (002), (101), (102) and (110) planes of the defined XRD pattern of the hexagonal 2D $SnS_2$ (JCPDS # 23–0677). Raman and XRD results indicate that the synthesized layers have high purity and crystallinity [Bharatula et al., 2016; Ou et al., 2015].

### 5.3.2. Vacancy and Doping Investigation using FE-SEM Raman Spectroscopy, and XPS

The surface morphology of vertically aligned $SnS_2$ (VA-$SnS_2$) flakes is significantly altered by nitrogen plasma treatment, as shown by the FESEM image, in Figure 5.2 (a). It is observed that $SnS_2$ nanoflakes were vertically oriented, indicating smooth $SnS_2$ nanoflakes and revealed a large number of edge site of $SnS_2$ by interconnecting one another, as shown in Figure 5.2 (a). Between vertical $SnS_2$ nanoflakes, open pores occur, which allow $N_2$ plasma to pass through more easily and thereby promoting S vacancy generation. The $N_2$ plasma bombardment, in which the etching is never ideally isotropic, may produce edge passivation and surface roughening. Energy-dispersive X-ray spectroscopy (EDX) was also used to evaluate the elemental mapping and structure of VA-$SnS_2$) flakes, after nitrogen plasma treatment, as shown in Figure 5.1 (b-d). The removal of the S-atoms and subsequent formation of S-vacancies in the structure are likely caused by the $N_2$-plasma. The atomic ratio of S/Sn of the pristine $SnS_2$ is ~2.12, near to the ideal stoichiometry of $SnS_2$. However, the S/Sn ratio gradually decreased to 1.13 for 12 min -$SnS_2$ after nitrogen plasma treatment (N12).

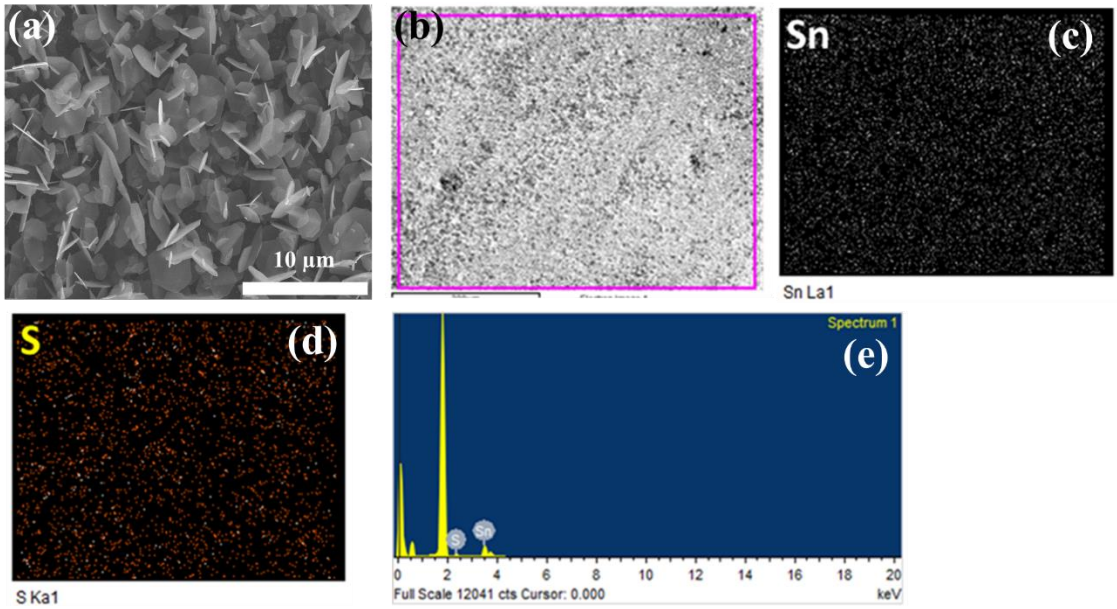



**Figure 5.2: (a)** FE-SEM image of the nitrogen plasma treated $SnS_2$ (Vs-$SnS_2$) flakes, Energy dispersive spectroscopy (EDX) elemental mapping of Vs-$SnS_2$ sample **(b)** Area selected, Elemental mapping of **(c)** Tin (Sn), **(d)** sulfur (S), **(e)** EDX spectrum of Vs-$SnS_2$ sample.

Raman spectroscopy may be used to examine the concurrent phase phenomena. The Raman spectra of pristine-$SnS_2$ and $N_2$ plasma treated samples are shown in Figure 5.3 (a). The spectra clearly show two different peaks at ~205 $cm^{-1}$ and ~314 $cm^{-1}$, which correspond to the in-plane $E_g$ and out-of-plane $A_{1g}$ vibrational modes of vertically aligned $SnS_2$ nanoflakes, respectively.[Huang et al., 2014; Ou et al., 2015] The shift in Raman peaks in $SnS_2$ are commonly attributed to defects, doping, and strain. Kim et al.,[Kim et al., 2013] found that in few-layer $MoS_2$, redshift in both modes of Raman peaks is due to vacancy of S atoms. Yang et al.,[Yang et al., 2014] discovered that compressive strain produced by a decreased spacing in crystal lattice, which result in redshift in the $E_{2g}{}^1$ and $A_{1g}$ vibration mode. The softening of the Sn–S phonon mode in the basal plane is illustrated by the increasing redshift of the $E_g$ peak of Vs-$SnS_2$, which may be attributed to the steadily declining number of Sn–S chemical bonds combined with the rising quantity of in-plane S vacancies.[Wang et al., 2020b] As a result, a feasible explanation is that S vacancies produce compressive strain and bond weakening due to decrease in the lattice spacing.

Furthermore, we identified that $A_{1g}$ mode have smaller redshift than $E_g$ mode, as depicted in Figure 5.3 (b). Due to the presence of in-plane chemical bonding between the S and Sn atoms, the vacancy of S atoms would have a greater influence on the $E_g$ mode.[Li et al., 2012b]

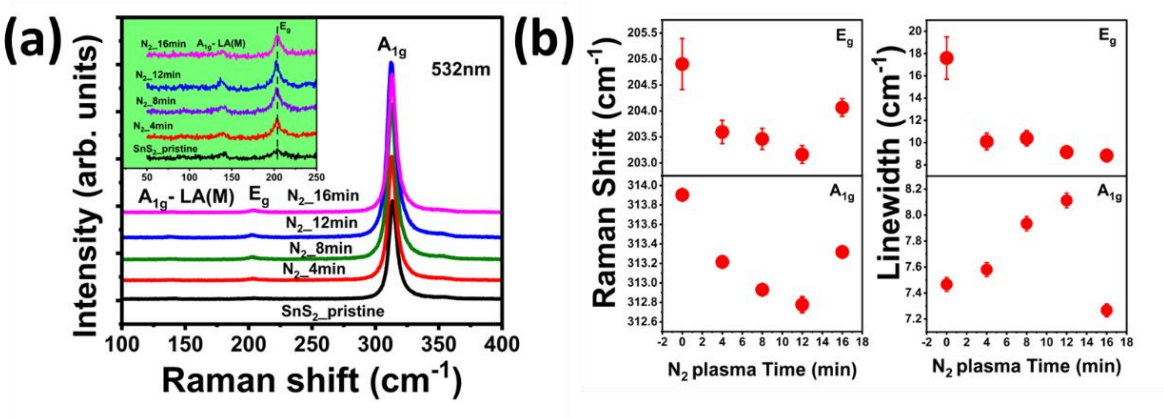



**Figure 5.3**: **(a)** Raman spectra of the $SnS_2$ nanoflakes, and **(b)** Change in Raman shift and Line width, before and after $N_2$ plasma treatment of $N_0$, $N_4$, $N_8$, $N_{12}$ and $N_{16}$ samples.

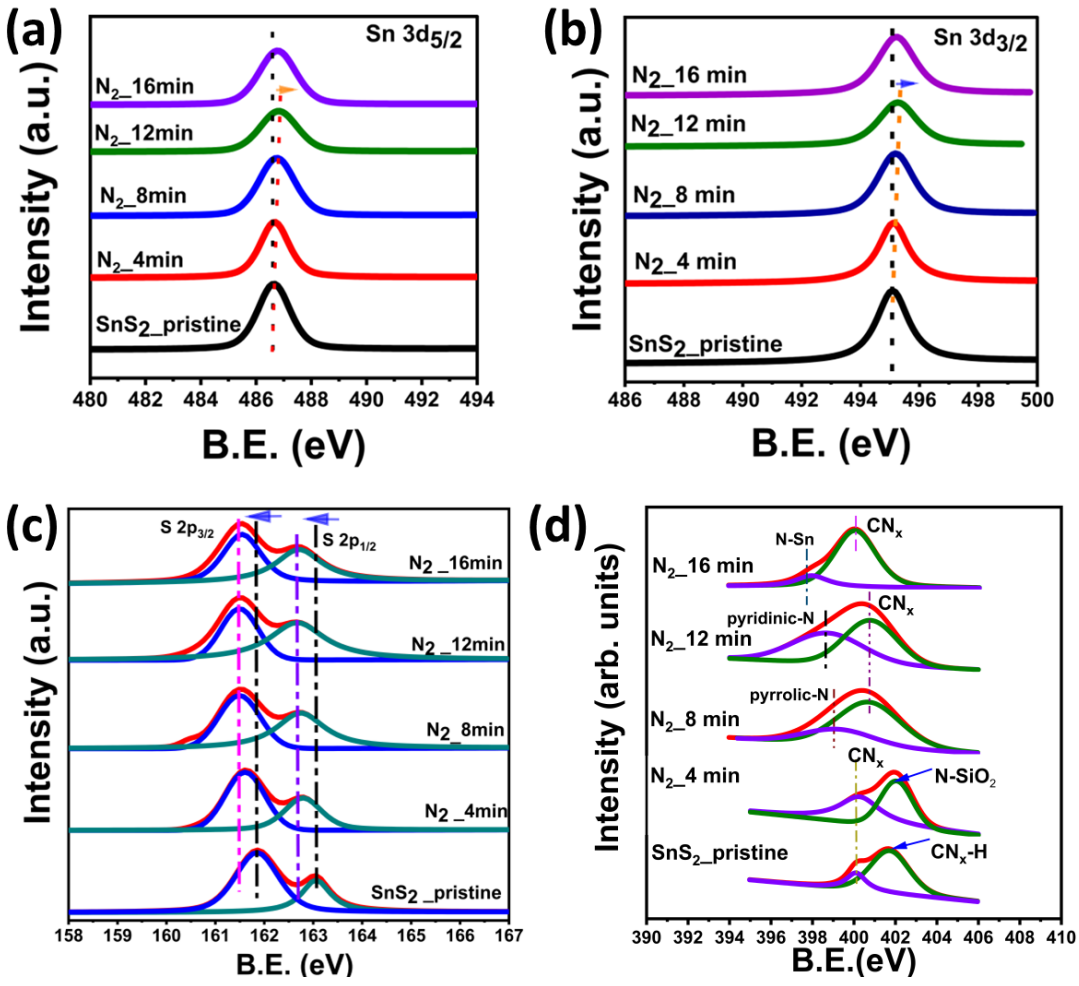



**Figure 5.4**: XPS spectra from pristine VA- $SnS_2$ and $N_2$ plasma treated VA- $SnS_2$, (a) Sn $3d_{5/2}$, (b) Sn $3d_{3/2}$, (c) S 2p, and (d) N1s.

The variations in chemical states and surface S vacancy concentrations were studied using X-ray photoelectron spectroscopy (XPS). The core-level spectra of Sn $3d_{5/2}$, Sn $3d_{3/2}$ and S 2p of the materials without and with treatment of RF plasma are shown in Figure 5.4 (a-c). Two prominent peaks observed in pristine $SnS_2$ at 486.64 eV and 495.08 eV may be ascribed to the Sn $3d_{5/2}$ and Sn $3d_{3/2}$, which show the existence of $Sn^{4+}$.[Liang et al., 2020; Zhang et al., 2020a] Figure 5.4 (c),

illustrates peaks of S $2p_{1/2}$ and S $2p_{3/2}$ centered at 163.06 eV and 161.85 eV, showing the $S^{2-}$ state of S of pristine $SnS_2$ and other S atoms like oxysulfide compounds, $SnS_x$ (with $x \neq 2$) phase, respectively. Furthermore, there is no evidence of $Sn^{2+}$ in the spectrum (binding energies 485.1 eV and 493.0 eV).[Ham et al., 2013; Yang et al., 2019] With increasing plasma-treatment time, the Sn $3d_{5/2}$ and S $2p_{3/2}$ peaks of $SnS_2$ are moved monotonically toward higher binding energy and lower binding energy respectively, which might be due to the increase in surrounding S vacancies.[Diao et al., 2021] XPS spectra of plasma treated Sn $3d_{3/2}$ and change in binding energy because of S vacancies are depicted in Figure 5.4 (b). Deconvolutions of 12 min plasma-treated S 2p XPS spectra reveal two peaks at 161.47 eV (S $2p_{3/2}$), and 162.71 eV (S $2p_{1/2}$) (bridging $S^{2-}$), implying the presence of sulfur defects in $SnS_2$, as illustrate in Figure 5.4 (c).

For comparison, the binding energy of S 2p spectra of RF plasma treated $SnS_2$ demonstrates lower binding energy than that of pristine-$SnS_2$ because of the presence of S vacancies and increase in electron density around the Sn and S sites.[Lu et al., 2016; Wang et al., 2020b] In the plasma treated sample, peak position shift effectively implies a change in the band structure of $SnS_2$. To the creation of S vacancies, the Fermi level has most likely been moved down to the valence band.[Ma et al., 2013] Furthermore, in the plasma-treated sample for 16 min (N16), a low intensity peak at 397.75 eV (violet fitted line in Figure 5.4 (d)) was observed in the N 1s spectra, confirming that nitrogen was present in $SnS_2$. The Sn-N bond is responsible for this peak.[Azcatl et al., 2016; Li et al., 2017; McDonnell et al., 2014; Xiao et al., 2017; Zhou et al., 2014] However, analytical study reveals that the Sn-N bond position is readily confused with the peak positions of $CN_x$ and $CN_{x\text{-}H}$ species, which may occur during $N_2$-plasma treatment of $SnS_2$ due to the large amount of carbon species in the ambient condition.[Azcatl et al., 2016] The pyridinic, pyrrolic, and graphitic N peaks in the N 1s spectra of $SnS_2$ and plasma treated $SnS_2$ for different duration may be split into three apparent peaks at 398.5, 399.97, and 400.2 eV, respectively.[Han et al., 2016] Therefore, the XPS analysis indicates that we had effectively prepared S vacancies in the vertically aligned $SnS_2$ nanoflakes using $N_2$-plasma, which increases the number of active sites to improve the gas sensing response.

## 5.4 Gas Sensing Properties of Vertically Aligned $SnS_2$ Flakes

### 5.4.1. Optimization of the operating temperature and Static response behaviour VA-$SnS_2$ sensor

We developed the chemiresistor by depositing two Au/Cr (300/20 nm) electrodes with 200 µm gap between them using shadow mask to determine the ability of $SnS_2$ flakes in gas sensing, as shown in Figure 5.5 (a). The sensing behavior of the device was investigated at different concentrations like 5, 10,20 and 50 ppm $NO_2$ at room temperature, 50 °C, 75 °C, 100 °C and 120 °C. The relative response was calculated using $\Delta R/R_a \times 100\%$ where $\Delta R = (R_g\text{-}R_a)/R_a$, $R_g$ and $R_a$ are the resistance of the sensing device in presence of the gas and air. Figure 5.5 (b, c) shows the gas responses of $SnS_2$ flakes at different concentrations of $NO_2$, in terms of the electrical resistance of the fabricated device at RT and 120 °C. The resistance value of the device before exposure of gas is about 14.50 kΩ, and 15.60 kΩ at RT and 120 °C, respectively. This suggests that the $SnS_2$-based device recovers its original characteristics after each sensing test. Since $SnS_2$ is an n-type semiconductor, when exposed to $NO_2$, the device's resistance increased because $NO_2$ is an oxidizing gas which takes electron from $SnS_2$, as it having an unpaired electron. Figure 5.5 (d), shows the device's response to various $NO_2$ concentrations at room temperature. The device's positive relative response improved as the concentration of $NO_2$ increased. However, owing to the tight binding between $NO_2$ and the reactive sites of $SnS_2$, the sensor only recovered partially at room temperature. We have performed the device's sensing operation from RT to 120 °C to determine the optimal temperature range for practical sensing. From the Figure 5.5 (e), it can be seen that the sensor having complete recovery from 5 ppm to 50 ppm $NO_2$ at 120 °C. Hence, the device requires a thermal energy to get the complete recovery. The relative response in the range of 72–164 % to $NO_2$ with concentrations ranging from 5 to 50 ppm at 120 °C is evidently superior to responses at room temperature, as seen in Figure 5.5 (e). Figure 5.5 (f) shows the sensor

response as a function of $NO_2$ concentration at RT and 120 °C, in which sensor response increase with the increasing $NO_2$ concentration. The sensor response exhibits almost a linear trend for concentrations of 5–50 ppm. Table 1 shows the $NO_2$ gas sensing performance of sensors based on $SnS_2$.

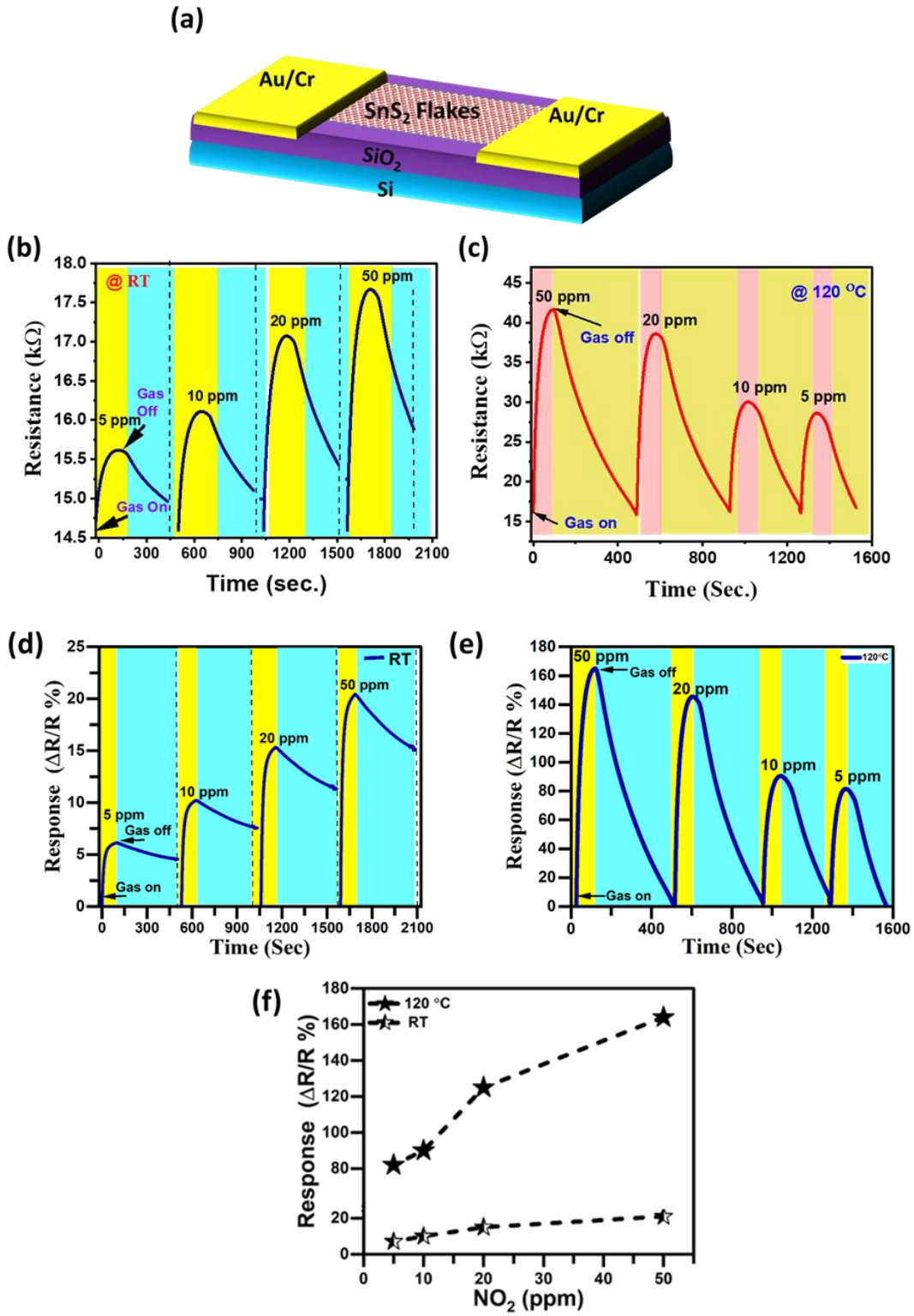



**Figure 5.5: (a)** Schematic diagram of the fabricated device, **(b, c)** Real-time change in resistance of the sensor with the temperature at RT, and 120 °C, respectively **(d)** Response time plot at RT with various concentration of $NO_2$, **(e)** Response verses concentration of $NO_2$ plot at 120 °C, and **(f)** Response of $SnS_2$ as a function of $NO_2$ concentration under room temperature, and 120 °C.

### 5.4.2. Repeatability, Response time, Selectivity, and Limit of Detection of VA-$SnS_2$ sensor

The sensor shows excellent repeatability at 120 °C for 50 ppm of $NO_2$ concentrations, as shown in Figure 5.6 (a). We measured the response time of 41 s and the recovery time of 379 s to 50 ppm $NO_2$ at the device's optimum operating temperature, as shown in Figure 5.6 (b) to gain insight into the response and recovery kinetics of the $SnS_2$ flakes. Here, the response and recovery time were defined as the time required to reach maximum value of 90% and 10% after loading and deloading the gas from the sensing chamber, respectively. The response and recovery time as a function of $NO_2$ concentration (5-50 ppm) for $SnS_2$ flakes-based sensor at 120 °C is displayed in Figure 5.6 (e). We also analyzed the response of sensor for 50 ppm of gas at various temperatures, as shown in Figure 5.6 (c).

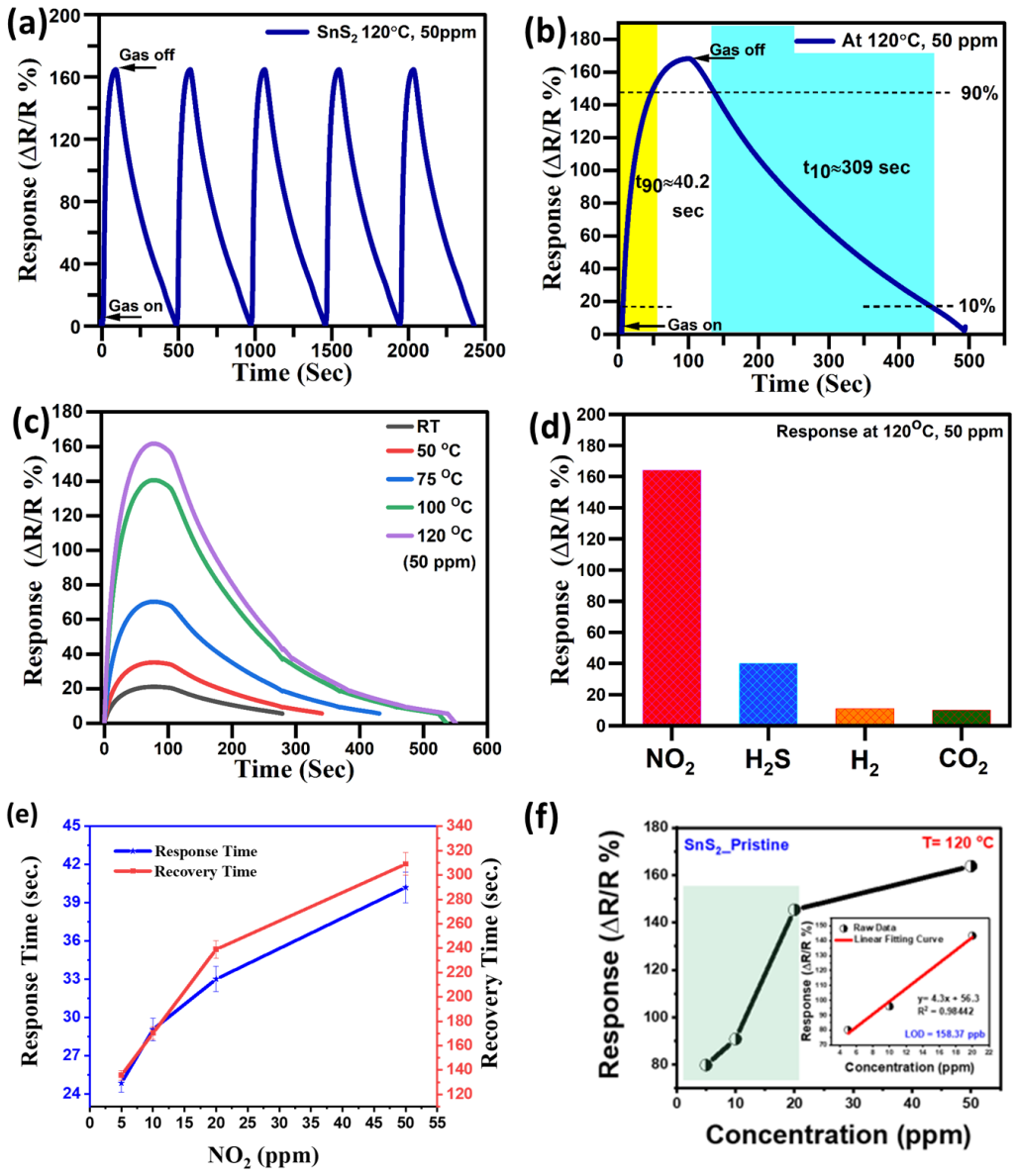



**Figure 5.6:** (a) Response at 120 °C with same concentration of 50 ppm of $NO_2$, (b) Response time plot of single cycle to calculate response time at 120 °C and 50 ppm of $NO_2$, (c) Response of 50 ppm of $NO_2$ at various temperature from RT to 120 °C, (d) Selectivity test histogram of $NO_2$, $H_2S$, $H_2$, $NH_3$, CO, $CO_2$, and $CH_4$ gas, (e) Response and recovery time as a function of $NO_2$ concentration (5-5- ppm) at 120 °C, and (f) Limit of detection calculation for $NO_2$ gas.

We have investigated the selectivity of the sensor to understand the selective nature of $SnS_2$ flakes for 50 ppm of other gases such as $H_2S$, $H_2$, $CO_2$ at optimal working temperature (120 °C). As shown in Figure 5.6 (d), the device exhibits a higher relative response to $NO_2$ than to other

gases at very low concentrations of $NO_2$ presence in the atmosphere. Using first-principal calculations, Ou et al., estimated that the adsorption binding energy of $SnS_2$ to $NO_2$ is greater than that of other gas species like $H_2$, $CO_2$, and $H_2S$ conforming that $SnS_2$ flakes has a good physical affinity for $NO_2$ [Ou et al., 2015]. They also clarified that the selectivity is likely due to the more desirable Fermi energy of $SnS_2$ compared to partly inhabited molecular orbitals of $NO_2$ as a result of observing the effect of gas molecules on the electronic band structure of $SnS_2$ [Ou et al., 2015]. The $SnS_2$ sensor's high selectivity for $NO_2$ means that it can correctly detect only $NO_2$ in a gaseous mixture.

Further, the current experimental method constrained the lowest detectable concentration in the experiments indicated above. The performance of the sensor's signal processing may be used to determine the detection limit as shown below. By varying the relative response change in the baseline and utilizing the root-mean-square deviation, the sensor noise may be computed (rmsd).[Indahl et al., 1998] For instance, we collected 10 data points at the baseline level, prior to the $NO_2$ exposure, as shown in Figure 5.6 (f) . When the data were plotted, a fifth-order polynomial fit was performed inside the data-point range, providing both the curve-fitting equation and the statistical parameters of the polynomial fit.

$$V_{x^2} = \sum(y_i - y)^2 \tag{5.1}$$

Where, yi is the measured data point and y is the corresponding value calculated from the curve-fitting equation. The rms noise (RMSnoise) is calculated as

$$RMS_{noise} = \sqrt{\frac{V_{x^2}}{N}} \tag{5.2}$$

where N is the number of data points used in the curve fitting.

As a key gas sensor parameter, the limit of detection (LOD) has been determined using the standard equation, according to signal to noise ratio is equal or greater than 3.[Li et al., 2003; Wu et al., 2018a]

$$LOD = \frac{3 \text{ x } RMS_{noise}}{S} \tag{5.3}$$

where S denoted the slope of calibration curves and $RMS_{noise}$ denoted the root-mean squared deviation of the baseline noise (ten points).

Here the sensor noise was calculated to 0.192. Meanwhile, the sensitivity to $NO_2$ gas was linearly fitted to be 96.714/ppm. The linear fitting plot of the pristine $SnS_2$ nanoflakes based gas sensor under 5–50 ppm $NO_2$ is depicted in the inset of Figure 5.6 (f), and it may be written as y= 4.3x + 56.3. Here, x represents the $NO_2$ concentration and y the response value. The gas sensor has high linearity, as evidenced by the correlation coefficient $R^2$, which is 0.98442. The LOD of pristine $SnS_2$ sensor is 158.7ppb.

### 5.4.3. Effect of humidity

Generally, water vapour has a significant impact on 2D material-based gas sensors. We looked at the effect of humidity on the $NO_2$ response of a vertically aligned $SnS_2$ flakes-based gas sensor. Adjusting the concentration of the incoming water vapour produces the desired relative humidity, which is an excellent representation of the real environment. The desired relative humidity can be obtained via changing the concentration of inlet water vapour, which is an excellent representation of the real environment. Figure 5.7 (a) depicts the baseline resistance as a function of relative humidity, from 25% to 70% at 120 °C. It seems that the base resistance reduced very marginally with relative humidity at 120 °C. It is exhibited in figure 5.7 b) that as humidity increased in the background, the response of the $SnS_2$ based sensor decreased. The following are some potential reasons for this phenomenon. The adsorption of water vapour on the sensor surface, which lowered the number of electrons on the sensing layer, may have

contributed to the drop in baseline resistance with humidity. Due to the reduced surface area, the adsorbed water vapour on the sensor surface resulted in a lesser amount of chemisorbed O ion production. As a result of the creation of water vapour on the sensor surface, $NO_2$ adsorption would have been delayed, resulting in a reduction in relative response [Gong et al., 2006; Yang et al., 2019]. Furthermore, in a humid environment, the interaction between $NO_2$ molecules and water vapour consumes a portion of $NO_2$ molecules, resulting in a reduced concentration of $NO_2$ that can efficiently exchange electrons with $SnS_2$ flakes. This is also a possible reason for the decreased in the response of sensors in a humid environment. In general, the sensor response was affected by humidity. As a result, in practical applications, it would be preferable if the effects of humidity could be corrected using appropriate mathematical methods or removed using a good filtering mechanism.

**Table 5.1:** Comparison of the $NO_2$ sensors based on $SnS_2$ materials

| Material/Structure | Synthesis Method | Sensing Temperature | NO2 Concentration | Response ΔR/Ro x100 % | Ref. |
|---|---|---|---|---|---|
| **SnS2 /nanoplates** | Hydrothermal | RT | 10 ppm | ~12.7 | [Pyeon et al., 2020b] |
| **SnS2 /nanoflakes** | CVD | 150 °C | 100 ppm | ~70* | [Kim et al., 2018a] |
| **SnS2 /nanoflakes** | Wet chemical | 120 °C | 10 ppm | ~35.3* | [Ou et al., 2015] |
| **SnS2 /nanograins** | CVD | RT | 10 ppm | ~7.01 | [Kwon et al., 2019] |
| **SnS2 /nanoparticles** | precipitation | 300 °C | 1 ppm | ~1 | [Gaiardo et al., 2016] |
| **SnS2 /nanoflowers** | Hydrothermal | 120 °C | 500 ppb | ~24.4* | [Liu et al., 2018a] |
| **SnS2 /nano powder** | High energy ball mining | 250 °C | 10 ppm | ~14.9 | [Kim et al., 2018b] |
| **SnS2 /vertical flakes** | CVD | 120 °C | 50 ppm | ~164 | This work |

*Response = $R_g/R_a$

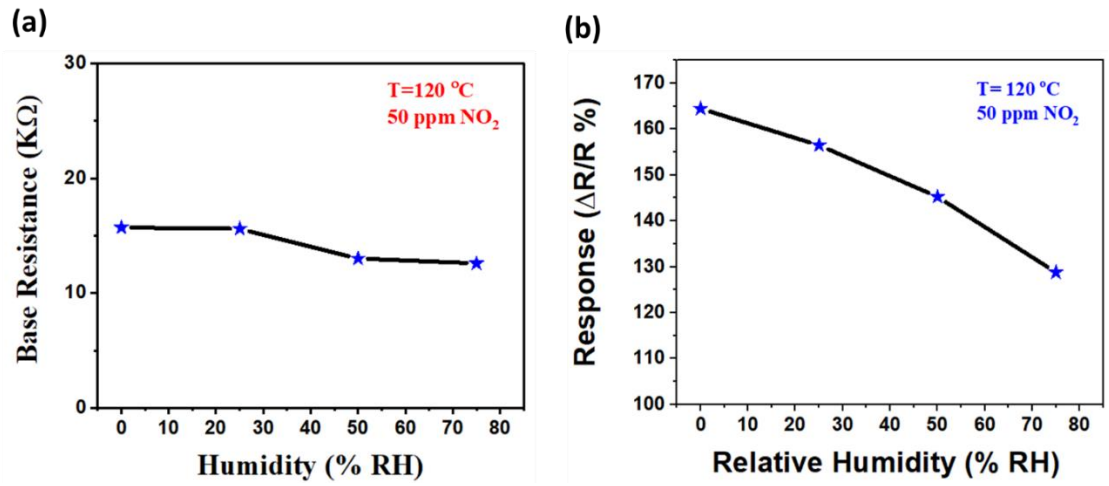



**Figure 5.7:** (a) Variation of baseline resistance with relative humidity from 25% to 75% for vertically aligned $SnS_2$ flakes at 120 °C, and (b) Response variations when $SnS_2$ gas sensor exposed to 50 ppm $NO_2$ under different relative humidity conditions at 120 °C.

### 5.4.4. Gas sensing mechanism

The mechanism of gas sensing of $SnS_2$ based on change in resistance due to chemisorption or physisorption or both, of gas molecules and result in change in carrier concentrations of $SnS_2$, as shown in Figure 5.8. The change in carrier density primarily depends on active site on the surface of $SnS_2$ as well as nature of gas (oxidizing or reducing). At room temperature, oxygen and humidity occupy a significant number of reactive sites, extracting electrons after quickly interacting with the exposed sites. Attributed to the existence of oxygen and humidity on the surface, less molecules were absorbed on the flakes when exposed to $NO_2$, resulting in lower response to $NO_2$ at room temperature. Hence, to desorb the humidity or oxygen molecules from the surface of $SnS_2$, annealing the sensor was performed at 120 °C in vacuum. As a result, it enhanced the concentration of electron and active edge sites, allowing $NO_2$ molecules to extract more electrons. The following equation may be used to describe the operation.

$$NO_2(gas) + e^- \rightarrow NO_2^- \tag{5.4}$$

Initially, when the device is in the air, some oxygen particles are already present. When the material heat at high temperature, these oxygen particles go out, and then the sensor gives the sensing after exposing the gas on the device. The electron will travel from material to gas, when the exposed gas is oxidizing, and if exposed gas is reducing, then electrons will move from gas to the material. Here $NO_2$ is the oxidizing gas and $SnS_2$ is n-type material, so $NO_2$ gas takes electrons from n-type $SnS_2$. Due to this, the electron density decreases in the device, and therefore current decreases, and hence resistance increases. By the change in the resistance before and after gas exposure, the response in percentage was calculated as the formula given below:

$$Response\ (\%) = \frac{\Delta R}{R_0}\ X\ 100 \tag{5.5}$$

Where $\Delta R = R_g - R_o$ and $R_g$ is the resistance of the device in presence of gas and $R_o$ is the resistance in air.

The response is increasing with the increment of temperature because the thermal energy can remove the barrier of the gas molecule to desorb from the sensing layer. Therefore, with increase of the temperature the desorption rate of the gas molecule is increases and hence the response is increases. Therefore, the device's high response at 120 °C can be due to defects and an excess of edge sites, as well as a large surface to volume ratio. We measured the device *I-V* characteristics at room temperature and 120 °C in a vacuum to confirm this, and observed that conduction was less at room temperature.

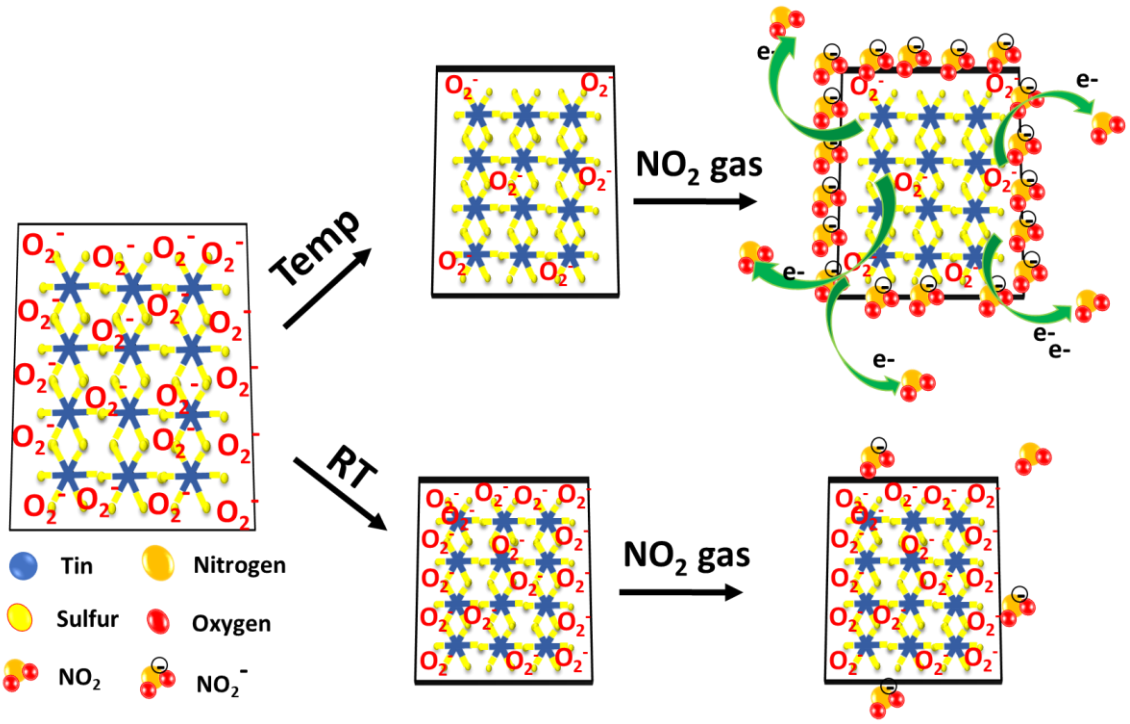



**Figure 5.8:** Schematic representation of sensing mechanism of the $SnS_2$ flakes.

## 5.5 Effects of Vacancy on Gas Sensing Characteristics of Vertically Aligned $SnS_2$ Flakes

### 5.5.1. *I-V* characteristics and surface resistances

To study the $NO_2$ gas sensing properties of $SnS_2$ nanoflakes, we developed a chemiresistor by depositing two electrode of Au/Cr (300/30 nm) by shadow mask having spacing of 200 µm between electrodes using thermal evaporation system, as depicted in Figure 5.9 (a). We measured the *I-V* characteristics of the pristine $SnS_2$ and plasma treated $SnS_2$ sample to confirm the semiconductor behaviour of the $SnS_2$ material and resistance of device before exposure of $NO_2$ gas at RT and 120 °C, as depict in Figure 5.9 (b). The device exhibits both ohmic behaviour and linear output curves, before and after $N_2$ plasma treatment in Figure 5.9 (c). The resistance decreases at the higher temperature, as expected for a semiconductor. From *I-V* characteristics in air, we can obtain the baseline resistance depicted in Figure 5.9 (d). The baseline resistance of $SnS_2$ is decreases with increase in plasma treatment time due to sulfur vacancies. Accordingly, the baseline resistance of different $SnS_2$ samples were steadily decreased from 15.60 kΩ (pristine-$SnS_2$) to 4.76 kΩ (N16) at 120 °C, which is a typical show a semiconducting behavior of the material (Figure S4c). These results indicate that nitrogen plasma can modify the surface state, such as by increasing the sulfur vacancies, leading to an enhancement of the gas sensing.

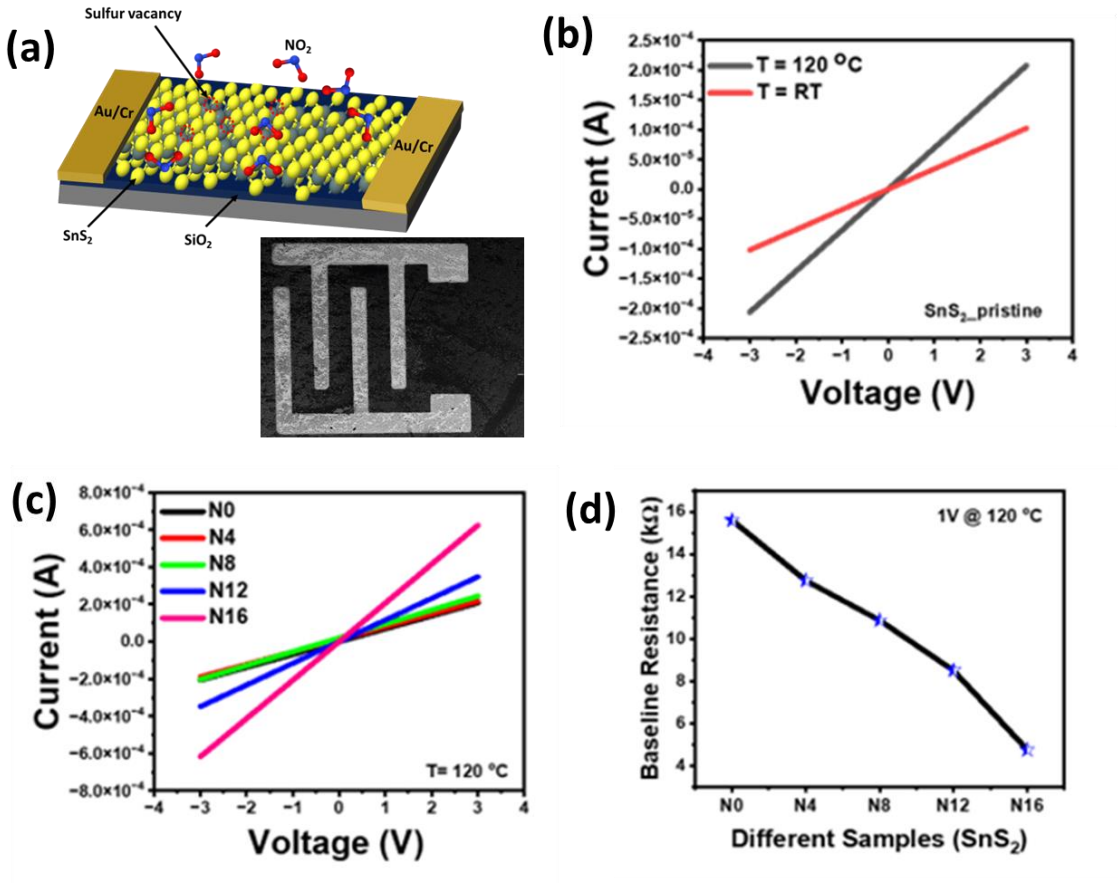



**Figure 5.9:** (a) Schematic illustration and SEM image of the fabricated Vs-$SnS_2$ device, (b) Linear *I-V* plots of the pristine $SnS_2$ sensor at RT and 120 °C, respectively, (c) *I-V* plots of the pristine $SnS_2$ and plasma treated $SnS_2$ (N4, N8, N12 and N16) samples sensor at 120 °C, respectively, and (d) Variation of baseline resistance at different interval of $N_2$ plasma (N0, N4, N8, N12, and N16) at 120 °C.

### 5.5.2. Static response behaviour Vs-$SnS_2$ sensor

For computing the relative response of gas, the change in electrical resistance of the device was evaluated using $((R_g - R_o)/R_g) \times 100\%$, where $R_g$ and $R_o$ are indicating the device's resistance to analyte gas and air, respectively. In our previous work, we measured the relative response curve of pristine-$SnS_2$ from room temperature to 120 °C at different concentration of $NO_2$ from 5-50 ppm.[Kumar et al., 2022] $NO_2$ gas molecules behave as electron acceptor, when $NO_2$ gas molecules physisorbed on the surface of $SnS_2$ and the electrostatic interaction between $SnS_2$ and $NO_2$ causes the transfer of electrons from the $SnS_2$ surface to produce a dipole moment. With an increase in concentration of $NO_2$ gas, the dipole moment rises, leading to a drop in the majority carrier (electron) concentrations in the nanoflakes. The increase in relative response and decrease in response and recovery times of device is due to increase in the operating temperature, which implies that raising the temperature enables the adsorption of $NO_2$ gas molecules onto the surface of $SnS_2$ nanoflakes and improves charge transfer. The best sensing occurs at 120 °C, with a maximum response of ~164 % and response and recovery times of 40.2 and 309 seconds, respectively.

To improve the relative response of the device, we generated S vacancies on the surface of $SnS_2$ nanoflakes using $N_2$-plasma of $SnS_2$ sample (details mentioned in experimental section). We studied the sensing response of Vs-$SnS_2$ device at different interval of time at 120 °C for different ppm of $NO_2$ exposure on the device. According to the theoretical investigations mentioned above, the Vs-$SnS_2$-based gas sensor should have a better relative response than the pristine $SnS_2$-based sensor. The calibration response graph of the untreated and plasma treated $SnS_2$-based sensors (N0, N4, N8, N12, and N16 samples) for 50 ppm of $NO_2$ gas concentrations at 120 °C are shown in Figure 5.10 (a). As illustrated in Figure 5.10(b),

we observed that Vs_$SnS_2$ (N12) device had a higher response of ~ 246.30 % to 50 ppm $NO_2$ at 120 °C, when compared to all other devices and 1.5 times higher than the pristine device (N0). It can be seen that the sensor current decreased as the concentration of $NO_2$ gas increased. The responses of the Vs-$SnS_2$ (N12) sensor to different concentration of $NO_2$ ranging from 250 ppb to 50 ppm at a temperature of 120 °C is depict in Figure 5.10 (c). Sulfur vacancies (Point defects) operate as active sites, allowing molecule adsorption and chemical functionalization to be facilitated. Figure 5.10 (d) shows bar graphs comparing the sensing response of N0 and N12 samples to 0.250-50 ppm $NO_2$ gas concentration at operating temperatures of 120 °C.

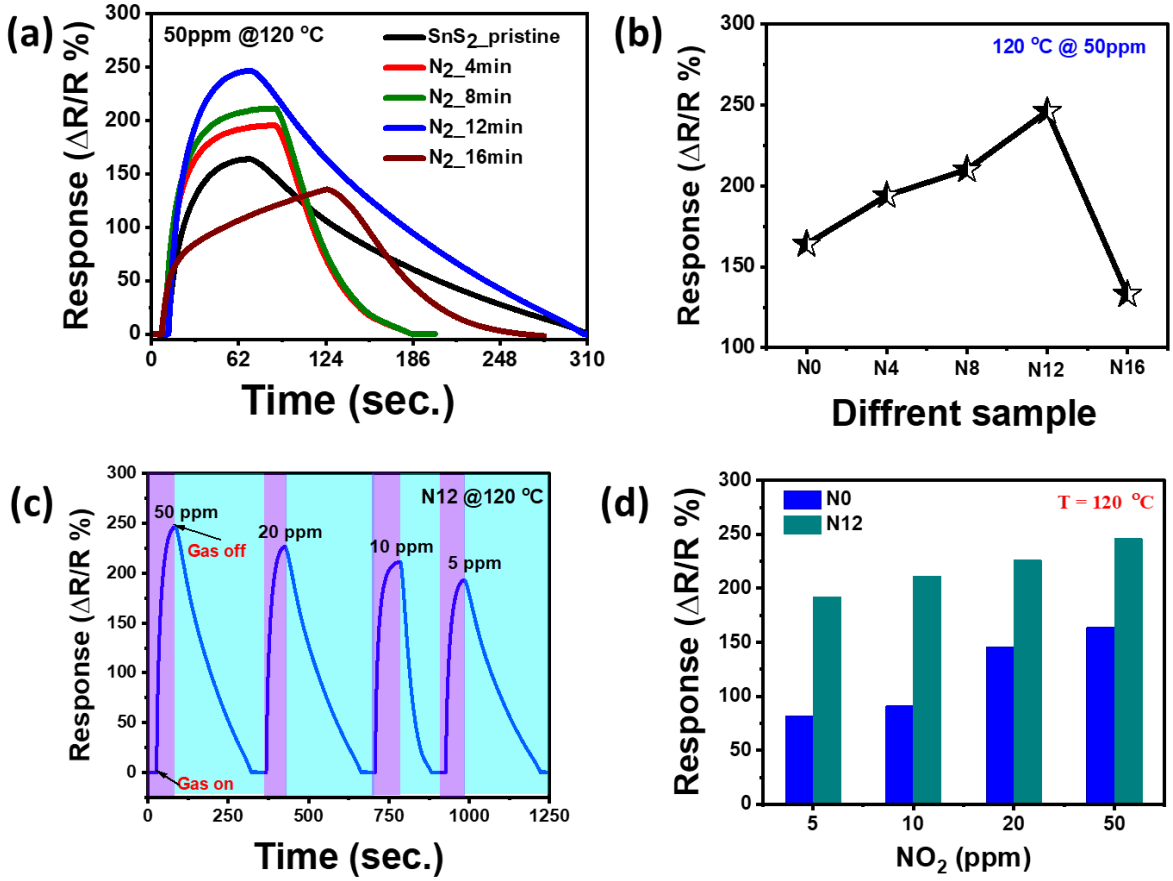



**Figure 5.10:** (a) Comparison of response of N0, N4, N8, N12, and N16 sensors for 50 ppm of $NO_2$ concentrations, respectively, (b) Comparison of the gas responses of N0, N4, N8, N12 and N16 samples at temperature 120 °C for 50 ppm $NO_2$ gas, (c) Sensing response of N12 device toward $NO_2$ gas at concentrations ranging from 1 to 50 ppm under the operation temperature of 120 °C, and (d) Response–concentration plot of pristine $SnS_2$ and Vs-$SnS_2$ (N12 )samples.

### 5.5.3. Repeatability, Selectivity, Response time, and Limit of Detection of Vs-$SnS_2$ sensor

Repeatability test is one of the critical performance parameters of any gas sensor. The Vs-$SnS_2$ ($N_{12}$) device demonstrated outstanding repeatability without decreasing relative response to 50 ppm $NO_2$ for five consecutive cycles, as illustrated in Figure 5.11 (a). Lastly, the device selectivity was tested at 120 °C, against several interfering gases including $NO_2$, $H_2$, $H_2S$, CO, $CO_2$, $CH_4$, and $NH_3$. The device's response to 50 ppm $NO_2$ was much higher than the response to 50 ppm concentrations of the other aforementioned gases, as shown in Figure 5.11 (b). In comparison to other gases, the N12 device demonstrated promising $NO_2$ selectivity. Furthermore, humidity has a little impact on the sensor's ability to detect $NO_2$, as reported in our previous work [Kumar et al., 2022]. Other than the device's high relative response to $NO_2$, it also showed quick response/recovery kinetics with complete recovery at 120 °C, with a fast response of 27 second and complete recovery of 183 second compared to pristine $SnS_2$ (response time 40.2 second and recovery time of 309 second), as shown in Figure 5.11 (c) [Kumar et al., 2022]. Table 5.2 provides

the $NO_2$ sensing performances of several 2D material nanostructures in the literature and Vs-$SnS_2$ nanoflakes with $N_2$ plasma in the present work.

Although the sensor built from Vs-$SnS_2$ nanoflakes possessed a superior sensing response to $NO_2$ gas, the limit of detection (LOD) was determined for the same, with an excellent linear regression value ($R^2$ = 0.9905) and a linear range of 5 to 50 ppm, as shown in Figure 5.11 (d). As shown in Figure 5.11 (d), the $N_{12}$ sample (12 min nitrogen plasma) relative response value at various $NO_2$ concentrations was fitted. The inset of Figure 5.11 (d), shows the linear relationship between relative response value of N12 sample and $NO_2$ gas concentrations. The calculated value of limit of detection is 5.9 ppb in case of Vs-$SnS_2$ based $NO_2$ gas sensor. The details of the calculations are given in the section 5.4.2.

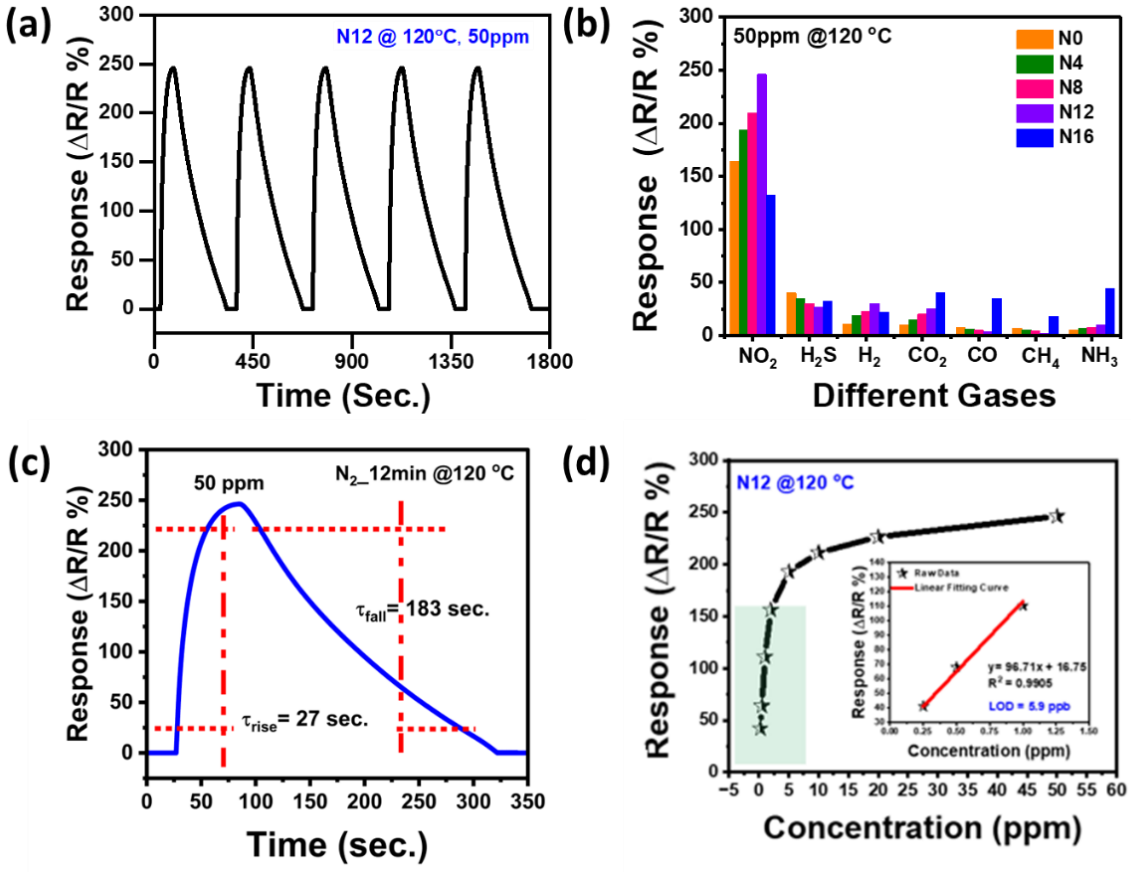



**Figure 5.11:** (a) Vs-$SnS_2$ sensor repeatability for 50 ppm gas at 120 °C, (b) Selectivity of sensor to 50 ppm different gases at 120 °C, (c) Response time and Recovery time of N12 gas sensor under a 50 ppm $NO_2$ concentration at 120 °C, and (d) Response versus $NO_2$ concentration curve. (Inset) Linear fitting curve of N12 sample of $SnS_2$ (12 min plasma treatment) at 120 °C, for calculation of the Limit of detection (LoD).

**Table 5.2:** A comparison of $NO_2$ sensor sensing performance based on 2D material.

| Sensing material | Operating Temp. (°C) | $NO_2$ concentration | Relative Response | Response/ Recovery time (s) | Ref. |
|---|---|---|---|---|---|
| $SnS_2$ flakes | 120 | 10 ppm | 36.3# | 172/138 | [Ou et al., 2015] |
| rGO/$SnS_2$ hybrid | 150 | 5 ppm | 32# | 50/48 s | [Cheng et al., 2019] |
| $SnS_2$-nanosheets | RT (Light) | 8 ppm | 10.8# | 164/236 | [Gu et al., 2020] |
| $SnS_2$/MXene derived $TiO_2$ (SMT) | RT | 1000 ppm | 115# | 64/10 | [Chen et al., 2021] |
| Mo-doped $SnS_2$ | 150 | 100 ppm | 4700* | 33.5/20 | [Zhou et al., 2021] |
| SnO2-rGO/$SnS_2$ | 120 | 10 ppm | 1064.0# | 42/111 | [Zheng et al., 2021] |
| $SnS_2$ flakes | 120 | 50 ppm | 164* | 40.2/309 | [Kumar et al., 2022] |
| CdTe/$MoS_2$ | RT | 10 ppm | 40* | 16/114 | [Jaiswal et al., 2020] |
| $WS_2$@CNFs | RT | 5 ppm | 46.3* | 54/305 | [Xu et al., 2021] |
| $MoS_2$ | RT (UV) | 100 ppm | 27* | 29/350 | [Kumar et al., 2017] |
| Mixed $MoS_2$ flakes | RT+UV | 10 ppm | 21.78* | 6.09/146.49 | [Agrawal et al., 2018] |
| Thin layered $MoS_2$ | RT | 100 ppm | 54* | 180/600 | [Late et al., 2013] |
| $MoS_2$ nanowire networks | 60 | 5 ppm | 18.1* | 16/172 | [Kumar et al., 2018a] |
| $WSe_2$ | RT | 500 ppm | 4140* | 15.5/85 min | [Ko et al., 2018] |
| Vs-$SnS_2$ flakes | 120 | 50 ppm | 246* | 27/183 | This work |

# Relative response = $R_g/R_a$

*Relative response = $(R_g-R_a / R_a) \times 100$

### 5.5.4. Gas sensing mechanism

In the perspective of electronic interaction between target analytes and adsorption sites, we explored the gas sensing mechanism of our $NO_2$ gas sensor by S-vacancy of the sensing material, as shown in Figure 5.12. The discrete S-vacancy in $SnS_2$ nanoflakes behave as a sensitizer for transporting of carrier charge in channel as well as absorption of gas. In our scenario, Raman and XPS data support the presence of sulfur vacancies ($V_S$). With the (0/–1) charged states, sulfur vacancies operate as a single electron acceptor.[Noh et al., 2014] Only a small portion of this level is inhabited due to the high energy level. These vacancies are singly ionised to $V_s'$ charged states before $O_2/NO_2$ exposure, causing a hole in the valence band (equation 6).[Kumar et al., 2021b]

$$V_s^* \rightarrow V_s' + h^+ \tag{5.6}$$

The chemisorbed $O^-_{(ads)}$ initially create a depletion layer on the surface of $SnS_2$ in the air. The oxygen ion $O_2^-$ is dominant at lower temperatures. The increase in electrical conductivity at low temperature is due to increase in the hole concentration in the valence band. $NO^-_{(ads)}$ would develop on the $SnS_2$ surface once the sensor was exposed to $NO_2$. As $NO_2$ is an oxidizing and electron-withdrawing gas, it extracts electrons from $SnS_2$ upon adsorption on the $SnS_2$ surface as shown in equations (7) and (8).[Liu et al., 2018a]

$$O_2\ (gas) + e^- \rightarrow O_2^- \tag{5.7}$$

$$NO_2\ (gas) + e^- \rightarrow NO_2^- \tag{5.8}$$

where $e^-$ is an electron in $SnS_2$'s conduction band, and $O_2^-$ and $NO_2^-$ are the physisorbed $NO_2^-$ and physisorbed $NO_2^-$ molecules on the surface of $SnS_2$ nanoflakes, respectively.

Electrons flow from Vs-$SnS_2$ to $NO_2$, when it is exposed to $NO_2$ and result in increase in resistance of the material, as shown in figure. $NO_2$ adsorption on the abundant active sites (sulfur vacancy, dangling bond at the edge) of the Vs-$SnS_2$ enhanced the carrier concentration in the transporting channel. The probable reaction process between Vs-$SnS_2$ and $NO_2$ is shown in equations 9 and 10.

$$SnS_2 + V_s + NO_2 + e^-_{CB} \rightarrow SnS_2 + (NO_2^- + V_S) \tag{5.9}$$

$$SnO_2 + V_O + NO_2 + e^-_{CB} \rightarrow SnO_2 + (NO_2^- + V_O) \tag{5.10}$$

Where, the adsorbed $NO_2$ on the S vacancies and oxygen are $(NO_2^- + V_S)$ and $(NO_2^- + V_O)$. The conduction band electron is denoted by $e^-_{CB}$. As a result of the interaction between $NO_2$ and $e^-_{CB}$, the conduction band electrons decrease while the electron resistance increases.

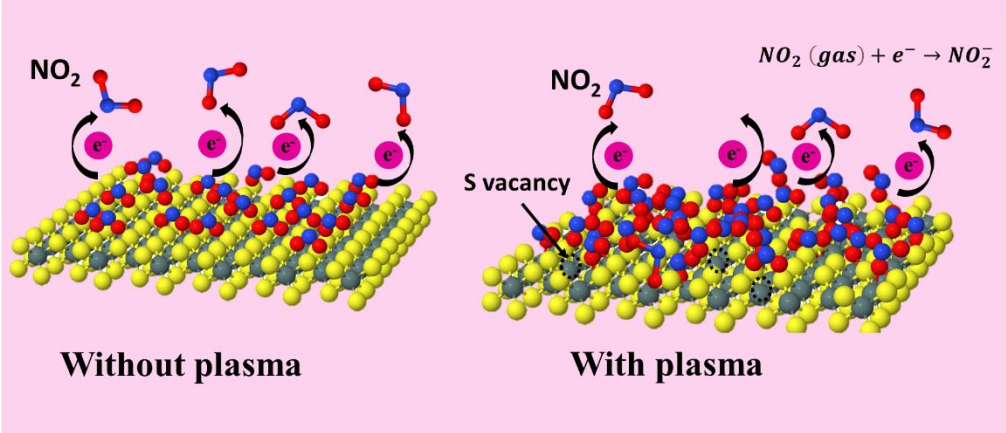



**Figure 5.12:** Schematic illustration of the sensing mechanism for the boosted gas response to $NO_2$

When the temperature increase, due to thermal energy electron gain enough energy to travel conduction band and absorbed by $NO_2$, which result in carrier concentration i.e., hole concentration (equation 8 takes over). As a result, there is an enhancement in relative response. The conduction band electrons and sulfur vacancy level raise the hole concentration, and a larger response is noticed when the temperature reaches its optimal value, which is 120 °C. The electron and hole concentrations grow as the temperature rises, and the vacancy states fill up completely. The vacancy states cannot provide $NO_2$ molecules with enough electrons. As a result, at high temperatures, the change in electron and hole concentration is less, lowering the relative response. The enhancement in $NO_2$ sensing performance with the S-vacancies compared to pristine $SnS_2$ due to a chemical sensitive effect induced by the S vacancy on the surface of $SnS_2$. The S defect was shown to be an efficient and promising center for $NO_2$ adsorption, as well as an electron transfer bridge.

## 5.6 Summary

` In summary, we have successfully synthesized a highly sensitive gas sensor predicated upon vertically aligned $SnS_2$ flakes through the application of the chemical vapor deposition (CVD) methodology, thereby demonstrating remarkable selectivity towards $NO_2$ in comparison to over a range of other toxic and combustible gases. The fabricated $SnS_2$ sensors exhibited commendable stability in performance, elevated sensitivity (164%), and expeditious response/recovery times (41/309 s), when exposed to 50 ppm $NO_2$ at 120 °C. Moreover, we investigated the fast nitrogen plasma treatment technique as a means to engender sulfur vacancies on the $SnS_2$ surface, thereby significantly augmenting its functionalization and gas sensing attributes. The sensors subjected to 12 minutes of nitrogen plasma treatment exhibited an extraordinary response of 246% to 50 ppm $NO_2$, signifying an approximate 1.5 order-of-magnitude enhancement relative to pristine $SnS_2$. The pronounced selectivity of the sensor towards $NO_2$, even amidst the presence of assorted interfering gases such as $CH_4$, CO, $H_2$, $H_2S$, $CO_2$, and $NH_3$, accentuates its promising applicability for low-concentration gas detection in domains such as medical diagnostics, industrial processing, and environmental monitoring.

The results imply that S-vacancy defects facilitate the transition from physisorption to chemisorption in the context of $NO_2$ detection, thereby underscoring the significance of defect engineering in optimizing the sensing characteristics of transition metal dichalcogenides (TMDs). This research not only enhances the comprehension of $SnS_2$-based gas sensors but also lays the groundwork for the advancement of TMD materials with adjustable sensing capabilities for next-generation smart and IoT-integrated applications.

# 6
# DFT studies and Gas Sensor Modelling

In this chapter, we explore the application of density functional theory (DFT) calculations to investigate the adsorption mechanisms of $NO_2$ gas molecules on the surfaces of $MoS_2$ and $SnS_2$ flakes grown using CVD. The study examines the impact of nitrogen plasma treatment and surface decoration with silver nanoparticles (Ag NPs) on the adsorption energy of $NO_2$ on $MoS_2$ surfaces. Additionally, electronic structure calculations of vertically aligned $SnS_2$ flakes and nitrogen plasma-treated $SnS_2$ flakes are presented. DFT computations reveal that sulfur vacancy defects on the surface significantly influence $NO_2$ detection by transitioning the adsorption mechanism from physisorption to chemisorption. The chapter also delves into the adsorption kinetics of $NO_2$ gas on $SnS_2$ nanoflake-based chemiresistor sensors, utilizing the Lee and Strano model. This model effectively describes the sensor's response curves and enables the extraction of the irreversible reaction rate for different $NO_2$ concentrations. Through these analyses, the interplay between surface modifications and $NO_2$ detection efficiency is comprehensively addressed.

## 6.1 Requirement of Theoretical Investigations of $NO_2$ Adsorption

A popular quantum computer modelling method for examining the electronic structure of many-body systems in physics, chemistry, and materials science is called density functional theory, or DFT. The fundamental Hohenberg-Kohn theorems were first presented by Pierre Hohenberg and Walter Kohn in 1964. The first theorem showed that the electron density function $\rho_0(x, y, z)$, which depends on just three variables, may uniquely identify the ground-state energy, wave function, and other electronic features for systems with a non-degenerate fundamental ground state. The ground-state energy might be represented as a functional, $E_0 = E[\rho_0]$, according to the second theorem [Levine, 2014; Sholl et al., 2022]. However, at first, only non-degenerate ground states were covered by the Hohenberg-Kohn theorems. Mel Levy and John P. Perdew expanded the theorem's application in 1967 by including systems with degenerate ground states[Levine, 2014; Sholl et al., 2022].

In addition to experimental investigations, theoretical research has significantly advanced the development of gas-sensing technologies and the prediction of the sensing characteristics of potential materials[Cohen et al., 2012]. Density functional theory (DFT) is a prominent theoretical approach that consistently demonstrates efficiency in terms of time, effort, and cost [Agrawal et al., 2021; Cohen et al., 2012]. DFT provides a comprehensive and precise explanation of the underlying mechanisms occurring between sensing devices and gas analytes [Jones, 2015]. Key features of DFT include the understanding of fundamental interactions between sensing materials and gas analytes, as well as pre-calculations of charge transfers. These characteristics facilitate the exploration of chemical and physical adsorption of gas analytes, theoretical assessments of composites and anchored nanoparticles, and the effects of noble metal and other material functionalization on $MoS_2$ and $SnS_2$. For instance, Wenli Li *et al.,* prepared few-layer $MoS_2$ nanosheets (FLMN) via mechanical exfoliation and coated them onto a substrate with interdigital electrodes for room-temperature $NO_2$ detection [Li et al., 2019a]. First-principles calculations based on DFT confirmed that the ultrafast recovery behavior is attributed to the weak van der Waals interactions between $NO_2$ and the $MoS_2$ surface.

Since the significant role of defects in enhancing sensing properties, the development of sensing materials with defective morphologies is crucial [Kumar et al., 2024b]. In this context, an $NO_2$ gas sensor was fabricated using edge-enriched and mixed in-plane $MoS_2$ flakes, which exhibited a rapid response time (8.5 s) and a response of approximately 10.36% to 10 ppm of $NO_2$ at room temperature. However, the sensor did not achieve complete recovery due to the high adsorption energy of $NO_2$ gas molecules on the sensor surface (-0.276 eV), as calculated by

DFT[Agrawal et al., 2018]. Additionally, Wang *et al.,* investigated the electronic properties and adsorption behavior of Pd and Rh-functionalized Se-vacancy $MoSe_2$ using DFT, focusing on four gases: $SOF_2$, $SO_2F_2$, $SO_2$, and $H_2S$. The Se vacancies in $MoSe_2$, along with Rh and Pd transition metal atoms, formed strong chemical bonds ($E_b$ = -3.950 eV and -4.780 eV, respectively). Both Rh and Pd-doped structures exhibited excellent adsorption characteristics for $SO_2$, although their adsorption capabilities varied for the four gases (Pd: $SO_2$ > $H_2S$ > $SOF_2$ > $SOF_2$; Rh: $SO_2$ > $SOF_2$ > $SOF_2$ > $H_2S$)[Sang et al., 2022].

The decoration of noble metal nanoparticles is a common strategy to improve the selectivity of chemical sensor arrays utilizing 2D semiconductor materials, such as $MoS_2$. Kim *et al.,* reported that 2D $MoS_2$ nanoflakes decorated with noble metals exhibited significant gas sensing selectivity [Kim et al., 2023]. First-principles DFT simulations were used to investigate the effect of noble metal nanoparticle decoration affects selectivity changes, a unique phenomenon resulting from the distinctive structure and highly active edge sites of 2D materials. For example, Ni was doped into $MoS_2$ nanosheets at concentrations of 3, 5, and 7 atomic percent for room-temperature $NO_2$ sensing. The increased edge active sites in Ni-incorporated sensors were responsible for the enhanced sensing performance. In pristine $MoS_2$, only a limited number of active adsorption sites were available for gas adsorption. However, as Ni content increased, more edges and active centers were generated within $MoS_2$, leading to a 115% improvement in response to 200 ppm of $NO_2$ at room temperature. DFT studies indicated that the bandgap of the $MoS_2$ film decreased from 1.73 eV to 1.44 eV after Ni doping, facilitating easier electron transfer from the valence band to the conduction band. Furthermore, the calculations demonstrated that Ni loses electrons while $MoS_2$ gains them, significantly tuning the sensor's response and chemical activity [Bharathi et al., 2022]. Additionally, Zange Li *et al.*, utilized DFT calculations to modify the $SnS_2$ monolayer through N, P, Ge, and Se doping, investigating the adsorption properties and gas-sensing mechanisms of each doped $SnS_2$ variant. Their analysis of adsorption energy, charge density differences, band structure, and recovery times revealed that Ge and Se doping negatively impacted $H_2S$ detection, while N and P doping effectively enhanced the interaction between $SnS_2$ and $H_2S$, maintaining physisorption with adsorption energies of -0.60 eV and -0.64 eV, respectively [Li et al., 2024]. In the realm of nanotubes, 2D, and 3D porous nanomaterials, Pd is a widely utilized transition metal for surface decoration. DFT calculations have been employed to assess the sensitivity of bare $MoSe_2$ and Pd-$MoSe_2$ against $SO_2F_2$ and $SOF_2$, revealing that Pd doping significantly enhances the gas response of $MoSe_2$[Qian et al., 2019].

## 6.2 Vienna Ab initio Simulation Package (VASP)

The Vienna Ab initio Simulation Package (VASP) is a software suite designed for quantum mechanical modeling from first principles. It employs methods such as the projected augmented wave (PAW) pseudopotentials or Vanderbilt pseudopotentials combined with a plane wave basis set[Panigrahi et al., 2019]. While its core methodology is based on density functional theory (DFT), VASP also supports post-DFT corrections, including hybrid functionals that integrate DFT with Hartree-Fock exchange, such as HSE [Heyd et al., 2003], PBE0 [Perdew et al., 1996], and B3LYP[Kim et al., 1994]. Additionally, it incorporates advanced techniques like many-body perturbation theory (the GW method) and dynamical electronic correlations using the random phase approximation.

Originally derived from code developed by Mike Payne at MIT, which also served as the foundation for CASTEP, VASP was transferred to the University of Vienna in July 1989 under the direction of Jürgen Hafner. The main program was subsequently developed by Jürgen Furthmüller and Georg Kresse, with Kresse currently leading its development. Recent enhancements include extending methods commonly used in molecular quantum chemistry, such as MP2, to periodic systems. Today, VASP is utilized by over 1,400 academic and industrial research groups worldwide under software license agreements with the University of Vienna.

## 6.3 Computational Method

### 6.3.1. Ag NPs anchored-nitrogen plasma treated $MoS_2$ (Ag-N-$MoS_2$) flakes

The electronic structure calculations reported in this study were conducted using the Vienna Ab initio Simulation Package (VASP) [Sun et al., 2003]. Ionic relaxation was conducted using the projector augmented wave (PAW) [Blöchl, 1994] method of density functional theory, and all atoms were assumed to have Perdew−Burke−Ernzerhof (PBE) pseudopotentials [Perdew et al., 1998]. Due to inadequacy of Generalized Gradient Approximation (GGA) to incorporate the Van-der Waal's (vDW) interactions, Grimme's DFT-D3 dispersion corrections were used in all calculations. The structural parameters of crystalline $MoS_2$ were obtained from the Materials Project database version 2023.11.1. The cell parameters of this structure were a= 3.19 Å, b= 3.19 Å, and c= 13.37 Å, with $\alpha = 90°$, $\beta = 90°$, and $\gamma = 120°$. For gas adsorption, a supercell of 4 × 4 × 1 $MoS_2$ monolayer was constructed, with a 20 Å vacuum maintained between two consecutive layers. K-point sampling was conducted for plane waves using a 4 × 4 × 1 grid with a 400-eV cutoff energy. We employed the conjugate gradient algorithm to relax the geometries, and all calculations were spin-polarized.

### 6.3.2. Vertically Aligned SnS2 (VA-$SnS_2$) flakes

The electronic structure calculations were done by Vianna Ab-Initio Simulation Package (VASP) package [Hafner, 2008] and optimised structures are visualised by VESTA software [Momma et al., 2011]. Projected Augmented Wave (PAW) method of density functional theory is used for ionic relaxation due to its reasonable accuracy and computational efficiency about to exhibit the core valance electronic interactions [Kresse et al., 1996]. Perdew-Burke-Ernzerhof (PBE) pseudopotentials are used for all the atoms. 3x3x1 supercell of $SnS_2$ monolayer is constructed for gas adsorption and vacuum layer of 20 Å is maintained between two consecutive layers. 8x8x1 grid is used for K-points sampling with 400 eV cut-off energy for plane waves. To investigate the adsorption of different gases on the monolayer, each gas molecule was kept 3.5 Å above the surface. All calculations are spin polarised and Conjugate gradient algorithm is employed for relaxing the geometry. All the electronic structure calculations reported here are 0 K calculations.

### 6.3.3. Vacancy-Assisted Vertically Aligned SnS2 (Vs-$SnS_2$) flakes

Vianna Ab-Initio Simulation Package (VASP) [Sun et al., 2003] was used for performing the electronic structure calculations reported in the present work. Projected Augmented Wave (PAW) [Blöchl, 1994] method of density functional theory was used for ionic relaxation and Perdew-Bruke-Ernzerhof (PBE)[Perdew et al., 1998] pseudopotentials were used for all atoms. The structural parameters of crystalline $SnS_2$ were received from the Materials Project for $SnS_2$ (mp-1170) from database version v2022.10.28. This structure exhibits hexagonal lattice system and $P\bar{3}m1$ space group with cell parameters: a=3.67Å, b=3.67Å and c=6.23Å with $\alpha = 90^0$, $\beta = 90^0$, $\gamma=120^0$. A supercell of 3x3x1 of $SnS_2$ monolayer was constructed for gas adsorption maintaining 20 Å vacuum between two consecutive layers. 8x8x1 grid was used for K-points sampling with 400 eV cut-off energy for plane waves. All calculations were done by keeping $NO_2$ at a distance of 3.5 Å above the monolayer surface. All calculations were spin polarized and conjugate gradient algorithm was employed for relaxing the geometries.

## 6.4 Result and Discussion

### 6.4.1. Adsorption properties of Ag NPs anchored-nitrogen plasma treated $MoS_2$ (Ag-N-$MoS_2$) flakes

To model the present experiments, three different functionalized $MoS_2$ monolayers were constructed to investigate the $NO_2$ gas adsorption properties. The initial system studied was pristine $MoS_2$ and rest of the systems were nitrogen-doped $MoS_2$ (N-$MoS_2$) and Ag-functionalized nitrogen-doped $MoS_2$ (Ag-N-$MoS_2$), which will establish the effectiveness of $N_2$ plasma exposure and silver NP functionalization. These structures were fully optimized before optimizing the gas adsorbed surfaces. The adsorption energy ($E_{ad}$) of the gas with respect to the surface is defined as,

$$E_{ad} = E_{MoS2+NO2} - E_{MoS2} - E_{NO2} \tag{6.1}$$

Where, the total energy of the surface-gas system is denoted as $E_{MoS2+NO2}$, $E_{MoS2}$ and $E_{NO2}$ are the energies of the surface and gas molecule, respectively.

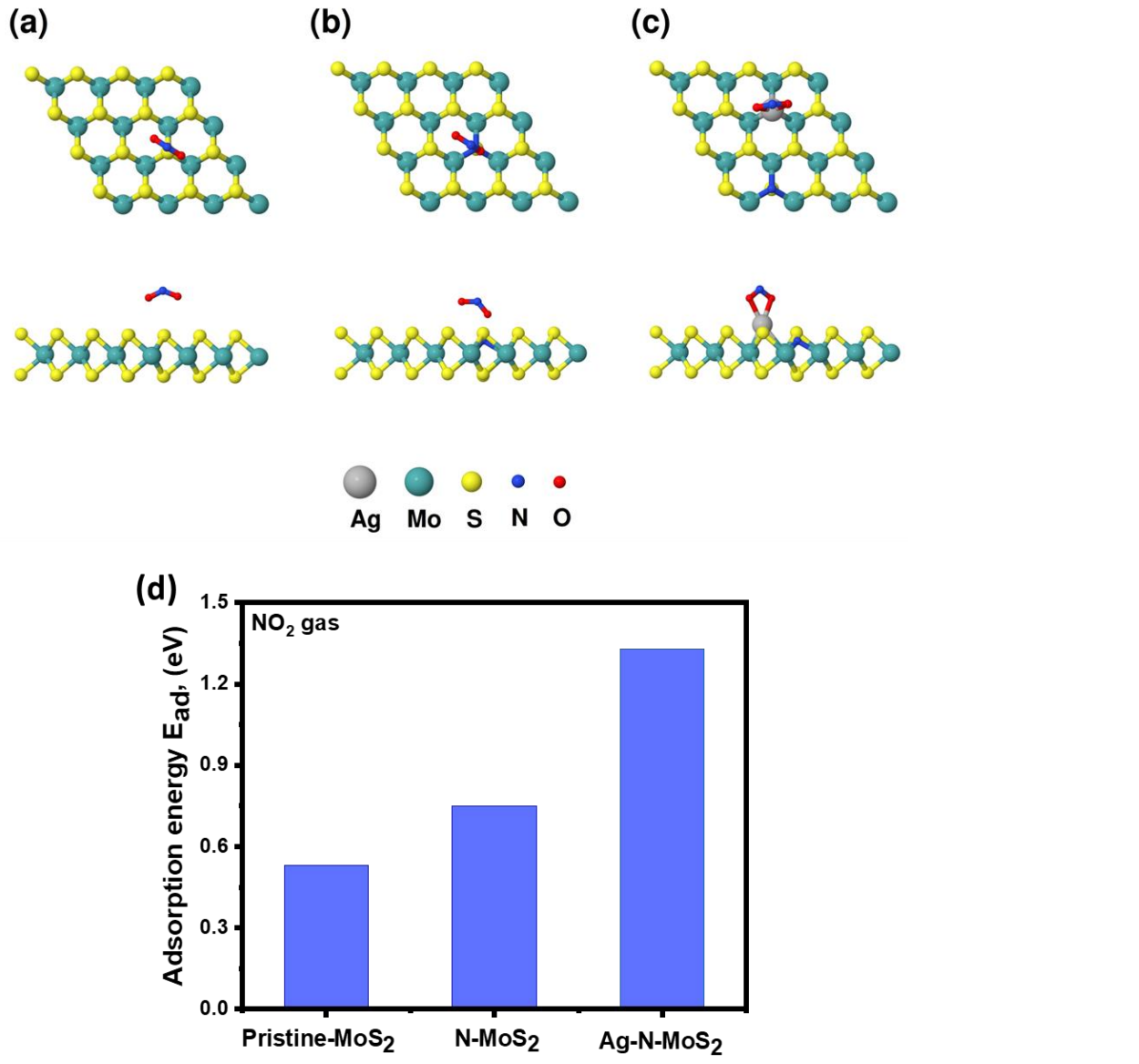



**Figure 6.1:** The top and side views of $NO_2$ gas adsorption on the (a) pristine $MoS_2$ (b) N-$MoS_2$ and (c) Ag decorated N-$MoS_2$, and (d) Histogram of adsorption energy pristine $MoS_2$, N-$MoS_2$, Ag decorated N-$MoS_2$, for $NO_2$ gas.

In the pristine case, a weak van-der Waals interaction between the $MoS_2$ surface and $NO_2$ gas was observed, with the lowest adsorption energy of -0.53 eV, suggesting physisorption of gas molecule over the surface, as depicted in Figure 6.1 (a). The relatively low adsorption capacity of pristine $MoS_2$ to adsorb $NO_2$ gas has been extensively studied in previous studies]. The material properties, specifically adsorption of the $MoS_2$ monolayer can be drastically improved by nitrogen doping or functionalizing the material with transition metals through surface modulation. The plasma exposure duration of the $MoS_2$ surface is a determining factor in the extent of nitrogen doping. The current study examines plasma exposure for a maximum of 8 minutes, which results in a 2-3% atomic nitrogen content of the material. For the theoretical study, the supercell was designed to replicate the effects of nitrogen doping after an 8-minute exposure of $N_2$ plasma by incorporating a single nitrogen atom into the 4x4x1 $MoS_2$ monolayer surface. The resultant $NO_2$ adsorption energy of -0.75 eV was observed. Further, bond lengths between the nitrogen and oxygen atoms in $NO_2$ gas molecule becomes unequal and, in turn, symmetry is broken (see table 6.1) through the oxygen atom leaning towards the surface nitrogen atom as illustrated in Figure 6.1 (b), resulting $d_{O\text{-}N}$(surface) = 2.06 Å, which suggests a dominant non-bonding interaction. Silver decorated nitrogen doped $MoS_2$ monolayer increases $NO_2$ adsorption energy further to -1.33 eV. Figure 6.1 (c) illustrates the adsorption geometry. The presence of two oxygen atoms of $NO_2$ molecule over the silver atom with an Ag-O bond length of 2.32 Å suggests the existence of robust covalent interactions between the gas molecule and the silver-decorated nitrogen-doped $MoS_2$ surface.

**Table 6.1:** Adsorption energies of NO2 gas over different surface systems. The structural changes in configurations are given by bond lengths and bond angles of the constituent elements

| System | Adsorption energy ($E_{ad}$/eV) | After adsorption of $NO_2$ molecule | |
|---|---|---|---|
| | | Bond length (Å) | Angles (degrees) |
| **Gas molecule** | - | dN-O = 1.21 | O-N-O = 133.3 |
| **(b) Pristine $MoS_2$** | -0.53 | dN-O = 1.22<br>dMo-O = 2.41<br>dO-S = 3.16 | O-N-O = 132.1 |
| **(c) Nitrogen doped $MoS_2$ (N- $MoS_2$)** | -0.75 | dN-O = 1.21 (away from surface)<br>dN-O = 1.25 (towards surface)<br>dMo-O = 2.41<br>dO-N(surface) = 2.06 | O-N-O = 129.0<br>N-O-N = 131.4 |
| **(d) Silver decorated N-$MoS_2$ (Ag-N- $MoS_2$)** | -1.33 | dN-O = 1.27<br>dAg-O = 2.32<br>dAg-Mo = 2.81<br>dMo-S = 2.42 | O-N-O = 113.7<br>Mo-O-N = 95.9<br>Mo-Ag-Mo = 67.9 |

### 6.4.2. Adsorption properties of Vertically Aligned $SnS_2$ (VA-$SnS_2$) flakes

The adsorption properties of $NO_2$ gas on vertically aligned $SnS_2$ were studied to identify the most favourable configuration and interaction mechanism. The adsorption energy was calculated using the equation:

$$E_{ads} = E_{[SnS2+NO2]} - E_{[SnS2]} - E_{[NO2]} \quad (6.2)$$

Where, $E_{[SnS2+NO2]}$, $E_{[SnS2]}$, and $E_{[NO2]}$ represent the energies of gas adsorbed system, isolated $SnS_2$ surface and isolated gas molecules, respectively.

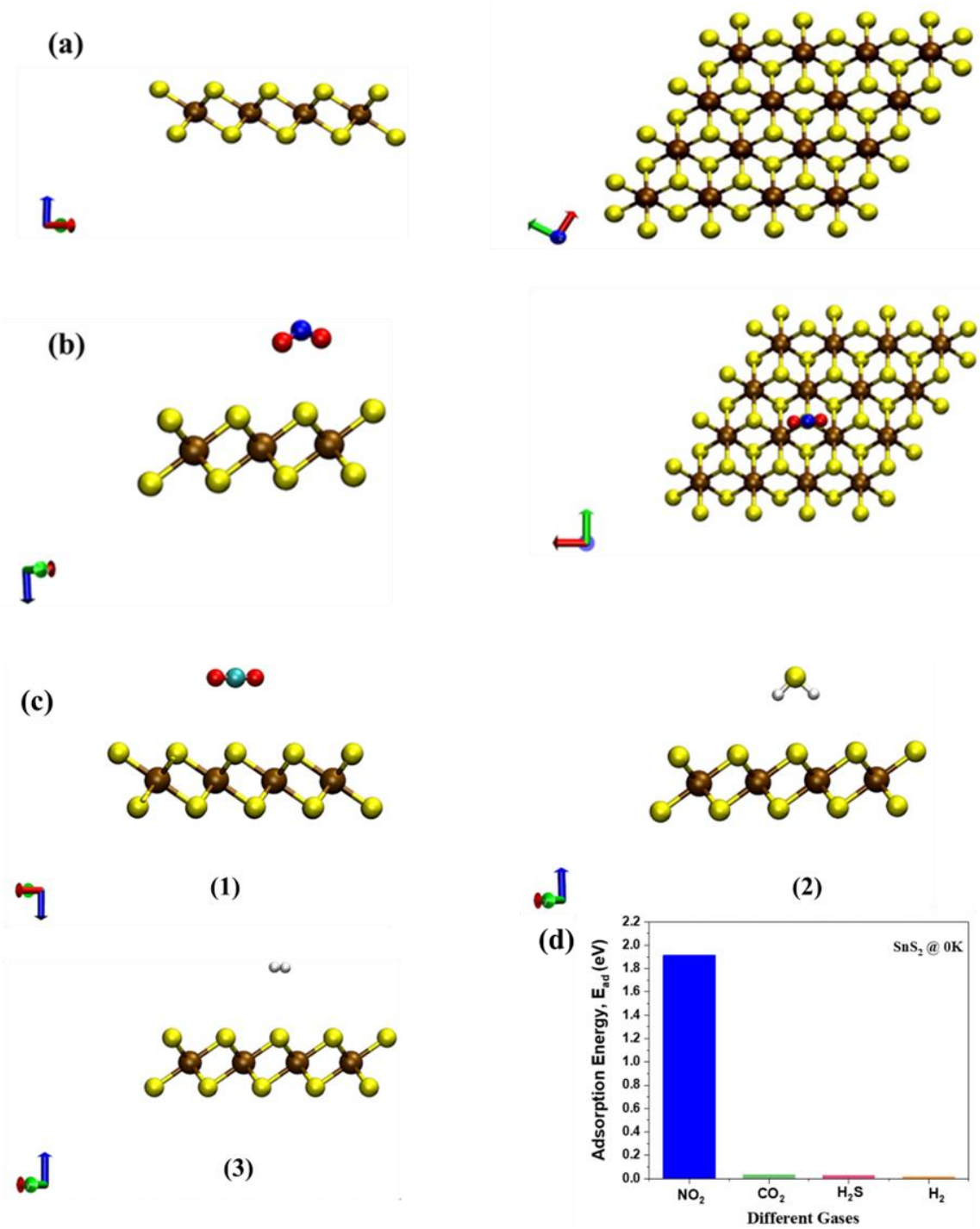



**Figure 6.2:** (a) The top and side view of a unit cell of monolayer $SnS_2$, (b) Optimized N atom of $NO_2$ molecule is adsorbed onto the surfaces of $SnS_2$ top and side view, (c) Other gases $CO_2$, $H_2S$ and $H_2$ kept similar fashion giving optimized structures (1)- (3), and (d) Histogram of adsorption energy for $NO_2$, $CO_2$, $H_2S$ and $H_2$ gas.

After structural optimization, the $NO_2$ molecule achieved a favorable configuration toward the $SnS_2$ adsorption surface, as shown in Figure 6.2. The results revealed that $NO_2$ exhibits the highest binding affinity to the $SnS_2$ monolayer with an adsorption energy of 1.91 eV, as summarized in Table 6.2. This binding energy is consistent with similar studies on Al-doped $SnS_2$ monolayers, demonstrating a strong interaction between $NO_2$ and $SnS_2$ [Qu et al., 2020]. Structural changes in the $NO_2$ molecule were evident upon adsorption. The N–O bond length decreased, and the O–N–O bond angle increased significantly by 38.5 degrees at the equilibrium geometry, indicating a substantial structural rearrangement. In contrast, no notable geometric changes were observed for other gases adsorbed on $SnS_2$, suggesting a unique interaction between $NO_2$ and the $SnS_2$ surface. Charge transfer analysis, performed using the Density-Derived Electrostatic and Chemical (DDEC) method, highlighted a significant charge transfer from the $NO_2$ molecule to the $SnS_2$ surface compared to other gases. This indicates that the interaction between $NO_2$ and $SnS_2$ has a pronounced ionic character, further emphasizing the strong binding affinity of $NO_2$. The interaction between the vertically aligned $SnS_2$ and $NO_2$ was thus confirmed to be highly favorable, with structural and electronic changes supporting its potential for gas-sensing applications.

**Table 6.2:** Adsorption energy and equilibrium distance along with charge transfer of the developed adsorption systems.

| System | Adsorption Energy (eV) | Adsorption length (Å) | Charge Transfer (e) |
|---|---|---|---|
| **$SnS_2$-$NO_2$** | 1.914 | 3.96 | -0.04851 |
| **$SnS_2$-$CO_2$** | 0.032 | 4.15 | 0.00001 |
| **$SnS_2$-$H_2S$** | 0.025 | 4.20 | 0.00297 |
| **$SnS_2$-$H_2$** | 0.016 | 4.23 | -0.00117 |

### 6.4.3. Adsorption properties of Vacancy-Assisted Vertically Aligned $SnS_2$ (Vs-$SnS_2$) flakes

We subsequently investigate the adsorption properties of $NO_2$ on vacancy assisted $SnS_2$ monolayers, focusing on adsorption energy, and charge transfer. The analysis is conducted based on the adsorption structure with the lowest energy configuration. To ensure that the global energy minimum is accurately identified and not confused with a local energy minimum, various adsorption sites and orientations are considered and optimized, as illustrated in Figure 6.3. Three types of supercells were constructed from pristine structure containing one vacant site (I), two conjugate vacant sites (II) and $N_2$ doped monolayer with one vacant site (III) i.e., one vacancy is replaced by a Nitrogen atom. All three structures were fully optimized before gas-surface calculations. The adsorption energies were calculated by

$$E_{ads} = - [E_{[SnS2\ monolayer+gas]} - E_{[SnS2\ monolayer]} - E_{[NO2]}] \quad (6.3)$$

Where, $E_{[SnS2\ monolayer\ +\ gas]}$, $E_{[SnS2\ monolayer]}$, and $E_{[NO2]}$ represent the energies of gas adsorbed system, isolated $SnS_2$ surface and isolated gas molecule, respectively. Gas-surface calculations were done by keeping $NO_2$ above the S vacant sites in all-mentioned structures. The optimized structures are visualized by VESTA[Momma et al., 2008] and JMOL [Hanson, 2010] packages and the relevant energies were computed.

Among all optimized structures, maximum adsorption energy was observed i.e., 2.19 eV with case (I) relative to other systems. This adsorption energy value is greater than $NO_2$ adsorption

energy with pristine sample (1.91 eV) as previously reported.[Kumar et al., 2022] In the above experiments, 50 ppm adsorption response at 120 °C showed significantly higher response with N12 sample over the pristine (N0) case. $NO_2$ molecule was chemisorbed on the surface forming strong covalent bond between Sn and O (bond length 1.17Å), in agreement with previously reported theoretical calculations by Rumeng Zhao et al.,[Zhao et al., 2017a] Case (II) has the lowest $NO_2$ adsorption energy (0.36 eV) whereas Case (III) depicts the intermediate adsorption energy (1.81 eV) as $NO_2$ binds by weak interactions with the surface. This is in consistent with the significant increase in adsorption of $NO_2$ gas as depicted by above experiments due to formation of single surface S vacancies up to certain $N_2$ plasma exposure time i.e., 12 min (N12 sample) and then decreasing after exposing for 16 min (N16 sample) as these vacant sites getting significantly occupied by Nitrogen (Figure 6.4 (a)). We computed the molecule-surface binding energies to evaluate the dispersion forces in order to comprehend the selectivity of Vs_$SnS_2$ (N12) towards $NO_2$ gas (Figure 6.4 (b-d)). An additional calculation was carried out for each case keeping gas molecule away from the vacant site above the surface resulting comparatively much lower adsorption energy of $NO_2$ gas (see Table 6.3).

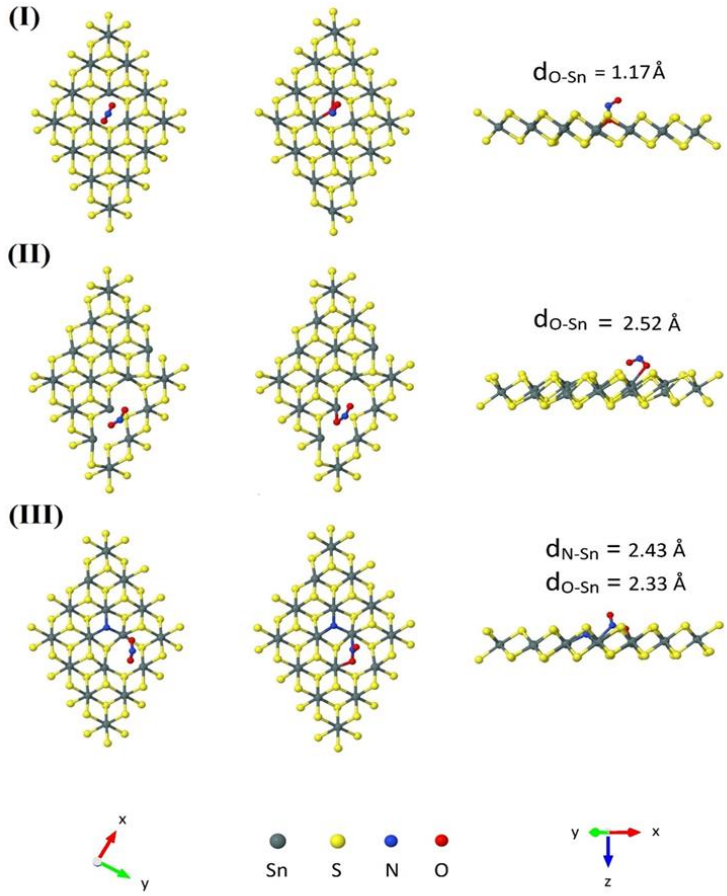



**Figure 6.3**: Computational model geometries of gas surface system. (a) Initial and optimized structures (from top and side view) of gas-monolayer adsorption system with $NO_2$ above the sulfur vacant sites with supercell containing single vacant site (I), (b) conjugated double vacant sites (II), and (c) Nitrogen doped single vacant site (III).

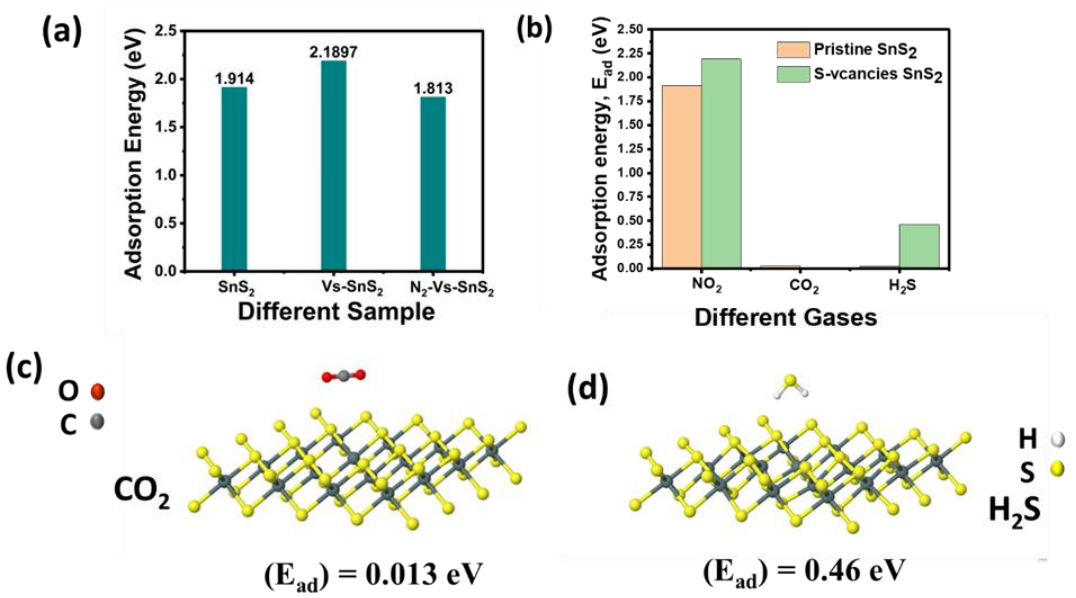



**Figure 6.4:** (a) Histogram of adsorption energy for pristine ($SnS_2$), structure containing sulfur vacant site (Vs-$SnS_2$) and Nitrogen doped monolayer with sulfur vacant site($N_2$-Vs-$SnS_2$), (b) Histogram of adsorption energy for $NO_2$, $CO_2$, and $H_2S$ gas, and optimized structures of other gases (c) $CO_2$, and (d) $H_2S$.

**Table 6.3:** Calculated gas adsorption energies of the gas adsorbed over $SnS_2$ surface

| System | Gas adsorption energy (eV) | |
|---|---|---|
| | $NO_2$ on top of Vacancy | $NO_2$ away from Vacancy |
| Case I | 2.19 | 0.48 |
| Case II | 0.36 | 0.047 |
| Case III | 1.813 | -0.0017 |

## 6.5 Gas sensor modelling

### 6.5.1. Gas adsorption-desorption kinetics in 2D material

Adsorption and desorption are vital processes in gas sensing mechanisms, governing how gas molecules interact with sensor materials and determining key performance metrics. In solid-state sensors, these processes influence sensitivity, response time, and recovery, which are essential for effective gas detection and continuous monitoring. Efficient adsorption enables the detection of low concentrations of target gases, while rapid desorption ensures the sensor can quickly return to its baseline state for real-time analysis. In 2D materials, adsorption-desorption dynamics play a pivotal role in defining the reversibility of the sensor's reactions, which is critical for applications requiring repeated use and accurate detection. Kinetic studies of these processes offer valuable insights into gas-surface interactions, impacting the sensor's selectivity and response. For carbon nanotube-based sensors, adsorption dynamics can be modeled using continuum site balance equations and mass action models, revealing both reversible and irreversible binding mechanisms. Irreversible adsorption shows a response time that inversely scales with analyte concentration, where detection is theoretically possible at any nonzero concentration but with longer transduction times for lower concentrations. In contrast, reversible sensors exhibit a fixed detection limit independent of geometry, with a response time that stabilizes at zero analyte concentration. A straightforward analytical test can distinguish these

mechanisms from transient response data, where consistent surface rate constants for irreversible components were identified across various sensor designs and analytes.

Benchmarking sensor responses and comparing the performance of different sensor types require careful consideration, particularly due to the distinct dynamics of reversible and irreversible adsorption mechanisms. Reversible gas sensors establish steady-state signals that correlate with analyte concentration, whereas carbon nanotube-based sensors often exhibit partially irreversible molecular binding for many analytes. This property enables the detection of extremely low analyte concentrations through integral trapping on the sensor surface. However, the presence of irreversible binding sites introduces a tradeoff between detection sensitivity and transduction time, as removing the analyte does not fully regenerate the sensor within the original transduction time scale. The Lee and Strano model provide a mathematical framework to analyse these dynamics, simplifying the interactions between gas molecules and sensor surfaces[Lee et al., 2005]. This model derives critical parameters, such as the adsorption rate constant ($k_{ads}$) and desorption rate constant ($k_{des}$), to quantify the interaction kinetics.

In the case of irreversible adsorption, the sensor response cannot be restored within the initial transduction time simply by removing the gas-phase analyte, necessitating alternative regeneration methods. The sensor array under consideration comprises a $SnS_2$ surface with a fixed number of adsorption sites (Tθ), which corresponds to the total accessible area available for analyte binding. These sites are divided into unoccupied (θ) and occupied (Aθ) categories. The analyte molecule (A), present in the gas phase at a constant concentration ($C_a$), reacts with an unoccupied site through a surface reaction:

$$\theta\ (sur) + A(g) \rightarrow A\theta(sur) \tag{6.4}$$

In this case, g and sur stand for gas phase and surface bound species, respectively, while k is the forward rate constant. The sensor surface has a conserved number of sites on the surface of $SnS_2$ sensor.

$$\theta(sur) + A\theta(sur) = T\theta\ (sur) \tag{6.5}$$

In this model, Tθ remains constant, determined by the sensor's accessible surface area. The sensor's signal (R) is proportional to the number of occupied sites (Aθ), as the analyte's interaction with the surface induces measurable changes in conductance (ΔG), which is normalized via the baseline conductance ($G_o$).

$$\frac{d^2R}{d\ (A\theta)^2} = 0$$

This relationship holds under specific scenarios, such as doping effects in semiconducting 2D-$SnS_2$, with the proportionality factor varying based on $SnS_2$ type and analyte electronegativity. Using a mass action framework, the sensor response rate is derived from the adsorption dynamics, assuming no pre-adsorbed analyte using eq (6.4).

$$\frac{dA\theta}{dt} = k_{ir(ads)}\theta C_a \tag{6.6}$$

Using a variant of an Eley-Rideal-type mechanism, the gas phase species A interacts directly with the empty site in the most basic scenario[Masel, 1996]. Since there is no polymer overlayer on an uncoated array, it is plausible to assume that there is no pre-adsorption isotherm. Applying site balance eq. 6.5

$$\frac{dA\theta}{dt} = k_{ir(ads)}[T\theta - A\theta]C_a \tag{6.7}$$

Solving eq 6.7 for the case of an initially clean array at $t$ = 0:

$$A\theta(t) = (T\theta)(1 - \exp[-k_{ir(ads)}C_a t]$$

$$R(t) = R_{max}(1 - \exp[-C_a . k_{ir(ads)} . t]) \qquad (6.8)$$

Where $R_{max}$ is the maximum response change when sensor is saturated, $C_a$ is the gas concentration, $k_{ir(ads)}$ is the forward rate constant, $t$ is time taken by sensor to reach the response at saturation.

### 6.5.2. Transient response cycles with fitting curve of Pristine $SnS_2$ flakes

The experimental transient response curves of $SnS_2$ sensors for different concentrations of $NO_2$ vapor (5 to 50 ppm) at room temperature (RT) and 120 °C, as illustrated in Figures 6.5. As depicted in Figure 6.5, the response of the $SnS_2$ sensing layer increased exponentially upon exposure to the oxidizing $NO_2$ gas and reached a steady-state saturation level within seconds for each concentration. The dashed red lines in the figures represent the fitting curves for the respective concentrations, showing excellent agreement with the experimental data, as no significant deviation was observed. Figures 6.5 (a, d), summarize the normalized response change ($R_{max}$) as a function of time for different $NO_2$ concentrations at RT and 120 °C. The forward rate constant (($k_{ir(ads)}$) is a critical kinetic parameter to evaluate the sensing performance, particularly for on-site detection applications. According to Equation 6.8, the forward rate constant ($k_{ir(ads)}$) varies with the $NO_2$ concentration ($C_a$) and is extracted from the fitting curves of the normalized time-dependent response data in Figure 6.5 (c, f). The values of ($k_{ir(ads)}$) for the examined concentration range (5 to 50 ppm) are listed in Table 6.4, showing that the forward rate constant increases with higher $NO_2$ concentrations, as expected from the theoretical model.

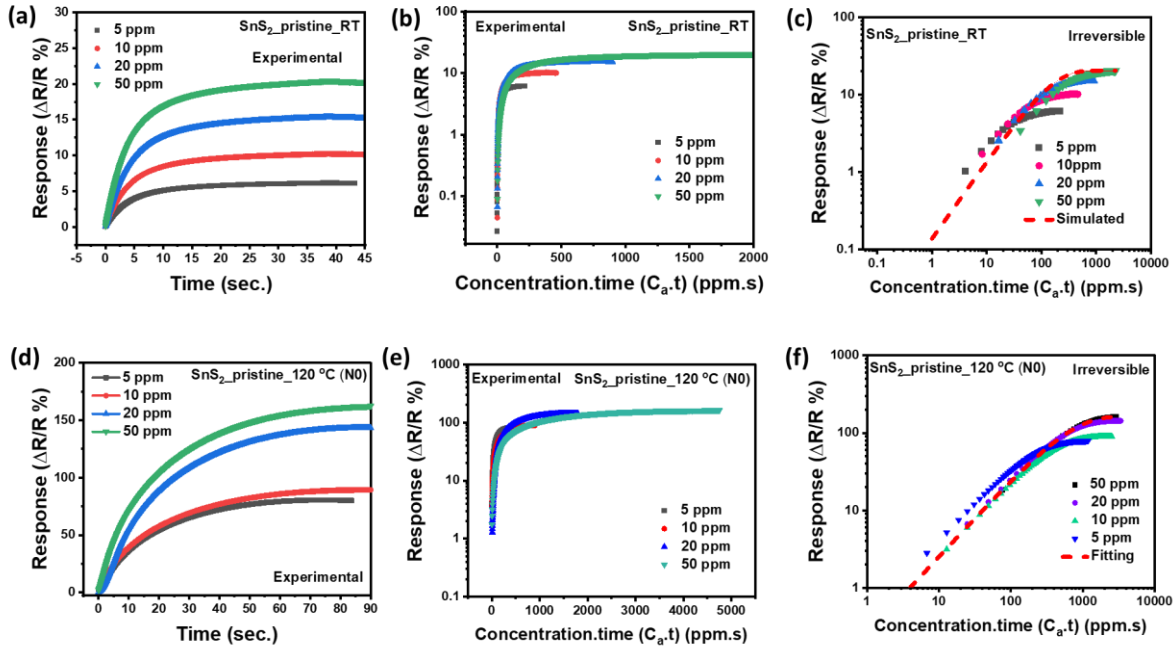



**Figure 6.5 Irreversible Adsorption:** Experimental (scattered point) and fitted (solid dashed red line) response of VA-$SnS_2$ based sensor to $NO_2$ gases for different concentration (5-50ppm) at (a-c) RT, and 120 °C.

### 6.5.3. Transient response curve with fitting curve of nitrogen plasma treated $SnS_2$ flakes

We investigate the $NO_2$ detection on pristine and nitrogen plasma CVD grown on $SnS_2$ nanoflakes. In our previous paper, the as grown $SnS_2$ nanoflakes have incomplete recovery and takes longer recovery time due to higher binding affinity and sticking coefficients between the active site of $SnS_2$ nanoflakes and $NO_2$. Figure 6.5 (d-f) and Figure 6.6 (e-g), illustrates the transient relative response change parametric for $NO_2$ concentration of pristine $SnS_2$ (N0) and Vs_$SnS_2$ (N12) sample. None attain a stable state, and the surface is renewed using temperature (external

heater) after an arbitrary exposure duration. The corresponding response for $NO_2$ concentrations of 5, 10, 20, and 50 ppm for N0 and N12 samples were fitted using eq (6.8) and the fitted results are displayed in Figure 6.5 and 6.6. When plotting the relative response against the product, $C_at$, the graph collapses into one graph, which is an indication of irreversible adsorption (Figure 6.6 (g)). By fitting the response curves of N0, N4, N8, N12 and N16 samples of $SnS_2$ to eq (6.8), the forward rate constants were determined (Table 6.5). The results revealed that the forward rate constants ($k_{ir(ads)}$) of the N12 sample was 1.39 x $10^{-4}$ $(ppm.s)^{-1}$, which are 8.93 times higher than the values (1.56 x $10^{-5}$ $(ppm.s)^{-1}$) of the N0 sample, respectively. As the duration of $N_2$ plasma was increased and $NO_2$ was exposed to the sensor, the adsorption rate constants increased till 12 min (N12 sample) and after that it decreased. Table 6.5 shows the forward rate constants ($k_{ir(ads)}$) of pristine and $N_2$ plasma treated samples toward $NO_2$ at different concentration of $NO_2$ gas calculated using irreversible adsorption model. The results revealed that N12 sample exhibited threefold higher adsorption rate constant than other samples, due to the high adsorption energy of $NO_2$ on the edge site of $SnS_2$, demonstrating the effect of sulfur vacancies of $SnS_2$ nanoflakes with abundant edges. In addition, the adsorption rate constant of N16 was decreased compared with N12 due to the formation of N-Sn bond with decreased edge sites, indicating the importance of edge abundant structure for $NO_2$ sensing.

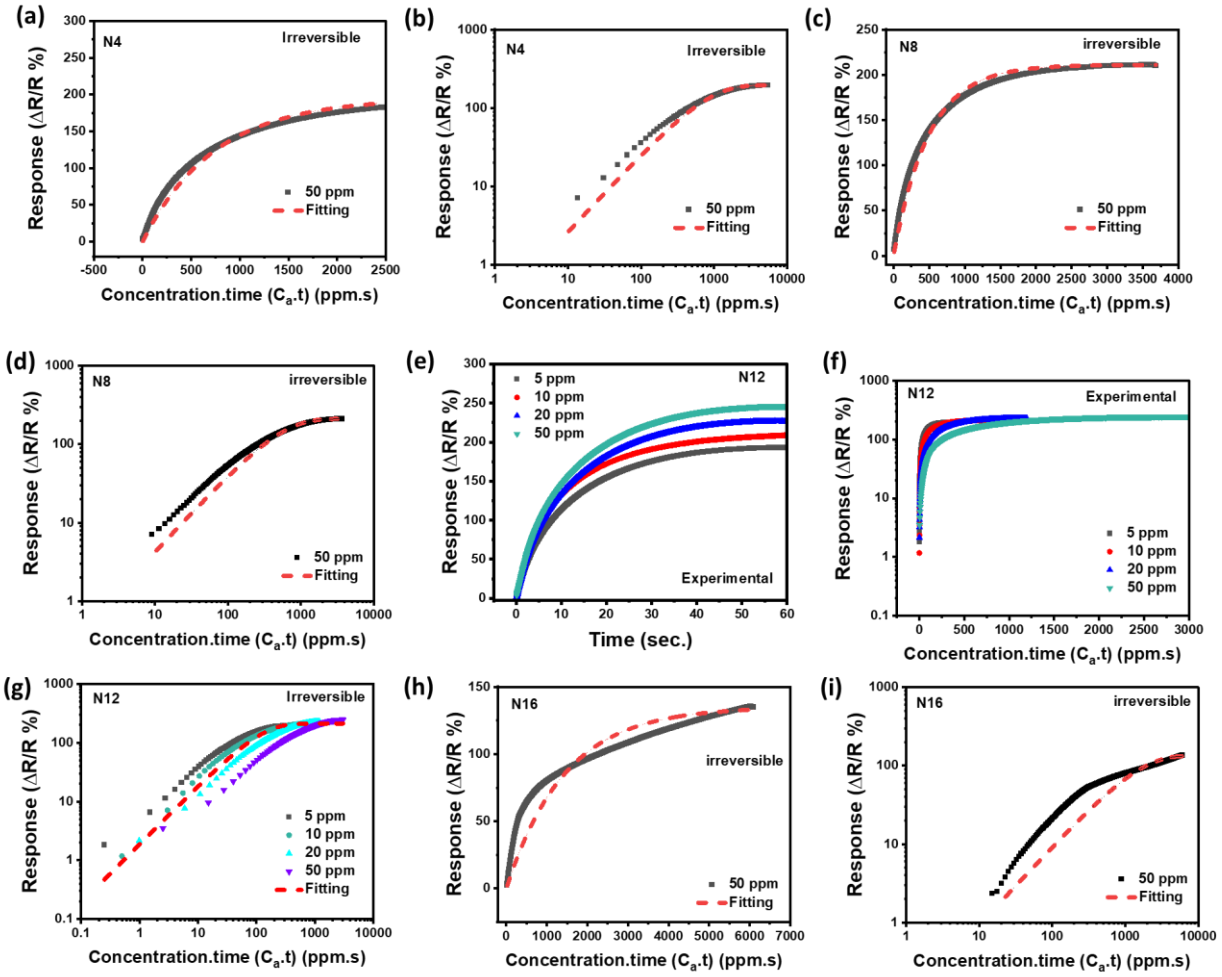



**Figure 6.6:** Irreversible Adsorption (Nonlinear fit model): Response transients of nitrogen plasma treated $SnS_2$ (Vs-$SnS_2$) samples are plotted as a function of ($C_at$) vs log response the points collapse to a single model operating at 120 °C (a, b) N4 sample, (c, d) N8 sample, (e, f, g) N12 sample, and (h, i) N16 sample, fitted (red color short dashed line), respectively.

**Table 6.4:** A summary of forward rate ($k_{ir(ads)}$) constant and maximum response of pristine $SnS_2$ and nitrogen plasma $SnS_2$ for various concentration of $NO_2$ at various operating temperatures using irreversible adsorption model.

| Sample | Operating Temp. | Gas concentration (PPM) | Maximum value of Response ($R_{max}$) | Forward rate constant ($k_{ir(ads)}$) $(ppm.s)^{-1}$ |
|---|---|---|---|---|
| **No** | RT | 5 | 6.12 | $7.45 \times 10^{-3}$ |
| | | 10 | 10.22 | $1.85 \times 10^{-3}$ |
| | | 20 | 15.33 | $4.62431 \times 10^{-4}$ |
| | | 50 | 20.42 | $7.42359 \times 10^{-5}$ |
| | | Single mode curve fitting | 20.42 | $5.97972 \times 10^{-5}$ |
| | 120 °C | 5 | 80.50 | $1 \times 10^{-3}$ |
| | | 10 | 89.33 | $2.85493 \times 10^{-5}$ |
| | | 20 | 143.45 | $9.58312 \times 10^{-5}$ |
| | | 50 | 162.66 | $3.14762 \times 10^{-5}$ |
| | | Single mode curve fitting | 162.66 | $1.55595 \times 10^{-5}$ |
| **N12** | 120 °C | 5 | 192.99 | $3.49 \times 10^{-3}$ |
| | | 10 | 208.72 | $9.52511 \times 10^{-4}$ |
| | | 20 | 226.45 | $2.16825 \times 10^{-4}$ |
| | | 50 | 246.30 | $3.44613 \times 10^{-5}$ |
| | | Single mode curve fitting | 246.30 | $1.38979 \times 10^{-4}$ |
| **N4** | | 50 | 195.18 | $2.71037 \times 10^{-5}$ |
| **N8** | | 50 | 211.12 | $4.05085 \times 10^{-5}$ |
| **N12** | | 50 | 135.17 | $1.882 \times 10^{-5}$ |

**Table 6.5:** Values of various parameter derived by fitting of the response curve as a function of concentration.

| Sample | Operating Temperature | Maximum value of Response ($R_{max}$) | Forward rate constant ($k_{ir(ads)}$) $(ppm.s)^{-1}$ |
|---|---|---|---|
| **No** | RT | 20.42 | $5.97972 \times 10^{-5}$ |
| **No** | 120 °C | 162.66 | $1.55595 \times 10^{-5}$ |
| **N4** | | 195.18 | $2.71037 \times 10^{-5}$ |
| **N8** | | 211.12 | $4.05085 \times 10^{-5}$ |
| **N12** | | 246.30 | $1.38979 \times 10^{-4}$ |
| **16** | | 135.17 | $1.882 \times 10^{-5}$ |

## 6.6 Summary

In summary, Density functional theory (DFT) calculations were conducted to evaluate the $NO_2$ gas adsorption properties on three functionalized $MoS_2$ monolayers: pristine $MoS_2$, nitrogen-doped $MoS_2$ (N-$MoS_2$), and silver-functionalized nitrogen-doped $MoS_2$ (Ag-N-$MoS_2$). For pristine $MoS_2$, weak van der Waals interactions were observed between the surface and $NO_2$ molecules, with the lowest adsorption energy of -0.53 eV. Nitrogen doping enhanced the adsorption energy to -0.75 eV, with noticeable symmetry breaking in the $NO_2$ molecule due to unequal bond lengths and a dominant non-bonding interaction between oxygen and nitrogen on the surface ($d_{O\text{-}N(surface)}$ = 2.06 Å). Further functionalization with silver nanoparticles significantly increased the adsorption energy to -1.33 eV. Additionally, $SnS_2$ monolayers demonstrated a higher $NO_2$ binding affinity compared to other gases, with an adsorption energy of -1.91 eV, attributed to an increase in carrier concentration upon $NO_2$ adsorption. DFT studies also revealed that sulfur-vacancy defects on $SnS_2$ surfaces shifted the adsorption mechanism from physisorption to chemisorption. Among three optimized structures, the highest adsorption energy (2.19 eV) was observed for the structure with one sulfur vacancy, outperforming pristine $SnS_2$. Using the Lee and Strano reaction mechanism to model gas sensing, it was found that the N12 sample exhibited a higher forward rate constant ($k_{ir(ads)}$ =1.39 x $10^{-4}$ $(ppm.s)^{-1}$) than NO sample $k_{ir(ads)}$ =1.56 x $10^{-5}$ $(ppm.s)^{-1}$) at an operating temperature of 120 °C, highlighting the enhanced sensing performance of functionalized materials.

# 7
# High-Performance Broadband Photodetector Based on $MoS_2$-$WS_2$ Heterojunction

In this chapter, we systematically explore the light sensing performance of $MoS_2$ and $MoS_2$-$WS_2$ heterojunction-based photodetectors in the visible to near-infrared wavelength spectrum. First, the growth of $MoS_2$ flakes network via the controlled kinetics conditions of conventional chemical vapor deposition (CVD) process and crumpled $WS_2$ nanoparticles via hydrothermal method were explained. Subsequent to the fabrication of the $MoS_2$-$WS_2$ heterojunctions, we rigorously characterize the resultant structures to evaluate their morphological features, crystallographic integrity, electron doping characteristics, elemental composition, and optical absorption properties. As a proof of concept, we investigate the light-induced electrical responses of both pristine $MoS_2$ flakes and the $MoS_2$-$WS_2$ heterojunctions under illumination conditions that extend from visible to near-infrared, while concurrently assessing the responsivity, detectivity, external quantum efficiency, stability, response time, and reproducibility of the photodetectors. Our analysis underscores the promising potential of two-dimensional $MoS_2$ for photodetector applications, particularly via the incorporation of heterostructures such as $MoS_2$-$WS_2$, which significantly enhance photoresponse capabilities for self-powered broadband photodetection across visible to near-infrared ranges. The energy band alignment at the heterojunction interface critically affects photodetector performance, and an understanding of photo-generated carrier dynamics at the interface is crucial for high-performance devices. To gain intrinsic physical insights into device behavior and light-sensing mechanism, we analyse charge carrier dynamics using photoelectron spectroscopy (XPS) and kelvin probe force microscopy (KPFM). The demonstration of $MoS_2$ heterostructures as high-performance broadband photodetectors offer exciting opportunities for efficient optoelectronics and imaging applications.

## 7.1 Requirement of highly sensitive, fast, and broadband photodetectors

The photodetector is an important component of optoelectronics devices, which use leveraging technology to transform optical signals into electrical signals. The process involves the absorption of photons, resulting in the creation of electron-hole pairs and separation of the pair at the junction. When subjected to an electric field, they generate a current that enables the detection of the related optical signal. The next generation of multifunctional systems is experiencing a technological roadblock due to the need for broadband sensing capabilities while also reaching miniaturised footprints [Vashishtha et al., 2023; Zeng et al., 2016; Zou et al., 2022]. The demand for broadband photodetectors is now high in the field of nano-optoelectronics due to their significant contributions to a number of different applications, such as the medical field, military, optoelectronic communication, imaging, environmental monitoring, space exploration, and other related domains [Goswami et al., 2020; Kumar et al., 2021a; Lien et al., 2020; Pan et al., 2022; Pospischil et al., 2013; Xiao et al., 2019]. Broadband photodetectors (PDs) are intriguing because they can detect light from a wide range of wavelengths without the need for additional devices. This spectrum encompasses the electromagnetic spectrum's visible and near-infrared (NIR) portions. Photodetectors need to be very sensitive to light over a wide spectrum and have rapid reaction times so that they can perform these functions efficiently. A narrow photon detection bandwidth is a common consequence of the usage of many photoactive semiconductors in commercial high-performance devices with proper band alignment. In this regard, silicon, InGaAs, and GaN are used for light detection in the visible, near-infrared (NIR), and ultraviolet (UV) regimes [Aggarwal et al., 2020; Ejeckam et al., 1995; Gundimeda et al., 2017; Ye et al., 2013].

Transition metal dichalcogenides (TMDs) have been the subject of intense research in recent years due to their unique semiconductor features, including the small band gap and high

carrier mobility, as compared to 3D semiconductors like silicon and germanium [Huang et al., 2006; Jariwala et al., 2014; Vivien et al., 2009]. However, the task of assuring certain attributes, such as flexibility, is a persistent challenge for devices based on 3D semiconductors. The optoelectronic properties of two-dimensional (2D) transition metal dichalcogenides (TMDCs) have garnered significant attention in research due to their large surface-to-volume ratio feature with excellent photoresponsivity, detectivity, external quantum efficiency, flexibility, and spectral response range capabilities [Lee et al., 2013; Lopez-Sanchez et al., 2013; Wang et al., 2012; Xie et al., 2017b]. Molybdenum disulfide ($MoS_2$) is one of the most extensively studied and leading 2D semiconductors, have garnered attention as a potential next-generation broadband photodetector (PD) due to its direct and adjustable bandgap, large current on/off ratio, high carrier mobility and a high absorption coefficient, among other interesting properties [Feng et al., 2021; Jariwala et al., 2014; Jiang et al., 2020]. $MoS_2$ is a popular layered transition metal dichalcogenide consisting of a stack of planes in which S-Mo-S atoms in each layer are covalently bound to one another in a hexagonal structure and each of the adjacent planes are kept connected through van der Waals interactions. As compared to the most prevalent sunlight absorbers Si and GaAs, $MoS_2$ has one order of magnitude higher sunlight absorption [Bernardi et al., 2013].

Considering the significant advancements in the performance of $MoS_2$ photodetectors, using a single material constrains the performance of photodetectors due to the low absorption of light. So, the performance of the photodetector may be significantly improved by integrating two or more high-absorbing materials to obtain outstanding light absorption and broad-spectrum response [Long et al., 2016b; Wadhwa et al., 2021b; Yu et al., 2013]. As a result, $MoS_2$ optical absorption may be increased by developing a heterostructure with other materials having high optical absorption. Heterostructure photodetector devices have a better photo response and can enable more functionality ability than single-material devices [Yang et al., 2017b]. Since 2D materials have several unique physical properties, including dangling-bond-free surfaces, which make it possible to produce heterostructures without any mismatches in the atomic lattice [Zhang et al., 2020b]. The fabrication of 2D material heterostructures yields atomically thin surfaces and novel optoelectronic features, allowing for room-temperature photodetection and providing a distinctive material framework for basic research. In recent years, a plethora of 2D material heterostructure-based photodetectors have been developed including graphene/$MoS_2$ [Thai et al., n.d.], $WSe_2$/$MoS_2$ [Shin et al., 2020], and $MoS_2$/black phosphorus [Bullock et al., 2018]. Despite the excellent physical properties, $MoS_2$/$WS_2$ heterostructures have seen relatively little research into optoelectronic applications. In a previous study, Wu, W. *et al*., successfully fabricated monolayer $MoS_2$-$WS_2$ in-plane heterostructures. These heterostructures demonstrated a spectrum responsivity ($R_\lambda$) of 4.36 mA/W and a detectivity (D*) of $4.36 \times 10^{13}$ Jones when subjected to an optical power density of 28.64 mW/cm$^2$ at a wavelength of 532 nm [Wu et al., 2018b]. Xin *et al*. present a polarization-sensitive based self-powered GeSe/$MoS_2$ p-n heterojunction photodetector. When illuminated by a 532 nm laser at zero bias, the self-powered photocurrent displays an impressive on-off ratio of over $10^4$, in addition to a high responsivity of 105 mA/W, a detectivity of $1.03 \times 10^{10}$ Jones, and an EQE of 24.2%, and a rapid photo response speed (rise time = 110 ms and decay time = 750 ms) [Xin et al., 2020]. Furthermore, the similar crystal structures of $MoS_2$ and $WS_2$, two examples of 2D layered materials, allow for the development of tailored heterojunctions without the significant constraint of lattice match seen in traditional semiconductor heterostructures [Samad et al., 2016].

## 7.2 Device fabrication from $MoS_2$-$WS_2$ heterojunction and light-sensing experimental details

Large-area $MoS_2$ flake networks were synthesized using a thermal chemical vapor deposition (CVD) method with $MoO_3$ and sulfur as precursors. During the process, the $MoO_3$ source was heated to 850°C, while the sulfur source was maintained at 200°C. Argon gas was used as the carrier at a flow rate of 80 SCCM under atmospheric pressure for 45 minutes. The synthesis procedure is described in detail in Chapter 3. $WS_2$ nanoparticles, on the other hand, were

prepared through a hydrothermal synthesis method. The complete fabrication process for the $WS_2/MoS_2$ heterojunction-based photodetector device, along with its characterization, has also been elaborated in Chapter 3 under the device fabrication setps.

## 7.3 Characterization of $MoS_2$-$WS_2$ heterojunctions

FE-SEM micrographs were used to investigate the continuity and surface morphology of the grown $MoS_2$ film and $MoS_2$-$WS_2$ heterostructure. Figure 7.1 (a), displays FE-SEM images of pristine $MoS_2$ nanosheet grown using CVD and functionalized $WS_2$ on the surface of $MoS_2$ at various locations of the samples. It can be seen that nearly all of the $WS_2$ NPs are coated over the edges of the $MoS_2$ flakes, and a few of the $WS_2$ NPs are anchored over the edges of the $MoS_2$ flakes, with some of the $WS_2$ NPs diffuse into $MoS_2$ nanosheets. As the surface area of $MoS_2$ flakes is very large [He et al., 2019], the decorated $WS_2$ will generate a large area of contact, which is highly suggested for adequate carrier movement at the interface. Elemental mapping via energy dispersive spectroscopy (EDS) confirmed the presence of Mo, S, and W elements at the $MoS_2$-$WS_2$ heterojunction, verifying the integration of both $MoS_2$ and $WS_2$ through their individual elemental signatures, as depicted in Figure 7.1 (b-d).

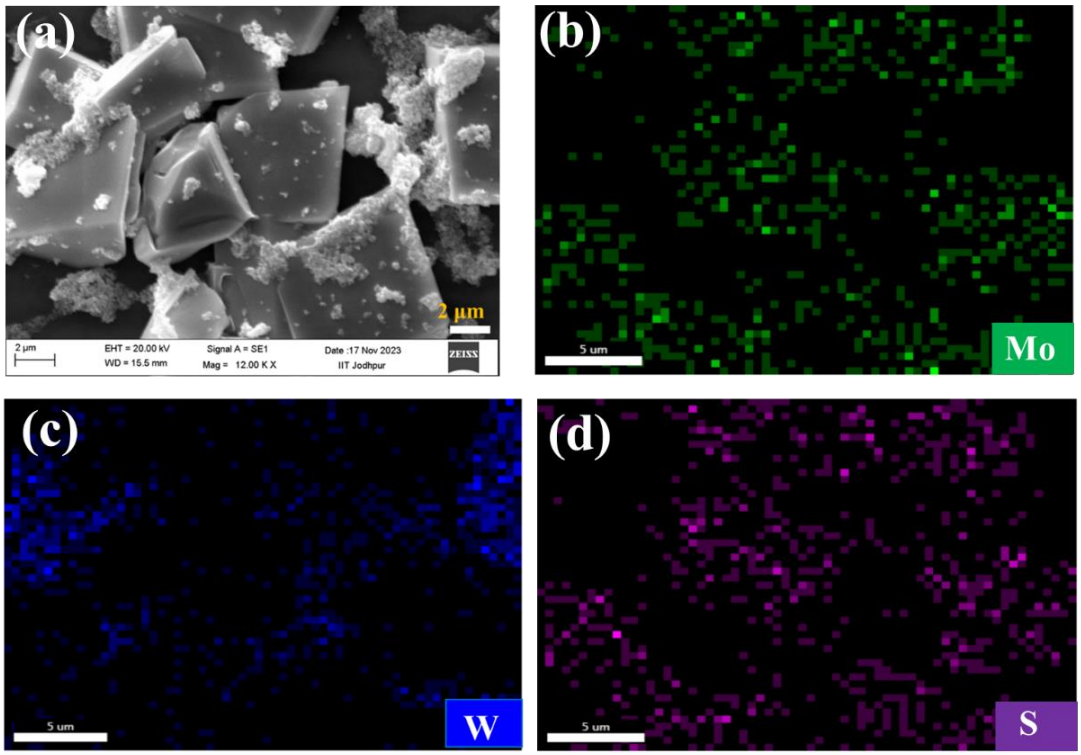



**Figure 7.1:** (a) FE-SEM image of WS2 nanoparticles decorated $MoS_2$ flakes network, (b, c, d) EDX element mapping pictures of the $MoS_2$-$WS_2$, confirming the existence of Mo, W and S.

We performed Raman measurements in order to confirm the existence of $MoS_2$, $WS_2$ and their heterostructure nature using optical phonon modes, as shown in Figure 7.2 (a). There are two prominent peaks in the Raman spectra of pristine $MoS_2$ at ~ 383 $cm^{-1}$ and ~ 408 $cm^{-1}$, with respect to in-plane vibration mode ($E^1_{2g}$) of both S and Mo in the opposite direction and out-of-plane vibration mode ($A_{1g}$) of only Mo with fixed S in opposite direction, respectively [Kumar et al., 2017; Lee et al., 2010]. We observe that pure $WS_2$ has two Raman peaks, at 353 $cm^{-1}$ ($E^1_{2g}$) and 416 $cm^{-1}$ ($A_{1g}$), respectively [Zhang et al., 2018d]. As demonstrated in Figure 1b, the presence of both materials and the development of a $MoS_2$-$WS_2$ heterojunction are confirmed by the signature of four Raman characteristic peaks positioned at 350 $cm^{-1}$, 382 $cm^{-1}$, 408 $cm^{-1}$, and 417 $cm^{-1}$ corresponding to each material $WS_2$ ($E^1_{2g}$), $MoS_2$ ($E^1_{2g}$), $MoS_2$ ($A_{1g}$), and $WS_2$ ($A_{1g}$), respectively. Figure 7.2 (b), shows the PL spectra of pristine $MoS_2$, $WS_2$, and $MoS_2$-$WS_2$ heterostructure using a focused excitation laser (532 nm). The $MoS_2$ films have a binding energy of PL peak at 1.84 eV

(red curve), corresponding to 674 nm. In addition, the A-exciton emission peak of single-layer $WS_2$ occurs at a wavelength of 626 nm, with a PL peak location of 1.98 eV [Chen et al., 2016]. The $MoS_2$ peak moves marginally to 1.84 eV in the $MoS_2$-$WS_2$ heterostructure, whereas the $WS_2$ peak moves slightly to 1.98 eV, both relative to their respective bulk peaks. Interlayer coupling between two layers is responsible for these energy changes, and the average coupling strength is found to be 0.045 eV [Han et al., 2020; Hong et al., 2014].

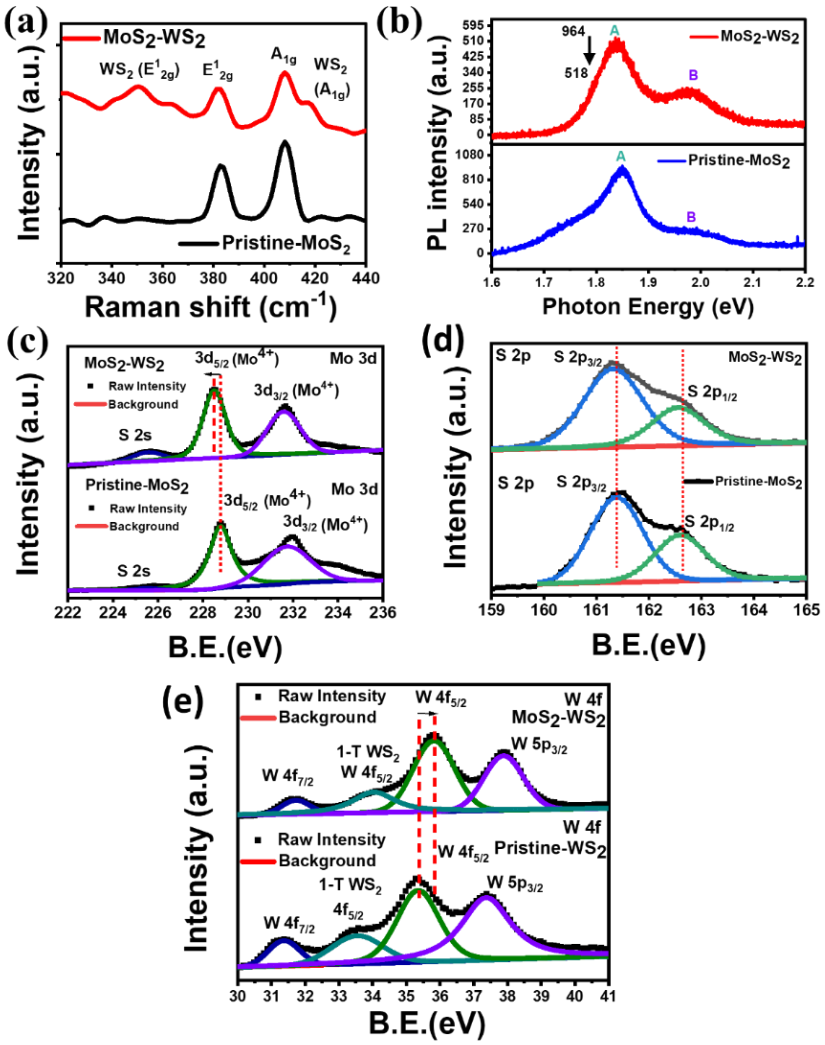



**Figure 7.2:** (a) Raman spectrum of pristine-$MoS_2$ and $MoS_2$-$WS_2$ heterostructures (b) PL spectra of pristine-$MoS_2$ and $MoS_2$-$WS_2$ heterostructures. XPS spectra of pristine-$MoS_2$ and $MoS_2$-$WS_2$ heterostructures (c) Mo 3d, (d) S 2p, and (e) W 4f peaks, respectively.

XPS spectroscopy was used to determine the Chemical states and surface composition of the $MoS_2$ that had been adorned with $WS_2$. Figure 7.2 (c-e), shows high-resolution core level spectra of Mo 3d, S 2p, and W 4f for $MoS_2$-$WS_2$ heterostructure and pristine $MoS_2$ respectively. The deconvolution peaks at 228.82, 228.48 and 231.72, 231.58 eV are related to Mo $3d_{5/2}$ and Mo $3d_{3/2}$ corresponding to pristine $MoS_2$ and $MoS_2$-$WS_2$ heterostructure, respectively. Also, the curve indicates that Mo peaks at 233.88 eV and 234.32 eV, corresponding to $Mo^{+6}$ state due to presence molybdenum oxides sample after CVD development and post-synthesis exposure to air [Xue et al., 2016]. Figure 7.2 (d), depicts the binding energy peaks for the S $2p_{3/2}$ and S $2p_{1/2}$ states at 161.41and 162.58 eV, respectively. Figure 7.2 (e), depicts the W 4f spectra having 1T-and 2H-$WS_2$ phase and 2H-$WS_2$ deconvoluted into two peaks located at 31.39, and 35.30 eV, which belong to W $4f_{7/2}$, and W $4f_{5/2}$, respectively. The observed peak positions and shape of W 4f and Mo 3d indicate the coexistence of $WS_2$ and $MoS_2$, as reported in the literature [Lonkar et al., 2020]. At the $MoS_2$-$WS_2$ heterostructure, it was found that a change in the binding energy of the Mo 3d core levels had occurred after detailed examination of the XPS core-level energy spectrum. Mo $3d_{5/2}$

and Mo $3d_{3/2}$ peak location had a redshift of 0.234 and 0.14 eV level spectra indicates combined actions of the inherently n-type TMDCs, $MoS_2$ and $WS_2$ both have a negative net charge within the heterostructure [Chiu et al., 2017]. This change in core-level spectra immediately points to interlayer interaction and transfer of charge between $MoS_2$ and $WS_2$.

## 7.4 Effects of visible to near-infrared wavelength on the $MoS_2$-$WS_2$ heterojunctions

We fabricated pristine-$MoS_2$ and $WS_2$ decorated on the $MoS_2$ sample to evaluate the photodetector performance parameters with a voltage biasing range of ±5V, as seen in Figure 7.3 (a). Figure 7.3 (b), depicts the current-voltage (*I-V*) behavior of pristine $MoS_2$ and $MoS_2$-$WS_2$ heterostructure photodetector in the dark condition. The photoresponse of a $MoS_2$-$WS_2$ heterostructure was studied by using a different volume of drop-cast $WS_2$ solution (1µl-20 µl). We find that the photoresponse of the heterostructure improves with increasing $WS_2$ concentration up to a saturation point at 10 µl. However, the photocurrent begins to decrease when the number of $WS_2$ NPs surpasses 10µl, indicating that this concentration is the optimum amount of $WS_2$ at the heterointerface for optimal device performance. The *I-V* characteristics of pristine $MoS_2$ photodetector in dark and exposure of Visible-NIR spectrum is depicted in Figure 7.3 (c). Figure 7.3 (d), depicts the current-voltage (*I-V*) behaviour of $MoS_2$-$WS_2$ heterostructure photodetector in the dark condition and under the illumination of different wavelength from visible to NIR domain (405-800 nm). The *I-V* curve shows that the $MoS_2$-$WS_2$ heterostructure displayed a significant rise in photocurrent in the Visible to NIR range, whereas the photo response of pristine $MoS_2$ showed only a small increase in current upon exposure to light (visible-NIR) as compared to its dark current. $MoS_2$-$WS_2$ heterostructure has an improved broadband photoresponse as a result of greater absorption in the Visible-NIR region and a significant built-in potential at the interface. Furthermore, we observe that the photocurrent created by the 580 nm light is higher than that of the other wavelength, which is due to the high photon energy. In addition, the comparison of the photocurrent of 10 µl solution-based $WS_2$-$MoS_2$ and pristine $MoS_2$ at 580nm of light, is mentioned in Figure 7.3 (e, f). It is observed that the current conduction behaviour was significantly affected by the decoration of $WS_2$ as compared to the pristine $MoS_2$ flakes.

In order to determine the performance of the device, we determined the self-powered photodetector's figures of merit, such as responsivity (R), external quantum efficiency (EQE), and detectivity (D*). One of the most important characteristics of a photodetector is its responsivity (R), which is defined as the ratio of the generated photocurrent to the incident optical power, can be written as equation 7.1[Lei et al., 2021]:

$$R = \frac{I_{Photo} - I_{dark}}{P_{in} \,.\, A} \quad (A/W) \tag{7.1}$$

Where, $I_{Photo}$ and $I_{dark}$ are photocurrent, and dark current $P_{in}$ is the optical power density of the incident light source, and A is an effective area of the device (0.0091 $cm^2$), respectively.

Figure 7.4 (a), shows the responsivity of pristine $MoS_2$, and $MoS_2$-$WS_2$ heterojunction under Visible-NIR (405-800 nm) light at zero bias voltage (0V). The $MoS_2$-$WS_2$ heterojunction exhibits a high responsivity (R=282.77 mA/W), 12 times higher than pristine $MoS_2$ (R=23.55 mA/W), under illumination of 580 nm light. Further, assuming that the shot noise is dominated by a dark current, we determined the specific detectivity (D*) of the fabricated photodetector, which determines the ability of the photodetector to detect the weak optical signal and is given by the following equation 3 [He et al., 2021]:

$$D^* = \frac{R.\sqrt{A}}{\sqrt{2q.I_{dark}}} \tag{7.2}$$

Where A represents an active area of the device, R is responsivity, q is the electron charge and $I_{dark}$ is the dark current of the device. According to equation (7.2), we calculated the specific detectivity

(D*) of pristine $MoS_2$ and $MoS_2$-$WS_2$ heterostructure self-power photodetector (0V) under irradiation of different wavelength, as shown in Figure 7.4 (b).

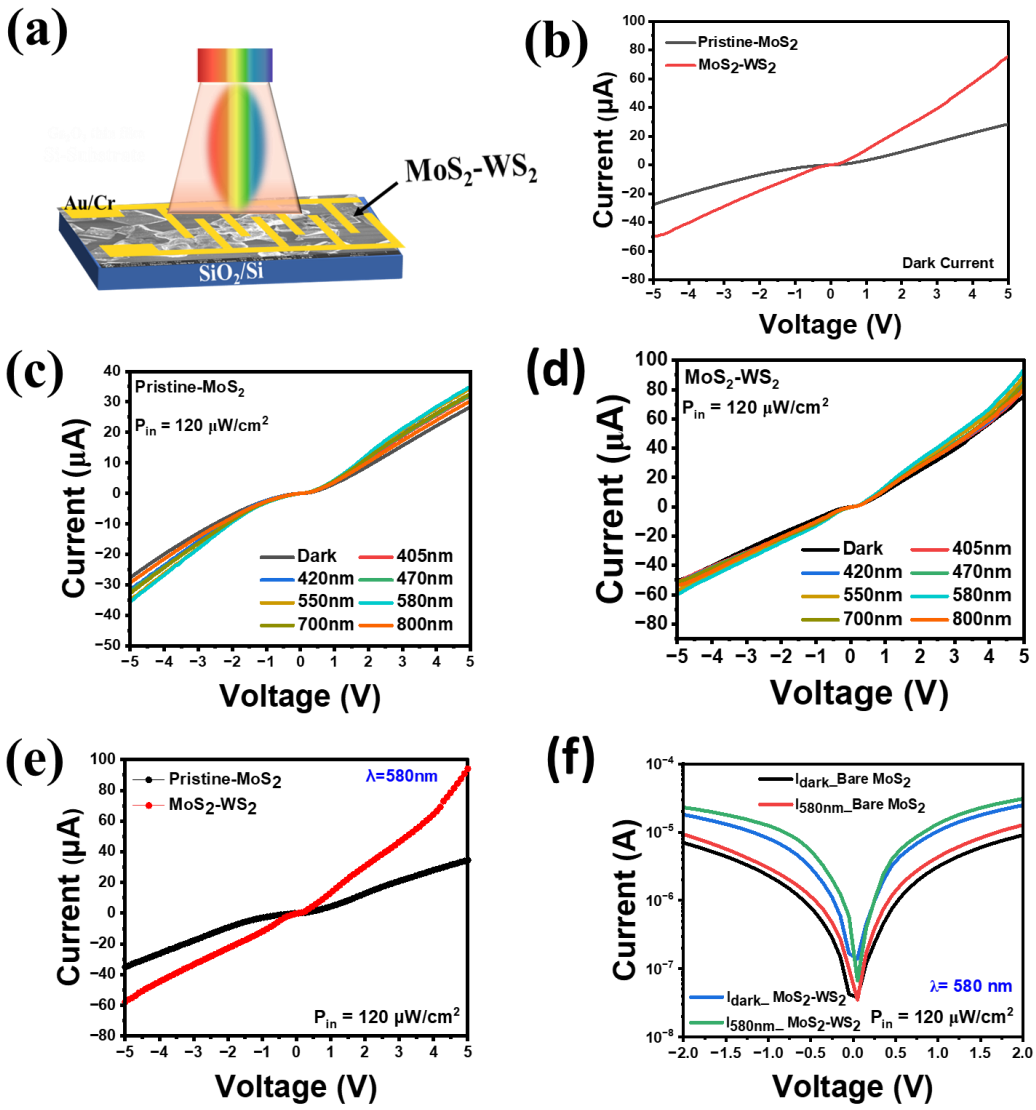



**Figure 7.3:** Self-powered Electrical characterizations and photoresponse characteristics $MoS_2$-$WS_2$ heterostructure devices. (a) Schematic of the device. Current-voltage (*I-V*) characteristics measured in the dark and under different wavelengths. (b) Dark current, (c) Pristine-$MoS_2$, (d) $MoS_2$-$WS_2$ heterostructure, (e) *I–V* curves of the pristine-$MoS_2$ and $MoS_2$-$WS_2$ heterojunction under light illumination (580 nm, 120 μW/cm$^2$), and (f) Comparison of semi-logirthm *I-V* of Pristine $MoS_2$ and $MoS_2$-$WS_2$ in the dark condition and light illumination (580 nm, 120 μW/cm$^2$).

The $MoS_2$-$WS_2$ heterostructure predicted detectivity is in the range of $10^{12}$ Jones, which is significantly higher than the pristine $MoS_2$ photodetector ($10^{11}$ Jones). At 580nm the $MoS_2$-$WS_2$ heterostructure-based photodetector has a maximum D*, which suggests that the visible region has a greater capacity for the detection of weak optical signals. Also, the photo-conversion efficiency of the device, known as EQE, is determined using the following mathematical equation 7.3[Xie et al., 2017a].

$$EQE = \frac{Rhc}{q.\lambda} \; x \; 100\% \qquad (7.3)$$

Here R, h, c, q, and λ are the responsivity, Planck's constant, speed of light, electron charge, and wavelength of incident optical light, respectively. Figure 7.4 (c), shows an EQE study of a self-powered photodetector performed under a broad spectral range for both the $MoS_2$-$WS_2$ heterostructure and pristine $MoS_2$ devices. Under 580 nm illumination, the computed EQE for the

$MoS_2$-$WS_2$ heterostructure and for pristine $MoS_2$ are 60.59 % and 5.01 %, respectively. The $MoS_2$-$WS_2$ heterostructure's EQE is 12 times more than pristine $MoS_2$.

Further, the performance of the self-power photodetector, including its detectivity and responsivity, is examined under the irradiation of 580 nm light with a power density ranging from 3 μW/cm²to 417 μW/cm². We can see that responsivity (R) and specific detectivity (D*), decreases monotonically as laser power increases, indicating a strong relationship with power intensity, as depicted in Figure 7.4 (d, e). This improvement is attributed to interlayer coupling and charge transfer of the heterojunction from the valence band to the conduction band in the $MoS_2$-$WS_2$ is caused by the increased number of incoming photons with rising power density. The $MoS_2$-$WS_2$ heterostructure predicted detectivity is in the range of $10^{12}$ Jones, which is significantly higher than the pristine $MoS_2$ photodetector ($10^{11}$ Jones), as shown in Figure 4b. At 580nm the $MoS_2$-$WS_2$ heterostructure-based photodetector has a maximum D*, which suggests that the visible region has a greater capacity for the detection of weak optical signals. We also measured the $MoS_2$-$WS_2$ heterostructure photodetector performance parameters R, as a function of bias voltage under 580 nm light are depicted in Figure 7.4 (f). The photodetector exhibits the *R* 7.37 A/W, at an applied bias voltage of 5 V under 580 nm light source illumination.

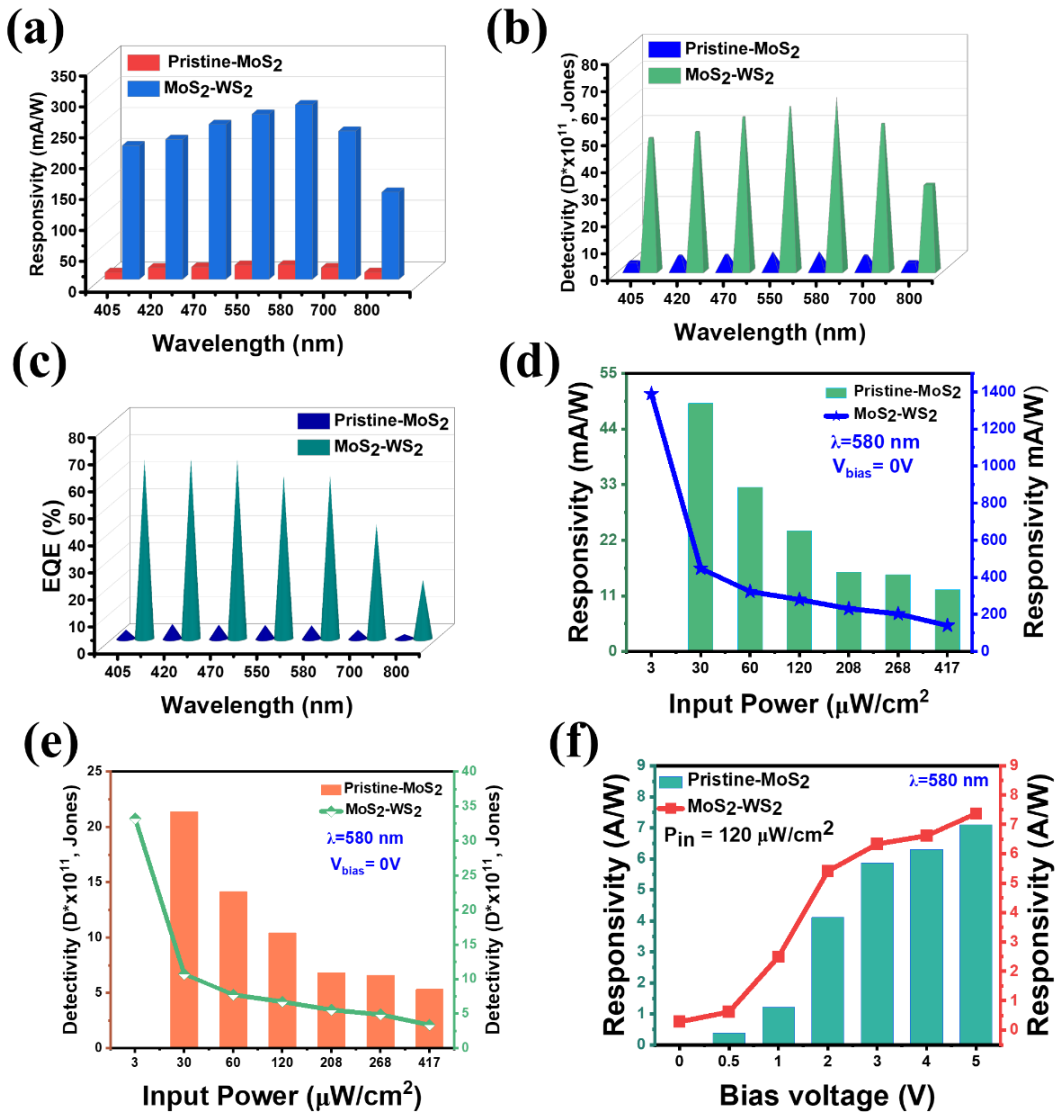



**Figure 7.4:** Photoresponse characteristics of self-powered device. (a) Responsivity, (b) Detectivity, (c) EQE of pristine $MoS_2$ and $MoS_2$-$WS_2$ under irradiation of Visible-NIR spectrum, respectively with an input power density ($P_{in}$) of 120 μW/cm², (d, e) Responsivity and Detectivity with function of different incident optical power density, and (f) Comparison of Responsivity of pristine $MoS_2$ and $MoS_2$-$WS_2$ under light illumination of 580nm with various bias voltages.

The transient photoresponse of the pristine $MoS_2$ and $MoS_2$-$WS_2$ heterostructure devices in self-powered mode was investigated in the wavelength range of 405 to 800 nm with repeatedly switching on/off in cycles of 30 s at a power density of 120 μW/cm², as depicted in Figure 7.5 (a, b). In order to understand the photoresponse stability of the pristine $MoS_2$ and $MoS_2$-$WS_2$ heterostructure-based photodetector for real-world use, the dynamic photocurrent response is examined by controlling the incident light intensity and applied bias voltage. The pristine $MoS_2$ and $MoS_2$-$WS_2$ heterostructure-based photodetector dynamic photocurrent response at various power densities, when repeatedly turned on and off the light of 580nm is shown in Figure 7.5 (c, d). As shown in Figure 7.5 (e, f), the time-related current of the pristine $MoS_2$ and $MoS_2$-$WS_2$ device is also measured at various positive bias voltages $V_{bias}$, while illuminated by a 580 nm (120 μW/cm²) light. We also It shows that the photocurrent of device increased with an increase in bias voltage. This is due to the thermionic field emission being proportional to the applied bias voltage i.e., an increase in bias voltage increases thermionic emission.

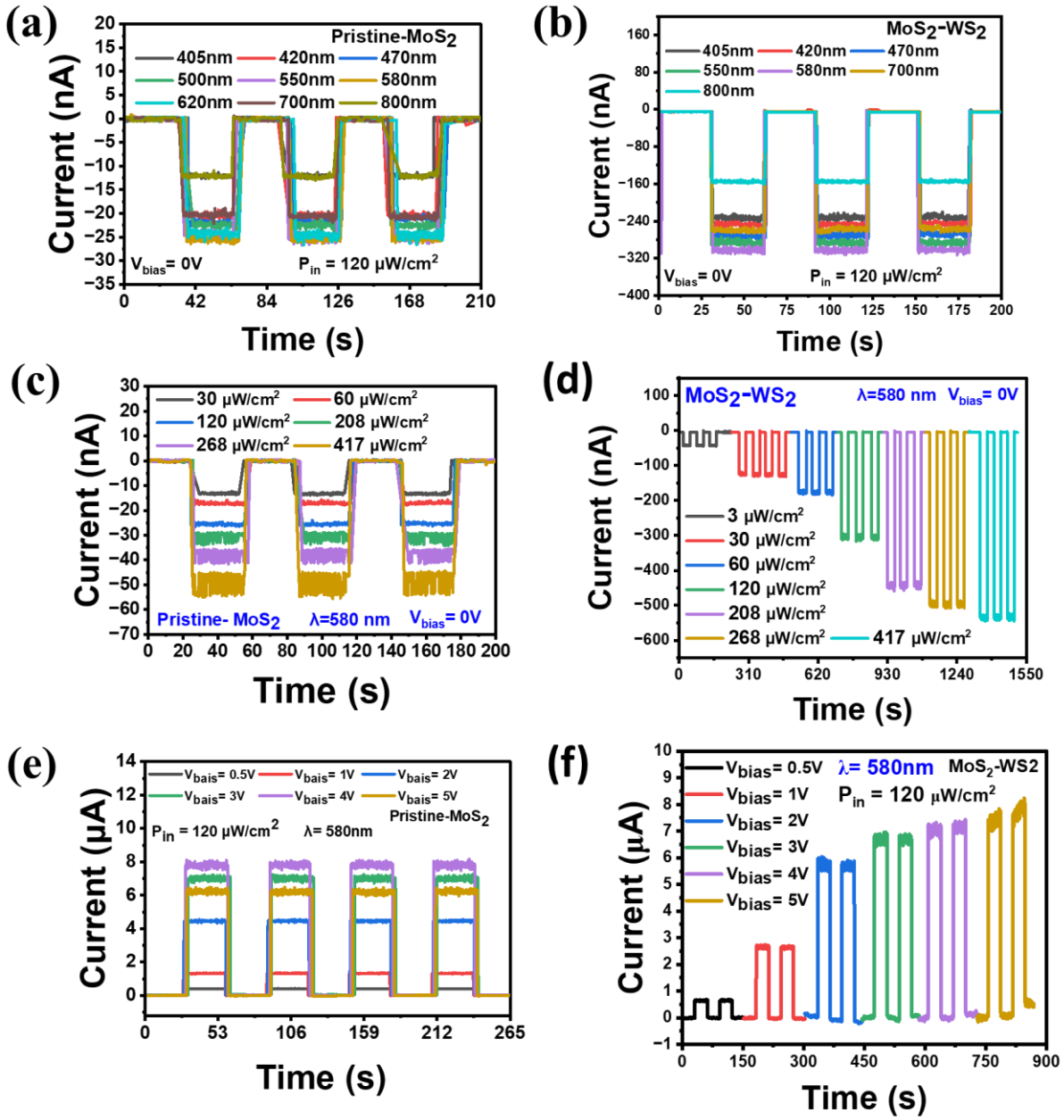



**Figure 7.5:** Comparative transient of pristine $MoS_2$ and $MoS_2$-$WS_2$ heterostructure with (a, b) Wavelength-dependent photoresponse, (c, d) different incident optical power density, and (e, f) Transient photoresponse measurement at different bias voltage at 580 nm wavelength of light at an incident optical power of 120 μW/cm².

## 7.5 Speed and stability of the photodetector

The device's performance is strongly reliant on its rise and fall times i.e., response speed. Therefore, we determine the response speed of the $MoS_2$-$WS_2$ heterostructure and pristine $MoS_2$ devices by fitting the temporal photo response of 580 nm light with the incident power of 120 $\mu W/cm^2$ as shown in Figure 7.6 (a, b). We can see that the rise/fall time of the $MoS_2$-$WS_2$ heterostructure is ~375µs/6ms and 7.2 ms/10.8 ms in case of pristine $MoS_2$ at 0 V under irradiation of 580 nm wavelength of light. Furthermore, for all incident visible-NIR light, rapid optical switching with low response speed (on the order of microsecond) has been seen in heterojunction. Due to the strong suppression of carrier recombination and effective carrier transportation at the interface of the $MoS_2$-$WS_2$ heterostructure, the photoresponse behaviour of the proposed heterostructure is greatly enhanced by the introduction of faster charge transport. Table 7.1 presents a comparison of the self-powered photodetector's figures of merit of $MoS_2$-$WS_2$ photodetector with other 2D/2D heterostructure devices. As illustrated in Figure 7.6 (c, d), the self-powered pristine $MoS_2$ and $MoS_2$-$WS_2$ heterostructure devices demonstrated outstanding repeatability and stability after 30 days of re-measuring at 580 nm light.

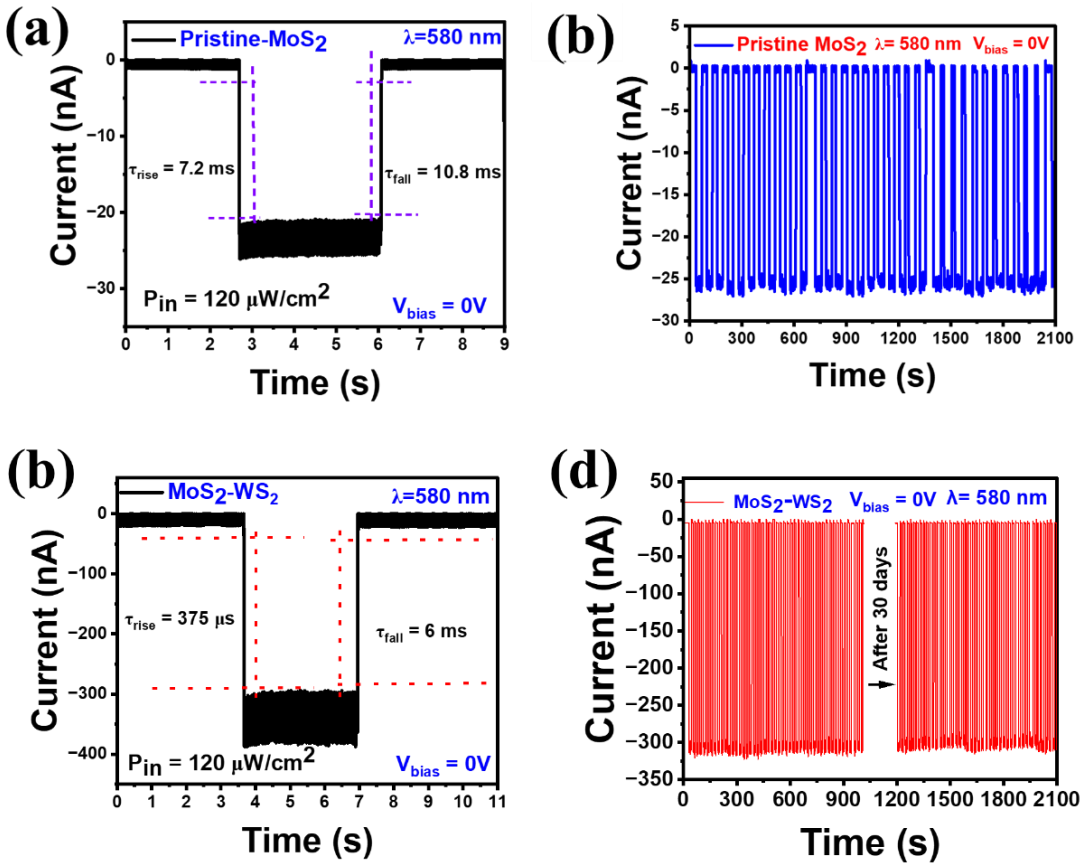



**Figure 7.6:** Rise time and fall time of (a) Pristine $MoS_2$, (B) $MoS_2$-$WS_2$ heterojunction, and (c, d ) Long-term stability of Pristine $MoS_2$ and $MoS_2$-$WS_2$ heterostructure device with 100 cycles under 580 nm light illumination after 30days in ambient air.

**Table 7.1:** Comparison of self-powered photodetector figure of merit.

| photodetectors | Detection range (nm) | Responsivity ($AW^{-1}$) | Detectivity (Jones) | Response time ($\tau_{rise}$/ $\tau_{fakk}$) (ms) | Ref. |
|---|---|---|---|---|---|
| $MoS_2$-$ReS_2$ | 400–1100 | 1.28 | 1.34 x $10^{13}$ | 30/71 | [Wadhwa et al., 2021b] |
| $MoS_2$/GeSe | 380–1064 | 0.105 | 1.03 × $10^{10}$ | 110/750 | [Xin et al., 2020] |
| $MoS_2$/$Ga_2O_3$ | 230–1000 | 94.92 | 7.72x $10^9$ | 290/300 | [Varshney et al., 2023] |
| $WS_2$/SnSe | 457-1064 | 0.099 | — | 8.2/8.4 | [Jia et al., 2016] |
| $MoS_2$/$LaVO_3$ | 300-800 | 0.14 | 5 × $10^9$ | 0.3/0.4 | [Lee et al., 2023] |
| nh-$MoS_2$/$WSe_2$ | 532-950 | 0.177 | 8 × $10^{10}$ | 33/38 | [Sharma et al., 2023] |
| $MoS_2$/CuO | 400-1200 | 10 | 1.8 × $10^{14}$ | 80/80 | [Kumawat et al., 2022] |
| $MoS_2$/$SnO_2$ | 400-1100 | 0.35 | 1.25 × $10^{11}$ | 153/200 | [Augustine et al., 2022] |
| Gr/$MoSe_2$ | 450-900 | 0.0895 | 2.24 × $10^{10}$ | 9.6/12.8 | [Liu et al., 2019] |
| $MoS_2$-$WS_2$ | 405-800 | 0.283 | 6.44 x $10^{12}$ | 375µs/6 | This work |

## 7.6 Self-powered functionality of CVD-synthesized $MoS_2$ photodetectors

With symmetric Au electrodes, we present a high-performance, self-powered $MoS_2$ photodetector that differs from the most common self-powered photodetectors based on the asymmetric contact electrodes or heterostructures mentioned above. Strong evidence that the self-powered functionality of CVD-synthesized $MoS_2$ photodetectors arises from the complex interaction between intrinsic defects, like sulphur vacancies, as well as interactions with environmental factors like temperature and humidity is presented by this comprehensive methodology, which combines electrical characterisation with structural and surface potential analyses[Kaushik et al., 2017; Park et al., 2013; Shu et al., 2016]. A built-in electric field may be generated in symmetric electrode photodetectors by charge trapping, particularly in CVD-grown $MoS_2$ containing defect states (such as sulphur vacancies)[Kunstmann et al., 2017; Senkić et al., 2023]. Typical flaws in CVD-grown $MoS_2$ include grain boundaries and vacancies, which can trap charge carriers[Ma et al., 2022]. Additional traps may form at the $MoS_2$/substrate interface, when grown on insulating substrates such as $SiO_2$/Si[Liu et al., 2018c]. Charge trapping and detrapping effects can be caused by these flaws' creation of localised energy states. Without the need for an external bias, this intrinsic field can assist in the separation of photogenerated electron-hole pairs, enabling a self-powered reaction when exposed to light. A potential difference across the $MoS_2$ layer may be created via the charge trapping effect, which changes the threshold voltage and enables the direct collection of photogenerated carriers. These findings are in line with other studies showing that adsorbed species and sulphur vacancies significantly affect charge trapping, hysteresis, and photodetection behaviour in $MoS_2$-based devices. This behaviour is confirmed by

a combination of Raman mapping, Kelvin Probe Force Microscopy (KPFM) studies, and hysteresis loop occurs in the *I-V* characteristics.

Hysteresis in *I-V* measurements performed in dark conditions at different voltage scan rates highlights the critical importance of surface charge changes, when the voltage is swept in one direction and does not quickly release when the sweep is reversed. Charge trapping and de-trapping processes enabled by defect states (such as sulphur vacancies) and adsorbed molecular entities on the $MoS_2$ surface cause a discernible hysteresis at reduced scan rate. At high scan speeds, these effects decrease because trapped charges do not have enough time to respond, which results in less hysteresis. The remarkable association between scan rate and hysteresis suggests that surface charges caused by adsorbed ambient species and sulphur vacancies play a significant role in the observed phenomena. Both internal and extrinsic factors have been implicated in the sustained photoconductivity observed in $MoS_2$ photodetector. Photocharge trapping in localised band-tail states of $MoS_2$ is the inherent effect [Di Bartolomeo et al., 2017; Furchi et al., 2014], whereas photocharge trapping in residues and adsorbates deposited on the top or bottom $MoS_2$ surface is an extrinsic cause. Trap states can be produced by dangling bonds in the underlying dielectric, whereas adsorbed oxygen and moisture molecules or processing residues are the primary causes of top trap states[Cho et al., 2014; Wu et al., 2015]. In the *I-V* characteristics of $MoS_2$, hysteresis is a phenomenon associated with persistent photoconductivity, which is also associated with charge transfer/trapping. The *I-V* characteristics in a sequence of voltage scan rates are displayed in Figure 7.7. The trap center, which might be on the surface of the channel material or at the interface between the dielectric surface and the channel material, is typically responsible for hysteresis, according to the study. It was reported that the hysteresis in $MoS_2$ transistors is caused by (i) the interfacial trap states between $MoS_2$ and the $SiO_2$ substrate and (ii) the sulphur vacancy, which serves as both the trap centre and a facilitator of external molecular adsorption, both of which increase the hysteresis performance[Late et al., 2012; Prasad et al., 2020; Urban et al., 2019]. However, it was subsequently shown that hysteresis is still present in a suspended $MoS_2$ transistor; the hysteresis is stronger in a thinner $MoS_2$ than in a thicker $MoS_2$, suggesting that the inherent sulphur vacancy in $MoS_2$ transistors is the source of the hysteresis[Shu et al., 2016]. Due to inherent flaws in the $MoS_2$ lattice and the interfacial trap at the $MoS_2/SiO_2$ contact, the present trap states are highly likely[Liu et al., 2018c]. Therefore, we suggest that the sulfur-vacancy-dominant hysteresis behaviour, which differs from that of the interfacial oxygen functional group at the $MoS_2/SiO_2$ interface, may be the origin of the current unexpected hysteresis behaviour.

When combined with the electrical evaluations, Raman mapping provides detailed structural information. It clarifies the spatial differences between the vibrational modes $E^1_{2g}$ and $A_{1g}$, which frequently undergo broadenings or shifts due to defects such as sulfur vacancies. Different colour contrasts were seen in the mapping of the $E^1_{2g}$ and $A_{1g}$ mode intensities, which corresponded to areas with varying concentrations of defects and strain, as shown in Figure 7.8 (a-d).These defects may be caused by substrate contacts or uneven growth conditions during CVD. Grain boundaries and sulphur vacancies, which are known to cause local disorder and impact the material's vibrational modes, frequently occurred with areas of high defect density and extreme colour contrast in the Raman maps. These features, which are known to impact charge dynamics and electrical properties inside $MoS_2$, provide unmistakable proof of structural defects. We also used Kelvin Probe Force Microscopy (KPFM) to investigate the distribution of surface charges on pristine $MoS_2$, as seen in Figure 7.8 (e-f). The surface potential difference, which represents the local differences in the work function caused by defects, doping, or surface charges, may be quantitatively mapped using KPFM [Yim et al., 2022]. Areas of increased surface potential correlating to regions identified as defect or strained using Raman mapping were corroborated by the surface potential mapping acquired through KPFM, which revealed the presence of localised charge heterogeneities throughout the $MoS_2$. The presence of defects, such sulphur vacancies or edge states, can lead to charge redistribution and changes in the local electronic structure of the material. This can be seen in variations in surface potential. These inherent fields

are essential for encouraging charge separation under light, which makes self-powered photodetection possible.

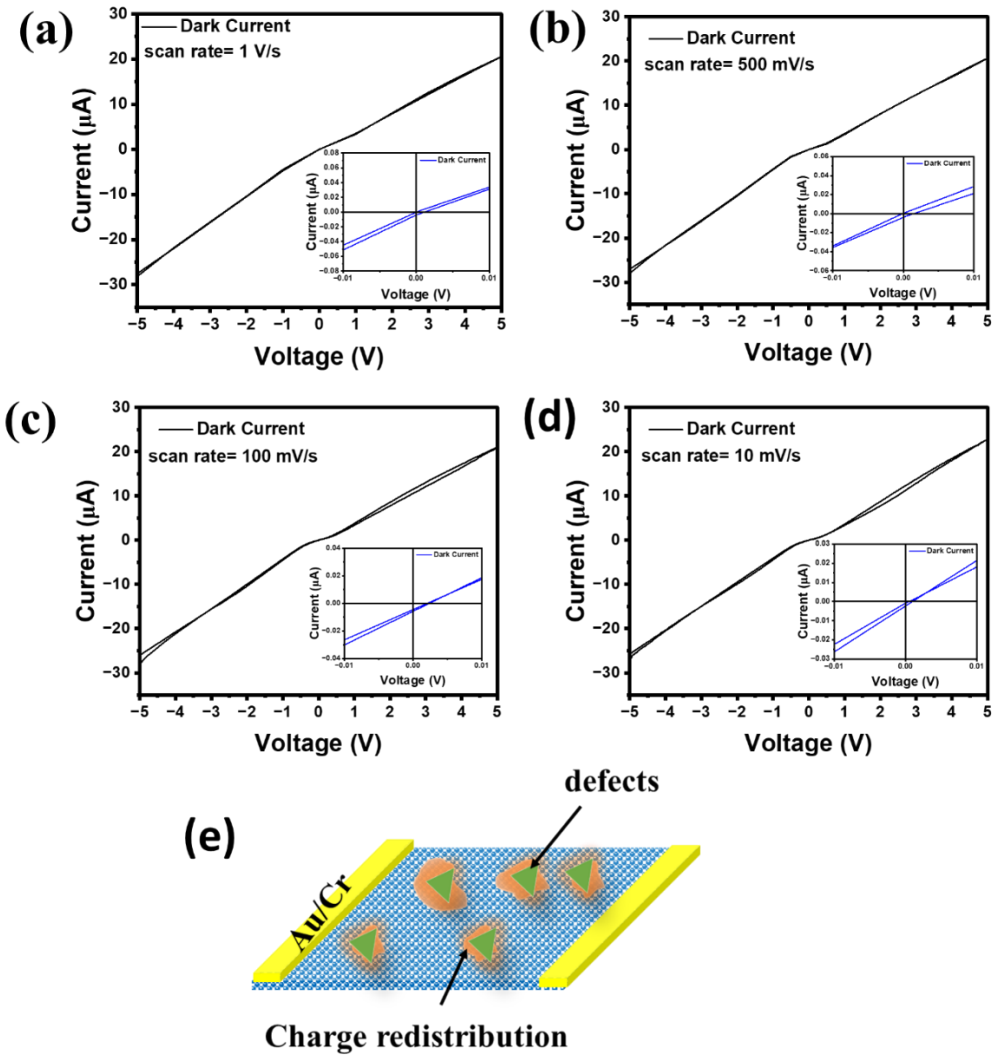



**Figure 7.7.:** Hysteresis behavior of I–V as a function of different sweeping rates (a) 1V/s, (b) 500 mV/s, (c) 100 mV/s, (d) 10 mV/s, with inset graph showing the magnified I-V of device, and (e) Schematic of the defects generate charge redistribution in pristine MoS2.

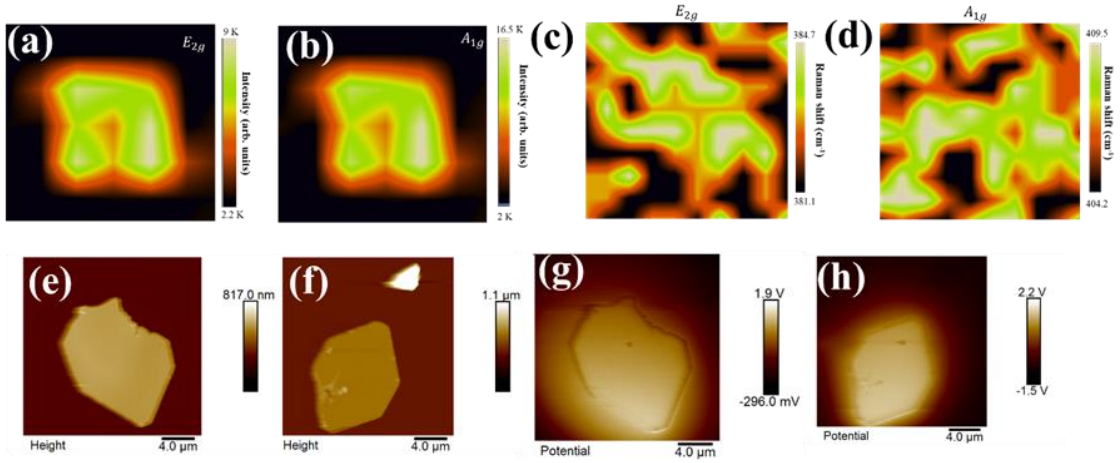



**Figure 7.8:** Raman mapping of Pristine MoS2 (a, b) position mapping shows clear intensity difference between E2g and A1g mode, (c, d) and KPFM study of Pristine MoS2 (e-f) mapping of variation in thickness, (g, h) Surface potential images for pristine-MoS2

## 7.7 Light sensing mechanism of the photodetector

For effective data transfer in high-speed optical communication and other sophisticated applications, high-frequency detection is necessary for fast decoding of optical signals. Significant applications include LIDAR and imaging systems, where it improves resolution and accuracy, time-resolved spectroscopy, which records quick transient events and dynamic processes, and so on. Hence, we investigated the device's frequency-dependent transient current (I-T) response throughout a wide frequency range (1 Hz to 1 kHz) using optical chopper, to execute the modulation of light with varying frequencies. Figure 7.9 (a), displays the schematic diagram illustrating the measuring process. Figure 7.9 (b-d), illustrates the typical temporal response characteristics of the heterojunction photodiode at a frequency of 1 Hz, 100 Hz, and 1 kHz, indicating the potential for high frequency photodetection, when subjected to a reverse bias of 1 V. With no indications of performance deterioration or cut-offs, the gadget continued to display outstanding repeatability even at the higher frequency of 1 kHz.

We have provided an in-depth understanding of the formation and motion of charge transfer at the interface between $WS_2$ and $MoS_2$ under the influence of light irradiation at various wavelengths. This was achieved by the use of an energy band diagram of the heterostructure, which demonstrates its self-powered behaviour under equilibrium conditions, as illustrated in Figure 7.9 (e). The stacking of $MoS_2$-$WS_2$ semiconductors facilitates the creation of high-quality heterostructures, without imposing limitations on lattice misfit. The photoconductive effect occurs when a single semiconductor material is exposed to visible-NIR radiation (at so). The electrons in the valence band (VB) absorb the photon's energy and migrate to the conduction band (CB) to create electron-hole pairs, increasing conductivity. However, a type II band alignment structure is created, when $MoS_2$ and $WS_2$ samples are combined to produce heterostructures, as seen in Figure 6f [Gong et al., 2014; Lin et al., 2021]. Electrons and holes would separate into different layers in order to achieve equilibrium, and electrons in the conduction band would be transferred from $WS_2$ to $MoS_2$ and the holes in the valence band would be transferred from $MoS_2$ to $WS_2$, resulting in n-doping and p-doping for $MoS_2$ and $WS_2$ respectively, as shown in Figure 7.9 (f). The passivated $MoS_2$ layer prevents surface leakage current, and the built-in electric field enables this device to operate at zero bias voltage. Photogeneration of electron-hole pairs takes place in the heterostructure when it is subjected to visible (Vis) light with an energy that is equivalent to or greater than its bandgap energy [Qin et al., 2022]. $MoS_2$ has the ability to absorb light in both the visible (Vis) and near-infrared (NIR) regions of the electromagnetic spectrum, resulting in the generation of electron-hole pairs. The presence of local electric fields at the interface between $WS_2$ and $MoS_2$ inhibits the recombination of photogenerated electrons from $MoS_2$ under the exposure of visible (Vis) or near-infrared (NIR) light [Lu et al., 2019]. The enhancement of charge separation resulting from the electric field developed at the interface between $WS_2$ and $MoS_2$ is attributed to the role of $WS_2$ in the detection of visible (Vis) and near-infrared (NIR) light. This is equivalent to increasing the conductance of the $MoS_2$ and $WS_2$ channels simultaneously, resulting in a larger photocurrent.

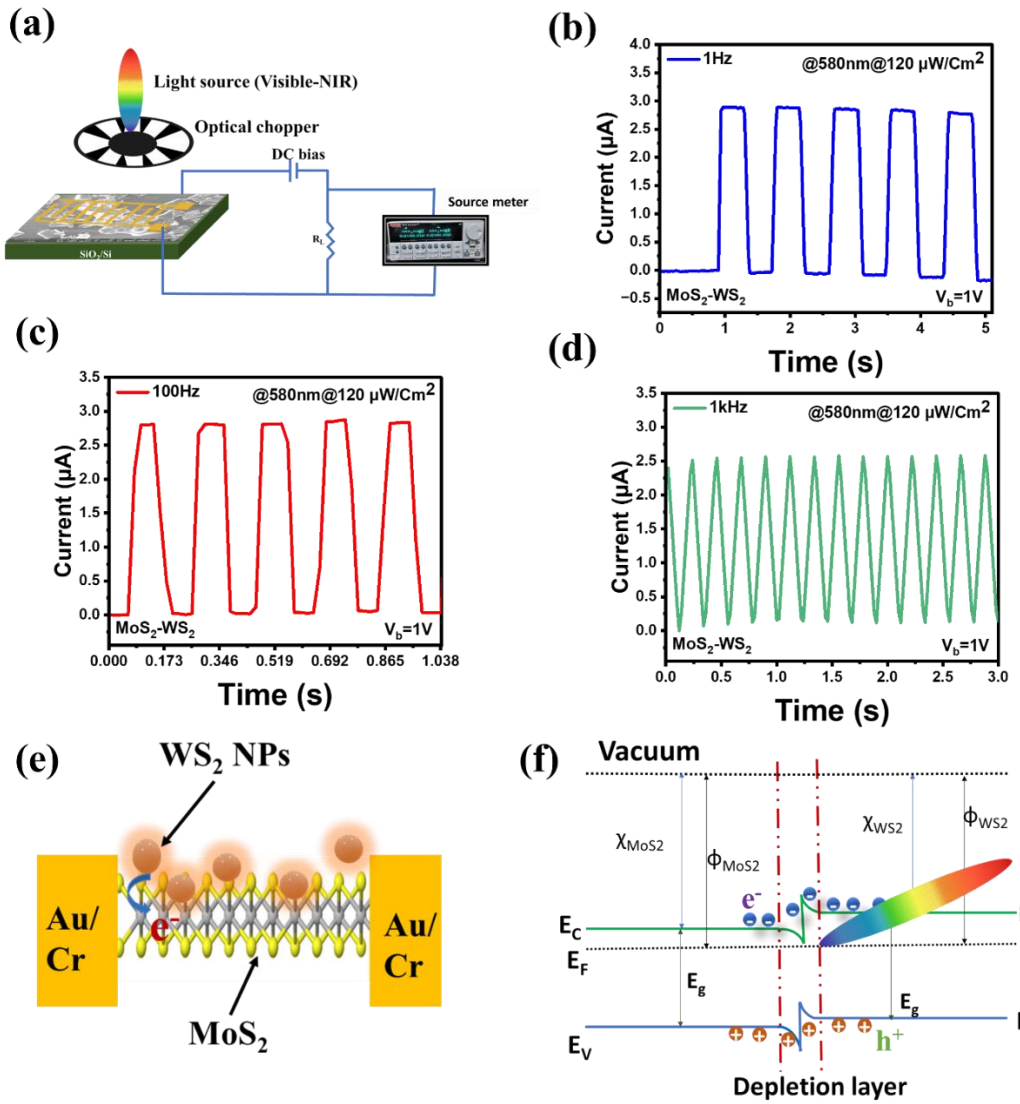



**Figure 7.9:** (a) Schematic illustration of the measurement configuration for the modulation of light, and (b-d) Representative photoresponse of the heterojunction photodiode under 580 nm light illumination with the modulated chopper frequency of 1 Hz, 100 Hz, and 1kHz respectively, Band alignment and charge transfer at the heterostructures. (e) a sketch of WS2 particle-decorated on MoS2-based photodetector, and (f) Schematic of Band profiles of MoS2 and WS2, which forms a type II heterojunction relative to the vacuum level.

## 7.8 Summary

In summary, self-powered photodetectors based on the $MoS_2$-$WS_2$ heterostructure were successfully fabricated by decorating $WS_2$ onto $MoS_2$ films grown using chemical vapour deposition (CVD) techniques. The surface morphology and structural features of the $MoS_2$-$WS_2$ heterojunctions were assessed using several analytical techniques, including XPS, Raman spectroscopy, FESEM and photoluminescence spectroscopy. By leveraging the effective interlayer charge transfer mechanism between $WS_2$ and $MoS_2$, the $MoS_2$-$WS_2$ device demonstrates a notable photoresponsivity of 282.77 mA/W and a specific detectivity of 6.44 x $10^{12}$ Jones. Additionally, the device exhibits a response time of ~375μs/6ms, which represents a significant improvement in photoresponsivity compared to the pristine $MoS_2$ and $WS_2$ devices. Moreover, anchored $WS_2$ with $MoS_2$ may pave the way towards the development of high-performance practical optoelectronic devices due to exceptional stability, high response and dependability in response to visible-NIR radiation in the air.

# 8
# Conclusions, and Scope for Future Work

This chapter summarizes the key challenges addressed and accomplishments achieved during this thesis work, aligning with the objectives outlined in Chapter 1. Significant progress was made in overcoming challenges related to the growth and application of 2D layered materials, $MoS_2$ and $SnS_2$, for gas sensing and photodetector devices. By optimizing the chemical vapor deposition (CVD) process, large-area, uniform flakes of $MoS_2$ and $SnS_2$ were successfully synthesized on $SiO_2$/Si substrates, resolving issues of uniformity and reproducibility. Advanced $NO_2$ gas sensors were developed using nitrogen plasma-treated $MoS_2$ with Ag nanoparticle functionalization and vacancy-assisted, vertically aligned $SnS_2$ structures, achieving selective, sensitive, and recoverable $NO_2$ detection. Additionally, photodetectors based on $MoS_2$-$WS_2$ heterostructures were fabricated, demonstrating enhanced optical absorption and responsivity compared to pristine $MoS_2$ devices. These advancements addressed critical challenges such as low optical absorption and large transient response times, paving the way for high-performance broadband photodetectors and sensitive gas sensors.

## 8.1 Conclusions

This thesis work addresses several important concerns and challenges pertaining to gas sensing and photodetectors. The following is a summary of all the results of this thesis work:

Our study underscores noteworthy progressions within the domain of gas sensing, particularly concerning the sensing of $NO_2$, leveraging two-dimensional materials such as $MoS_2$ and $SnS_2$. An extensive investigation was undertaken regarding the wafer-scale fabrication of $MoS_2$ and $SnS_2$ flakes exhibiting precisely controlled morphologies, facilitating a transition from in-plane to vertically oriented configurations, achieved by optimizing pivotal growth parameters including gas flow rate and temperature throughout the thermal chemical vapor deposition (CVD) methodology. The pivotal role of gas flow rate in shaping the morphology and orientation of the flakes was accentuated. Comprehensive morphological, structural, optical, and spectroscopic evaluations were executed utilizing techniques such as SEM, FESEM, XRD, Raman, PL, and XPS to elucidate the electrical and optical characteristics of the synthesized films. These characterizations validated the exceptional uniformity, reproducibility, and wafer-scale coverage of the synthesized $MoS_2$ and $SnS_2$ flakes on $SiO_2$/Si substrates. A growth mechanism was proposed to elucidate the kinetic processes involved in the transition from 2D in-plane to 3D vertically aligned structures. Interdigitated electrode (IDE) patterns were employed to facilitate electrical measurements of the devices, leveraging the tailored properties of $MoS_2$ and $SnS_2$.

Moreover, this investigation delved into the formulation of diverse $MoS_2$ and $SnS_2$ based $NO_2$ gas sensor with enhanced performance. The gas sensing experiments demonstrated that $SnS_2$ serves as a highly suitable candidate for $NO_2$ gas sensors as compared to $MoS_2$. The sensitivity of these sensors was further enhanced through generation of defect and doing using nitrogen plasma treatment, and surface engineering using noble metal nanoparticle like Ag, whereby alterations in morphology and structure generated varying quantities of reactive sites for interactions with gas molecules. Additionally, the application of CVD-grown $MoS_2$ in optoelectronics was scrutinized through the fabrication of $WS_2$/$MoS_2$ heterojunction photodetectors capable of functioning across the visible to near-infrared light spectrum. These advancements provide significant insights and practical contributions towards the evolution of high-performance gas sensors and photodetectors for commercial applications.

Research on $MoS_2$ gas sensing generally demonstrated excellent gas sensing performance by interface and defect engineering independently, but no investigation on a thorough

combined effect of both was provided. This is the cause; we demonstrate that the sensing performance of CVD grown $MoS_2$-based $NO_2$ gas sensors can be significantly improved through the nitrogen doped and defect-selective surface functionalization of Ag NPs. Utilizing a combination of Raman spectroscopy and X-ray photoelectron spectroscopy, we validated the effective p-doping of $MoS_2$ through nitrogen plasma treatment and established beneficial band alignment, which is integral to the dynamics of charge carriers. Our comparative evaluation of the sensing responses from pristine $MoS_2$, N-$MoS_2$, Ag-$MoS_2$, and Ag-N-$MoS_2$ devices at an elevated temperature of 100 °C reveals that the Ag-N-$MoS_2$ configuration displays the most pronounced sensitivity to $NO_2$, thereby highlighting the synergistic interactions between silver nanoparticles and nitrogen doping. The Ag-N-$MoS_2$ sensor exhibited a remarkable response to $NO_2$ achieving 71.02% at 50 ppm at at 100 °C, with fast response (27.17 s) and recovery times (132.24 s). These results imply that Ag-N-$MoS_2$ possesses significant promise for the development of highly sensitive and efficient gas sensors.

Moreover, the response of the $NO_2$ gas sensor based on $MoS_2$, even after nitrogen plasma treatment to introduce doping and defects, as well as surface functionalization with Ag nanoparticles, is relatively lower compared to other 2D materials due to its inherently lower adsorption energy towards $NO_2$ molecules. Hence. we have successfully synthesized a highly sensitive gas sensor predicated upon vertically aligned $SnS_2$ flakes through the application of the chemical vapor deposition (CVD) methodology, thereby demonstrating remarkable selectivity towards $NO_2$ in comparison to over a range of other toxic and combustible gases. The fabricated $SnS_2$ sensors exhibited commendable stability in performance, elevated sensitivity (164%), and expeditious response/recovery times (41/309 s), when exposed to 50 ppm $NO_2$ at 120 °C. Moreover, we investigated the fast nitrogen plasma treatment technique as a means to engender sulfur vacancies on the $SnS_2$ surface, thereby significantly augmenting its functionalization and gas sensing attributes. The sensors subjected to 12 minutes of nitrogen plasma treatment exhibited an extraordinary response of 246% to 50 ppm $NO_2$, signifying an approximate 1.5 order-of-magnitude enhancement relative to pristine $SnS_2$. The pronounced selectivity of the sensor towards $NO_2$, even amidst the presence of assorted interfering gases such as $CH_4$, CO, $H_2$, $H_2S$, $CO_2$, and $NH_3$, accentuates its promising applicability for low-concentration gas detection in domains such as medical diagnostics, industrial processing, and environmental monitoring.

In addition, Density functional theory (DFT) calculations were conducted to evaluate the $NO_2$ gas adsorption properties on three functionalized $MoS_2$ monolayers: pristine $MoS_2$, nitrogen-doped $MoS_2$ (N-$MoS_2$), and silver-functionalized nitrogen-doped $MoS_2$ (Ag-N-$MoS_2$). For pristine $MoS_2$, weak van der Waals interactions were observed between the surface and $NO_2$ molecules, with the lowest adsorption energy of -0.53 eV. Nitrogen doping enhanced the adsorption energy to -0.75 eV, with noticeable symmetry breaking in the $NO_2$ molecule due to unequal bond lengths and a dominant non-bonding interaction between oxygen and nitrogen on the surface ($d_{O\text{-}N(surface)}$ = 2.06 Å). Further functionalization with silver nanoparticles significantly increased the adsorption energy to -1.33 eV. Additionally, $SnS_2$ monolayers demonstrated a higher $NO_2$ binding affinity compared to other gases, with an adsorption energy of -1.91 eV, attributed to an increase in carrier concentration upon $NO_2$ adsorption. DFT studies also revealed that sulfur-vacancy defects on $SnS_2$ surfaces shifted the adsorption mechanism from physisorption to chemisorption. Among three optimized structures, the highest adsorption energy (2.19 eV) was observed for the structure with one sulfur vacancy, outperforming pristine $SnS_2$. Using the Lee and Strano reaction mechanism to model gas sensing, it was found that the N12 sample exhibited a higher forward rate constant ($k_{ir(ads)}$ =1.39 x $10^{-4}$ $(ppm.s)^{-1}$) than NO sample $k_{ir(ads)}$ =1.56 x $10^{-5}$ $(ppm.s)^{-1}$) at an operating temperature of 120°C, highlighting the enhanced sensing performance of functionalized materials.

We also demonstrated a self-powered photodetectors based on the $MoS_2$-$WS_2$ heterostructure were successfully fabricated by decorating $WS_2$ onto $MoS_2$ films grown using chemical vapour deposition (CVD) techniques. The surface morphology and structural

features of the $MoS_2$-$WS_2$ heterojunctions were assessed using several analytical techniques, including XPS, Raman spectroscopy, FESEM and photoluminescence spectroscopy. By leveraging the effective interlayer charge transfer mechanism between $WS_2$ and $MoS_2$, the $MoS_2$-$WS_2$ device demonstrates a notable photoresponsivity of 282.77 mA/W and a specific detectivity of 6.44 x $10^{12}$ Jones. Additionally, the device exhibits a response time of ~375µs/6ms, which represents a significant improvement in photoresponsivity compared to the pristine $MoS_2$ and $WS_2$ devices. Moreover, anchored $WS_2$ with $MoS_2$ may pave the way towards the development of high-performance practical optoelectronic devices due to exceptional stability, high response and dependability in response to visible-NIR radiation in the air.

## 8.2 Scope for Future Work

The present thesis has made significant contributions to the field of 2D materials, particularly in the development of $MoS_2$ and $SnS_2$ for applications in gas sensing and photodetection. However, there remain exciting opportunities to further advance this research. One promising direction is the adoption of transfer techniques to create heterojunctions on large-area $MoS_2$ and $SnS_2$, which could significantly enhance the performance and functionality of these materials by enabling the integration of diverse components. Additionally, the fabrication of flexible and wearable devices is increasingly important due to their potential applications in healthcare and consumer electronics. This requires innovative fabrication techniques and the use of flexible materials, leading to the development of versatile devices that can be seamlessly integrated into daily life.

Moreover, the creation of photodetectors and gas sensors capable of operating under extreme conditions presents a significant opportunity for various industries. For instance, high-temperature photodetectors could be utilized in industrial processes, while gas sensors designed to function in high humidity environments would be valuable in agriculture and environmental monitoring. The current experimental findings have established a foundation for these advancements, but further exploration is needed in several areas.

The CVD growth of $MoS_2$ and $SnS_2$ flakes still offers room for discovering new morphologies that could enhance their electrical and optical properties across different dimensions (zero, one, and three-dimensional). Understanding the growth mechanisms behind these morphologies is essential, as combining different dimensionalities could lead to improved optical and electronic characteristics. Additionally, while the response and recovery times of gas sensors are critical, achieving rapid response times in the milliseconds or microseconds range remains a challenge. The influence of morphology on gas diffusion within the sensing film warrants further investigation, as the position of gas molecule adsorption on $MoS_2$ and $SnS_2$ significantly affects sensor performance. Enhancing the number of adsorption sites for $NO_2$ could not only improve sensor response but also increase selectivity.

Despite the advancements in optical absorption through heterojunction formation, the low optical absorption of bare $MoS_2$ and $SnS_2$ remains a challenge. This issue could be addressed by synthesizing various morphologies of these materials, such as transitioning from in-plane to vertically aligned structures, which would enhance optical absorption. Investigating the role of plasmonic nanoparticles embedded between vertically aligned $MoS_2$ and $SnS_2$ flakes could further improve light absorption for broadband photodetectors. Additionally, the impact of metal nanoparticles on different morphologies of $MoS_2$ and $SnS_2$ should be explored to enhance and selectively target $NO_2$ gas sensing.

Overall, while the ongoing efforts in developing $MoS_2$ and $SnS_2$ gas sensors have yielded promising results, there is still a need to optimize their morphologies, structures, and hybrid configurations for practical applications. A more detailed understanding of the gas sensing mechanisms, considering factors such as surface states, edge sites, defects, crystallinity, and electronic properties, is essential. Quantitative calculations of adsorption energy and the number of adsorption sites are crucial for elucidating the gas-sensitive properties of these

materials. The exploration of van der Waals heterostructures involving $MoS_2$ and $SnS_2$ is still in its infancy, presenting exciting opportunities for researchers to advance this field toward commercial applications.

Furthermore, the integration of 2D materials like $MoS_2$ and $SnS_2$ into flexible and stretchable devices is a burgeoning area of research. Their low power consumption, high charge carrier mobility, lightweight nature, and excellent mechanical properties make them ideal candidates for applications in flexible gas sensors and broadband photodetectors. The potential for these materials to be used in wearable technology is vast, particularly for real-time environmental monitoring and healthcare applications. The replacement of rigid metal electrodes with flexible 2D metallic materials in sensor devices could enhance performance, transmittance, and flexibility, paving the way for e-skin and e-textile nano-gas sensors that improve conformal contact with the human body.

# List of Publications

## Journals: -

(1) **Ashok Kumar**, Suraj Barala, Akash Popat Gutal, Atul G. Chakkar, Pradeep Kumar, Manikandan Paranjothy, and Mahesh Kumar. "Silver-atom catalysts boosted nitrogen-doped $MoS_2$ for chemiresistive $NO_2$ gas sensor." *Sensors and Actuators B: Chemical* (2025): 137839.

(2) **Ashok Kumar**, Atul G. Chakkar, Chayan Das, Pradeep Kumar, Satyajit Sahu, Michael Saliba, and Mahesh Kumar. "Self-Powered Broadband Photodetectors Based on WS2-Anchored $MoS_2$ with Enhanced Responsivity and Detectivity." *Small*: 2502900.

(3) **Ashok Kumar**, Akash Popat Gutal, Neelu Sharma, Deepu Kumar, Ge Zhang, Hyunah Kim, Pradeep Kumar, Manikandan Paranjothy, Mahesh Kumar, and Michael S. Strano. "Investigations of vacancy-assisted selective detection of $NO_2$ molecules in vertically aligned $SnS_2$." *ACS sensors* 8, no. 3 (2023): 1357-1367.

(4) **Ashok Kumar**, Neelu Sharma, Akash Popat Gutal, Deepu Kumar, Pradeep Kumar, Manikandan Paranjothy, and Mahesh Kumar. "Growth and $NO_2$ gas sensing mechanisms of vertically aligned 2D $SnS_2$ flakes by CVD: Experimental and DFT studies." *Sensors and Actuators B: Chemical* 353 (2022): 131078.

(5) **Ashok Kumar**, Ali Mirzaei, Myoung Hoon Lee, Zahra Ghahremani, Tae-Un Kim, Jin-Young Kim, Monika Kwoka, Mahesh Kumar, Sang Sub Kim, and Hyoun Woo Kim. "Strategic review of gas sensing enhancement ways of 2D tungsten disulfide/selenide based chemiresistive sensors: Decoration and composite." *Journal of Materials Chemistry A* (2024).

(6) **Ashok Kumar**, and Mahesh Kumar. "Recent Progress in Emerging Two-dimensional Transition-metal dichalcogenides based Gas Sensors: A review." *IEEE Sensors Journal*, vol. 24, no. 16, pp. 25221-25226, 15 Aug.15, 2024.

(7) **Ashok Kumar**, Mustaque A. Khan, and Mahesh Kumar. "Recent advances in UV photodetectors based on 2D materials: A review." *Journal of Physics D: Applied Physics* 55, no. 13 (2021): 133002.

(8) Wadhwa, Riya, **Ashok Kumar**, Ranjini Sarkar, Prajna Parimita Mohanty, Deepu Kumar, Sonia Deswal, Pradeep Kumar et al. "Pt nanoparticles on vertically aligned large-area $MoS_2$ flakes for selective $H_2$ sensing at room temperature." *ACS Applied Nano Materials* 6, no. 4 (2023): 2527-2537.

(9) Biswas, Arpita, **Ashok Kumar**, Amit Kumar, Monika Kwoka, Gaurav Bassi, Mukesh Kumar, and Mahesh Kumar. "High performance Pt-anchored $MoS_2$ based chemiresistive ascorbic acid sensor." *Nanotechnology* (2024).

(10) K Das, Chayan, **Ashok Kumar**, Suresh Kumar, Neha V. Dambhare, Mahesh Kumar, Arup K. Rath, and Satyajit Sahu. "Photogating induced high sensitivity and speed from heterostructure of few-layer $MoS_2$ and reduced graphene oxide-based photodetector." *Physical Chemistry Chemical Physics* 25, no. 44 (2023): 30419-30427.

(11) Kumar, Suresh, **Ashok Kumar**, Amit Kumar, Atul G. Chakkar, Atanu Betal, Pradeep Kumar, Satyajit Sahu, and Mahesh Kumar. "Catalytic synergy of $WS_2$-anchored $PdSe_2$ for highly sensitive hydrogen gas sensor." *Nanoscale* 16, no. 19 (2024): 9593-9602.

(12) Kumar, Amit, **Ashok Kumar**, Monika Kwoka, Meng Gang, and Mahesh Kumar. "IoT-enabled surface-active Pd-anchored metal oxide chemiresistor for $H_2S$ gas detection." *Sensors and Actuators B: Chemical* 402 (2024): 135065.

(13) Das, Surajit, **Ashok Kumar**, Jitendra Singh, and Mahesh Kumar. "Fabrication and modeling of laser ablated NiO nanoparticles decorated $SnO_2$ based formaldehyde sensor." *Sensors and Actuators B: Chemical* 387 (2023): 133824.

(14) Bhati, Vijendra Singh, **Ashok Kumar**, Manila Ozhukil Valappil, Subbiah Alwarappan, and Mahesh Kumar. "Phosphorene oxide quantum dots decorated ZnO nanostructure-based hydrogen gas sensor." *IEEE Sensors Journal* 21, no. 6 (2020): 7283-7290.

(15) Kumar, Sumit, Rahul Mitra, Suraj Barala, **Ashok Kumar**, Monika Kwoka, Krishnau Biswas, and Mahesh Kumar. "Resistance-driven low power $H_2S$ sensors based on MWCNT@CuO heterojunction." *Journal of Applied Physics* 136, no. 7 (2024).

# References


Abbas, A. N., Liu, B., Chen, L., Ma, Y., Cong, S., Aroonyadet, N., Köpf, M., Nilges, T., and Zhou, C., (2015), "Black phosphorus gas sensors", *ACS Nano*, Vol.9, No.5, pp.5618–5624.

Acerce, M., Voiry, D., and Chhowalla, M., (2015), "Metallic 1T phase MoS2 nanosheets as supercapacitor electrode materials", *Nature Nanotechnology*, Vol.10, No.4, pp.313–318.

Afroozeh, A., Akbari, E., and Yupapin, P., (2019), "Recent advance in gas sensing by using two-dimensional transition metal disulfides materials", *Journal of Nanoelectronics and Optoelectronics*, Vol.14, No.9, pp.1225–1229.

Aftab, S., Iqbal, M. Z., Hussain, S., Hegazy, H. H., Kabir, F., Jaffery, S. H. A., and Koyyada, G., (2023), "New developments in gas sensing using various two-dimensional architectural designs", *Chemical Engineering Journal*, pp.144039.

Aggarwal, N., and Gupta, G., (2020), "Enlightening gallium nitride-based UV photodetectors", *Journal of Materials Chemistry C*, Vol.8, No.36, pp.12348–12354.

Agrawal, A. V, Kumar, N., and Kumar, M., (2021), "Strategy and future prospects to develop room-temperature-recoverable NO 2 gas sensor based on two-dimensional molybdenum disulfide", *Nano-Micro Letters*, Vol.13, pp.1–58.

Agrawal, A. V, Kumar, R., Venkatesan, S., Zakhidov, A., Yang, G., Bao, J., Kumar, M., and Kumar, M., (2018), "Photoactivated mixed in-plane and edge-enriched p-type MoS2 flake-based NO2 sensor working at room temperature", *ACS Sensors*, Vol.3, No.5, pp.998–1004.

Agrawal, A. V, Kumar, R., Venkatesan, S., Zakhidov, A., Zhu, Z., Bao, J., Kumar, M., and Kumar, M., (2017), "Fast detection and low power hydrogen sensor using edge-oriented vertically aligned 3-D network of MoS2 flakes at room temperature", *Applied Physics Letters*, Vol.111, No.9.

Akinwande, D., Petrone, N., and Hone, J., (2014), "Two-dimensional flexible nanoelectronics", *Nature Communications*, Vol.5, No.1, pp.1–12.

Alam, S., Chowdhury, M. A., Shahid, A., Alam, R., and Rahim, A., (2021), "Synthesis of emerging two-dimensional (2D) materials--Advances, challenges and prospects", *FlatChem*, Vol.30, pp.100305.

Amin, R., Hossain, M. A., and Zakaria, Y., (2018), "Interfacial Kinetics and Ionic Diffusivity of the Electrodeposited MoS2 Film", *ACS Applied Materials & Interfaces*, Vol.10, No.16, pp.13509–13518.

Ansari, H. R., Mirzaei, A., Shokrollahi, H., Kumar, R., Kim, J.-Y., Kim, H. W., Kumar, M., and Kim, S. S., (2023), "Flexible/wearable resistive gas sensors based on 2D materials", *Journal of Materials Chemistry C*.

Ansari, J. R., Singh, N., Anwar, S., Mohapatra, S., and Datta, A., (2022), "Silver nanoparticles decorated two dimensional MoS2 nanosheets for enhanced photocatalytic activity", *Colloids and Surfaces A: Physicochemical and Engineering Aspects*, Vol.635, pp.128102.

Arshak, K., Moore, E., Lyons, G. M., Harris, J., and Clifford, S., (2004), "A review of gas sensors employed in electronic nose applications", *Sensor Review*, Vol.24, No.2, pp.181–198.

Augustine, P., Kumawat, K. L., Singh, D. K., Krupanidhi, S. B., and Nanda, K. K., (2022), "MoS2/SnO2 heterojunction-based self-powered photodetector", *Applied Physics Letters*, Vol.120, No.18.

Azcatl, A., Qin, X., Prakash, A., Zhang, C., Cheng, L., Wang, Q., Lu, N., Kim, M. J., Kim, J., Cho, K., and others, (2016), "Covalent nitrogen doping and compressive strain in MoS2 by remote N2 plasma exposure", *Nano Letters*, Vol.16, No.9, pp.5437–5443.

Bag, A., and Lee, N.-E., (2019), "Gas sensing with heterostructures based on two-dimensional nanostructured materials: a review", *Journal of Materials Chemistry C*, Vol.7, No.43, pp.13367–13383.

Bai, X., Lv, H., Liu, Z., Chen, J., Wang, J., Sun, B., Zhang, Y., Wang, R., and Shi, K., (2021), "Thin-layered MoS2 nanoflakes vertically grown on SnO2 nanotubes as highly effective room-temperature NO2 gas sensor", *Journal of Hazardous Materials*, Vol.416, pp.125830.

Baig, N., (2023), "Two-dimensional nanomaterials: A critical review of recent progress, properties, applications, and future directions", *Composites Part A: Applied Science and Manufacturing*, Vol.165, pp.107362.

Barba-Nieto, I., Christoforidis, K. C., Fernández-Garc\'\ia, M., and Kubacka, A., (2020), "Promoting H2 photoproduction of TiO2-based materials by surface decoration with Pt nanoparticles and SnS2 nanoplatelets", *Applied Catalysis B: Environmental*, Vol.277, pp.119246.

Bernardi, M., Palummo, M., and Grossman, J. C., (2013), "Extraordinary sunlight absorption and one nanometer thick photovoltaics using two-dimensional monolayer materials", *Nano Letters*, Vol.13, No.8, pp.3664–3670.

Bharathi, P., Harish, S., Mathankumar, G., Mohan, M. K., Archana, J., Kamalakannan, S., Prakash, M., Shimomura, M., and Navaneethan, M., (2022), "Solution processed edge activated Ni-MoS2 nanosheets for highly sensitive room temperature NO2 gas sensor applications", *Applied Surface Science*, Vol.600, pp.154086.

Bharatula, L. D., Erande, M. B., Mulla, I. S., Rout, C. S., and Late, D. J., (2016), "SnS 2 nanoflakes for efficient humidity and alcohol sensing at room temperature", *RSC Advances*, Vol.6, No.107, pp.105421–105427.

Binions, R., and Naik, A. J. T., (2013), "Metal oxide semiconductor gas sensors in environmental monitoring",In *Semiconductor gas sensors* (pp. 433–466). Elsevier.

Blöchl, P. E., (1994), "Projector augmented-wave method", *Physical Review B*, Vol.50, No.24, pp.17953.

Bollinger, M. V, Lauritsen, J. V, Jacobsen, K. W., Nørskov, J. K., Helveg, S., and Besenbacher, F., (2001), "One-dimensional metallic edge states in MoS 2", *Physical Review Letters*, Vol.87, No.19, pp.196803.

Bullock, J., Amani, M., Cho, J., Chen, Y.-Z., Ahn, G. H., Adinolfi, V., Shrestha, V. R., Gao, Y., Crozier, K. B., Chueh, Y.-L., and others, (2018), "Polarization-resolved black phosphorus/molybdenum disulfide mid-wave infrared photodiodes with high detectivity at room temperature", *Nature Photonics*, Vol.12, No.10, pp.601–607.

Burton, L. A., Whittles, T. J., Hesp, D., Linhart, W. M., Skelton, J. M., Hou, B., Webster, R. F., O'Dowd, G., Reece, C., Cherns, D., Fermin, D. J., Veal, T. D., Dhanak, V. R., and Walsh, A., (2016), "Electronic and optical properties of single crystal SnS2: an earth-abundant disulfide photocatalyst", *Journal of Materials Chemistry A*, Vol.4, No.4, pp.1312–1318.

Cao, M., Yao, K., Wu, C., Huang, J., Yang, W., Zhang, L., Lei, F., Sun, Y., Wang, L., and Shen, Y., (2018), "Facile Synthesis of SnS and SnS2 Nanosheets for FTO/SnS/SnS2/Pt Photocathode", *ACS Applied Energy Materials*, Vol.1, No.11, pp.6497–6504.

Casalino, M., Coppola, G., Iodice, M., Rendina, I., and Sirleto, L., (2010), "Near-infrared sub-bandgap all-silicon photodetectors: state of the art and perspectives", *Sensors*, Vol.10, No.12, pp.10571–10600.

Castellanos-Gomez, A., Quereda, J., van der Meulen, H. P., Agra\"\it, N., and Rubio-Bollinger, G., (2016), "Spatially resolved optical absorption spectroscopy of single-and few-layer MoS2 by hyperspectral imaging", *Nanotechnology*, Vol.27, No.11, pp.115705.

Chakraborty, B., Bera, A., Muthu, D. V. S., Bhowmick, S., Waghmare, U. V, and Sood, A. K., (2012), "Symmetry-dependent phonon renormalization in monolayer MoS${}_{2}$ transistor", *Phys. Rev. B*, Vol.85, No.16, pp.161403.

Chastain, J., and King Jr, R. C., (1992), "Handbook of X-ray photoelectron spectroscopy", *Perkin-Elmer Corporation*, Vol.40, pp.221.

Chava, R. K., Do, J. Y., and Kang, M., (2019), "Enhanced photoexcited carrier separation in CdS–SnS2 heteronanostructures: a new 1D–0D visible-light photocatalytic system for the hydrogen evolution reaction", *Journal of Materials Chemistry A*, Vol.7, No.22, pp.13614–13628.

Cheiwchanchamnangij, T., and Lambrecht, W. R. L., (2012), "Quasiparticle band structure calculation of monolayer, bilayer, and bulk MoS 2", *Physical Review B — Condensed Matter and Materials Physics*, Vol.85, No.20, pp.205302.

Chen, A., Xia, S., Pan, X., Lu, H., and Ji, Z., (2018), "Easily removable visible-light-driven photocatalyst of nickel modified SnS2 nanosheets for reduction of Cr(VI)", *Journal of Alloys and Compounds*, Vol.735, pp.1314–1318.

Chen, H., Wen, X., Zhang, J., Wu, T., Gong, Y., Zhang, X., Yuan, J., Yi, C., Lou, J., Ajayan, P. M., and others, (2016), "Ultrafast formation of interlayer hot excitons in atomically thin MoS2/WS2 heterostructures", *Nature Communications*, Vol.7, No.1, pp.12512.

Chen, T., Yan, W., Wang, Y., Li, J., Hu, H., and Ho, D., (2021), "SnS 2/MXene derived TiO 2 hybrid for ultra-fast room temperature NO 2 gas sensing", *Journal of Materials Chemistry C*, Vol.9, No.23, pp.7407–7416.

Cheng, M., Wu, Z., Liu, G., Zhao, L., Gao, Y., Zhang, B., Liu, F., Yan, X., Liang, X., Sun, P., and others, (2019), "Highly sensitive sensors based on quasi-2D rGO/SnS2 hybrid for rapid detection of NO2 gas", *Sensors and Actuators B: Chemical*, Vol.291, pp.216–225.

Chhowalla, M., Shin, H. S., Eda, G., Li, L.-J., Loh, K. P., and Zhang, H., (2013), "The chemistry of two-dimensional layered transition metal dichalcogenide nanosheets", *Nature Chemistry*, Vol.5, No.4, pp.263–275.

Chiu, M.-H., Tseng, W.-H., Tang, H.-L., Chang, Y.-H., Chen, C.-H., Hsu, W.-T., Chang, W.-H., Wu, C.-I., and Li, L.-J., (2017), "Band alignment of 2D transition metal dichalcogenide heterojunctions", *Advanced Functional Materials*, Vol.27, No.19, pp.1603756.

Cho, B., Hahm, M. G., Choi, M., Yoon, J., Kim, A. R., Lee, Y.-J., Park, S.-G., Kwon, J.-D., Kim, C. S., Song, M., and others, (2015a), "Charge-transfer-based gas sensing using atomic-layer MoS2", *Scientific Reports*, Vol.5, No.1, pp.8052.

Cho, B., Yoon, J., Lim, S. K., Kim, A. R., Kim, D.-H., Park, S.-G., Kwon, J.-D., Lee, Y.-J., Lee, K.-H., Lee, B.

H., and others, (2015b), "Chemical sensing of 2D graphene/MoS2 heterostructure device", *ACS Applied Materials \& Interfaces*, Vol.7, No.30, pp.16775–16780.
Cho, K., Kim, T.-Y., Park, W., Park, J., Kim, D., Jang, J., Jeong, H., Hong, S., and Lee, T., (2014), "Gate-bias stress-dependent photoconductive characteristics of multi-layer MoS2 field-effect transistors", *Nanotechnology*, Vol.25, No.15, pp.155201.
Cho, S.-Y., Kim, S. J., Lee, Y., Kim, J.-S., Jung, W.-B., Yoo, H.-W., Kim, J., and Jung, H.-T., (2015c), "Highly enhanced gas adsorption properties in vertically aligned MoS2 layers", *ACS Nano*, Vol.9, No.9, pp.9314–9321.
Choi, S.-J., Choi, H.-J., Koo, W.-T., Huh, D., Lee, H., and Kim, I.-D., (2017), "Metal--organic framework-templated PdO-Co3O4 nanocubes functionalized by SWCNTs: improved NO2 reaction kinetics on flexible heating film", *ACS Applied Materials \& Interfaces*, Vol.9, No.46, pp.40593–40603.
Choi, S.-W., Katoch, A., Kim, J.-H., and Kim, S. S., (2015), "Remarkable Improvement of Gas-Sensing Abilities in p-type Oxide Nanowires by Local Modification of the Hole-Accumulation Layer", *ACS Applied Materials & Interfaces*, Vol.7, No.1, pp.647–652.
Chu, K., Wang, J., Liu, Y., Li, Q., and Guo, Y., (2020), "Mo-doped SnS2 with enriched S-vacancies for highly efficient electrocatalytic N2 reduction: the critical role of the Mo–Sn–Sn trimer", *Journal of Materials Chemistry A*, Vol.8, No.15, pp.7117–7124.
Coehoorn, R., Haas, C., and De Groot, R. A., (1987), "Electronic structure of MoSe 2, MoS 2, and WSe 2. II. The nature of the optical band gaps", *Physical Review B*, Vol.35, No.12, pp.6203.
Cohen, A. J., Mori-Sánchez, P., and Yang, W., (2012), "Challenges for density functional theory", *Chemical Reviews*, Vol.112, No.1, pp.289–320.
Coleman, J. N., Lotya, M., O'Neill, A., Bergin, S. D., King, P. J., Khan, U., Young, K., Gaucher, A., De, S., Smith, R. J., and others, (2011), "Two-dimensional nanosheets produced by liquid exfoliation of layered materials", *Science*, Vol.331, No.6017, pp.568–571.
Conley, H. J., Wang, B., Ziegler, J. I., Haglund, R. F. J., Pantelides, S. T., and Bolotin, K. I., (2013), "Bandgap Engineering of Strained Monolayer and Bilayer MoS2", *Nano Letters*, Vol.13, No.8, pp.3626–3630.
Cullity, B. D., and Stock, S. R., (n.d.), "“Elements of X-ray Diffraction”, (Prentice Hall: Upper Saddle River NJ, 2001) p. 388.".
Das Mahapatra, A., and Basak, D., (2021), "Biodegradable Filter Paper Based Broad-Band Photodetection by Chemical Bath Deposited SnS2 2D-Nanosheet Array Film", *ACS Applied Electronic Materials*, Vol.3, No.5, pp.2114–2122.
David, L., Bhandavat, R., and Singh, G., (2014), "MoS2/graphene composite paper for sodium-ion battery electrodes", *ACS Nano*, Vol.8, No.2, pp.1759–1770.
de la Hoz, R. E., Schlueter, D. P., and Rom, W. N., (1996), "Chronic lung disease secondary to ammonia inhalation injury: a report on three cases", *American Journal of Industrial Medicine*, Vol.29, No.2, pp.209–214.
Dehm, G., Howe, J. M., and Zweck, J., (2012), "*In-situ electron microscopy: Applications in physics, chemistry and materials science*". John Wiley \& Sons.
Deng, S., Yang, F., Zhang, Q., Zhong, Y., Zeng, Y., Lin, S., Wang, X., Lu, X., Wang, C.-Z., Gu, L., and others, (2018), "Phase modulation of (1T-2H)-MoSe2/TiC-C shell/core arrays via nitrogen doping for highly efficient hydrogen evolution reaction", *Advanced Materials*, Vol.30, No.34, pp.1802223.
Deng, S., Zhong, Y., Zeng, Y., Wang, Y., Yao, Z., Yang, F., Lin, S., Wang, X., Lu, X., Xia, X., and others, (2017), "Directional construction of vertical nitrogen-doped 1T-2H MoSe2/graphene shell/core nanoflake arrays for efficient hydrogen evolution reaction", *Advanced Materials*, Vol.29, No.21, pp.1700748.
Dey, A., (2018), "Semiconductor metal oxide gas sensors: A review", *Materials Science and Engineering: B*, Vol.229, pp.206–217.
Dey, S., Matte, H. S. S., Shirodkar, S. N., Waghmare, U. V, and Rao, C. N. R., (2013), "Charge-Transfer Interaction between Few-Layer MoS 2 and Tetrathiafulvalene.", *Chemistry-An Asian Journal*, Vol.8, No.8.
Dhakal, K. P., Duong, D. L., Lee, J., Nam, H., Kim, M., Kan, M., Lee, Y. H., and Kim, J., (2014), "Confocal absorption spectral imaging of MoS 2: optical transitions depending on the atomic thickness of intrinsic and chemically doped MoS 2", *Nanoscale*, Vol.6, No.21, pp.13028–13035.
Di Bartolomeo, A., Genovese, L., Foller, T., Giubileo, F., Luongo, G., Croin, L., Liang, S.-J., Ang, L. K., and Schleberger, M., (2017), "Electrical transport and persistent photoconductivity in monolayer MoS2 phototransistors", *Nanotechnology*, Vol.28, No.21, pp.214002.
Diao, M., Li, H., Sun, Y., Liang, Y., Yu, Z., Boukhvalov, D. W., Huang, Z., and Zhang, C., (2021), "Enhancing Reverse Saturable Absorption in SnS2 Nanosheets by Plasma Treatment", *ACS Applied Materials \& Interfaces*, Vol.13, No.3, pp.4211–4219.

Donarelli, M., Ottaviano, L., Giancaterini, L., Fioravanti, G., Perrozzi, F., and Cantalini, C., (2016), "Exfoliated black phosphorus gas sensing properties at room temperature", *2D Materials*, Vol.3, No.2, pp.25002.

Ejeckam, F. E., Chua, C. L., Zhu, Z. H., and Lo, Y. H., (1995), "High-performance InGaAs photodetectors on Si and GaAs substrates",In *Proceedings IEEE/Cornell Conference on Advanced Concepts in High Speed Semiconductor Devices and Circuits* (pp. 194–200).

El Garah, M., Bertolazzi, S., Ippolito, S., Eredia, M., Janica, I., Melinte, G., Ersen, O., Marletta, G., Ciesielski, A., and Samorì, P., (2018), "MoS2 nanosheets via electrochemical lithium-ion intercalation under ambient conditions", *FlatChem*, Vol.9, pp.33–39.

Enujekwu, F. M., Zhang, Y., Ezeh, C. I., Zhao, H., Xu, M., Besley, E., George, M. W., Besley, N. A., Do, H., and Wu, T., (2021), "N-doping enabled defect-engineering of MoS2 for enhanced and selective adsorption of CO2: A DFT approach", *Applied Surface Science*, Vol.542, pp.148556.

Fang, H., and Hu, W., (2017), "Photogating in low dimensional photodetectors", *Advanced Science*, Vol.4, No.12, pp.1700323.

Fang, Z., and Zhao, C. Z., (2012), "Recent progress in silicon photonics: a review", *International Scholarly Research Notices*, Vol.2012, No.1, pp.428690.

Feng, Q., Sun, Y., Li, Y., Yan, J., Zhong, W., Yang, G., Liu, W., Xu, H., and Liu, Y., (2021), "Highly Photoluminescent Monolayer MoS2 and WS2 Achieved via Superacid Assisted Vacancy Reparation and Doping Strategy (Laser Photonics Rev. 15 (12)/2021)", *Laser \& Photonics Reviews*, Vol.15, No.12, pp.2170064.

Filipovic, L., and Selberherr, S., (2022), "Application of Two-Dimensional Materials towards CMOS-Integrated Gas Sensors", *Nanomaterials*, Vol.12, No.20.

Fong, H., Chun, I., and Reneker, D. H., (1999), "Beaded nanofibers formed during electrospinning", *Polymer*, Vol.40, No.16, pp.4585–4592.

Fontana, M., Deppe, T., Boyd, A. K., Rinzan, M., Liu, A. Y., Paranjape, M., and Barbara, P., (2013), "Electron-hole transport and photovoltaic effect in gated MoS2 Schottky junctions", *Scientific Reports*, Vol.3, No.1, pp.1–6.

Freddi, S., Emelianov, A. V, Bobrinetskiy, I. I., Drera, G., Pagliara, S., Kopylova, D. S., Chiesa, M., Santini, G., Mores, N., Moscato, U., and others, (2020), "Development of a sensing array for human breath analysis based on swcnt layers functionalized with semiconductor organic molecules", *Advanced Healthcare Materials*, Vol.9, No.12, pp.2000377.

Furchi, M. M., Polyushkin, D. K., Pospischil, A., and Mueller, T., (2014), "Mechanisms of Photoconductivity in Atomically Thin MoS2", *Nano Letters*, Vol.14, No.11, pp.6165–6170.

Gaiardo, A., Fabbri, B., Guidi, V., Bellutti, P., Giberti, A., Gherardi, S., Vanzetti, L., Malagù, C., and Zonta, G., (2016), "Metal sulfides as sensing materials for chemoresistive gas sensors", *Sensors*, Vol.16, No.3, pp.296.

Gao, J., Yang, H., Mao, H., Liu, T., Zheng, Y., Wang, Y., Xiang, D., Han, C., and Chen, W., (2020), "Out-of-plane homojunction enabled high performance SnS2 lateral phototransistor", *Advanced Optical Materials*, Vol.8, No.9, pp.1901971.

Geim, A. K., (2009), "Graphene: status and prospects", *Science*, Vol.324, No.5934, pp.1530–1534.

Geim, A. K., and Novoselov, K. S., (2007), "The rise of graphene, nature materials, 6".

Generation, M., (2009), "Colloidal Quantum-Dot Photodetectors Exploiting", *Science*, Vol.1173812, No.1542, pp.324.

Gong, C., Zhang, H., Wang, W., Colombo, L., Wallace, R. M., and Cho, K., (2013), "Band alignment of two-dimensional transition metal dichalcogenides: Application in tunnel field effect transistors", *Applied Physics Letters*, Vol.103, No.5.

Gong, J., Chen, Q., Lian, M.-R., Liu, N.-C., Stevenson, R. G., and Adami, F., (2006), "Micromachined nanocrystalline silver doped SnO2 H2S sensor", *Sensors and Actuators B: Chemical*, Vol.114, No.1, pp.32–39.

Gong, Y., Lin, J., Wang, X., Shi, G., Lei, S., Lin, Z., Zou, X., Ye, G., Vajtai, R., Yakobson, B. I., and others, (2014), "Vertical and in-plane heterostructures from WS 2/MoS 2 monolayers", *Nature Materials*, Vol.13, No.12, pp.1135–1142.

Goswami, L., Aggarwal, N., Singh, M., Verma, R., Vashishtha, P., Jain, S. K., Tawale, J., Pandey, R., and Gupta, G., (2020), "GaN nanotowers grown on Si (111) and functionalized with Au nanoparticles and ZnO nanorods for highly responsive UV photodetectors", *ACS Applied Nano Materials*, Vol.3, No.8, pp.8104–8116.

Gu, D., Wang, X., Liu, W., Li, X., Lin, S., Wang, J., Rumyantseva, M. N., Gaskov, A. M., and Akbar, S. A., (2020), "Visible-light activated room temperature NO2 sensing of SnS2 nanosheets based chemiresistive sensors", *Sensors and Actuators B: Chemical*, Vol.305, pp.127455.

Gundimeda, A., Krishna, S., Aggarwal, N., Sharma, A., Sharma, N. D., Maurya, K. K., Husale, S., and Gupta, G., (2017), "Erratum:"Fabrication of non-polar GaN based highly responsive and fast UV photodetector"[Appl. Phys. Lett. 110, 103507 (2017)]", *Applied Physics Letters*, Vol.111, No.1, pp.19901.

Hafner, J., (2008), "Ab-initio simulations of materials using VASP: Density-functional theory and beyond", *Journal of Computational Chemistry*, Vol.29, No.13, pp.2044–2078.

Ham, G., Shin, S., Park, J., Choi, H., Kim, J., Lee, Y.-A., Seo, H., and Jeon, H., (2013), "Tuning the electronic structure of tin sulfides grown by atomic layer deposition", *ACS Applied Materials \& Interfaces*, Vol.5, No.18, pp.8889–8896.

Han, F., Zhang, C., Yang, J., Ma, G., He, K., and Li, X., (2016), "Well-dispersed and porous FeP@ C nanoplates with stable and ultrafast lithium storage performance through conversion reaction mechanism", *Journal of Materials Chemistry A*, Vol.4, No.33, pp.12781–12789.

Han, T., Liu, H., Wang, S., Chen, S., and Yang, K., (2020), "The large-scale preparation and optical properties of MoS2/WS2 vertical hetero-junction", *Molecules*, Vol.25, No.8, pp.1857.

Han, Y., Huang, D., Ma, Y., He, G., Hu, J., Zhang, J., Hu, N., Su, Y., Zhou, Z., Zhang, Y., and Yang, Z., (2018), "Design of Hetero-Nanostructures on MoS2 Nanosheets to Boost NO2 Roomerature Sensing", *ACS Applied Materials and Interfaces*, Vol.10, No.26, pp.22640–22649.

Hanson, R. M., (2010), "Jmol--a paradigm shift in crystallographic visualization", *Journal of Applied Crystallography*, Vol.43, No.5, pp.1250–1260.

Hao, J., Zhang, D., Sun, Q., Zheng, S., Sun, J., and Wang, Y., (2018), "Hierarchical SnS2/SnO2 nanoheterojunctions with increased active-sites and charge transfer for ultrasensitive NO2 detection", *Nanoscale*, Vol.10, No.15, pp.7210–7217.

Hashemzadeh, B., Idani, E., Goudarzi, G., Ankali, K. A., Sakhvidi, M. J. Z., Babaei, A. A., Hashemzadeh, H., Vosoughi, M., Mohammadi, M. J., and Neisi, A., (2019), "Effects of PM2. 5 and NO2 on the 8-isoprostane and lung function indices of FVC and FEV1 in students of Ahvaz city, Iran", *Saudi Journal of Biological Sciences*, Vol.26, No.3, pp.473–480.

He, M., Lei, J., Zhou, C., Shi, H., Sun, X., and Gao, B., (2019), "Growth of vertical MoS2 nanosheets on carbon materials by chemical vapor deposition: influence of substrates", *Materials Research Express*, Vol.6, No.11, pp.1150c1.

He, Q., Zeng, Z., Yin, Z., Li, H., Wu, S., Huang, X., and Zhang, H., (2012), "Fabrication of flexible MoS2 thin-film transistor arrays for practical gas-sensing applications", *Small*, Vol.8, No.19, pp.2994–2999.

He, T., Lan, C., Zhou, S., Li, Y., Yin, Y., Li, C., and Liu, Y., (2021), "Enhanced responsivity of a graphene/Si-based heterostructure broadband photodetector by introducing a WS 2 interfacial layer", *Journal of Materials Chemistry C*, Vol.9, No.11, pp.3846–3853.

He, Z., and Que, W., (2016), "Molybdenum disulfide nanomaterials: Structures, properties, synthesis and recent progress on hydrogen evolution reaction", *Applied Materials Today*, Vol.3, pp.23–56.

Heyd, J., Scuseria, G. E., and Ernzerhof, M., (2003), "Hybrid functionals based on a screened Coulomb potential", *The Journal of Chemical Physics*, Vol.118, No.18, pp.8207–8215.

Hien, N. D., Nguyen, C. V, Hieu, N. N., Kubakaddi, S. S., Duque, C. A., Mora-Ramos, M. E., Dinh, L., Bich, T. N., and Phuc, H. V, (2020), "Magneto-optical transport properties of monolayer transition metal dichalcogenides", *Phys. Rev. B*, Vol.101, No.4, pp.45424.

Hong, X., Kim, J., Shi, S.-F., Zhang, Y., Jin, C., Sun, Y., Tongay, S., Wu, J., Zhang, Y., and Wang, F., (2014), "Ultrafast charge transfer in atomically thin MoS2/WS2 heterostructures", *Nature Nanotechnology*, Vol.9, No.9, pp.682–686.

Hu, C., Yuan, C., Hong, A., Guo, M., Yu, T., and Luo, X., (2018), "Work function variation of monolayer MoS2 by nitrogen-doping", *Applied Physics Letters*, Vol.113, No.4, pp.41602.

Hu, K., Ming, C., Liu, Y., Zheng, C., Zhang, S., Wang, D., Zhao, W., and Huang, F., (2020), "Introducing sulfur vacancies and in-plane SnS2/SnO2 heterojunction in SnS2 nanosheets to promote photocatalytic activity", *Chinese Chemical Letters*, Vol.31, No.10, pp.2809–2813.

Hu, N., Yang, Z., Wang, Y., Zhang, L., Wang, Y., Huang, X., Wei, H., Wei, L., and Zhang, Y., (2014), "Ultrafast and sensitive room temperature NH3 gas sensors based on chemically reduced graphene oxide", *Nanotechnology*, Vol.25, No.2, pp.25502.

Huang, Y., Jiao, W., Chu, Z., Ding, G., Yan, M., Zhong, X., and Wang, R., (2019), "Ultrasensitive room temperature ppb-level NO2 gas sensors based on SnS2/rGO nanohybrids with P–N transition and optoelectronic visible light enhancement performance", *Journal of Materials Chemistry C*, Vol.7, No.28, pp.8616–8625.

Huang, Y., Sutter, E., Sadowski, J. T., Cotlet, M., Monti, O. L. A., Racke, D. A., Neupane, M. R., Wickramaratne, D., Lake, R. K., Parkinson, B. A., and others, (2014), "Tin Disulfide□ An Emerging Layered Metal Dichalcogenide Semiconductor: Materials Properties and Device Characteristics", *ACS Nano*, Vol.8, No.10, pp.10743–10755.

Huang, Z., Carey, J. E., Liu, M., Guo, X., Mazur, E., and Campbell, J. C., (2006), "Microstructured silicon photodetector", *Applied Physics Letters*, Vol.89, No.3.
Hübert, T., Boon-Brett, L., Black, G., and Banach, U., (2011), "Hydrogen sensors--a review", *Sensors and Actuators B: Chemical*, Vol.157, No.2, pp.329–352.
Hui, Y. Y., Liu, X., Jie, W., Chan, N. Y., Hao, J., Hsu, Y.-T., Li, L.-J., Guo, W., and Lau, S. P., (2013), "Exceptional Tunability of Band Energy in a Compressively Strained Trilayer MoS2 Sheet", *ACS Nano*, Vol.7, No.8, pp.7126–7131.
Huo, N., Gupta, S., and Konstantatos, G., (2017), "MoS2--HgTe quantum dot hybrid photodetectors beyond 2 $μ$m", *Advanced Materials*, Vol.29, No.17, pp.1606576.
Iitani, K., Sato, T., Naisierding, M., Hayakawa, Y., Toma, K., Arakawa, T., and Mitsubayashi, K., (2018), "Fluorometric Sniff-Cam (gas-imaging system) utilizing alcohol dehydrogenase for imaging concentration distribution of acetaldehyde in breath and transdermal vapor after drinking", *Analytical Chemistry*, Vol.90, No.4, pp.2678–2685.
Indahl, U. G., and Naes, T., (1998), "Evaluation of alternative spectral feature extraction methods of textural images for multivariate modelling", *Journal of Chemometrics: A Journal of the Chemometrics Society*, Vol.12, No.4, pp.261–278.
Island, J. O., Steele, G. A., van der Zant, H. S. J., and Castellanos-Gomez, A., (2015), "Environmental instability of few-layer black phosphorus", *2D Materials*, Vol.2, No.1, pp.11002.
Jaiswal, J., Sanger, A., Tiwari, P., and Chandra, R., (2020), "MoS2 hybrid heterostructure thin film decorated with CdTe quantum dots for room temperature NO2 gas sensor", *Sensors and Actuators B: Chemical*, Vol.305, pp.127437.
Jariwala, D., Sangwan, V. K., Lauhon, L. J., Marks, T. J., and Hersam, M. C., (2014), "Emerging device applications for semiconducting two-dimensional transition metal dichalcogenides", *ACS Nano*, Vol.8, No.2, pp.1102–1120.
Jia, Z., Xiang, J., Wen, F., Yang, R., Hao, C., and Liu, Z., (2016), "Enhanced photoresponse of SnSe-nanocrystals-decorated WS2 monolayer phototransistor", *ACS Applied Materials \& Interfaces*, Vol.8, No.7, pp.4781–4788.
Jiang, J., Zou, X., Lv, Y., Liu, Y., Xu, W., Tao, Q., Chai, Y., and Liao, L., (2020), "Rational design of Al2O3/2D perovskite heterostructure dielectric for high performance MoS2 phototransistors", *Nature Communications*, Vol.11, No.1, pp.4266.
Jin, Q., Liu, N., Chen, B., and Mei, D., (2018), "Mechanisms of semiconducting 2H to metallic 1T phase transition in two-dimensional MoS2 nanosheets", *The Journal of Physical Chemistry C*, Vol.122, No.49, pp.28215–28224.
Jones, R. O., (2015), "Density functional theory: Its origins, rise to prominence, and future", *Reviews of Modern Physics*, Vol.87, No.3, pp.897.
Kaushik, N., Mackenzie, D. M. A., Thakar, K., Goyal, N., Mukherjee, B., Boggild, P., Petersen, D. H., and Lodha, S., (2017), "Reversible hysteresis inversion in MoS2 field effect transistors", *Npj 2D Materials and Applications*, Vol.1, No.1, pp.34.
Keuleyan, S., Lhuillier, E., Brajuskovic, V., and Guyot-Sionnest, P., (2011), "Mid-infrared HgTe colloidal quantum dot photodetectors", *Nature Photonics*, Vol.5, No.8, pp.489–493.
Khan, M. A. H., Rao, M. V, and Li, Q., (2019), "Recent advances in electrochemical sensors for detecting toxic gases: NO2, SO2 and H2S", *Sensors*, Vol.19, No.4, pp.905.
Kim, B. H., Park, M., Lee, M., Baek, S. J., Jeong, H. Y., Choi, M., Chang, S. J., Hong, W. G., Kim, T. K., Moon, H. R., and others, (2013), "Effect of sulphur vacancy on geometric and electronic structure of MoS 2 induced by molecular hydrogen treatment at room temperature", *RSC Advances*, Vol.3, No.40, pp.18424–18429.
Kim, C., Park, J.-C., Choi, S. Y., Kim, Y., Seo, S.-Y., Park, T.-E., Kwon, S.-H., Cho, B., and Ahn, J.-H., (2018a), "Self-formed channel devices based on vertically grown 2D materials with large-surface-area and their potential for chemical sensor applications", *Small*, Vol.14, No.15, pp.1704116.
Kim, J.-S., Yoo, H.-W., Choi, H. O., and Jung, H.-T., (2014), "Tunable volatile organic compounds sensor by using thiolated ligand conjugation on MoS2", *Nano Letters*, Vol.14, No.10, pp.5941–5947.
Kim, K., and Jordan, K. D., (1994), "Comparison of density functional and MP2 calculations on the water monomer and dimer", *The Journal of Physical Chemistry*, Vol.98, No.40, pp.10089–10094.
Kim, T., Lee, T. H., Park, S. Y., Eom, T. H., Cho, I., Kim, Y., Kim, C., Lee, S. A., Choi, M. J., Suh, J. M., Hwang, I. S., Lee, D., Park, I., and Jang, H. W., (2023), "Drastic Gas Sensing Selectivity in 2-Dimensional MoS2 Nanoflakes by Noble Metal Decoration", *ACS Nano*, Vol.17, No.5, pp.4404–4413.
Kim, Y.-H., Phan, D.-T., Ahn, S., Nam, K.-H., Park, C.-M., and Jeon, K.-J., (2018b), "Two-dimensional SnS2 materials as high-performance NO2 sensors with fast response and high sensitivity", *Sensors and Actuators B: Chemical*, Vol.255, pp.616–621.

Klots, A. R., Newaz, A. K. M., Wang, B., Prasai, D., Krzyzanowska, H., Lin, J., Caudel, D., Ghimire, N. J., Yan, J., Ivanov, B. L., and others, (2014), "Probing excitonic states in suspended two-dimensional semiconductors by photocurrent spectroscopy", *Scientific Reports*, Vol.4, No.1, pp.6608.

Ko, K. Y., Park, K., Lee, S., Kim, Y., Woo, W. J., Kim, D., Song, J.-G., Park, J., and Kim, H., (2018), "Recovery improvement for large-area tungsten diselenide gas sensors", *ACS Applied Materials \& Interfaces*, Vol.10, No.28, pp.23910–23917.

Kohl, D., (2001), "Function and applications of gas sensors", *Journal of Physics D: Applied Physics*, Vol.34, No.19, pp.R125.

Kolobov, A. V, Tominaga, J., Kolobov, A. V, and Tominaga, J., (2016), "Chemistry of chalcogenides and transition metals", *Two-Dimensional Transition-Metal Dichalcogenides*, pp.7–27.

Korotcenkov, G., Han, S. Do, and Stetter, J. R., (2009), "Review of electrochemical hydrogen sensors", *Chemical Reviews*, Vol.109, No.3, pp.1402–1433.

Kresse, G., and Furthmüller, J., (1996), "Efficient iterative schemes for ab initio total-energy calculations using a plane-wave basis set", *Physical Review B*, Vol.54, No.16, pp.11169.

Kuc, A., Zibouche, N., and Heine, T., (2011), "Influence of quantum confinement on the electronic structure of the transition metal sulfide TS 2", *Physical Review B – Condensed Matter and Materials Physics*, Vol.83, No.24, pp.245213.

Kufer, D., Nikitskiy, I., Lasanta, T., Navickaite, G., Koppens, F. H., and Konstantatos, G., (2014), "Hybrid 2D-0D MoS2-PbS quantum dot photodetectors.", *Advanced Materials (Deerfield Beach, Fla.)*, Vol.27, No.1, pp.176–180.

Kukucska, G., and Koltai, J., (2017), "Theoretical investigation of strain and doping on the Raman spectra of monolayer MoS2", *Physica Status Solidi (B)*, Vol.254, No.11, pp.1700184.

Kumar, A., Gutal, A. P., Sharma, N., Kumar, D., Zhang, G., Kim, H., Kumar, P., Paranjothy, M., Kumar, M., and Strano, M. S., (2023a), "Investigations of Vacancy-Assisted Selective Detection of NO2 Molecules in Vertically Aligned SnS2", *ACS Sensors*, Vol.8, No.3, pp.1357–1367.

Kumar, A., Khan, M. A., and Kumar, M., (2021a), "Recent advances in UV photodetectors based on 2D materials: A review", *Journal of Physics D: Applied Physics*, Vol.55, No.13, pp.133002.

Kumar, A., Mirzaei, A., Lee, M. H., Ghahremani, Z., Kim, T.-U., Kim, J.-Y., Kwoka, M., Kumar, M., Kim, S. S., and Kim, H. W., (2024a), "Strategic review of gas sensing enhancement ways of 2D tungsten disulfide/selenide based chemiresistive sensors: Decoration and composite", *Journal of Materials Chemistry A*.

Kumar, A., Sharma, N., Gutal, A. P., Kumar, D., Kumar, P., Paranjothy, M., and Kumar, M., (2022), "Growth and NO2 gas sensing mechanisms of vertically aligned 2D SnS2 flakes by CVD: Experimental and DFT studies", *Sensors and Actuators B: Chemical*, Vol.353, pp.131078.

Kumar, R., Goel, N., and Kumar, M., (2017), "UV-activated MoS2 based fast and reversible NO2 sensor at room temperature", *ACS Sensors*, Vol.2, No.11, pp.1744–1752.

Kumar, R., Goel, N., and Kumar, M., (2018a), "High performance NO2 sensor using MoS2 nanowires network", *Applied Physics Letters*, Vol.112, No.5, pp.53502.

Kumar, R., Kulriya, P. K., Mishra, M., Singh, F., Gupta, G., and Kumar, M., (2018b), "Highly selective and reversible NO2 gas sensor using vertically aligned MoS2 flake networks", *Nanotechnology*, Vol.29, No.46, pp.464001.

Kumar, R. R., Habib, M. R., Khan, A., Chen, P.-C., Murugesan, T., Gupta, S., Anbalagan, A. K., Tai, N.-H., Lee, C.-H., and Lin, H.-N., (2021b), "Sulfur Monovacancies in Liquid-Exfoliated MoS2 Nanosheets for NO2 Gas Sensing", *ACS Applied Nano Materials*, Vol.4, No.9, pp.9459–9470.

Kumar, S., Chaurasiya, R., Mishra, S. S., Kumbhakar, P., Meng, G., Tiwary, C. S., Biswas, K., and Kumar, M., (2023b), "Nanocomposites of Quasicrystal Nanosheets and MoS2 Nanoflakes for NO2 Gas Sensors", *ACS Applied Nano Materials*, Vol.6, No.7, pp.5952–5962.

Kumar, S., Mirzaei, A., Kumar, A., Lee, M. H., Ghahremani, Z., Kim, T.-U., Kim, J.-Y., Kwoka, M., Kumar, M., Kim, S. S., and others, (2024b), "Nanoparticles anchored strategy to develop 2D MoS2 and MoSe2 based room temperature chemiresistive gas sensors", *Coordination Chemistry Reviews*, Vol.503, pp.215657.

Kumawat, K. L., Augustine, P., Singh, D. K., Krupanidhi, S. B., and Nanda, K. K., (2022), "A MoS 2/CuO-based hybrid p--n junction for high-performance self-powered photodetection", *Journal of Materials Chemistry C*, Vol.10, No.38, pp.14159–14168.

Kunstmann, J., Wendumu, T. B., and Seifert, G., (2017), "Localized defect states in MoS2 monolayers: Electronic and optical properties", *Physica Status Solidi (B)*, Vol.254, No.4, pp.1600645.

Kuru, C., Choi, C., Kargar, A., Choi, D., Kim, Y. J., Liu, C. H., Yavuz, S., and Jin, S., (2015), "MoS2 nanosheet--Pd nanoparticle composite for highly sensitive room temperature detection of hydrogen", *Advanced Science*, Vol.2, No.4, pp.1500004.

Kwon, K. C., Suh, J. M., Lee, T. H., Choi, K. S., Hong, K., Song, Y. G., Shim, Y.-S., Shokouhimehr, M., Kang, C.-Y., Kim, S. Y., and others, (2019), "SnS2 nanograins on porous SiO2 nanorods template for highly sensitive NO2 sensor at room temperature with excellent recovery", *ACS Sensors*, Vol.4, No.3, pp.678–686.

Late, D. J., Huang, Y.-K., Liu, B., Acharya, J., Shirodkar, S. N., Luo, J., Yan, A., Charles, D., Waghmare, U. V, Dravid, V. P., and others, (2013), "Sensing behavior of atomically thin-layered MoS2 transistors", *ACS Nano*, Vol.7, No.6, pp.4879–4891.

Late, D. J., Liu, B., Matte, H. S. S. R., Dravid, V. P., and Rao, C. N. R., (2012), "Hysteresis in Single-Layer MoS2 Field Effect Transistors", *ACS Nano*, Vol.6, No.6, pp.5635–5641.

Lee, C.-H., Lee, G.-H., Van Der Zande, A. M., Chen, W., Li, Y., Han, M., Cui, X., Arefe, G., Nuckolls, C., Heinz, T. F., and others, (2014), "Atomically thin p--n junctions with van der Waals heterointerfaces", *Nature Nanotechnology*, Vol.9, No.9, pp.676–681.

Lee, C. Y., and Strano, M. S., (2005), "Understanding the dynamics of signal transduction for adsorption of gases and vapors on carbon nanotube sensors", *AIChE Annual Meeting, Conference Proceedings*, , No.13, pp.14039.

Lee, C., Yan, H., Brus, L. E., Heinz, T. F., Hone, J., and Ryu, S., (2010), "Anomalous lattice vibrations of single-and few-layer MoS2", *ACS Nano*, Vol.4, No.5, pp.2695–2700.

Lee, E., Yoon, Y. S., and Kim, D.-J., (2018), "Two-dimensional transition metal dichalcogenides and metal oxide hybrids for gas sensing", *ACS Sensors*, Vol.3, No.10, pp.2045–2060.

Lee, G.-H., Yu, Y.-J., Cui, X., Petrone, N., Lee, C.-H., Choi, M. S., Lee, D.-Y., Lee, C., Yoo, W. J., Watanabe, K., and others, (2013), "Flexible and transparent MoS2 field-effect transistors on hexagonal boron nitride-graphene heterostructures", *ACS Nano*, Vol.7, No.9, pp.7931–7936.

Lee, H. S., Min, S.-W., Chang, Y.-G., Park, M. K., Nam, T., Kim, H., Kim, J. H., Ryu, S., and Im, S., (2012a), "MoS2 nanosheet phototransistors with thickness-modulated optical energy gap", *Nano Letters*, Vol.12, No.7, pp.3695–3700.

Lee, J. J., Shin, D. H., Jung, D. H., Oh, S. D., and Lee, H., (2023), "A high-performance broadband self-powered photodetector employing an MoS2/LaVO3 heterojunction structure", *Journal of Alloys and Compounds*, Vol.937, pp.168404.

Lee, Y.-H., Zhang, X.-Q., Zhang, W., Chang, M.-T., Lin, C.-T., Chang, K.-D., Yu, Y.-C., Wang, J. T.-W., Chang, C.-S., Li, L.-J., and Lin, T.-W., (2012b), "Synthesis of Large-Area MoS2 Atomic Layers with Chemical Vapor Deposition", *Advanced Materials*, Vol.24, No.17, pp.2320–2325.

Leenaerts, O., Partoens, B., and Peeters, F. M., (2008), "Adsorption of H 2 O, NH 3, CO, NO 2, and NO on graphene: A first-principles study", *Physical Review B – Condensed Matter and Materials Physics*, Vol.77, No.12, pp.125416.

Lei, Y., Yang, X., and Feng, W., (2021), "Synthesis of vertically-aligned large-area MoS2 nanofilm and its application in MoS2/Si heterostructure photodetector", *Nanotechnology*, Vol.33, No.10, pp.105709.

Levine, I. N., (2014), "*Quantum Chemistry, 7th edition*". Pearson.

Li, H., Wu, J., Yin, Z., and Zhang, H., (2014), "Preparation and applications of mechanically exfoliated single-layer and multilayer MoS2 and WSe2 nanosheets", *Accounts of Chemical Research*, Vol.47, No.4, pp.1067–1075.

Li, H., Yin, Z., He, Q., Li, H., Huang, X., Lu, G., Fam, D. W. H., Tok, A. I. Y., Zhang, Q., and Zhang, H., (2012a), "Fabrication of single-and multilayer MoS2 film-based field-effect transistors for sensing NO at room temperature", *Small*, Vol.8, No.1, pp.63–67.

Li, H., Zhang, Q., Yap, C. C. R., Tay, B. K., Edwin, T. H. T., Olivier, A., and Baillargeat, D., (2012b), "From bulk to monolayer MoS2: evolution of Raman scattering", *Advanced Functional Materials*, Vol.22, No.7, pp.1385–1390.

Li, J., Lu, Y., Ye, Q., Cinke, M., Han, J., and Meyyappan, M., (2003), "Carbon nanotube sensors for gas and organic vapor detection", *Nano Letters*, Vol.3, No.7, pp.929–933.

Li, R., Yang, L., Xiong, T., Wu, Y., Cao, L., Yuan, D., and Zhou, W., (2017), "Nitrogen doped MoS2 nanosheets synthesized via a low-temperature process as electrocatalysts with enhanced activity for hydrogen evolution reaction", *Journal of Power Sources*, Vol.356, pp.133–139.

Li, T., and Galli, G., (2007), "Electronic properties of MoS2 nanoparticles", *The Journal of Physical Chemistry C*, Vol.111, No.44, pp.16192–16196.

Li, W., Zhang, Y., Long, X., Cao, J., Xin, X., Guan, X., Peng, J., and Zheng, X., (2019a), "Gas sensors based on mechanically exfoliated MoS2 nanosheets for room-temperature NO2 detection", *Sensors*, Vol.19, No.9, pp.2123.

Li, Y., Song, Z., Li, Y., Chen, S., Li, S., Li, Y., Wang, H., and Wang, Z., (2019b), "Hierarchical hollow MoS2 microspheres as materials for conductometric NO2 gas sensors", *Sensors and Actuators B: Chemical*, Vol.282, pp.259–267.

Li, Y., Wang, H., Xie, L., Liang, Y., Hong, G., and Dai, H., (2011), "MoS2 nanoparticles grown on graphene: an advanced catalyst for the hydrogen evolution reaction", *Journal of the American Chemical Society*, Vol.133, No.19, pp.7296–7299.

Li, Z., Guo, S., Wang, Y., Yang, S., Hu, J., and Zhang, S., (2024), "Density Functional Theory Study of Two-Dimensional SnS2 Doping for Detection of Hydrogen Sulfide", *ACS Applied Nano Materials*, Vol.7, No.20, pp.23842–23849.

Liang, T., Liu, Y., Cheng, Y., Ma, F., and Dai, Z., (2020), "Scalable Synthesis of a MoS2/Black Phosphorus Heterostructure for pH-Universal Hydrogen Evolution Catalysis", *ChemCatChem*, Vol.12, No.10, pp.2840–2848.

Lien, M.-B., Liu, C.-H., Chun, I. Y., Ravishankar, S., Nien, H., Zhou, M., Fessler, J. A., Zhong, Z., and Norris, T. B., (2020), "Ranging and light field imaging with transparent photodetectors", *Nature Photonics*, Vol.14, No.3, pp.143–148.

Lin, X., Wang, F., Shan, X., Miao, Y., Chen, X., Yan, M., Zhang, L., Liu, K., Luo, J., and Zhang, K., (2021), "High-performance photodetector and its optoelectronic mechanism of MoS2/WS2 vertical heterostructure", *Applied Surface Science*, Vol.546, pp.149074.

Lin, Y.-C., Ghosh, R. K., Addou, R., Lu, N., Eichfeld, S. M., Zhu, H., Li, M.-Y., Peng, X., Kim, M. J., Li, L.-J., and others, (2015), "Atomically thin resonant tunnel diodes built from synthetic van der Waals heterostructures", *Nature Communications*, Vol.6, No.1, pp.1–6.

Liu, B., Chen, L., Liu, G., Abbas, A. N., Fathi, M., and Zhou, C., (2014a), "High-performance chemical sensing using Schottky-contacted chemical vapor deposition grown monolayer MoS2 transistors", *ACS Nano*, Vol.8, No.5, pp.5304–5314.

Liu, B., Zhao, C., Chen, X., Zhang, L., Li, Y., Yan, H., and Zhang, Y., (2019), "Self-powered and fast photodetector based on graphene/MoSe2/Au heterojunction", *Superlattices and Microstructures*, Vol.130, pp.87–92.

Liu, D., Tang, Z., and Zhang, Z., (2018a), "Nanoplates-assembled SnS2 nanoflowers for ultrasensitive ppb-level NO2 detection", *Sensors and Actuators B: Chemical*, Vol.273, pp.473–479.

Liu, F., Shimotani, H., Shang, H., Kanagasekaran, T., Zólyomi, V., Drummond, N., Fal'ko, V. I., and Tanigaki, K., (2014b), "High-sensitivity photodetectors based on multilayer GaTe flakes", *ACS Nano*, Vol.8, No.1, pp.752–760.

Liu, H.-L., Shen, C.-C., Su, S.-H., Hsu, C.-L., Li, M.-Y., and Li, L.-J., (2014c), "Optical properties of monolayer transition metal dichalcogenides probed by spectroscopic ellipsometry", *Applied Physics Letters*, Vol.105, No.20.

Liu, H., Neal, A. T., Zhu, Z., Luo, Z., Xu, X., Tománek, D., and Ye, P. D., (2014d), "Phosphorene: an unexplored 2D semiconductor with a high hole mobility", *ACS Nano*, Vol.8, No.4, pp.4033–4041.

Liu, L., Ikram, M., Ma, L., Zhang, X., Lv, H., Ullah, M., Khan, M., Yu, H., and Shi, K., (2020), "Edge-exposed MoS2 nanospheres assembled with SnS2 nanosheet to boost NO2 gas sensing at room temperature", *Journal of Hazardous Materials*, Vol.393, pp.122325.

Liu, Q., Weijun, X., Wu, Z., Huo, J., Liu, D., Wang, Q., and Wang, S., (2016), "The origin of the enhanced performance of nitrogen-doped MoS2 in lithium ion batteries", *Nanotechnology*, Vol.27, No.17, pp.175402.

Liu, X., Ma, T., Pinna, N., and Zhang, J., (2017), "Two-dimensional nanostructured materials for gas sensing", *Advanced Functional Materials*, Vol.27, No.37, pp.1702168.

Liu, Y., Duan, X., Huang, Y., and Duan, X., (2018b), "Two-dimensional transistors beyond graphene and TMDCs", *Chemical Society Reviews*, Vol.47, No.16, pp.6388–6409.

Liu, Y., Guo, J., Zhu, E., Liao, L., Lee, S.-J., Ding, M., Shakir, I., Gambin, V., Huang, Y., and Duan, X., (2018c), "Approaching the Schottky–Mott limit in van der Waals metal–semiconductor junctions", *Nature*, Vol.557, No.7707, pp.696–700.

Long, H., Harley-Trochimczyk, A., Pham, T., Tang, Z., Shi, T., Zettl, A., Carraro, C., Worsley, M. A., and Maboudian, R., (2016a), "High surface area MoS2/graphene hybrid aerogel for ultrasensitive NO2 detection", *Advanced Functional Materials*, Vol.26, No.28, pp.5158–5165.

Long, M., Liu, E., Wang, P., Gao, A., Xia, H., Luo, W., Wang, B., Zeng, J., Fu, Y., Xu, K., and others, (2016b), "Broadband photovoltaic detectors based on an atomically thin heterostructure", *Nano Letters*, Vol.16, No.4, pp.2254–2259.

Lonkar, S. P., Pillai, V. V, and Alhassan, S. M., (2020), "Three dimensional (3D) nanostructured assembly of MoS2-WS2/Graphene as high performance electrocatalysts", *International Journal of Hydrogen Energy*, Vol.45, No.17, pp.10475–10485.

Lopez-Sanchez, O., Lembke, D., Kayci, M., Radenovic, A., and Kis, A., (2013), "Ultrasensitive photodetectors based on monolayer MoS2", *Nature Nanotechnology*, Vol.8, No.7, pp.497–501.

Lou, C., Wang, K., Mei, H., Xie, J., Zheng, W., Liu, X., and Zhang, J., (2021), "ZnO nanoarrays via a thermal

decomposition--deposition method for sensitive and selective NO 2 detection", *CrystEngComm*, Vol.23, No.20, pp.3654–3663.
Lu, C., Ma, J., Si, K., Xu, X., Quan, C., He, C., and Xu, X., (2019), "Band alignment of WS2/MoS2 photoanodes with efficient photoelectric responses based on mixed Van der Waals heterostructures", *Physica Status Solidi (A)*, Vol.216, No.20, pp.1900544.
Lu, F., Zhou, M., Li, W., Weng, Q., Li, C., Xue, Y., Jiang, X., Zeng, X., Bando, Y., and Golberg, D., (2016), "Engineering sulfur vacancies and impurities in NiCo2S4 nanostructures toward optimal supercapacitive performance", *Nano Energy*, Vol.26, pp.313–323.
Ma, Q., Odenthal, P. M., Mann, J., Le, D., Wang, C. S., Zhu, Y., Chen, T., Sun, D., Yamaguchi, K., Tran, T., and others, (2013), "Controlled argon beam-induced desulfurization of monolayer molybdenum disulfide", *Journal of Physics: Condensed Matter*, Vol.25, No.25, pp.252201.
Ma, X., Zhang, J., Sun, Y., Wu, C., Geng, G., Zhang, J., Wu, E., Xu, L., Wu, S., Hu, X., and Liu, J., (2022), "Engineering of Oxidized Line Defects on CVD-Grown MoS2 Flakes", *ACS Applied Materials & Interfaces*, Vol.14, No.41, pp.47288–47299.
Mabiala-Poaty, H. B., Douma, D. H., M'Passi-Mabiala, B., and Mapasha, R. E., (2018), "Structural and electronic properties of SnS2 stacked nanosheets: An ab-initio study", *Journal of Physics and Chemistry of Solids*, Vol.120, pp.211–217.
Mak, K. F., He, K., Lee, C., Lee, G. H., Hone, J., Heinz, T. F., and Shan, J., (2013), "Tightly bound trions in monolayer MoS2", *Nature Materials*, Vol.12, No.3, pp.207–211.
Mak, K. F., Lee, C., Hone, J., Shan, J., and Heinz, T. F., (2010a), "Atomically Thin ${\mathrm{MoS}}_{2}$: A New Direct-Gap Semiconductor", *Phys. Rev. Lett.*, Vol.105, No.13, pp.136805.
Mak, K. F., Lee, C., Hone, J., Shan, J., and Heinz, T. F., (2010b), "Atomically thin MoS 2: a new direct-gap semiconductor", *Physical Review Letters*, Vol.105, No.13, pp.136805.
Mas-Balleste, R., Gomez-Navarro, C., Gomez-Herrero, J., and Zamora, F., (2011), "2D materials: to graphene and beyond", *Nanoscale*, Vol.3, No.1, pp.20–30.
Masel, R. I., (1996), "*Principles of adsorption and reaction on solid surfaces*" (Vol. 3). John Wiley \& Sons.
Mattheiss, L. F., (1973), "Band structures of transition-metal-dichalcogenide layer compounds", *Physical Review B*, Vol.8, No.8, pp.3719.
Mattox, D. M., (2010), "*Handbook of physical vapor deposition (PVD) processing*". William Andrew.
McDonnell, S., Addou, R., Buie, C., Wallace, R. M., and Hinkle, C. L., (2014), "Defect-dominated doping and contact resistance in MoS2", *ACS Nano*, Vol.8, No.3, pp.2880–2888.
Melitz, W., Shen, J., Kummel, A. C., and Lee, S., (2011), "Kelvin probe force microscopy and its application", *Surface Science Reports*, Vol.66, No.1, pp.1–27.
Miao, J., Hu, W., Jing, Y., Luo, W., Liao, L., Pan, A., Wu, S., Cheng, J., Chen, X., and Lu, W., (2015), "Surface plasmon-enhanced photodetection in few layer MoS2 phototransistors with Au nanostructure arrays", *Small*, Vol.11, No.20, pp.2392–2398.
Mirzaei, A., Lee, J.-H., Majhi, S. M., Weber, M., Bechelany, M., Kim, H. W., and Kim, S. S., (2019), "Resistive gas sensors based on metal-oxide nanowires", *Journal of Applied Physics*, Vol.126, No.24.
Mishra, R. K., Choi, H. J., Ryu, J. W., Choi, G. J., Kumar, V., Kumar, P., Singh, J., Kumar, S., and Gwag, J. S., (2024), "Recent progress in gas sensing based on 2D SnS2 and its heterostructure platforms: A review", *Sensors and Actuators A: Physical*, Vol.365, pp.114860.
Momma, K., and Izumi, F., (2008), "VESTA: a three-dimensional visualization system for electronic and structural analysis", *Journal of Applied Crystallography*, Vol.41, No.3, pp.653–658.
Momma, K., and Izumi, F., (2011), "VESTA 3 for three-dimensional visualization of crystal, volumetric and morphology data", *Journal of Applied Crystallography*, Vol.44, No.6, pp.1272–1276.
Mondal, S., Sahoo, L., Vinod, C. P., and Gautam, U. K., (2021), "Facile transfer of excited electrons in Au/SnS2 nanosheets for efficient solar-driven selective organic transformations", *Applied Catalysis B: Environmental*, Vol.286, pp.119927.
Mouri, S., Miyauchi, Y., and Matsuda, K., (2013), "Tunable photoluminescence of monolayer MoS2 via chemical doping", *Nano Letters*, Vol.13, No.12, pp.5944–5948.
Mukherjee, S., Chowdhury, R. K., Karmakar, D., Wan, M., Jacob, C., Das, S., and Ray, S. K., (2021), "Plasmon Triggered, Enhanced Light–Matter Interactions in Au–MoS2 Coupled System with Superior Photosensitivity", *The Journal of Physical Chemistry C*, Vol.125, No.20, pp.11023–11034.
Nan, H., Zhou, R., Gu, X., Xiao, S., and (Ken) Ostrikov, K., (2019), "Recent advances in plasma modification of 2D transition metal dichalcogenides", *Nanoscale*, Vol.11, No.41, pp.19202–19213.
Nasir, M. Z. M., Mayorga-Martinez, C. C., Sofer, Z., and Pumera, M., (2017), "Two-dimensional 1T-phase transition metal dichalcogenides as nanocarriers to enhance and stabilize enzyme activity for electrochemical pesticide detection", *Acs Nano*, Vol.11, No.6, pp.5774–5784.
Noh, J.-Y., Kim, H., and Kim, Y.-S., (2014), "Stability and electronic structures of native defects in single-

layer MoS 2", *Physical Review B*, Vol.89, No.20, pp.205417.
Nourbakhsh, A., Zubair, A., Dresselhaus, M. S., and Palacios, T., (2016), "Transport properties of a MoS2/WSe2 heterojunction transistor and its potential for application", *Nano Letters*, Vol.16, No.2, pp.1359–1366.
Novoselov, K. S., (2011), "Nobel lecture: Graphene: Materials in the flatland", *Reviews of Modern Physics*, Vol.83, No.3, pp.837–849.
Novoselov, K. S., Jiang, D., Schedin, F., Booth, T. J., Khotkevich, V. V, Morozov, S. V, and Geim, A. K., (2005), "Two-dimensional atomic crystals", *Proceedings of the National Academy of Sciences*, Vol.102, No.30, pp.10451–10453.
Novoselov, K. S., Mishchenko, A., Carvalho, A., and Neto, A. H. C., (2016), "2D materials and van der Waals heterostructures", *Science*, Vol.353, No.6298, pp.aac9439.
Ou, J. Z., Ge, W., Carey, B., Daeneke, T., Rotbart, A., Shan, W., Wang, Y., Fu, Z., Chrimes, A. F., Wlodarski, W., and others, (2015), "Physisorption-based charge transfer in two-dimensional SnS2 for selective and reversible NO2 gas sensing", *ACS Nano*, Vol.9, No.10, pp.10313–10323.
Pan, Q., Sun, Y., Su, M., Chen, S., Cai, Z., Zhang, Z., Zou, M., Chen, B., Mikhailova, J. V, Zuev, D., and others, (2022), "Circular Subwavelength Photodetectors for 3D Space Exploration", *Advanced Optical Materials*, Vol.10, No.6, pp.2102163.
Panda, S. K., Antonakos, A., Liarokapis, E., Bhattacharya, S., and Chaudhuri, S., (2007), "Optical properties of nanocrystalline SnS2 thin films", *Materials Research Bulletin*, Vol.42, No.3, pp.576–583.
Panigrahi, P., Hussain, T., Karton, A., and Ahuja, R., (2019), "Elemental substitution of two-dimensional transition metal dichalcogenides (MoSe2 and MoTe2): implications for enhanced gas sensing", *ACS Sensors*, Vol.4, No.10, pp.2646–2653.
Park, J., Mun, J., Shin, J.-S., and Kang, S.-W., (2018), "Highly sensitive two-dimensional MoS2 gas sensor decorated with Pt nanoparticles", *Royal Society Open Science*, Vol.5, No.12, pp.181462.
Park, S., Park, J., Selvaraj, R., and Kim, Y., (2015), "Facile microwave-assisted synthesis of SnS2 nanoparticles for visible-light responsive photocatalyst", *Journal of Industrial and Engineering Chemistry*, Vol.31, pp.269–275.
Park, W., Park, J., Jang, J., Lee, H., Jeong, H., Cho, K., Hong, S., and Lee, T., (2013), "Oxygen environmental and passivation effects on molybdenum disulfide field effect transistors", *Nanotechnology*, Vol.24, No.9, pp.95202.
Patel, C., Verma, V. K., Chaudhary, S., Bhardwaj, R., and Mukherjee, S., (2024), "Synergistic Approach for Controlled Doping in a MoS2 Monolayer for Enhanced NH3 Sensing", *ACS Applied Nano Materials*, Vol.7, No.4, pp.4546–4554.
Pei, J., Yang, J., Xu, R., Zeng, Y.-H., Myint, Y. W., Zhang, S., Zheng, J.-C., Qin, Q., Wang, X., Jiang, W., and others, (2015), "Exciton and trion dynamics in bilayer MoS2", *Small*, Vol.11, No.48, pp.6384–6390.
Perdew, J. P., Burke, K., and Ernzerhof, M., (1998), "Perdew, burke, and ernzerhof reply", *Physical Review Letters*, Vol.80, No.4, pp.891.
Perdew, J. P., Ernzerhof, M., and Burke, K., (1996), "Rationale for mixing exact exchange with density functional approximations", *The Journal of Chemical Physics*, Vol.105, No.22, pp.9982–9985.
Perkampus, H.-H., (2013), "*UV-VIS Spectroscopy and its Applications*". Springer Science \& Business Media.
Perkowitz, S., (2012), "*Optical characterization of semiconductors: infrared, Raman, and photoluminescence spectroscopy*". Elsevier.
Pospischil, A., Humer, M., Furchi, M. M., Bachmann, D., Guider, R., Fromherz, T., and Mueller, T., (2013), "CMOS-compatible graphene photodetector covering all optical communication bands", *Nature Photonics*, Vol.7, No.11, pp.892–896.
Prasad, P., Garg, M., and Chandni, U., (2020), "Tailoring the transfer characteristics and hysteresis in MoS2 transistors using substrate engineering", *Nanoscale*, Vol.12, No.46, pp.23817–23823.
Pyeon, J. J., Baek, I.-H., Song, Y. G., Kim, G. S., Cho, A.-J., Lee, G.-Y., Han, J. H., Chung, T.-M., Hwang, C. S., Kang, C.-Y., and Kim, S. K., (2020a), "Highly sensitive flexible NO2 sensor composed of vertically aligned 2D SnS2 operating at room temperature", *J. Mater. Chem. C*, Vol.8, No.34, pp.11874–11881.
Pyeon, J. J., Baek, I.-H., Song, Y. G., Kim, G. S., Cho, A.-J., Lee, G.-Y., Han, J. H., Chung, T.-M., Hwang, C. S., Kang, C.-Y., and others, (2020b), "Highly sensitive flexible NO 2 sensor composed of vertically aligned 2D SnS 2 operating at room temperature", *Journal of Materials Chemistry C*, Vol.8, No.34, pp.11874–11881.
Qi, X., Ding, C., Gao, M., Wang, F., Hui, Y., Yao, Y., Qu, R., Guo, Y., Zhang, Z., Zhao, W., and Xing, H., (2021), "High-efficient production of mono- to few-layer GaSe nanosheets via a novel Na2CO3-promoted ultrasonic exfoliation method", *Materials Letters*, Vol.305, pp.130747.
Qian, H., Deng, J., Zhou, H., Yang, X., and Chen, W., (2019), "First-principles study of Pd-MoSe2 as sensing material for characteristic SF6 decomposition components", *AIP Advances*, Vol.9, No.12.

Qiang, T., and Xia, Y., (2020), "Facile-controllable synthesis of SnS2 with sulfur vacancy for boosted Cr(VI) photoreduction performance", *Journal of Alloys and Compounds*, Vol.845, pp.156155.

Qin, C., Liu, W., Liu, N., Zhou, Z., Song, J., Ma, S., Jiao, Z.-Y., and Lei, S., (2022), "Observation of hole transfer in MoS2/WS2 van der waals heterostructures", *ACS Photonics*, Vol.9, No.5, pp.1709–1716.

Qin, Z., Xu, K., Yue, H., Wang, H., Zhang, J., Ouyang, C., Xie, C., and Zeng, D., (2018), "Enhanced room-temperature NH3 gas sensing by 2D SnS2 with sulfur vacancies synthesized by chemical exfoliation", *Sensors and Actuators B: Chemical*, Vol.262, pp.771–779.

Qu, A., and Zhang, Y., (2020), "The interaction of gas molecules with aluminum/silicone doped SnS2 nanosheets: A density functional theory investigation", *Computational and Theoretical Chemistry*, Vol.1188, pp.112946.

Ra, H.-S., Kwak, D.-H., and Lee, J.-S., (2016), "A hybrid MoS 2 nanosheet--CdSe nanocrystal phototransistor with a fast photoresponse", *Nanoscale*, Vol.8, No.39, pp.17223–17230.

Rahmati, B., Hajzadeh, I., Taheri, M., Karimzadeh, R., Mohajerzadeh, S., and Mohseni, S. M., (2019), "Plasmonic improvement photoresponse of vertical-MoS2 nanostructure photodetector by Au nanoparticles", *Applied Surface Science*, Vol.490, pp.165–171.

Raizada, P., Nguyen, T. H. C., Patial, S., Singh, P., Bajpai, A., Nguyen, V.-H., Nguyen, D. L. T., Cuong Nguyen, X., Aslam Parwaz Khan, A., Rangabhashiyam, S., Young Kim, S., and Le, Q. Van, (2021), "Toward practical solar-driven photocatalytic water splitting on two-dimensional MoS2 based solid-state Z-scheme and S-scheme heterostructure", *Fuel*, Vol.303, pp.121302.

Ramaraj, S. G., Nundy, S., Zhao, P., Elamaran, D., Tahir, A. A., Hayakawa, Y., Muruganathan, M., Mizuta, H., and Kim, S.-W., (2022), "RF Sputtered Nb-Doped MoS2 Thin Film for Effective Detection of NO2 Gas Molecules: Theoretical and Experimental Studies", *ACS Omega*, Vol.7, No.12, pp.10492–10501.

Ramirez-Torres, A., Turkowski, V., and Rahman, T. S., (2014), "Time-dependent density-matrix functional theory for trion excitations: Application to monolayer MoS 2 and other transition-metal dichalcogenides", *Physical Review B*, Vol.90, No.8, pp.85419.

Rehman, A. ur, Khan, M. F., Shehzad, M. A., Hussain, S., Bhopal, M. F., Lee, S. H., Eom, J., Seo, Y., Jung, J., and Lee, S. H., (2016), "n-MoS2/p-Si solar cells with Al2O3 passivation for enhanced photogeneration", *ACS Applied Materials \& Interfaces*, Vol.8, No.43, pp.29383–29390.

Ren, X., Ma, Q., Ren, P., and Wang, Y., (2018), "Synthesis of nitrogen-doped MoSe2 nanosheets with enhanced electrocatalytic activity for hydrogen evolution reaction", *International Journal of Hydrogen Energy*, Vol.43, No.32, pp.15275–15280.

Richards, P. L., (1994), "Bolometers for infrared and millimeter waves", *Journal of Applied Physics*, Vol.76, No.1, pp.1–24.

Richter, B., Kuhlenbeck, H., Freund, H.-J., and Bagus, P. S., (2004), "Cluster Core-Level Binding-Energy Shifts: The Role of Lattice Strain", *Phys. Rev. Lett.*, Vol.93, No.2, pp.26805.

Rogalski, A., (2005), "HgCdTe infrared detector material: history, status and outlook", *Reports on Progress in Physics*, Vol.68, No.10, pp.2267.

Saha, D., and Kruse, P., (2020), "Editors' Choice—Review—Conductive Forms of MoS2 and Their Applications in Energy Storage and Conversion", *Journal of The Electrochemical Society*, Vol.167, No.12, pp.126517.

Samad, L., Bladow, S. M., Ding, Q., Zhuo, J., Jacobberger, R. M., Arnold, M. S., and Jin, S., (2016), "Layer-controlled chemical vapor deposition growth of MoS2 vertical heterostructures via van der Waals epitaxy", *Acs Nano*, Vol.10, No.7, pp.7039–7046.

Sang, T. Y., Li, T., Yang, Y., Song, Y., Tian, H., Song, R., Wang, C., Hu, X., Yang, Z., Lu, Y., and Chen, W., (2022), "Pd, Rh-decorated Se-vacancy MoSe2 monolayer: A promising candidate for sensing and detecting SO2F2, SOF2, H2S and SO2", *Surfaces and Interfaces*, Vol.33, No.July, pp.1–8.

Sarkar, D., Xie, X., Liu, W., Cao, W., Kang, J., Gong, Y., Kraemer, S., Ajayan, P. M., and Banerjee, K., (2015), "A subthermionic tunnel field-effect transistor with an atomically thin channel", *Nature*, Vol.526, No.7571, pp.91–95.

Senkić, A., Supina, A., Akturk, M., Gadermaier, C., Maiuri, M., Cerullo, G., and Vujičić, N., (2023), "Microscopic investigation of intrinsic defects in CVD grown MoS2 monolayers", *Nanotechnology*, Vol.34, No.47, pp.475705.

Shafiei, M., Bradford, J., Khan, H., Piloto, C., Wlodarski, W., Li, Y., and Motta, N., (2018), "Low-operating temperature NO2 gas sensors based on hybrid two-dimensional SnS2-reduced graphene oxide", *Applied Surface Science*, Vol.462, pp.330–336.

Shao, G., Xue, X.-X., Wu, B., Lin, Y.-C., Ouzounian, M., Hu, T. S., Xu, Y., Liu, X., Li, S., Suenaga, K., and others, (2020), "Template-assisted synthesis of metallic 1T'-Sn0. 3W0. 7S2 nanosheets for hydrogen evolution reaction", *Advanced Functional Materials*, Vol.30, No.5, pp.1906069.

Sharma, A., Varshney, U., Vashishtha, P., Yadav, A., Prajapat, P., Singh, P., and Gupta, G., (2023), "Self-

driven Vis-NIR broadband photodetector based on nano-hedge-like MoS2/WSe2 heterostructure", *Materials Science in Semiconductor Processing*, Vol.164, pp.107611.
Shin, G. H., Park, C., Lee, K. J., Jin, H. J., and Choi, S.-Y., (2020), "Ultrasensitive phototransistor based on WSe2--MoS2 van der Waals heterojunction", *Nano Letters*, Vol.20, No.8, pp.5741–5748.
Sholl, D. S., and Steckel, J. A., (2022), "*Density functional theory: a practical introduction*". John Wiley \& Sons.
Shu, J., Wu, G., Guo, Y., Liu, B., Wei, X., and Chen, Q., (2016), "The intrinsic origin of hysteresis in MoS2 field effect transistors", *Nanoscale*, Vol.8, No.5, pp.3049–3056.
Snow, E. S., Perkins, F. K., and Robinson, J. A., (2006), "Chemical vapor detection using single-walled carbon nanotubes", *Chemical Society Reviews*, Vol.35, No.9, pp.790–798.
Soref, R. A., (1993), "Silicon-based optoelectronics", *Proceedings of the IEEE*, Vol.81, No.12, pp.1687–1706.
Splendiani, A., Sun, L., Zhang, Y., Li, T., Kim, J., Chim, C. Y., Galli, G., and Wang, F., (2010), "Emerging photoluminescence in monolayer MoS2", *Nano Letters*, Vol.10, No.4, pp.1271–1275.
Stevie, F. A., and Donley, C. L., (2020), "Introduction to x-ray photoelectron spectroscopy", *Journal of Vacuum Science \& Technology A*, Vol.38, No.6.
Strand, V., Rak, S., Svartengren, M., and Bylin, G., (1997), "Nitrogen dioxide exposure enhances asthmatic reaction to inhaled allergen in subjects with asthma.", *American Journal of Respiratory and Critical Care Medicine*, Vol.155, No.3, pp.881–887.
Sun, G., Kürti, J., Rajczy, P., Kertesz, M., Hafner, J., and Kresse, G., (2003), "Performance of the Vienna ab initio simulation package (VASP) in chemical applications", *Journal of Molecular Structure: THEOCHEM*, Vol.624, No.1–3, pp.37–45.
Sun, L., Yuan, G., Gao, L., Yang, J., Chhowalla, M., Gharahcheshmeh, M. H., Gleason, K. K., Choi, Y. S., Hong, B. H., and Liu, Z., (2021), "Chemical vapour deposition", *Nature Reviews Methods Primers*, Vol.1, No.1, pp.5.
Sun, Q., Hao, J., Zheng, S., Wan, P., Li, J., Zhang, D., Li, Y., Wang, T., and Wang, Y., (2020a), "2D/2D heterojunction of g--C3N4/SnS2: room-temperature sensing material for ultrasensitive and rapid-recoverable NO2 detection", *Nanotechnology*, Vol.31, No.42, pp.425502.
Sun, Q., Wang, J., Hao, J., Zheng, S., Wan, P., Wang, T., Fang, H., and Wang, Y., (2019), "SnS2/SnS p-n heterojunctions with an accumulation layer for ultrasensitive room-temperature NO2 detection", *Nanoscale*, Vol.11, No.29, pp.13741–13749.
Sun, Y., and Wang, Z., (2020b), "Density Functional Theory Study on the Hydrogen Evolution Reaction in the S-rich SnS2 Nanosheets", *Electrocatalysis*, Vol.11, No.6, pp.604–611.
Swan, M., (2012), "Sensor mania! the internet of things, wearable computing, objective metrics, and the quantified self 2.0", *Journal of Sensor and Actuator Networks*, Vol.1, No.3, pp.217–253.
Sze, S. M., Li, Y., and Ng, K. K., (2021), "*Physics of semiconductor devices*". John wiley \& sons.
Tan, P., Ding, K., Zhang, X., Ni, Z., Ostrikov, K. (Ken), Gu, X., Nan, H., and Xiao, S., (2021), "Bidirectional doping of two-dimensional thin-layer transition metal dichalcogenides using soft ammonia plasma", *Nanoscale*, Vol.13, No.36, pp.15278–15284.
Tang, B., Yu, Z. G., Seng, H. L., Zhang, N., Liu, X., Zhang, Y.-W., Yang, W., and Gong, H., (2018), "Simultaneous edge and electronic control of MoS 2 nanosheets through Fe doping for an efficient oxygen evolution reaction", *Nanoscale*, Vol.10, No.43, pp.20113–20119.
Tang, J., Zhang, X., Xiao, S., and Gui, Y., (2017), "Experimental Analysis of Modified CNTs-Based Gas Sensor",In M. M. Rahman & A. M. Asiri (Eds.), *Electrochemical Sensors Technology*. Rijeka: IntechOpen.
Tao, P., He, J., Shen, T., Hao, Y., Yan, J., Huang, Z., Xu, X., Li, M., and Chen, Y., (2019), "Nitrogen-doped MoS2 foam for fast sodium ion storage", *Advanced Materials Interfaces*, Vol.6, No.13, pp.1900460.
Thai, K. Y., Park, I., Kim, B. J., Hoang, A. T., Na, Y., Park, C. U., Chae, Y., and Ahn, J. H., (n.d.), "MoS2/Graphene Photodetector Array with Strain-Modulated Photoresponse up to the Near-Infrared Regime, ACS Nano. 15 (2021) 12836--12846".
Tillack, B., Zaumseil, P., Morgenstern, G., Krüger, D., Dietrich, B., and Ritter, G., (1995), "Strain compensation in ternary Si1 − x − yGexBy films", *Journal of Crystal Growth*, Vol.157, No.1, pp.181–184.
Timmer, B., Olthuis, W., and Van Den Berg, A., (2005), "Ammonia sensors and their applications—a review", *Sensors and Actuators B: Chemical*, Vol.107, No.2, pp.666–677.
Tong, X., Ashalley, E., Lin, F., Li, H., and Wang, Z. M., (2015), "Advances in MoS 2-based field effect transistors (FETs)", *Nano-Micro Letters*, Vol.7, pp.203–218.
Tongay, S., Zhou, J., Ataca, C., Liu, J., Kang, J. S., Matthews, T. S., You, L., Li, J., Grossman, J. C., and Wu, J., (2013), "Broad-range modulation of light emission in two-dimensional semiconductors by molecular physisorption gating", *Nano Letters*, Vol.13, No.6, pp.2831–2836.
Tsai, M.-Y., Tarasov, A., Hesabi, Z. R., Taghinejad, H., Campbell, P. M., Joiner, C. A., Adibi, A., and Vogel, E. M., (2015), "Flexible MoS2 field-effect transistors for gate-tunable piezoresistive strain sensors", *ACS Applied Materials \& Interfaces*, Vol.7, No.23, pp.12850–12855.

Urban, F., Giubileo, F., Grillo, A., Iemmo, L., Luongo, G., Passacantando, M., Foller, T., Madauß, L., Pollmann, E., Geller, M. P., Oing, D., Schleberger, M., and Di Bartolomeo, A., (2019), "Gas dependent hysteresis in MoS2 field effect transistors", *2D Materials*, Vol.6, No.4, pp.45049.

Varshney, U., Sharma, A., Vashishtha, P., Singh, P., and Gupta, G., (2023), "Highly responsive self-driven broadband photodetector based on MoS2 nanorods/$β$-Ga2O3 heterojunction", *Materials Science in Semiconductor Processing*, Vol.164, pp.107612.

Vashishtha, P., Prajapat, P., Sharma, A., Singh, P., Walia, S., and Gupta, G., (2023), "Self-Driven UVC--NIR Broadband Photodetector with High-Temperature Reliability Based on a Coco Palm-Like MoS2/GaN Heterostructure", *ACS Applied Electronic Materials*, Vol.5, No.3, pp.1891–1902.

Vivien, L., Osmond, J., Fédéli, J.-M., Marris-Morini, D., Crozat, P., Damlencourt, J.-F., Cassan, E., Lecunff, Y., and Laval, S., (2009), "42 GHz pin Germanium photodetector integrated in a silicon-on-insulator waveguide", *Optics Express*, Vol.17, No.8, pp.6252–6257.

Voiry, D., Salehi, M., Silva, R., Fujita, T., Chen, M., Asefa, T., Shenoy, V. B., Eda, G., and Chhowalla, M., (2013), "Conducting MoS2 nanosheets as catalysts for hydrogen evolution reaction", *Nano Letters*, Vol.13, No.12, pp.6222–6227.

Wadhwa, R., Agrawal, A. V, and Kumar, M., (2021a), "A strategic review of recent progress, prospects and challenges of MoS2-based photodetectors", *Journal of Physics D: Applied Physics*, Vol.55, No.6, pp.63002.

Wadhwa, R., Agrawal, A. V, Kushavah, D., Mushtaq, A., Pal, S. K., and Kumar, M., (2021b), "Investigation of charge transport and band alignment of MoS2-ReS2 heterointerface for high performance and self-driven broadband photodetection", *Applied Surface Science*, Vol.569, pp.150949.

Wadhwa, R., Ghosh, A., Kumar, D., Kumar, P., and Kumar, M., (2022a), "Platinum nanoparticle sensitized plasmonic-enhanced broad spectral photodetection in large area vertical-aligned MoS2 flakes", *Nanotechnology*, Vol.33, No.25, pp.255702.

Wadhwa, R., Kumar, A., Sarkar, R., Mohanty, P. P., Kumar, D., Deswal, S., Kumar, P., Ahuja, R., Chakraborty, S., Kumar, M., and Kumar, M., (2022b), "Pt Nanoparticles on Vertically Aligned Large-Area MoS2 Flakes for Selective H2 Sensing at Room Temperature", *ACS Applied Nano Materials*.

Wadhwa, R., Kumar, A., Sarkar, R., Mohanty, P. P., Kumar, D., Deswal, S., Kumar, P., Ahuja, R., Chakraborty, S., Kumar, M., and others, (2023), "Pt Nanoparticles on Vertically Aligned Large-Area MoS2 Flakes for Selective H2 Sensing at Room Temperature", *ACS Applied Nano Materials*, Vol.6, No.4, pp.2527–2537.

Walsh, P. T., (1996), "Toxic gas sensing for the workplace", *Measurement and Control*, Vol.29, No.1, pp.5–12.

Walters, W. W., and Hastings, M. G., (2018), "Collection of ammonia for high time-resolved nitrogen isotopic characterization utilizing an acid-coated honeycomb denuder", *Analytical Chemistry*, Vol.90, No.13, pp.8051–8057.

Wang, F., Li, G., Zheng, J., Ma, J., Yang, C., and Wang, Q., (2018), "Hydrothermal synthesis of flower-like molybdenum disulfide microspheres and their application in electrochemical supercapacitors", *RSC Advances*, Vol.8, No.68, pp.38945–38954.

Wang, H., Nie, S., Li, H., Ali, R., Fu, J., Xiong, H., Li, J., Wu, Z., Lau, W. M., Mahmood, N., Jia, R., Liu, Y., and Jian, X., (2019), "3D Hollow Quasi-Graphite Capsules/Polyaniline Hybrid with a High Performance for Room-Temperature Ammonia Gas Sensors", *ACS Sensors*, Vol.4, No.9, pp.2343–2350.

Wang, J., Huang, J., Huang, S., Notohara, H., Urita, K., Moriguchi, I., and Wei, M., (2020a), "Rational design of hierarchical SnS2 microspheres with S vacancy for enhanced sodium storage performance", *ACS Sustainable Chemistry \& Engineering*, Vol.8, No.25, pp.9519–9525.

Wang, L., Jie, J., Shao, Z., Zhang, Q., Zhang, X., Wang, Y., Sun, Z., and Lee, S.-T., (2015a), "MoS2/Si heterojunction with vertically standing layered structure for ultrafast, high-detectivity, self-driven visible--near infrared photodetectors", *Advanced Functional Materials*, Vol.25, No.19, pp.2910–2919.

Wang, Q. H., Kalantar-Zadeh, K., Kis, A., Coleman, J. N., and Strano, M. S., (2012), "Electronics and optoelectronics of two-dimensional transition metal dichalcogenides", *Nature Nanotechnology*, Vol.7, No.11, pp.699–712.

Wang, W., Klots, A., Prasai, D., Yang, Y., Bolotin, K. I., and Valentine, J., (2015b), "Hot electron-based near-infrared photodetection using bilayer MoS2", *Nano Letters*, Vol.15, No.11, pp.7440–7444.

Wang, X., Zhang, Y., Si, H., Zhang, Q., Wu, J., Gao, L., Wei, X., Sun, Y., Liao, Q., Zhang, Z., and others, (2020b), "Single-atom vacancy defect to trigger high-efficiency hydrogen evolution of MoS2", *Journal of the American Chemical Society*, Vol.142, No.9, pp.4298–4308.

Wang, Y., Zhou, Y., Li, J., Zhang, R., Zhao, H., and Wang, Y., (2022), "Ag decoration-enabled sensitization enhancement of black phosphorus nanosheets for trace NO2 detection at room temperature", *Journal of Hazardous Materials*, Vol.435, pp.129086.

Wei, T.-Y., Yeh, P.-H., Lu, S.-Y., and Wang, Z. L., (2009), "Gigantic enhancement in sensitivity using Schottky contacted nanowire nanosensor", *Journal of the American Chemical Society*, Vol.131, No.48,

pp.17690–17695.
Wilson, J. A., and Yoffe, A. D., (1969), "The transition metal dichalcogenides discussion and interpretation of the observed optical, electrical and structural properties", *Advances in Physics*, Vol.18, No.73, pp.193–335.
Wu, J., Feng, S., Li, Z., Tao, K., Chu, J., Miao, J., and Norford, L. K., (2018a), "Boosted sensitivity of graphene gas sensor via nanoporous thin film structures", *Sensors and Actuators B: Chemical*, Vol.255, pp.1805–1813.
Wu, R., Yan, K., Zhao, J., Cai, Z., Jian, S., and Qiu, L., (2023), "2D/2D SnS2/SnSe2 van der Waals heterostructure for highly sensitive room-temperature NO2 sensor: Key role of interface contact", *Chemical Engineering Journal*, Vol.466, pp.143369.
Wu, S., Huang, C., Aivazian, G., Ross, J. S., Cobden, D. H., and Xu, X., (2013), "Vapor--solid growth of high optical quality MoS2 monolayers with near-unity valley polarization", *ACS Nano*, Vol.7, No.3, pp.2768–2772.
Wu, W., Zhang, Q., Zhou, X., Li, L., Su, J., Wang, F., and Zhai, T., (2018b), "Self-powered photovoltaic photodetector established on lateral monolayer MoS2-WS2 heterostructures", *Nano Energy*, Vol.51, pp.45–53.
Wu, Y.-C., Liu, C.-H., Chen, S.-Y., Shih, F.-Y., Ho, P.-H., Chen, C.-W., Liang, C.-T., and Wang, W.-H., (2015), "Extrinsic Origin of Persistent Photoconductivity in Monolayer MoS2 Field Effect Transistors", *Scientific Reports*, Vol.5, No.1, pp.11472.
Xia, C., Zhao, X., Peng, Y., Zhang, H., Wei, S., and Jia, Y., (2015), "First-principles study of group V and VII impurities in SnS2", *Superlattices and Microstructures*, Vol.85, pp.664–671.
Xiao, H., Liang, T., and Xu, M., (2019), "Growth of Ultraflat PbI2 Nanoflakes by Solvent Evaporation Suppression for High-Performance UV Photodetectors", *Small*, Vol.15, No.33, pp.1901767.
Xiao, W., Liu, P., Zhang, J., Song, W., Feng, Y. P., Gao, D., and Ding, J., (2017), "Dual-Functional N Dopants in Edges and Basal Plane of MoS2 Nanosheets Toward Efficient and Durable Hydrogen Evolution", *Advanced Energy Materials*, Vol.7, No.7, pp.1602086.
Xie, C., Mak, C., Tao, X., and Yan, F., (2017a), "Photodetectors based on two-dimensional layered materials beyond graphene", *Advanced Functional Materials*, Vol.27, No.19, pp.1603886.
Xie, J., Zhang, J., Li, S., Grote, F., Zhang, X., Zhang, H., Wang, R., Lei, Y., Pan, B., and Xie, Y., (2013), "Controllable Disorder Engineering in Oxygen-Incorporated MoS2 Ultrathin Nanosheets for Efficient Hydrogen Evolution", *Journal of the American Chemical Society*, Vol.135, No.47, pp.17881–17888.
Xie, Y., Zhang, B., Wang, S., Wang, D., Wang, A., Wang, Z., Yu, H., Zhang, H., Chen, Y., Zhao, M., and others, (2017b), "Ultrabroadband MoS2 photodetector with spectral response from 445 to 2717 nm", *Advanced Materials*, Vol.29, No.17, pp.1605972.
Xin, Y., Wang, X., Chen, Z., Weller, D., Wang, Y., Shi, L., Ma, X., Ding, C., Li, W., Guo, S., and others, (2020), "Polarization-sensitive self-powered type-II GeSe/MoS2 van der Waals heterojunction photodetector", *ACS Applied Materials \& Interfaces*, Vol.12, No.13, pp.15406–15413.
Xiong, Y., Xu, W., Ding, D., Lu, W., Zhu, L., Zhu, Z., Wang, Y., and Xue, Q., (2018), "Ultra-sensitive NH3 sensor based on flower-shaped SnS2 nanostructures with sub-ppm detection ability", *Journal of Hazardous Materials*, Vol.341, pp.159–167.
Xu, K., Ha, N., Hu, Y., Ma, Q., Chen, W., Wen, X., Ou, R., Trinh, V., McConville, C. F., Zhang, B. Y., and others, (2022), "A room temperature all-optical sensor based on two-dimensional SnS2 for highly sensitive and reversible NO2 sensing", *Journal of Hazardous Materials*, Vol.426, pp.127813.
Xu, Y., Xie, J., Zhang, Y., Tian, F., Yang, C., Zheng, W., Liu, X., Zhang, J., and Pinna, N., (2021), "Edge-enriched WS2 nanosheets on carbon nanofibers boosts NO2 detection at room temperature", *Journal of Hazardous Materials*, Vol.411, pp.125120.
Xu, Z., Lin, S., Li, X., Zhang, S., Wu, Z., Xu, W., Lu, Y., and Xu, S., (2016), "Monolayer MoS2/GaAs heterostructure self-driven photodetector with extremely high detectivity", *Nano Energy*, Vol.23, pp.89–96.
Xue, Y., Zhang, Y., Liu, Y., Liu, H., Song, J., Sophia, J., Liu, J., Xu, Z., Xu, Q., Wang, Z., and others, (2016), "Scalable production of a few-layer MoS2/WS2 vertical heterojunction array and its application for photodetectors", *Acs Nano*, Vol.10, No.1, pp.573–580.
Yamazoe, N., (1991), "New approaches for improving semiconductor gas sensors", *Sensors and Actuators B: Chemical*, Vol.5, No.1, pp.7–19.
Yamazoe, N., (2005), "Toward innovations of gas sensor technology", *Sensors and Actuators B: Chemical*, Vol.108, No.1–2, pp.2–14.
Yan, J., Wang, Y., Yang, C., Deng, H., and Hu, N., (2024), "MoS2/MoO3 heterojunctions enabled by surface oxidization of MoS2 nanosheets for high-performance room-temperature NO2 gas sensing", *Journal of Alloys and Compounds*, Vol.976, pp.173208.

Yang, L., Cui, X., Zhang, J., Wang, K., Shen, M., Zeng, S., Dayeh, S. A., Feng, L., and Xiang, B., (2014), "Lattice strain effects on the optical properties of MoS2 nanosheets", *Scientific Reports*, Vol.4, No.1, pp.1–7.

Yang, S., Jiang, C., and Wei, S., (2017a), "Gas sensing in 2D materials", *Applied Physics Reviews*, Vol.4, No.2.

Yang, T., Zheng, B., Wang, Z., Xu, T., Pan, C., Zou, J., Zhang, X., Qi, Z., Liu, H., Feng, Y., and others, (2017b), "Van der Waals epitaxial growth and optoelectronics of large-scale WSe2/SnS2 vertical bilayer p--n junctions", *Nature Communications*, Vol.8, No.1, pp.1906.

Yang, Z., Su, C., Wang, S., Han, Y., Chen, X., Xu, S., Zhou, Z., Hu, N., Su, Y., and Zeng, M., (2019), "Highly sensitive NO2 gas sensors based on hexagonal SnS2 nanoplates operating at room temperature", *Nanotechnology*, Vol.31, No.7, pp.75501.

Ye, M., Winslow, D., Zhang, D., Pandey, R., and Yap, Y. K., (2015), "Recent advancement on the optical properties of two-dimensional molybdenum disulfide (MoS2) thin films",In *Photonics* (Vol. 2, pp. 288–307).

Ye, W. N., and Xiong, Y., (2013), "Review of silicon photonics: history and recent advances", *Journal of Modern Optics*, Vol.60, No.16, pp.1299–1320.

Yim, W., Nguyen, V. T., Phung, Q. T., Kim, H. S., Ahn, Y. H., Lee, S., and Park, J.-Y., (2022), "Imaging Spatial Distribution of Photogenerated Carriers in Monolayer MoS2 with Kelvin Probe Force Microscopy", *ACS Applied Materials & Interfaces*, Vol.14, No.22, pp.26295–26302.

Yin, M., Wang, Y., Yu, L., Wang, H., Zhu, Y., and Li, C., (2020), "Ag nanoparticles-modified Fe2O3@MoS2 core-shell micro/nanocomposites for high-performance NO2 gas detection at low temperature", *Journal of Alloys and Compounds*, Vol.829, pp.154471.

Yin, Z., Li, H., Li, H., Jiang, L., Shi, Y., Sun, Y., Lu, G., Zhang, Q., Chen, X., and Zhang, H., (2012), "Single-layer MoS2 phototransistors", *ACS Nano*, Vol.6, No.1, pp.74–80.

Yoo, D., Kim, M., Jeong, S., Han, J., and Cheon, J., (2014), "Chemical Synthetic Strategy for Single-Layer Transition-Metal Chalcogenides", *Journal of the American Chemical Society*, Vol.136, No.42, pp.14670–14673.

Yu, W. J., Liu, Y., Zhou, H., Yin, A., Li, Z., Huang, Y., and Duan, X., (2013), "Highly efficient gate-tunable photocurrent generation in vertical heterostructures of layered materials", *Nature Nanotechnology*, Vol.8, No.12, pp.952–958.

Yue, Q., Shao, Z., Chang, S., and Li, J., (2013), "Adsorption of gas molecules on monolayer MoS 2 and effect of applied electric field", *Nanoscale Research Letters*, Vol.8, pp.1–7.

Yunusa, Z., Hamidon, M. N., Kaiser, A., and Awang, Z., (2014), "Gas sensors: a review", *Sens. Transducers*, Vol.168, No.4, pp.61–75.

Zavabeti, A., Jannat, A., Zhong, L., Haidry, A. A., Yao, Z., and Ou, J. Z., (2020), "Two-Dimensional Materials in Large-Areas: Synthesis, Properties and Applications", *Nano-Micro Letters*, Vol.12, No.1, pp.66.

Zeng, L., Tao, L., Tang, C., Zhou, B., Long, H., Chai, Y., Lau, S. P., and Tsang, Y. H., (2016), "High-responsivity UV-Vis photodetector based on transferable WS2 film deposited by magnetron sputtering", *Scientific Reports*, Vol.6, No.1, pp.20343.

Zhan, S., Zheng, L., Xiao, Y., and Zhao, L.-D., (2020), "Phonon and Carrier Transport Properties in Low-Cost and Environmentally Friendly SnS2: A Promising Thermoelectric Material", *Chemistry of Materials*, Vol.32, No.24, pp.10348–10356.

Zhang, B., Cheng, M., Liu, G., Gao, Y., Zhao, L., Li, S., Wang, Y., Liu, F., Liang, X., Zhang, T., and others, (2018a), "Room temperature NO2 gas sensor based on porous Co3O4 slices/reduced graphene oxide hybrid", *Sensors and Actuators B: Chemical*, Vol.263, pp.387–399.

Zhang, B., Liu, G., Cheng, M., Gao, Y., Zhao, L., Li, S., Liu, F., Yan, X., Zhang, T., Sun, P., and others, (2018b), "The preparation of reduced graphene oxide-encapsulated $α$-Fe2O3 hybrid and its outstanding NO2 gas sensing properties at room temperature", *Sensors and Actuators B: Chemical*, Vol.261, pp.252–263.

Zhang, B., Liu, Y., Liang, T., Sakthivel, T., Yu, L., and Dai, Z., (2020a), "Activating the basal plane of defective SnS2 nanosheets for NH3 gas sensing", *ACS Applied Nano Materials*, Vol.3, No.5, pp.4642–4653.

Zhang, D., Wu, Z., Li, P., Zong, X., Dong, G., and Zhang, Y., (2018c), "Facile fabrication of polyaniline/multi-walled carbon nanotubes/molybdenum disulfide ternary nanocomposite and its high-performance ammonia-sensing at room temperature", *Sensors and Actuators B: Chemical*, Vol.258, pp.895–905.

Zhang, J., Yu, H., Chen, W., Tian, X., Liu, D., Cheng, M., Xie, G., Yang, W., Yang, R., Bai, X., and others, (2014a), "Scalable growth of high-quality polycrystalline MoS2 monolayers on SiO2 with tunable grain sizes", *ACS Nano*, Vol.8, No.6, pp.6024–6030.

Zhang, L., Khan, K., Zou, J., Zhang, H., and Li, Y., (2019), "Recent advances in emerging 2D material-based

gas sensors: potential in disease diagnosis", *Advanced Materials Interfaces*, Vol.6, No.22, pp.1901329.
Zhang, L., Liu, K., Wong, A. B., Kim, J., Hong, X., Liu, C., Cao, T., Louie, S. G., Wang, F., and Yang, P., (2014b), "Three-dimensional spirals of atomic layered MoS2", *Nano Letters*, Vol.14, No.11, pp.6418–6423.
Zhang, W., Huang, J.-K., Chen, C.-H., Chang, Y.-H., Cheng, Y.-J., and Li, L.-J., (2013), "High-gain phototransistors based on a CVD MoS2 monolayer", *Advanced Materials*, Vol.25, No.25, pp.3456–3461.
Zhang, W., Xiao, X., Zeng, X., Li, Y., Zheng, L., and Wan, C., (2016), "Enhanced photocatalytic activity of TiO2 nanoparticles using SnS2/RGO hybrid as co-catalyst: DFT study and photocatalytic mechanism", *Journal of Alloys and Compounds*, Vol.685, pp.774–783.
Zhang, X., Huang, X., Xue, M., Ye, X., Lei, W., Tang, H., and Li, C., (2015), "Hydrothermal synthesis and characterization of 3D flower-like MoS2 microspheres", *Materials Letters*, Vol.148, pp.67–70.
Zhang, X., Xiao, S., Nan, H., Mo, H., Wan, X., Gu, X., and Ostrikov, K. K., (2018d), "Controllable one-step growth of bilayer MoS2--WS2/WS2 heterostructures by chemical vapor deposition", *Nanotechnology*, Vol.29, No.45, pp.455707.
Zhang, Y., Huang, P., Guo, J., Shi, R., Huang, W., Shi, Z., Wu, L., Zhang, F., Gao, L., Li, C., and others, (2020b), "Graphdiyne-based flexible photodetectors with high responsivity and detectivity", *Advanced Materials*, Vol.32, No.23, pp.2001082.
Zhao, K., Chang, X., Zhang, J., Yuan, F., and Liu, X., (2023a), "Electronic Modulation of MoS2 Nanosheets by N-Doping for Highly Sensitive NO2 Detection at Room Temperature", *ACS Sensors*, Vol.9, No.1, pp.388–397.
Zhao, K., Chang, X., Zhang, J., Yuan, F., and Liu, X., (2024a), "Electronic Modulation of MoS2 Nanosheets by N-Doping for Highly Sensitive NO2 Detection at Room Temperature", *ACS Sensors*, Vol.9, No.1, pp.388–397.
Zhao, M., Casiraghi, C., and Parvez, K., (2024b), "Electrochemical exfoliation of 2D materials beyond graphene", *Chemical Society Reviews*, Vol.53, No.6, pp.3036–3064.
Zhao, P., Desai, S., Tosun, M., Roy, T., Fang, H., Sachid, A., Amani, M., Hu, C., and Javey, A., (2015), "2D layered materials: from materials properties to device applications",In *2015 IEEE International Electron Devices Meeting (IEDM)* (pp. 23–27).
Zhao, R., Wang, T., Zhao, M., Xia, C., Zhao, X., An, Y., and Dai, X., (2017a), "A theoretical simulation of small-molecules sensing on an S-vacancy SnS 2 monolayer", *Physical Chemistry Chemical Physics*, Vol.19, No.16, pp.10470–10480.
Zhao, R., Wang, T., Zhao, M., Xia, C., Zhao, X., An, Y., and Dai, X., (2017b), "A theoretical simulation of small-molecules sensing on an S-vacancy SnS2 monolayer", *Physical Chemistry Chemical Physics*, Vol.19, No.16, pp.10470–10480.
Zhao, W., Ribeiro, R. M., Toh, M., Carvalho, A., Kloc, C., Castro Neto, A. H., and Eda, G., (2013a), "Origin of indirect optical transitions in few-layer MoS2, WS2, and WSe2", *Nano Letters*, Vol.13, No.11, pp.5627–5634.
Zhao, W., Yan, R., Li, H., Ding, K., Chen, Y., and Xu, D., (2023b), "Highly sensitive NO2 gas sensor with a low detection limit based on Pt-modified MoS2 flakes", *Materials Letters*, Vol.330, pp.133386.
Zhao, Y., Luo, X., Li, H., Zhang, J., Araujo, P. T., Gan, C. K., Wu, J., Zhang, H., Quek, S. Y., Dresselhaus, M. S., and others, (2013b), "Interlayer breathing and shear modes in few-trilayer MoS2 and WSe2", *Nano Letters*, Vol.13, No.3, pp.1007–1015.
Zheng, S., Li, Y., Hao, J., Fang, H., Yuan, Y., Tsai, H.-S., Sun, Q., Wan, P., Zhang, X., and Wang, Y., (2021), "Hierarchical assembly of graphene-bridged SnO2-rGO/SnS2 heterostructure with interfacial charge transfer highway for high-performance NO2 detection", *Applied Surface Science*, Vol.568, pp.150926.
Zhou, J., Xue, K., Liu, Y., Liang, T., Zhang, P., Zhang, X., Zhang, W., and Dai, Z., (2021), "Highly sensitive NO2 response and abnormal PN sensing transition with ultrathin Mo-doped SnS2 nanosheets", *Chemical Engineering Journal*, Vol.420, pp.127572.
Zhou, W., Hou, D., Sang, Y., Yao, S., Zhou, J., Li, G., Li, L., Liu, H., and Chen, S., (2014), "MoO 2 nanobelts@ nitrogen self-doped MoS 2 nanosheets as effective electrocatalysts for hydrogen evolution reaction", *Journal of Materials Chemistry A*, Vol.2, No.29, pp.11358–11364.
Zhou, X., Zhang, Q., Gan, L., Li, H., and Zhai, T., (2016), "Large-Size Growth of Ultrathin SnS2 Nanosheets and High Performance for Phototransistors", *Advanced Functional Materials*, Vol.26, No.24, pp.4405–4413.
Zhu, Z. Y., Cheng, Y. C., and Schwingenschlögl, U., (2011), "Giant spin-orbit-induced spin splitting in two-dimensional transition-metal dichalcogenide semiconductors", *Physical Review B – Condensed Matter and Materials Physics*, Vol.84, No.15, pp.153402.
Zivin, J. G., and Neidell, M., (2012), "The impact of pollution on worker productivity", *American Economic Review*, Vol.102, No.7, pp.3652–3673.

Zou, J., Ke, Y., Zhou, X., Huang, Y., Du, W., Lin, L., Wei, S., Luo, L., Liu, H., Li, C., and others, (2022), "Broadband Visible- Near Infrared Two-Dimensional WSe2/In2Se3 Photodetector for Underwater Optical Communications", *Advanced Optical Materials*, Vol.10, No.12, pp.2200143.